

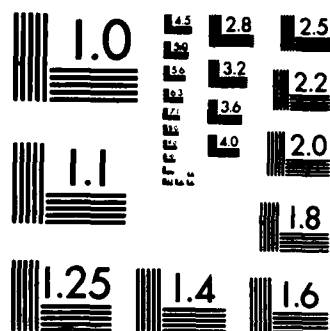
AD-A174 586 CALCULATIONS OF THE FORMATION AND TRANSPORT OF HIGH 1/3

1/3

N00014-81-C-0704

NL

This figure displays a 10x10 grid of 100 small, dark, rectangular images. These images appear to be a subset of the handwritten digit dataset described in the text, showing various examples of digits (0-9) in a noisy, low-contrast format. The grid is used to illustrate the data used for training and testing the proposed model.



MICROCOPY RESOLUTION TEST CHART
NATIONAL BUREAU OF STANDARDS-1963-A

AD-A174 586

I-ARA-86-U-44

12

CALCULATIONS OF THE FORMATION AND TRANSPORT OF
HIGH QUALITY, HIGH CURRENT RELATIVISTIC ELECTRON BEAMS

J. R. Thompson
M. L. Sloan
B. N. Moore
J. R. Uglum

DTIC
ELECTE
NOV 26 1986
S D

Austin Research Associates
1901 Rutland Drive
Austin, Texas 78758

Submitted to the
OFFICE OF NAVAL RESEARCH

OCTOBER 1986

Final Technical Report
Contract No. ONR N00014-81-C-0704

Approved for public release; distribution unlimited.
Reproduction in whole or in part is permitted for any purpose
of the United States Government.

86 11 26 001

DTIC FILE COPY

CALCULATIONS OF THE FORMATION AND TRANSPORT OF
HIGH QUALITY, HIGH CURRENT RELATIVISTIC ELECTRON BEAMS

J. R. Thompson
M. L. Sloan
B. N. Moore
J. R. Uglum

Austin Research Associates
1901 Rutland Drive
Austin, Texas 78758

Submitted to the
OFFICE OF NAVAL RESEARCH

OCTOBER 1986

Final Technical Report
Contract No. ONR N00014-81-C-0704

Approved for public release; distribution unlimited.
Reproduction in whole or in part is permitted for any purpose
of the United States Government.



Accession For	
NTIS CRA&I	<input checked="" type="checkbox"/>
DTIC TAB	<input type="checkbox"/>
Unannounced	<input type="checkbox"/>
Justification	
By	
Distribution /	
Availability Codes	
Dist	Avail and/or Special
A-1	

REPORT DOCUMENTATION PAGE

1a. REPORT SECURITY CLASSIFICATION UNCLASSIFIED			1b. RESTRICTIVE MARKINGS	
2a. SECURITY CLASSIFICATION AUTHORITY N/A since UNCLASSIFIED			3 DISTRIBUTION / AVAILABILITY OF REPORT Approved for public release; distribution unlimited.	
2b. DECLASSIFICATION / DOWNGRADING SCHEDULE N/A since UNCLASSIFIED				
4. PERFORMING ORGANIZATION REPORT NUMBER(S) I-ARA-86-U-44			5. MONITORING ORGANIZATION REPORT NUMBER(S)	
6a. NAME OF PERFORMING ORGANIZATION Austin Research Associates		6b. OFFICE SYMBOL (If applicable)	7a. NAME OF MONITORING ORGANIZATION Office of Naval Research	
6c. ADDRESS (City, State, and ZIP Code) 1901 Rutland Drive Austin, Texas 78758			7b. ADDRESS (City, State, and ZIP Code) Physics Division, Code 421 Arlington, VA 22217	
8a. NAME OF FUNDING / SPONSORING ORGANIZATION Office of Naval Research		8b. OFFICE SYMBOL (If applicable)	9. PROCUREMENT INSTRUMENT IDENTIFICATION NUMBER ONR N00014-81-C-0704	
8c. ADDRESS (City, State, and ZIP Code) Department of the Navy 800 N. Quincy Street Arlington, Virginia 22217			10. SOURCE OF FUNDING NUMBERS	
			PROGRAM ELEMENT NO.	PROJECT NO.
11. TITLE (Include Security Classification) CALCULATIONS OF THE FORMATION AND TRANSPORT OF HIGH QUALITY, HIGH CURRENT RELATIVISTIC ELECTRON BEAMS (U)				
12. PERSONAL AUTHOR(S) J. R. Thompson, M. L. Sloan, B. N. Moore, and J. R. Uglum				
13a. TYPE OF REPORT Final Technical Report		13b. TIME COVERED FROM 8-1-81 TO 7-31-85	14. DATE OF REPORT (Year, Month, Day) October 1986	15. PAGE COUNT 245
16. SUPPLEMENTARY NOTATION				
17. COSATI CODES			18. SUBJECT TERMS (Continue on reverse if necessary and identify by block number) high quality electron beams emittance growth high current beam transport	
FIELD	GROUP	SUB-GROUP		
19. ABSTRACT (Continue on reverse if necessary and identify by block number) This report reviews the results of calculations of the formation and transport of high quality, high current relativistic electron beams. As a prototype, we examined beam injection and transport through the Long Pulse Induction Linac (LPIL) system operated at the Naval Research Laboratory from 1980-1984. In order to have a well-behaved injector diode without significant diode closure during the beam pulse, it is necessary to have a large area cathode with a wide anode-cathode gap spacing. Introduction of electrodes to control the equipotential grading in the A-K gap, (and arranged to have sub-Child-Langmuir electric field stresses near the cathode) was found to allow the formation and injection of a high quality, laminar, convergent beam into the LPIL transport system. By exercising a one-dimensional beam envelope code and a steady state, two-dimensional (x,z) beam transport code, it was possible to obtain transport coil current settings to minimize current loss through the (Continued)				
20. DISTRIBUTION / AVAILABILITY OF ABSTRACT <input type="checkbox"/> UNCLASSIFIED/UNLIMITED <input checked="" type="checkbox"/> SAME AS RPT. <input type="checkbox"/> DTIC USERS			21. ABSTRACT SECURITY CLASSIFICATION UNCLASSIFIED	
22a. NAME OF RESPONSIBLE INDIVIDUAL C. W. Roberson			22b. TELEPHONE (Include Area Code) (202) 696-4220	22c. OFFICE SYMBOL Code 421

ABSTRACT (Continued)

complex beam transport system. However, radial expansions and abrupt contraction in the conducting walls plus strong axial acceleration in the induction gaps of the accelerator were found to introduce perturbations to the radial beam forces which drive oscillations in the beam envelope. The largest radial oscillations were excited when the beam was injected into a strong solenoidal magnetic field to compress its size by an order of magnitude prior to transport into an FEL wiggler. A Hamiltonian analysis was performed of the beam cyclotron oscillations excited during beam transport. It was shown that the beam emittance may be related to the action $J = \oint p dq$, which is preserved when the axial gradients in the radial beam forces are low enough that J is adiabatically invariant. However, sudden beam compression at the entrance to the wiggler solenoid was predicted to excite large amplitude cyclotron oscillations on the beam which would phase mix to create the dominant source of emittance growth for this particular transport system. Calculations were also performed of the beam quality achievable in a high current, magnetic field-immersed diode. It was found that the best beam quality results from gently-shaped anode and cathode structures which create electric fields whose radial components have long axial gradient lengths. When the diode axial magnetic field strength is high enough that the beam electrons are tied to the field lines and the inverse cyclotron wave number is below the axial gradient length of the radial diode forces, extremely high quality electron beams can be created. Beam emittance up to two orders of magnitude below the Lawson-Penner emittance was observed in some cases.

TABLE OF CONTENTS

<u>Section</u>	<u>Page</u>
<p>I. CALCULATIONS OF THE FORMATION AND TRANSPORT OF HIGH QUALITY, HIGH CURRENT RELATIVISTIC ELECTRON BEAMS - - - - -</p>	1
<p>II. LIST OF REFERENCES - - - - -</p>	28

APPENDICES

<p>A Letter Progress Report, dated April 2, 1982, from Dr. James R. Thompson to Dr. C. W. Roberson - - - -</p>	29
<p>B Letter Progress Report, dated April 27, 1982, from Dr. James R. Thompson to Dr. C. W. Roberson - - - -</p>	61
<p>C Letter Progress Report, dated May 13, 1982, from Dr. James R. Thompson to Dr. C. W. Roberson - - - -</p>	91
<p>D Letter Progress Report, dated June 29, 1982, from Dr. Barry N. Moore to Dr. C. W. Roberson - - - - -</p>	127
<p>E Review of Beam Formation and Transport Through an Induction Linac - - - - -</p>	159
<p>F Review of Previous Results on Beam Transport Studies - - - - -</p>	185
<p>G Beam Emittance Due to Excitation and Phase Mixing of Cyclotron Oscillations - - - - -</p>	213
<p>H A Brief Note on Beam Quality in High Current, Field-Immersed Diodes - - - - -</p>	229

I. CALCULATIONS OF THE FORMATION AND TRANSPORT OF HIGH QUALITY, HIGH CURRENT RELATIVISTIC ELECTRON BEAMS

Our research on the formation and transport of high quality, high current relativistic electron beams began in August 1981 under Contract ONR N00014-81-C-0704 and continued for four years until July 31, 1985. During the latter portion of this contract, work was also initiated on the subject of the phase area displacement mode of free electron laser operation. This latter work has been continued under Contract ONR N00014-86-C-0088 and will be documented in the reports for that contract. Therefore, this final technical report for Contract ONR N00014-81-C-0704 will be confined to the subject of the formation and transport of high quality, high current electron beams.

The initial impetus for research on this topic derived from the early appreciation of the difficult tradeoff which appeared between higher current beams and higher quality beams. For a variety of applications of relativistic electron beams, including their employment as drivers of free electron laser radiation, performance enhancement requires increasing both the beam current and the beam quality. Unfortunately, it was discovered that because of space charge effects, higher current beams tend to possess diminished beam quality and, conversely,

higher quality beams can often be produced only at the expense of some reduction in beam current.

The importance of the electron beam driver being of high quality, with low emittance and low energy spread, in order to achieve high gain FEL operation and reduce competition from other radiation mechanisms driven by transverse beam thermal energy has long been well recognized (Refs. 1,2,3). Although higher electron currents tend to produce higher FEL gain due to more electrons participating in the FEL interaction, this result may not be achieved if the beam quality is reduced. In fact, linear gain can plummet if the electron beam quality is degraded enough.

The tradeoff which must be confronted between beam current and beam quality is illustrated by the empirical Lawson-Penner relation (Refs. 4,5)

$$\frac{\epsilon_n}{\pi} = \gamma \beta r \theta = 0.35 \left[I_e (\text{kA}) \right]^{\frac{1}{2}} \text{ rad-cm} \quad (1)$$

where ϵ_n is the normalized beam emittance. Large dividends from improved FEL performance will accrue to the extent that this empirical standard can be surpassed through dedicated and clever beam design. It was one of the primary goals of the research performed under this contract to explore the physics of beam formation and transport which causes the beam emittance to tend to worsen (i.e., increase) with increased current. It was hoped that out of such understanding might emerge design techniques for delivering relatively lower emittance beams at higher currents.

As a prototype for our studies, we selected the Long Pulse Induction Linac (LPIL), which was built at the National Bureau of Standards (Ref. 6) and operated at the Naval Research Laboratory (Refs. 3,7) from 1980-1984. The device is illustrated in Figure 1 and had nominal operating parameters of 0.8 MeV, 0.8 kA, and a pulse time of 2 μ sec. The electron accelerator consisted of two major components, an injector and an induction accelerator module, with magnetic focusing coils and solenoids arrayed axially along the system to assist in beam transport. Downstream of the final focusing coil shown in Figure 1, the electron beam was strongly compressed and injected into a wiggler solenoid for the production of free electron laser radiation.

The desired objective of our design studies was to learn how to best form a high current, high quality, laminar beam in the injector; then smoothly transport this beam several meters downstream through the induction accelerator module, while preserving as much of the beam current and quality as possible; and finally compress the beam strongly and inject it into the wiggler solenoid. Unless each of these goals are well achieved, the fruits of success in the early stages of the device may be lost further downstream before the beam delivers its payoff in the wiggler interaction. The resultant necessity for achieving a comprehensive design for beam formation and transport, which encompasses the entire region from the cathode to the wiggler, is common to a wide variety of similar experimental situations. At the same time, focusing our computational and theoretical studies

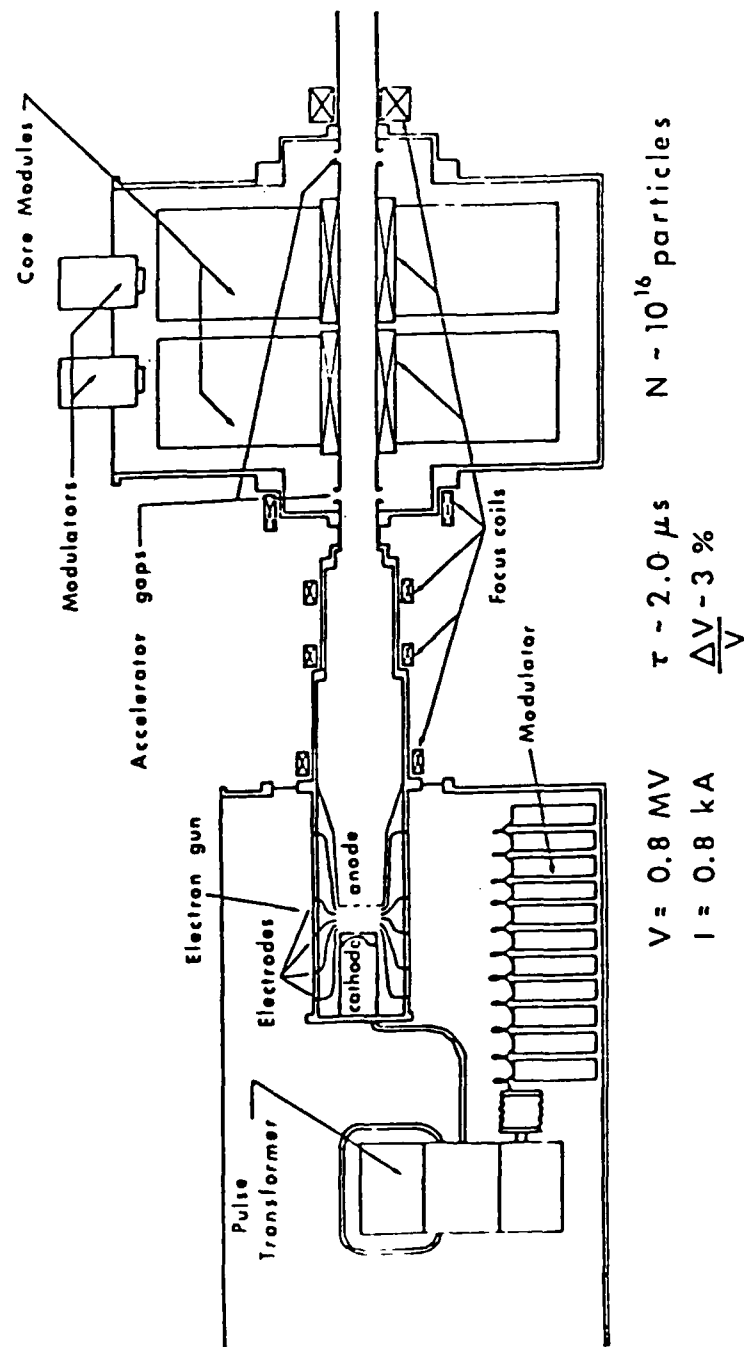


Figure 1. Induction Linac

upon this specific device, from which experimental data was concurrently available, afforded the opportunity to achieve those more comprehensive gains in understanding which flow from an active interplay between theoretical and experimental studies.

The results of our studies of beam formation and transport have been described in some detail in Appendices A through H hereto. Appendices A through D comprise four letter progress reports which describe some of the calculations of beam formation in the diode, as well as many of the detailed calculations of beam transport through the first four meters of the induction linac. Additional calculations of beam formation and diode transport are described in Appendix E, and the beam transport through the accelerator is further discussed as well. In Appendix F, the beam formation and transport is summarized and the results are also compared with the predictions of a one-dimensional envelope equation for $R(z)$. A Hamiltonian analysis is also presented in Appendix F of the excitation of cyclotron oscillations upon the beam, and it is shown how one may strive to design the transport fields to minimize these cyclotron waves. Appendix G contains a calculation of the beam emittance which results from the excitation of magnetic cyclotron oscillations during beam transport. Finally, Appendix H contains a calculation of beam quality improvements which may be achieved through the use of high magnetic fields and gentle wall gradients in field-immersed diodes. Below we will mention some of the

highlights of the research described in these Appendices A through H.

Beam formation in the injector was studied using the REEFER code (Ref. 8) and the STAGEN code (developed at Austin Research Associates) to compute steady state diode flow patterns in r, z geometry. Early examination of a cantilevered button field emission cathode (shown in Figure 22 of Appendix A) of 14 cm radius, 2.5 cm thickness, and -400 kV potential inside a grounded cylindrical housing of 19 cm radius with a grounded anode mesh located 10 cm downstream, revealed that pre-breakdown electric field stresses on the cathode tip would exceed 170 kV/cm. This was found to lead to complete breakdown of the cathode surface, a current density profile highly peaked on edge, some 5 kA of emitted current, and an expanding flow pattern in the anode-cathode gap in the absence of a strong magnetic guide field. This beam was judged unacceptable due to its excessive size (> 14 cm vs. < 0.6 cm desired downstream in the wiggler), its excessive current (5 kA vs. ~ 1 kA desired), and its expansive flow (see Figure 23 of Appendix A) in the diode--making laminar compression difficult downstream. Consequently, the remainder of our diode studies contemplated the use of either warm or cold cathodes with annular electrode rings in the anode-cathode gap to provide a graded potential axially through the diode and to reduce the pre-breakdown stresses on the cathode surface, with emission out to ~ 8 cm radius controlled by the presence of fibers on the cathode.

Such controlled emission cathodes were found to produce reasonable, high quality beams with laminar flow patterns. Diode parameters selected were

anode-cathode gap spacing = $d = 11.0$ cm

cathode emission radius = $a = 8.0$ cm

cathode potential = $-\Delta\phi = -400$ kV.

The gap spacing of 11 cm is sufficient to minimize the problem of diode closure at velocities of ~ 2.5 cm/ μ sec during the 1-2 μ sec pulse time of the beam. The emission radius of 8 cm is large enough to ensure that the current density at the cathode surface is less than 4 A/cm², as required for reliable operation and to avoid the Child-Langmuir space charge limit (see calculation in Appendix E). However, the requirement that the beam should eventually be compressed to a radius of about 0.6 cm in the wiggler solenoid places a very high premium on techniques for beam convergence.

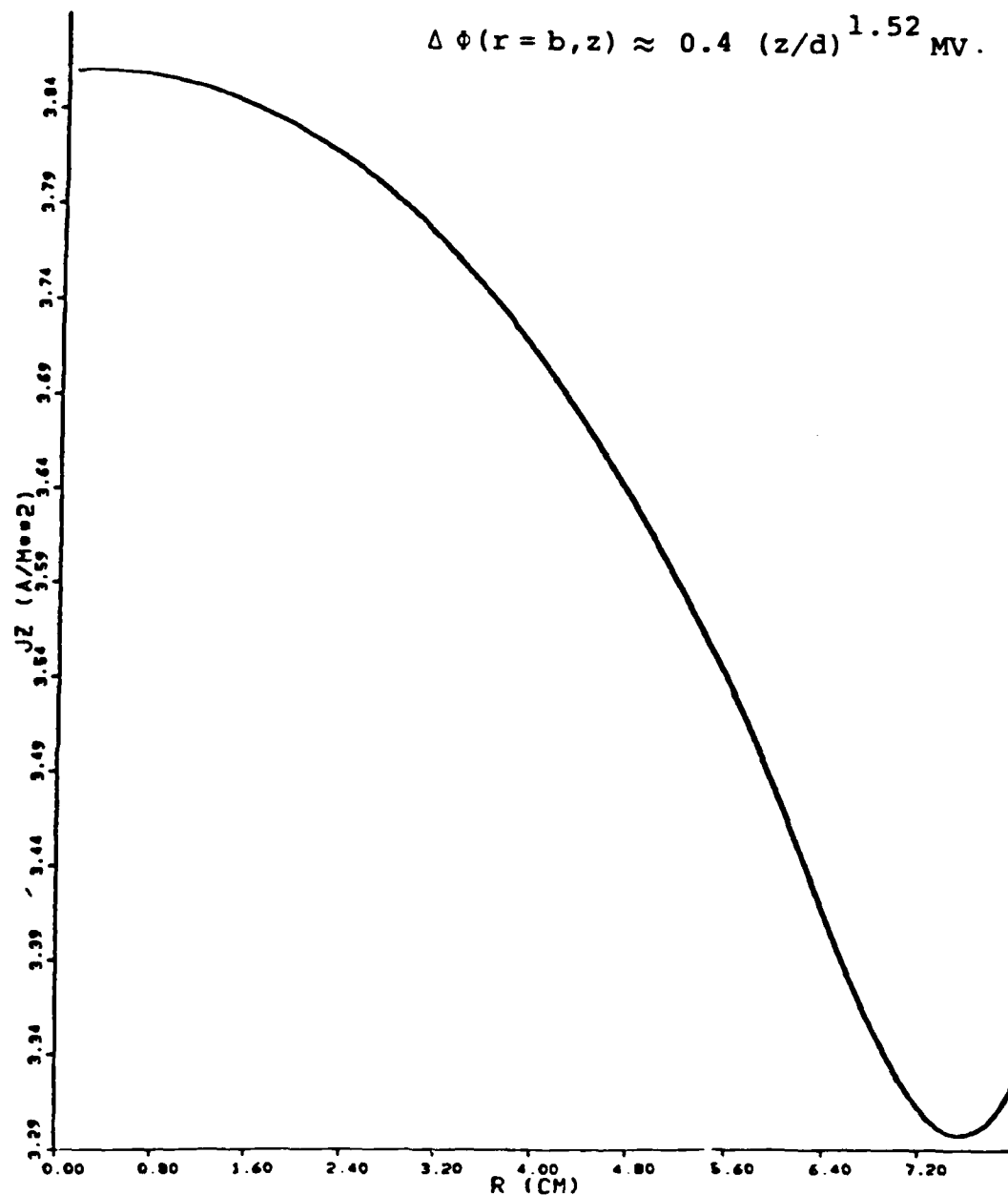
It is easy to see that complete reliance on magnetic compression to achieve this hundredfold increase in the beam current density is hardly feasible. Hundreds of gauss would be required to tie the beam well to field lines in the diode region (see magnetic tying formula in Appendix E) and then compression to some tens of kilogauss would be needed to reduce the magnetic flux surface radius to 0.6 cm in the wiggler solenoid. Consequently, it is desirable to achieve some beam convergence electrostatically while the magnetic field is weak, leaving a

lesser amount of compression to be achieved magnetically. Electrostatic beam convergence is possible in a graded potential parallel plate geometry. The resistively graded electrodes lead to a radial boundary condition in the anode-cathode gap which may be modeled as

$$\frac{\phi(r=b,z) - \phi_{\text{cathode}}}{\Delta\phi} = \left(\frac{z}{d}\right)^p \quad (2)$$

By varying p , one may vary the cathode stresses, the radial current density profile, and the diode flow pattern. We evaluated computationally the choices $p=1$, $4/3$, 1.52 , and 1.58 , as discussed in Appendices C and E. These diode potential gradings are illustrated in Figure 1 of Appendix C. The most desirable results were obtained for a sub-Child-Langmuir grading of $p \approx 1.52$, which produced relatively weak cathode stresses, current of $I_b \approx 720$ A, and a convergent flow pattern with axially peaked current density as illustrated in Figures 2 and 3. The convergent beam flow occurs because the graded electrode structure tends to short out the radial electric fields normally associated with the beam space charge, such that the $v_z \times B_\theta$ pinch force is left to compress the beam radially.

As shown in Figure 1 (and in more detail in Figure 1 of Appendix A), the electron beam, once formed, must be transported through a complex array of magnetic field coils and radially varying conducting boundaries, and through two accelerating gaps in the induction module before being finally compressed and



JZ VS R

Figure 3. Current Density Profile @ Cathode for
Sub-Child-Langmuir Potential Grading
(Modified Design)

13-MAY-82

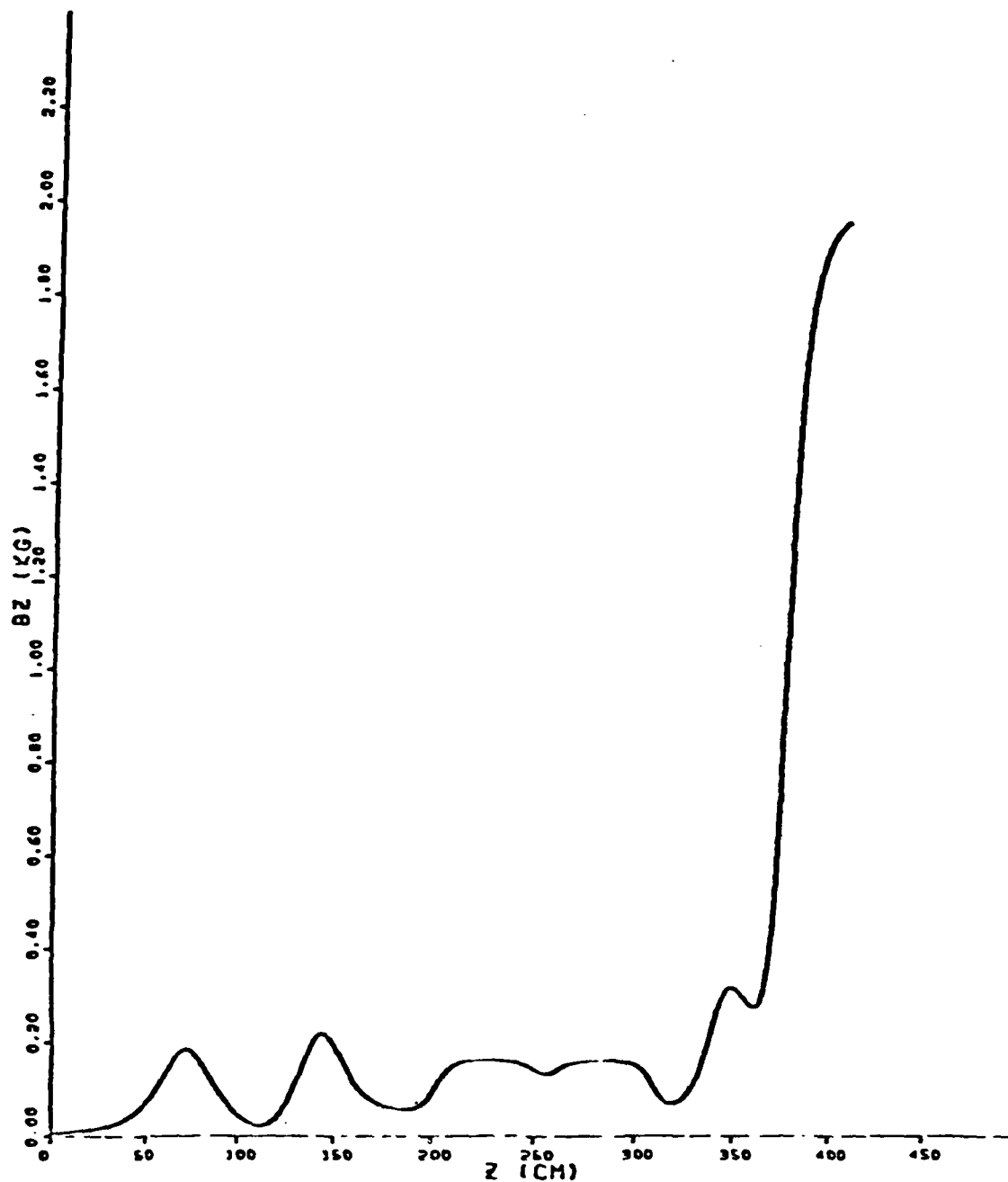
05:42:45

injected into the wiggler solenoid, which begins 380 cm downstream of the cathode surface. In order to study this challenging transport problem, we employed in addition to theoretical analysis, a one-dimensional $R(z)$ beam envelope code and the two-dimensional (r,z) , steady state, relativistic particle simulation code STAGEN.

The STAGEN code retains all three components of velocity and of the electric and magnetic fields, but is restricted to the two independent variables r,z , appropriate to situations which are symmetric in the azimuthal coordinate θ . In order to reduce the computing requirements to a manageable level, the axial transport is divided into four "stages." The first stage extends to $z = 23$ cm, encompassing the 11 cm length of the anode-cathode region plus 12 cm beyond the anode mesh. The flow is initiated from an equipotential near but not on the cathode surface-- typically $\phi - \phi_{\text{cathode}} \leq 20$ kV. Stage 2 extends from $z = 23$ cm to $z = 111$ cm, encompassing the initial focusing coil and the conductor wall flaring out to a radius of 17.5 cm. Stage 3 extends from $z = 111$ cm to $z = 258$ cm, and encompasses three more focusing coils, the first induction accelerating gap (of 200 kV), and the first induction solenoid. Stage 4 extends from $z = 258$ cm to $z = 406$ cm, and encompasses the second induction solenoid, the second induction accelerating gap (also of 200 kV), another focusing coil, and the first 26 cm of the wiggler solenoid.

Under this contract, STAGEN was exercised repeatedly to examine the beam transport through the first four meters of the long pulse induction linac for a variety of diode potential gradings and for several magnetic field configurations. Because the constraints of operating with the existing coil configuration and achieving an order of magnitude beam radius compression into the wiggler solenoid make the transport so difficult, emphasis on the STAGEN runs was first placed on simulating typical experimental parameters. In this way, support for the experiment was provided, feedback was received, and an appreciation for the crucial elements of the transport physics was obtained. An example of these transport simulations is provided in Figures 4 through 7. Figure 4 displays the magnetic field profile in the LPIL for a typical set of coil currents, including the magnetic ramp into the 2 kG wiggler solenoid. A separate magnetic field code was written and exercised in order to generate magnetic field profiles such as that shown in Figure 4, from the known coil currents, dimensions, and locations (shown in Figure 1 of Appendix A).

Figure 5 shows the equipotentials in the diode region and in the 12 cm beyond the anode mesh. It may be seen that the graded electrode structure does an excellent job of shorting out the radial beam space charge electric field in the diode region, allowing the gently convergent, laminar beam flow seen in Figure 2. A theoretical calculation was made of the rms scatter which would occur in the transverse beam velocity as the beam



BZ VS Z

Figure 4. Magnetic Field Profile from
December 1981 Data

2-APR-82

12:20:30

(ora)

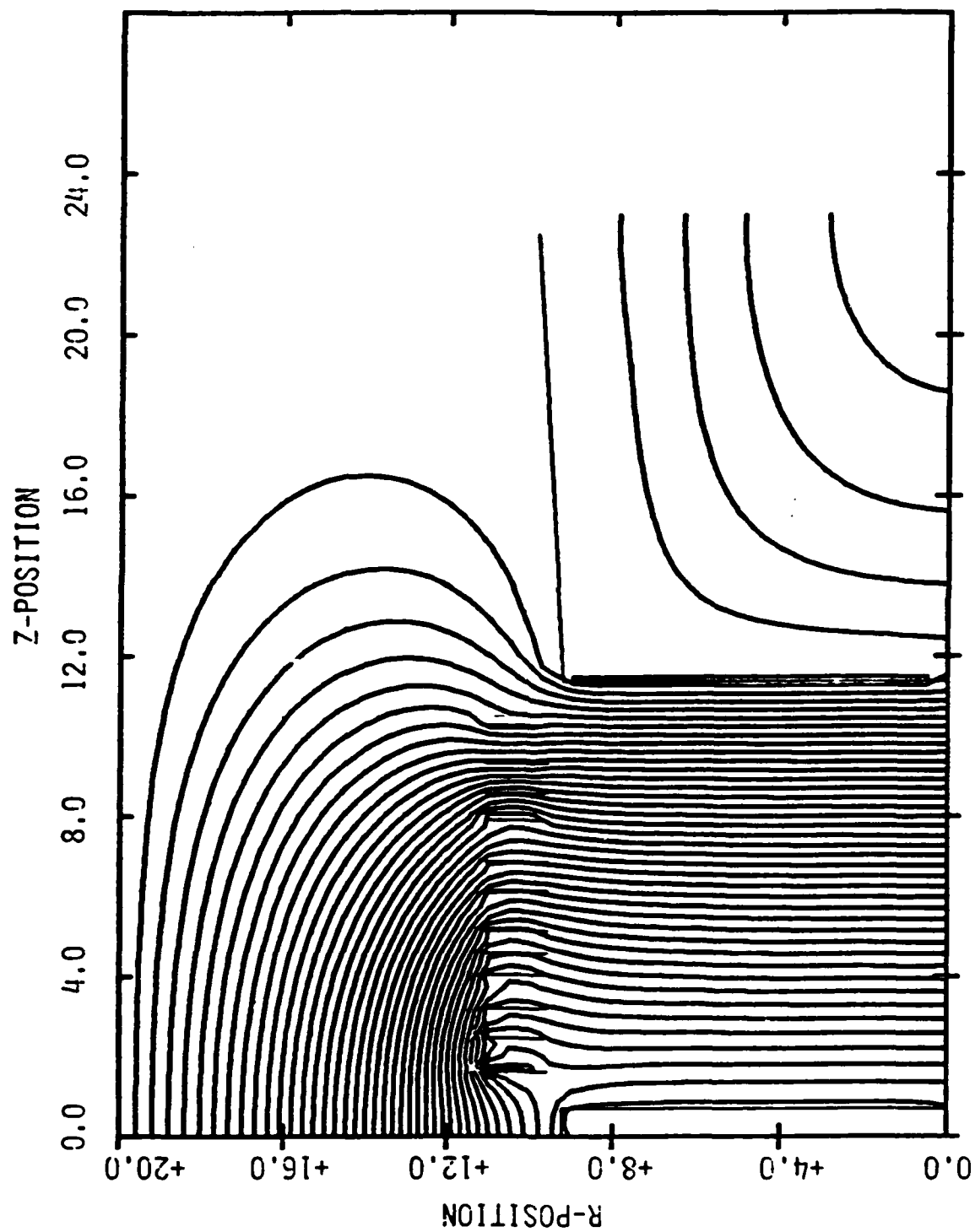


Figure 5. EQUIPOTENTIAL CONTOURS a DIODE REGION

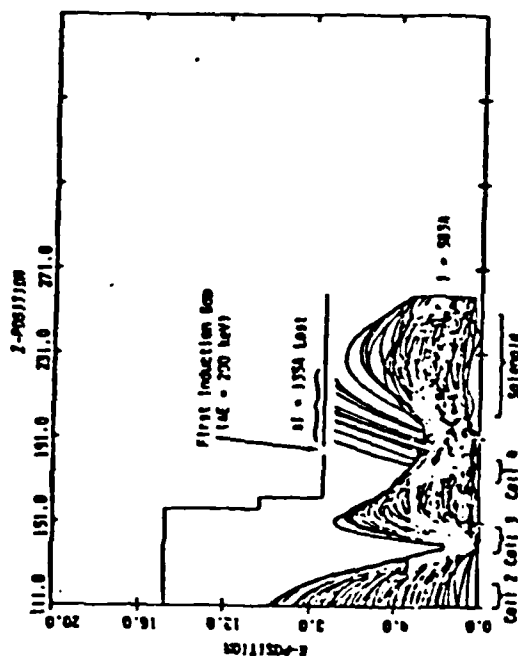
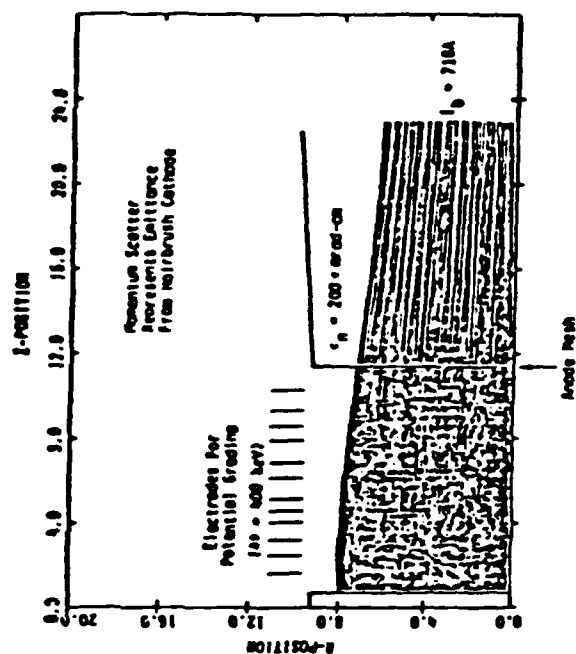
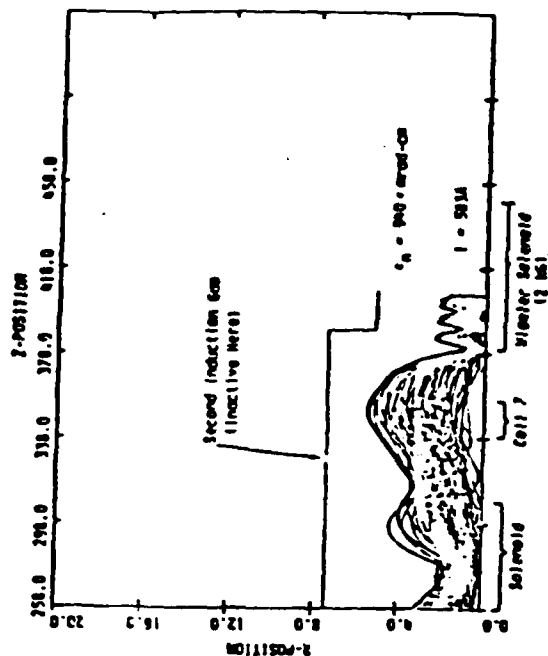
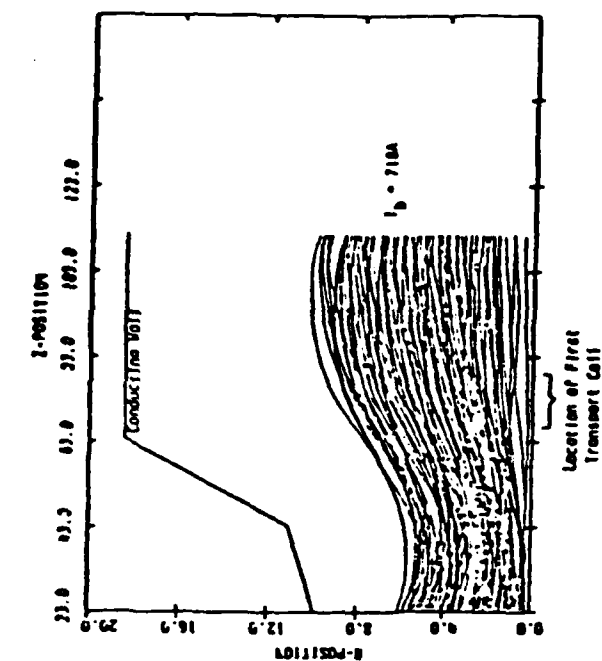


Figure 6. Transport and Compression of LPIL Beam

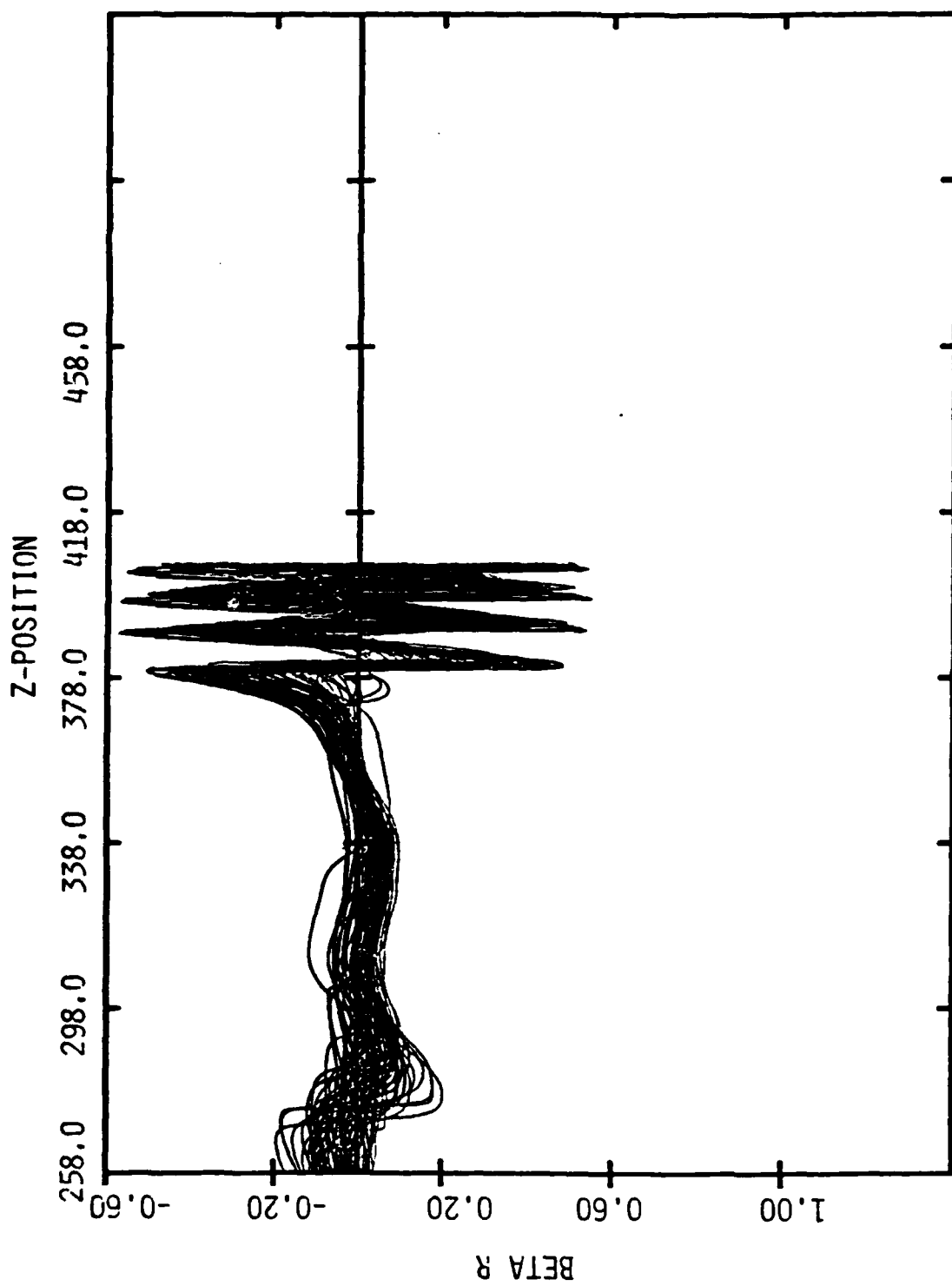


Figure 7. β_r -z Phase Space @ State 4 (2nd Induction Gap Off)

passed through the anode mesh at $z = 11$ cm, due to the charge induced on the wire mesh. It was estimated that

$$\delta\beta_{\perp \text{rms}} \approx \frac{1}{2\sqrt{6}} \frac{b}{d} \sqrt{\frac{\gamma_0 - 1}{\gamma_0 + 1}} \quad (3)$$

where b is the distance between wires in the anode mesh, d is the anode-cathode separation, and $(\gamma_0 - 1) mc^2$ is the diode injection energy. For diode parameters of 400 keV injection energy, with one mil tungsten anode mesh wires on a grid of 98% transparency, one finds that $b/d \approx 0.025$ and $\gamma\delta\beta_{\perp \text{rms}} \approx 0.005$, corresponding to emittance growth of about $\sim 25\pi$ mrad-cm at the anode mesh. However, this anode mesh emittance growth is small in comparison with the experimentally estimated emittance of $\sim 200\pi$ mrad-cm created at the surface of the hairbrush cathodes. To mock up the effect of this cathode-generated emittance, a scatter corresponding to 200π mrad-cm emittance was therefore introduced at the anode mesh for these runs. Figure 6 displays the beam transport through Stages 1-4 of the LPIL device, and the beam compression and injection into the wiggler solenoid. (Full-scale versions of these figures appear as Figures 5 and 7 through 9 of Appendix F.) It may be seen that 135A of current is lost to the wall just beyond the first induction gap. For this particular case, the second induction gap was inactive. The strong beam compression of the remaining 583A of current is seen in Stage 4 (Figure 9 of Appendix F). However, this strong compression excites large amplitude zero frequency cyclotron

oscillations which are displayed in the β_r - z phase space plot of Figure 7. This strong sausageing will subsequently phase mix to create a downstream emittance of $\sim 940\pi$ mrad-cm for this transport example. In Figure 8, the variation of γ_z with z is displayed for the electrons in Stage 4. At the throat of the wiggler, the median value of γ_z is found to be ≈ 1.6 ; there is a considerable spread since the outer electrons have been excited to much higher transverse velocities than have the inner electrons. These details on the phase space distribution of the electrons turned out to be quite useful (Ref. 3) in interpreting that certain of the experimental radiation measurements indeed signify an FEL mode, as expected.

Examination of these STAGEN calculations of beam transport over several meters distance with multiple magnetic coils, multiple accelerating gaps, and variable wall geometry (appropriate to the LPIL accelerator at NRL) revealed several sources of beam quality degradation. Noteworthy is the significant wall flaring at $z = 42$ - 60 cm, the abrupt reduction of wall radius near $z = 160$ cm, the strong axial electric fields applied at the two induction gaps, and the very strong magnetic compression at the entrance to the wiggler solenoid. Each of these transport features can perturb the radial force balance of the electron beam, so as to excite radial beam oscillations which may lead to emittance growth (and in some case to current loss as well).

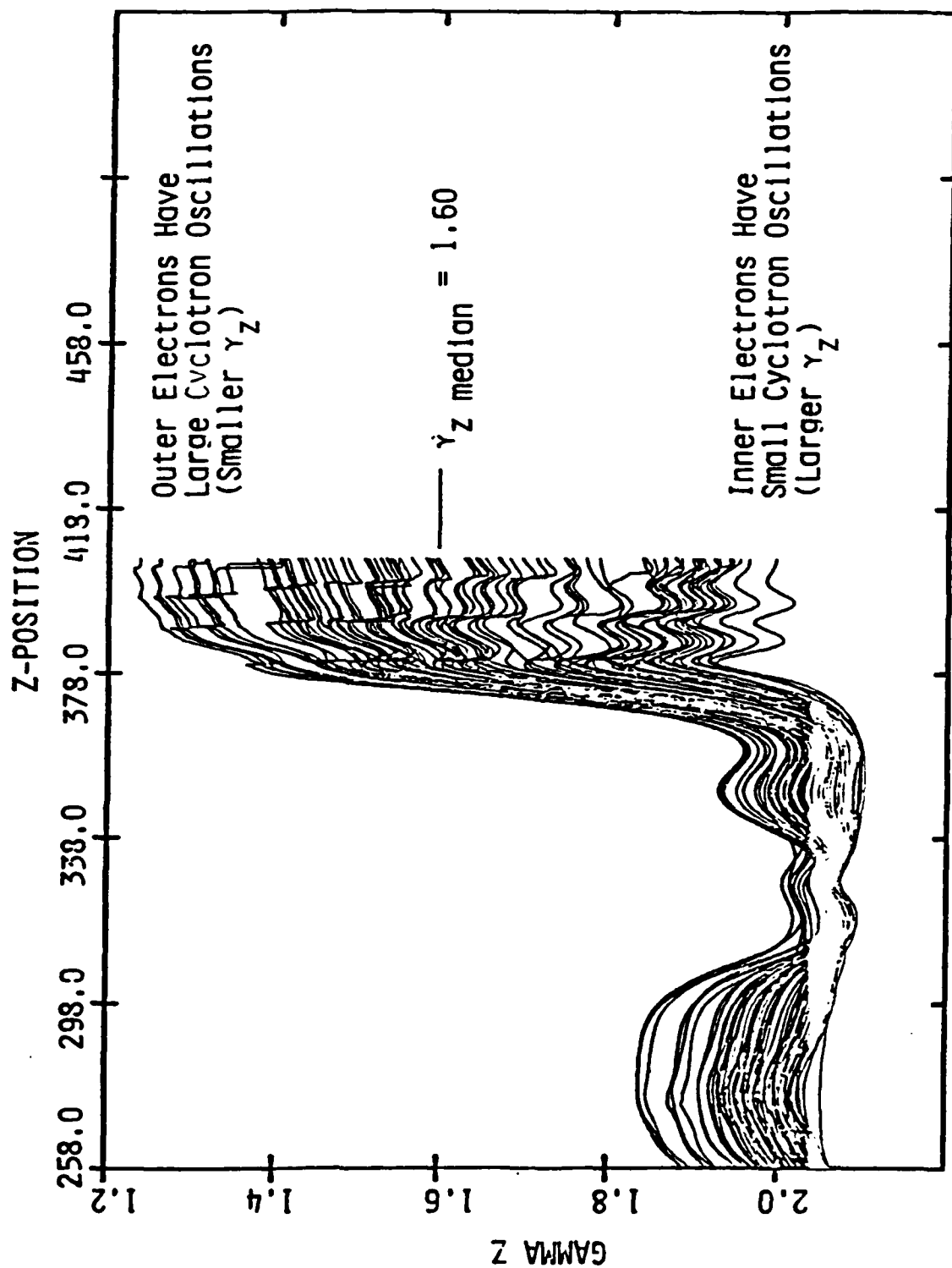


Figure 8. γ_z - z Phase Space @ Stage 4 (2nd Induction Gap Off)

In order to theoretically analyze emittance growth in a complex transport scenario such as this, we found it useful to employ a Hamiltonian treatment (Ref. 9) of the axially-dependent, radial confining fields. This Hamiltonian may be made consistent with a one-dimensional envelope equation for $R(z)$, similar to the equation developed by Lee and Cooper (Ref. 10). This analysis is described in Appendix F and provides guidance for improving the beam transport. The assumptions, equations, and symbols used in this analysis are summarized in Tables 1 and 2 of Appendix F. A normalized form of the envelope equation appears as

$$\mathcal{R}'' + \left[\frac{\Omega_0^2(z)}{4\gamma^2\beta^2c^2} + \frac{(\gamma^2 + 2)\gamma'^2}{4\gamma^4\beta^4} \right] \mathcal{R} - \frac{I_b}{mc^3/e} \frac{1}{\gamma^2\beta^2} \frac{1}{\mathcal{R}} - \frac{(\epsilon^2 + P_\phi^2)}{\mathcal{R}^3} = 0 \quad (4)$$

where $\mathcal{R} = (\gamma\beta)^{\frac{1}{2}} R(z)$

$R(z)$ = rms beam radius

$\Omega_0(z) = \frac{eB_z(z)}{mc} = \text{nonrelativistic cyclotron frequency}$

I_b = beam current

$\epsilon = \gamma R \delta\beta_{\perp \text{rms}} = \text{normalized beam emittance, a constant}$

$P_\phi = \gamma r \beta_\phi - \frac{\Omega_0(z)}{2c} R^2 = \text{canonical momentum of beam, a constant}$

and where the beam energy $[\gamma(z) - 1] mc^2$ is obtained from

$$\gamma(z) = \gamma_0 + \frac{e\phi_{\text{wall}}(z)}{mc^2} - \frac{I_b}{mc^3/e} \frac{2}{\beta} \ln \frac{b(z)}{R(z)} \quad (5)$$

where $(\gamma_0 - 1) mc^2$ = diode injection energy

$b(z)$ = conducting wall radius

$e\phi_{\text{wall}}(z)$ = wall potential.

The primary source of beam quality degradation during beam transport is the excitation of beam cyclotron oscillations as a result of (frequently) abrupt axial variations in the radial beam focusing forces. The beam equilibrium radius is that for which the radial "force" terms of Equation (4) are in balance, when $R'' = \frac{d^2}{dz^2} R = 0$. The physical significance of these force terms is discussed in Table 1 (extracted from Appendix F). The γ'^2 term is seen to represent primarily the focusing kicks that the beam receives in the diode and in the induction gaps. During the early portion of the transport, while $B_z \lesssim 200$ G, the beam radius is determined by competition between the magnetic $v_\phi B_z$ focusing force and the defocusing space charge force [terms (1) and (3) of Table 1]. However, as the magnetic field is increased toward 2 kG, the defocusing space charge force is outweighed by the centrifugal and pressure forces [term (4) of Table 1]. Then the beam radius is determined by competition between this term (4) and the magnetic pinch term (1) of Table 1, leading to a smaller equilibrium radius at very large magnetic fields.

Table 1

RELATIVE SIGNIFICANCE OF TERMS IN ENVELOPE EQUATION

- (1) $\frac{\Omega_0^2(z)}{\gamma^2 \beta^2 c^2} R$ -- Magnetic $v_\phi B_z$ focusing forces which are important everywhere except in the diode region where B_z is very weak.
- (2) $\frac{(\gamma^2 + 2)\gamma'^2}{4\gamma^4 \beta^4} R$ -- Radial focusing forces which are significant (for beam current \ll Alfvén current) only in the diode and in the induction gaps. These forces represent the replacement of E_r by E_z fields, and tend to locally unbalance the radial force equilibrium.
- (3) $\frac{I_b}{\gamma^2 \beta^2 m c^3 / e} \frac{1}{R}$ -- Defocusing space charge forces which are in competition with magnetic focusing forces during the first three meters of large radius beam transport.
- (4) $\frac{\epsilon^2 + P_\phi^2}{R^3}$ -- Centrifugal and pressure forces which are in competition with magnetic focusing forces during the strong magnetic compression of the beam to a very small radius. Both ϵ and P_ϕ are constant downstream of the anode, and $\epsilon_{\text{diode}} \approx 200\text{-}300 \text{ mrad-cm}$ dominates the $P_\phi \approx 50 \text{ mrad-cm}$ due to the weak leakage magnetic field at the cathode.

In order to transport a fairly cool laminar beam, one would desire the focusing forces to vary rather slowly in z , so that the beam never received large radial kicks corresponding to large departure from radial force balance. However, many beam transport systems, including the LPIL system, do not afford the luxury of gentle axial variations. For example, in the injector diode and particularly in the induction gaps, large $\gamma' = d\gamma/dz$ appears and tends to locally imbalance the radial force equilibrium. Likewise, when the conductor walls abruptly flare or contract (as they may be seen to do in Figure 6), this forces the beam to propagate across equipotentials, which introduces γ' via the logarithmic space charge term of Equation (5). When the beam transport is magnetically focused, axial variations in the magnetic field strength will directly unbalance the force equilibrium. When force equilibrium is unbalanced, the beam will subsequently oscillate about the equilibrium radius. For magnetically focused transport, these oscillations will occur at the cyclotron frequency. Due to radial variations in the particle energy, these cyclotron oscillations will subsequently phase mix to produce an effective increase in the beam temperature, or transverse emittance.

The principal emittance growth observed during the transport of the beam through the LPIL system occurred due to the strong excitation of cyclotron oscillations during magnetic compression at the mouth of the wiggler solenoid. The magnetic compression is shown in Figure 4, the tight beam cyclotron

oscillations may be seen in Figure 6, near $z = 400$ cm, and the corresponding large perturbations in the radial electron velocity may be seen in Figure 7. The beam was also observed to undergo significant radial oscillations and occasional tight pinching at earlier stages of the transport. For example, Figure 6 displays a fairly tight beam pinch near $z = 140$ cm under the third focusing coil. For some transport cases computed under this contract, the pinching was so severe that a space charge virtual cathode was established and some electrons were reflected backward from the pinch to limit the current transmitted. Such "limiting current" phenomena can occur when the logarithmic space charge term of Equation (5) becomes so large that electrons are slowed and Equation (5) cannot be obeyed unless the beam current is reduced. Radial beam oscillation and pinching can also result in the loss of some beam current to the walls, as illustrated in Figure 6 near $z = 200$ cm.

We have also performed a Hamiltonian analysis of the cyclotron oscillations excited upon the electron beam, which is summarized in Table 4 of Appendix F. It is shown that the beam envelope oscillations may be viewed as anharmonic oscillations in the pseudopotential $P(R)$, illustrated in Figure 12 of Appendix F. One may analytically evaluate the effect of sudden or adiabatic variations in the force coefficients of the Hamiltonian, so as to assess the magnitude of transverse oscillations produced on the beam during transport. The beam emittance may be related to the action $J = \oint p dq$, and is found

to be preserved when changes occur slowly so that J is also adiabatically invariant.

On the other hand, the magnetic compression illustrated near $z = 400$ cm in Figure 4 occurs suddenly rather than adiabatically, and was observed to produce large cyclotron oscillations (see Figure 7). Theoretically, it is indeed found that large cyclotron oscillations of the magnitude observed should be created if the magnetic field is suddenly increased greatly at a point where the beam radius is relatively large. Appendix G contains a calculation of the beam emittance which results from the phase mixing of cyclotron oscillations excited by the propagation of a beam through a sudden magnetic discontinuity.

Some experimental attempts were made to comply with the theoretical recommendations, by introducing an additional transport coil to make the magnetic compression more adiabatic--and indeed some improvement in transport was seen. However, the continued necessity for substantial magnetic compression in order to inject into the small wiggler solenoid, a large portion of the beam created in a large area, low magnetic field diode, implied a certain irreducible amount of cyclotron oscillation emittance growth at the mouth of the wiggler. (The constraint of working with the existing accelerator configuration presented a limitation to the improvements which could be practically realized by adding or modifying the transport field coils.) These induced transverse cyclotron oscillations were in turn found

experimentally to produce a high level of cyclotron radiation, while the emittance growth reduced the level of FEL radiation which could be obtained. Consequently, a decision was eventually taken by NRL experimentalists to eliminate the strong magnetic compression into the wiggler (which hence became free of the guide field), thereby aperturing away most of the transported beam. This step essentially eliminated the unwanted cyclotron radiation, although the FEL radiation amplitude was consequently low because of the low driving current.

The remainder of our research under this contract on the production and transport of high quality, high current electron beams was concentrated on a calculation of the beam quality achievable in high current, magnetic field-immersed diodes. This calculation is presented in Appendix H. We found that the best beam quality results from gently-shaped anode and cathode structures, which create electric fields whose radial components have long axial gradient lengths. When the diode axial magnetic field strength is high enough that the beam electrons are tied to the field lines and the inverse cyclotron wave number $\beta_z c / \Omega$ is below the axial gradient length of the radial diode forces, extremely high quality electron beams can be created. Improvements in the beam emittance of one to two orders of magnitude over the Lawson-Penner emittance of Equation (1) were observed in some cases. In one calculation of diode emittance from a smoothly tapered anode structure, it was found that doubling the magnetic guide field caused the transverse electron

velocity to decrease by a factor of nine--which illustrates the potential of magnetic field-immersed diodes for producing high quality electron beams.

We are hopeful that the research completed under this contract has confirmed the importance of enlightened beam transport design to the goal of producing high quality, high current beams and, further, that it has indicated certain avenues toward the achievement of this goal through the use of gentle axial variation in the transport structure, and strong focusing fields.

II. LIST OF REFERENCES

1. R. C. Davidson and H. S. Uhm, Phys. Fluids 23, 2076 (1980).
2. H. S. Uhm and R. C. Davidson, Phys. Fluids 24, 1541 (1981).
3. C. W. Roberson, J. A. Pasour, F. Mako, R. F. Lucey, Jr., and P. Sprangle, "A Free Electron Laser Driven by a Long-Pulse Induction Linac," Infrared and Millimeter Waves, 10, 361, Academic Press, Inc., New York, New York (1983).
4. G. Dattoli, T. Letardi, J. M. J. Madey, and A. Renieri, "Considerations about the Lawson-Penner Limit and FEL Operation by Single-Pass Devices," in Free Electron Generators of Coherent Radiation, edited by C. A. Brau, S. F. Jacobs, and M. O. Scully, SPIE Conference Proceedings, 453, 189 (SPIE, Bellingham, Washington, 1984).
5. J. D. Lawson and S. Penner, "Note on the Lawson-Penner Limit," IEEE J. Quantum Electron., QE-21, 174 (1985).
6. J. E. Leiss, N. J. Norris, and M. A. Wilson, Particle Accelerators, 10, 223 (1980).
7. J. A. Pasour, R. F. Lucey, C. W. Roberson, "Long Pulse Free Electron Laser Driven by a Linear Induction Accelerator," in Free Electron Generators of Coherent Radiation, edited by C. A. Brau, S. F. Jacobs, and M. O. Scully, SPIE Conference Proceedings, 453, 328 (SPIE, Bellingham, Washington, 1984).
8. J. E. Boers, "Digital Computer Simulation of High-Current, Relativistic, and Field Emission Electron Tubes," Record of 11th Symposium on Electron, Ion and Laser Beam Technology, San Francisco Press, Inc. (1971).
9. J. R. Thompson, B. N. Moore, M. L. Sloan, and J. R. Uglum, Bull. Am. Phys. Soc. 27, 1011 (1982).
10. E. P. Lee and R. K. Cooper, Particle Accelerator 7, 83 (1976).

A P P E N D I X A

Letter from Dr. James R. Thompson to Dr. C. W. Roberson,
dated April 2, 1982.

-- includes 25 figures

Austin Research Associates
1901 Rutland Drive-Austin, Texas 78758-Phone (512) 837-6623

April 2, 1982

Dr. C. W. Roberson
Plasma Physics Division, Code 4704
Naval Research Laboratory
4555 Overlook Avenue
Washington, D.C. 20375

Dear Chuck:

Enclosed is some computer output to illustrate some of our preliminary results on the beam transport problem through the first four meters of the NBS induction accelerator, and also some preliminary diode calculations with the tentative cold cathode design which you supplied. I have numbered the figures and will provide some brief commentary keyed to those numbers.

Figure 1 shows the layout of the machine. The cathode has a radius of about 8 cm and is located at $z = 0$. The wiggler solenoid begins at $z = 380$ cm. We have moved the break point between Stages 1 and 2 to $z = 23$ cm, as shown. Stage 4 extends from $z = 258$ cm to $z = 406$ cm, which is 26 cm into the wiggler solenoid.

Figure 2 shows the magnetic field profile which we used for our initial transport studies. It does not include the strong 2 kG magnetic field in the final solenoid. Figure 3 shows how the magnetic field profile is changed in the presence of the 2 kG solenoidal field. However, we have only just today submitted our first runs to attempt to propagate the beam through the strong magnetic compression in the wiggler solenoid, and we don't have the results back yet.

Figure 4 shows the Stage 1 propagation from near the cathode through the anode screen and into the first drift section. The electrons are initiated at 20 keV energy, 1.2 cm downstream of the true cathode surface, in accordance with the Child-Langmuir law. The vertical tic marks represent the resistively graded electrodes between the cathode and anode. The electrode potentials were in accordance with the $z^{3/2}$ Child-Langmuir law, to yield vertical equipotentials for space-charge limited flow. A current of 850 amperes was emitted, and the A-K potential jump was 400 kV. Scatter was not introduced in the initial electron momenta to mock up the anode screen scatter or

Dr. C. W. Roberson
Naval Research Laboratory
April 2, 1982
Page 2

cold-cathode emission effects. A uniform current density profile was assumed. Hence this run might represent a hot cathode run, had you been able to extract 850 A from your hot cathode.

Figure 5 shows the equipotential contours. It is clear that the graded electrode structure does a good job in eliminating E_r within the A-K gap. This is why the beam flow in Figure 4 is initially convergent, since the $v_z B_\phi$ pinch force is dominant in the A-K gap. Near $z = 20$ cm, the usual E_r beam fields have been established.

Figure 6 shows the magnetic flux contours. The leakage field in the A-K gap region is around 5-10 G.

Figures 7 and 8 show β_r and β_θ for the Stage 1 flow. Note that the sign should be reversed on all of the vertical axis quantities that are plotted.

Figure 9 shows the Stage 2 flow pattern. The Stage 2 z -coordinates are relative to the start of Stage 2 at $z = 23$ cm (i.e., $z - 23$ cm should be the label). The zero frequency oscillations which are set up as the beam propagates into the 18 cm radius tube and encounters the first magnetic field peak near $z = 72$ cm ($z - 23$ cm = 49 cm) are clearly evident.

Figure 10 shows the Stage 2 flux lines, while Figures 11 and 12 show the β_r and β_θ flow field. the beam seems to be transporting fairly well here, without too much phase mixing. At the end of Stage 2, the counter-current in coil 2 has driven the B_z field near zero, so that β_θ is back near zero.

Figure 13 shows the Stage 3 flow pattern. During this stage, the electron beam propagates through two B_z peaks and across the first 200 kV induction gap at $z \approx 182$ cm (or $z - 111$ cm ≈ 71 cm). The outer beam electrons come very near the wall at $z = 154$ cm and $z = 258$ cm. Figure 14 shows the equipotential contours, including the effect of the induction gap. Figure 15 shows the Stage 3 flux contours.

Figures 16 and 17 show β_r and β_θ for Stage 3. The beginnings of phase mixing are here apparent.

Figure 18 shows the Stage 4 flow pattern, encompassing the second induction gap, and the 320 G magnetic field peak under

Dr. C. W. Roberson
Naval Research Laboratory
April 2, 1982
Page 3

coil 7. The beam expands near the end of Stage 4 due to the absence of the strong wiggler solenoidal magnetic field. Figure 19 shows the magnetic flux surfaces, revealing the fall-off in B_z near $z = 400$ cm, just as in Figure 2.

Figures 20 and 21 show β_r and β_θ in Stage 4, and considerable phase mixing seems to be apparent here. The beam "thermal velocity" component may be a few %c here. It remains to be seen how well this beam can be compressed to ~ 2 kG by using the Figure 3 magnetic profile, and what its emittance then is.

Subsequent transport runs will include introducing initial beam scatter to gauge the transport sensitivity to this, studying transport through the strong magnetic compression into the wiggler, and trying to numerically repeat the B_z profile optimization experiments to some degree.

The remaining figures concern our initial code diode studies. We began by considering the tentative design which you had given us, shown in Figure 22. The 12.7 cm dimension was changed to 14 cm, upon the assumption that the figure was drawn to scale. The guide magnetic field was set to zero, and an anode screen was placed 10 cm downstream of the cathode face.

Figure 23 shows the preliminary flow field obtained from the REEFER code. Because of the absence of electrode grating or of pierce electrode structure, the flow is somewhat expansive. We have arbitrarily cutoff emission at $r = 11$ cm, in agreement with the outermost fibers shown in Figure 22. However, one problem which is apparent is that field stresses on the cathode tip are measured to be about 170 kV/cm, and it would seem likely that the cathode would field emit all the way out to the tip under these stresses. This is in rough agreement with analytic estimates of ~ 200 kV/cm at the tip. The stresses are this high because of the thinness (Δz is small) of the cathode tip, and its nearness (4.7 cm) to the inside surface of the outer wall. The cathode potential is assumed to be -400 kV w.r.t. ground at the outer wall and at the anode screen.

Because of the high electric field stresses near the outer portion of the cathode, the current pulled off in an edge-peaked profile, as shown in Figure 24. Across most of the cathode face, the current density is about 5 to 6 A/cm², in crude agreement with the Child-Langmuir expectation for parallel plate

Dr. C. W. Roberson
Naval Research Laboratory
April 2, 1982
Page 4

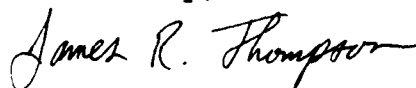
geometry. All total, 3.3 kA are pulled out of the cathode. It is tempting to consider aperturing the beam down to an 8 cm radius, thus transmitting the central 1.2 kA or so, which has a much more uniform current profile.

Figure 25 shows $\phi(r=0,z)/V_0$ plotted against z/d , where $V_0 = 400$ kV and $d = 10$ cm. Apparently, $\phi \propto z^{1.28}$, in close agreement with the $z^{4/3}$ of Child-Langmuir.

Subsequent runs will include introducing a magnetic guide field into the diode region, exploring foilless situations, and considering other cathode designs.

We realize that we are still in the preliminary stages of this study of beam transport and diode design, but we are optimistic that the pace of obtaining physics results may quicken somewhat now. I hope these results will nevertheless be interesting and helpful to you, and we will keep you informed of our further progress.

Sincerely,



Bob Thompson

P.S. The ARA participants in this study are Barry Moore, John Uglum, Lee Sloan, and myself.

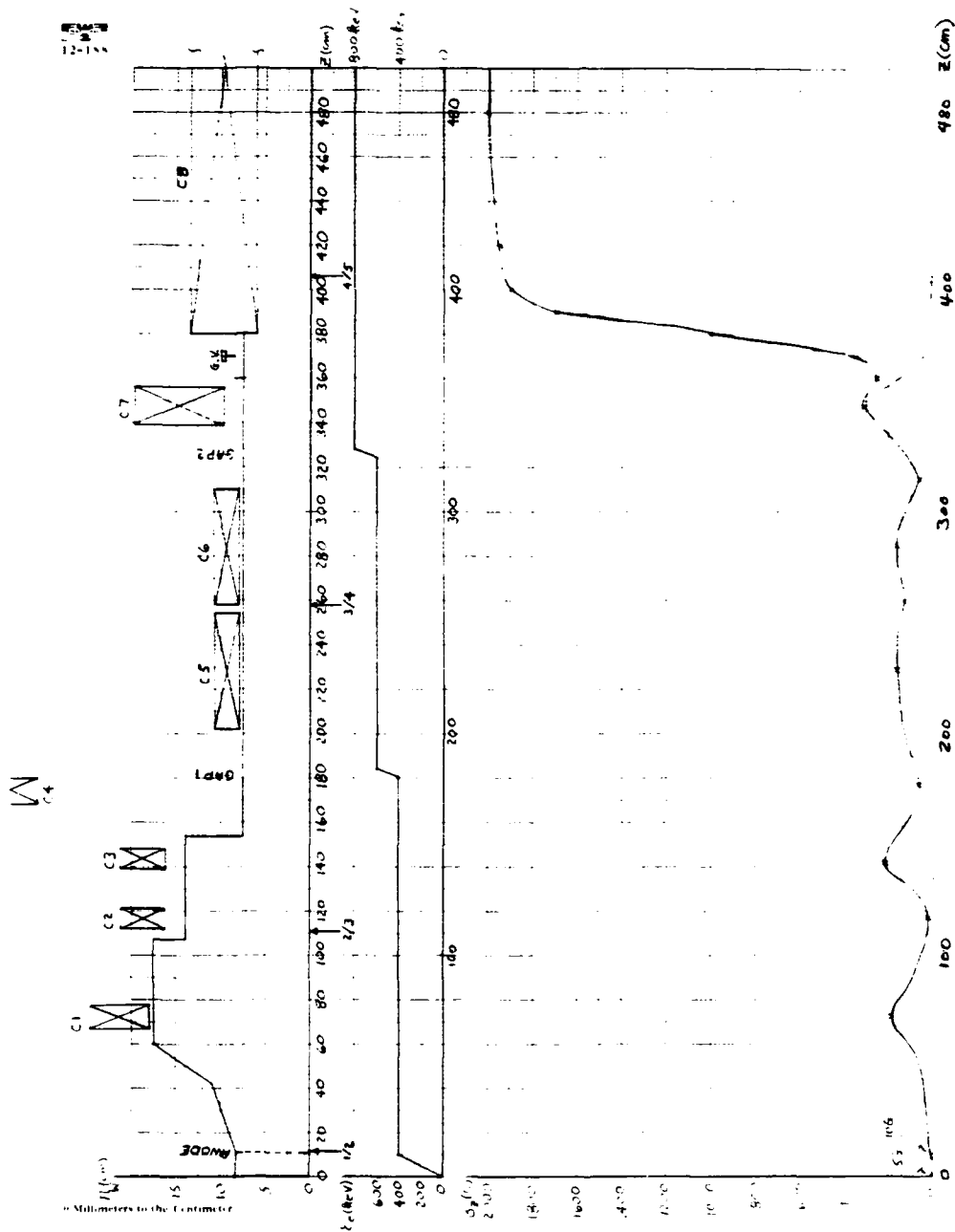
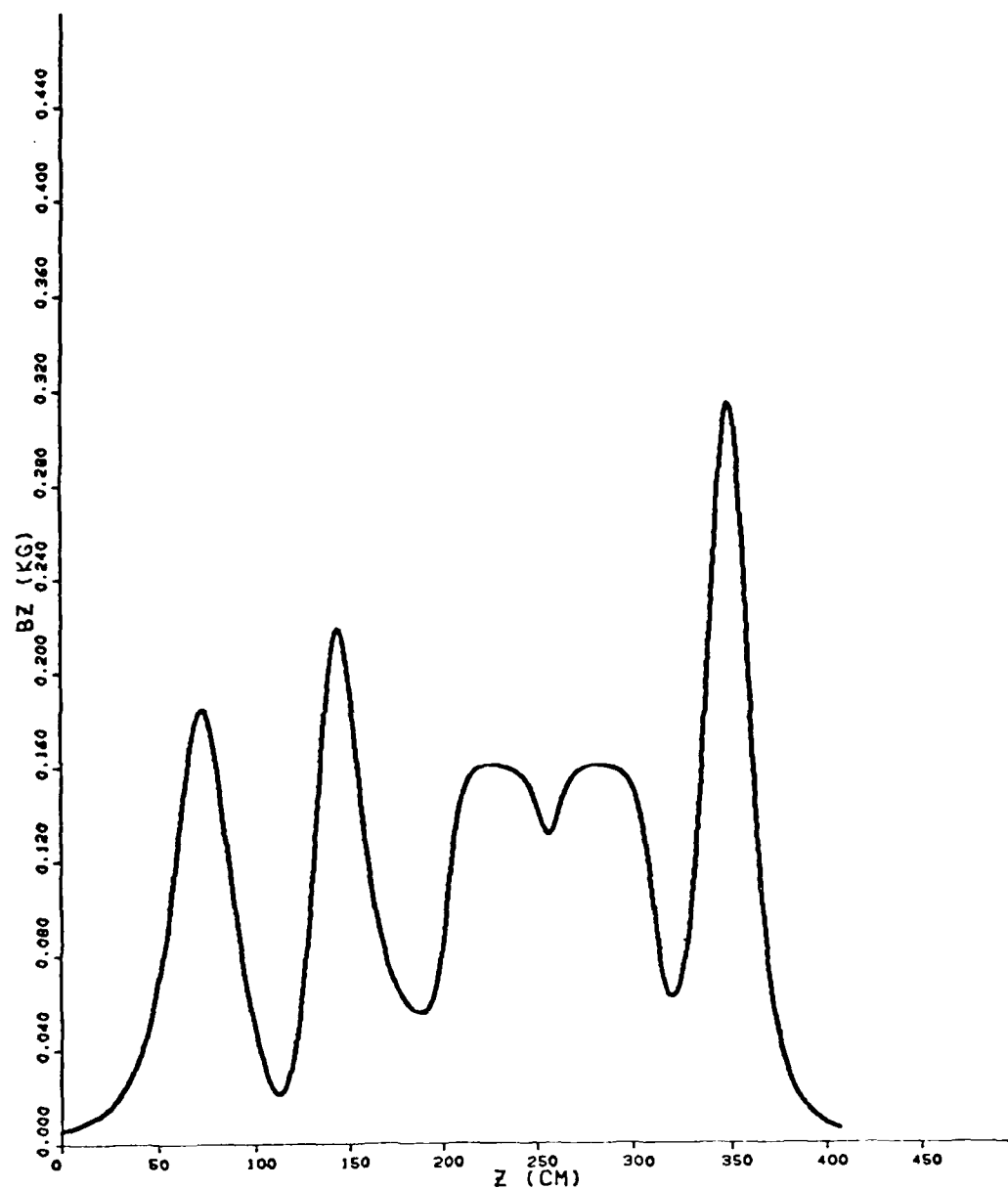


Figure 1. NBS Induction Accelerator

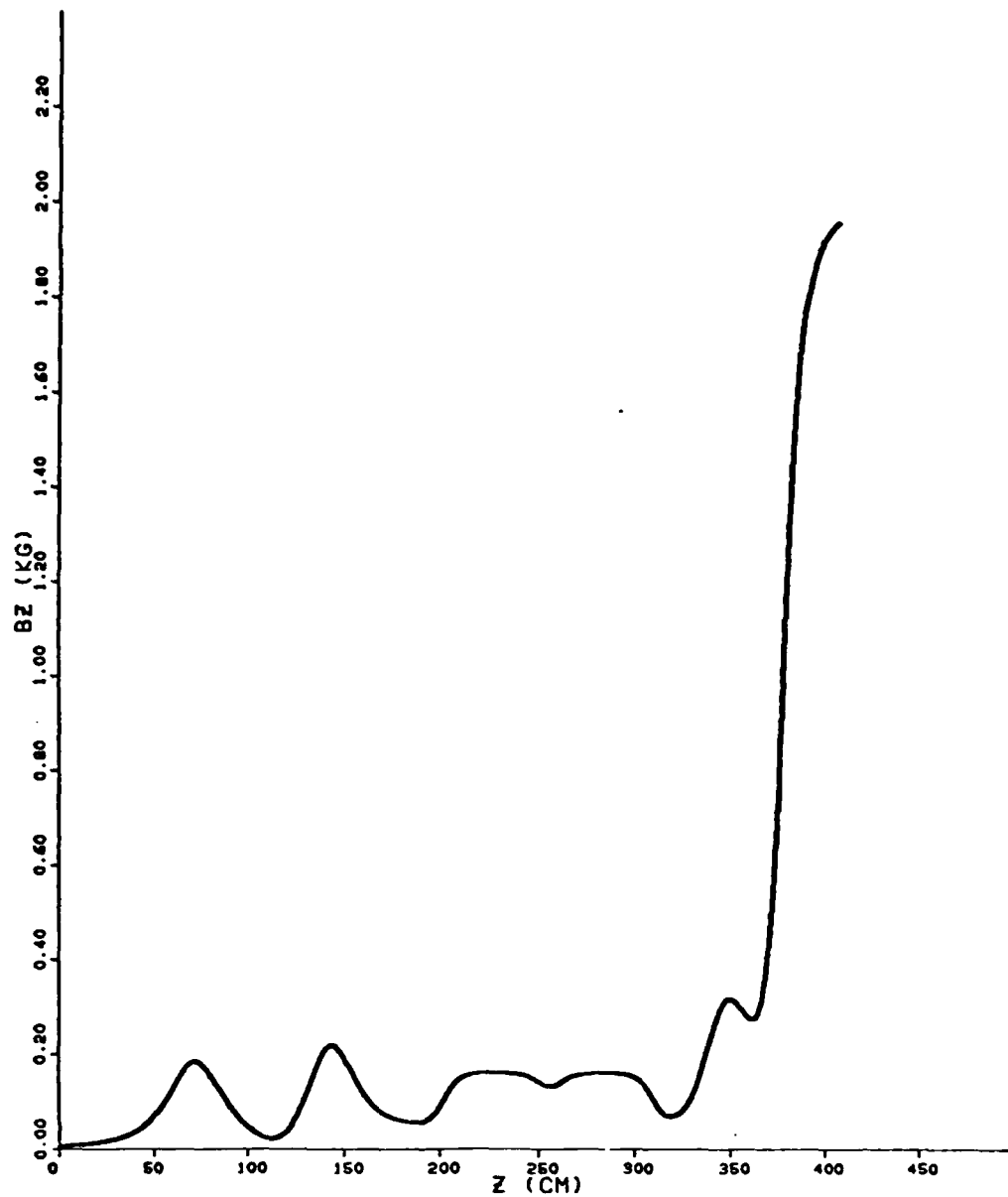


BZ VS Z

Figure 2. Magnetic Field Profile Thru Accelerator

22-FEB-82
16:41:52

aro



BZ VS Z

Figure 3. Magnetic Field Profile with
Strong Wiggler Solenoidal Field

2-APR-82
12:20:30

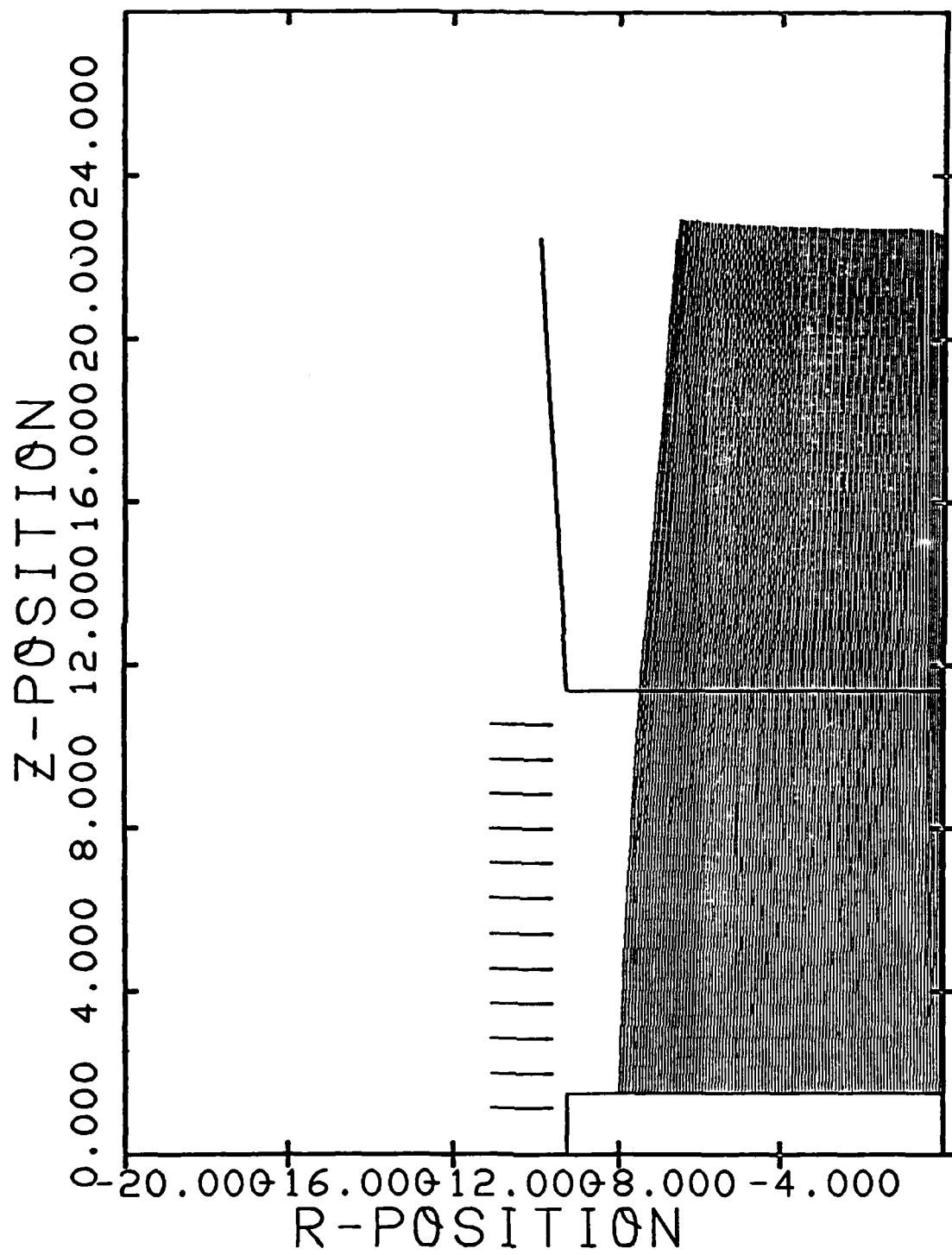


Figure 4. Stage 1 Beam Propagation Thru Diode

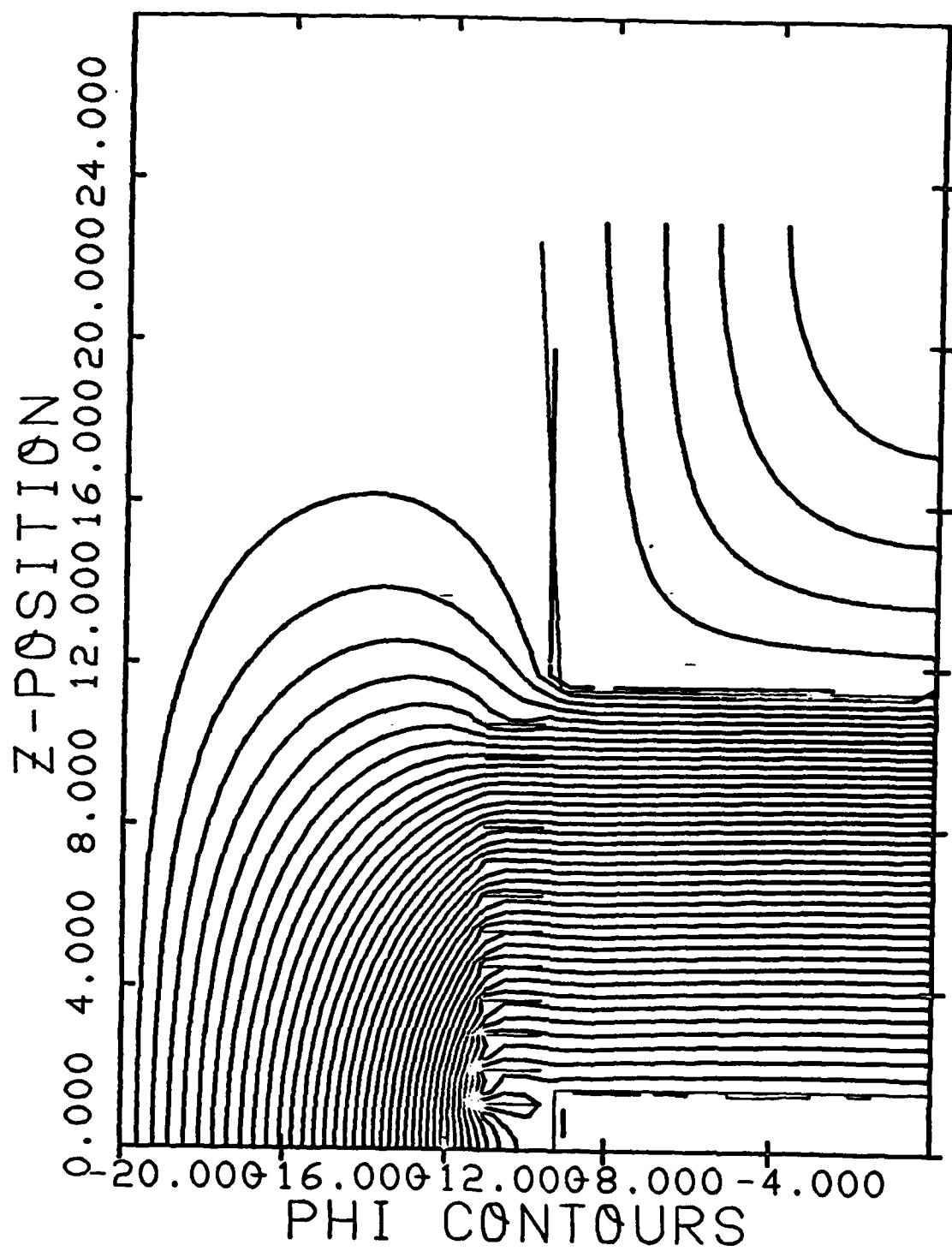


Figure 5. Equipotential Contours in the Diode

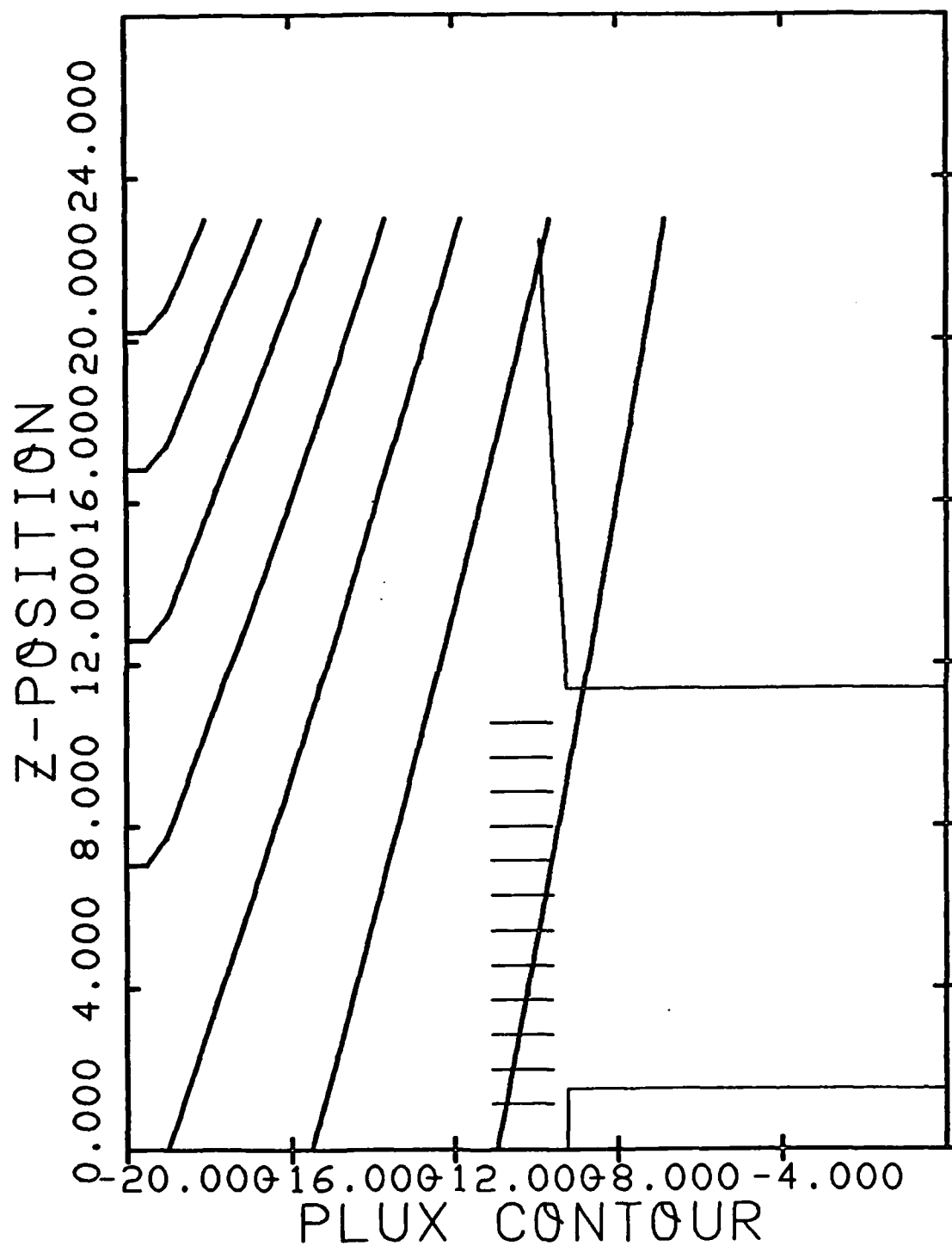


Figure 6. Magnetic Flux Contours in the Diode

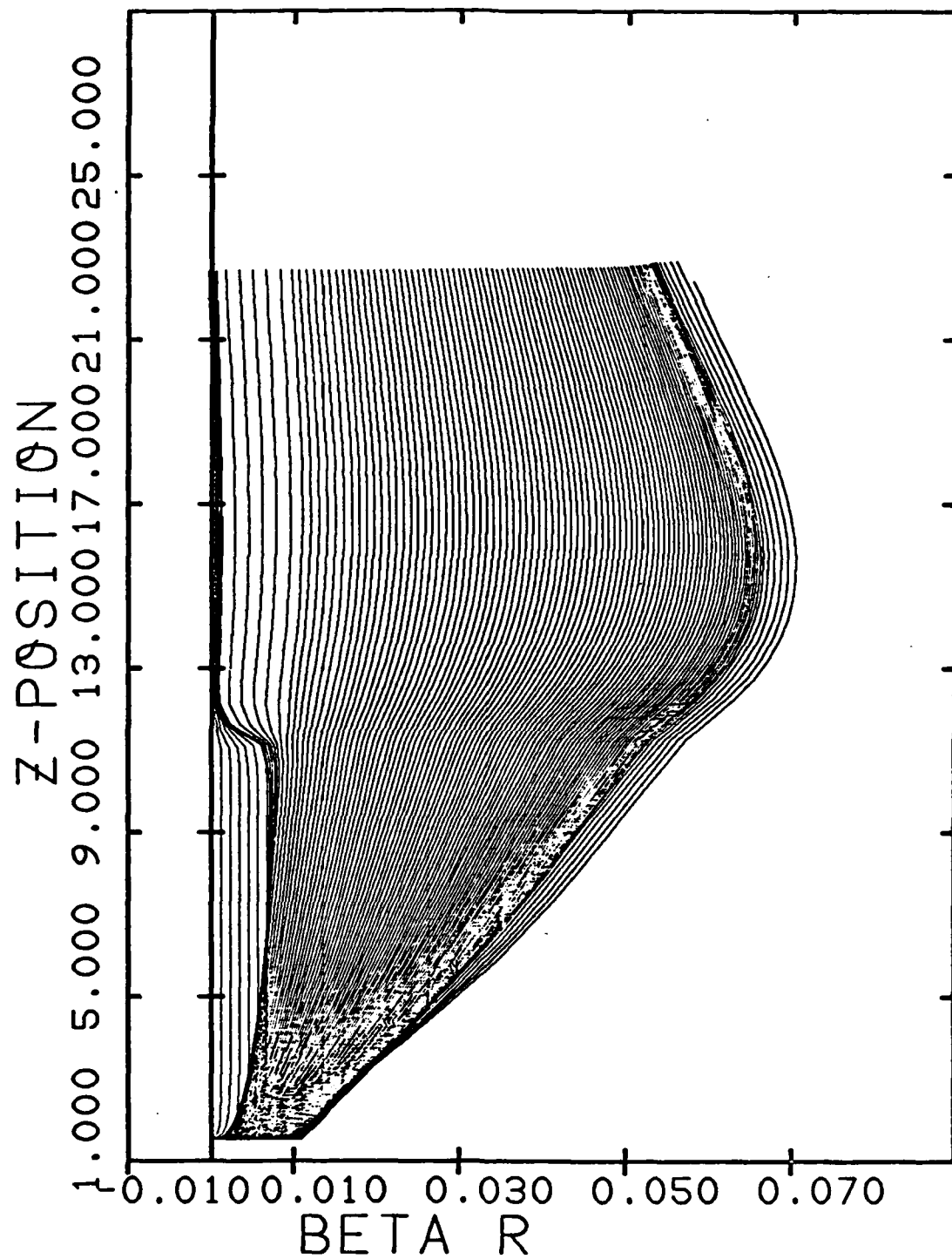


Figure 7. Radial Velocity in the Diode

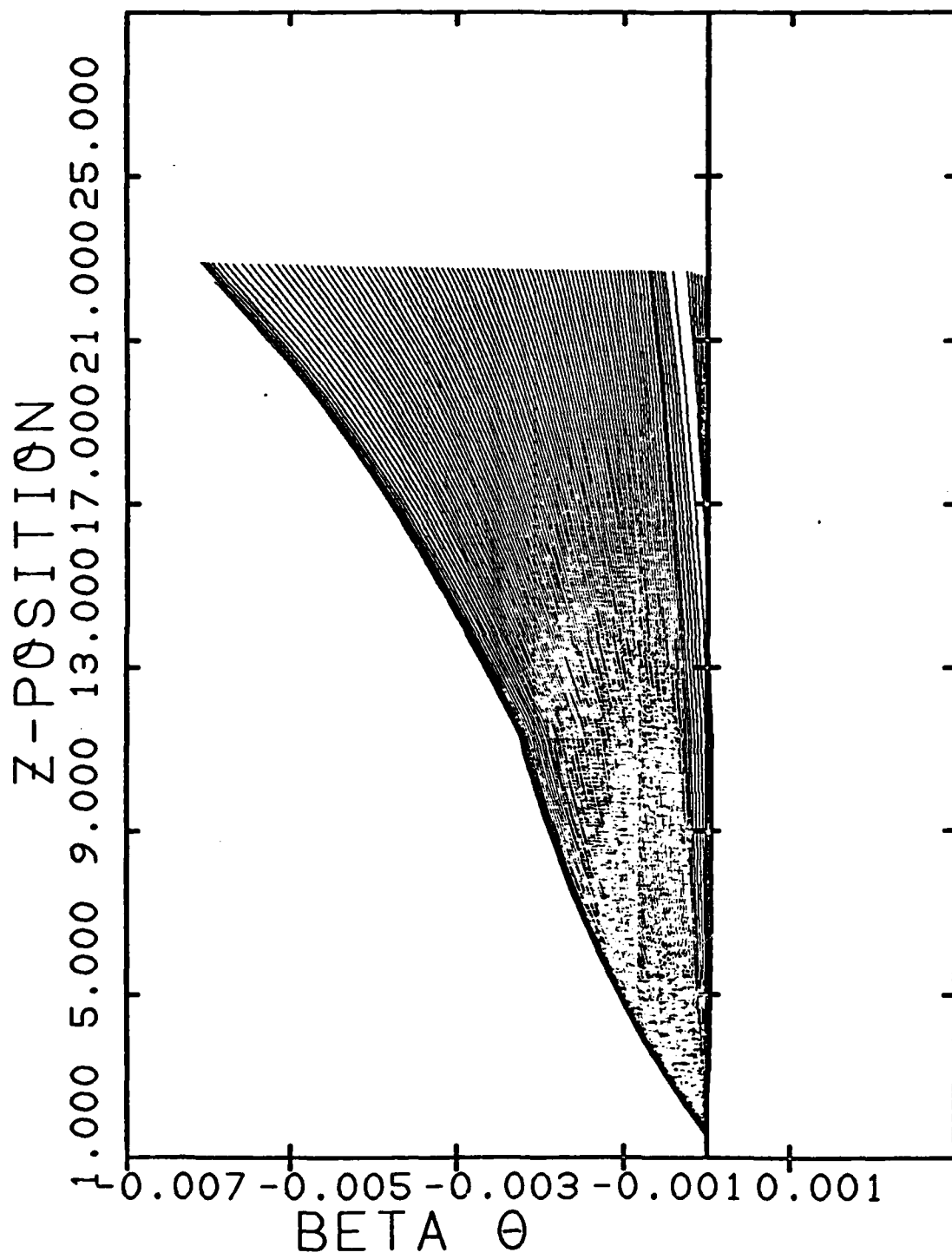


Figure 8. Azimuthal Velocity in the Diode

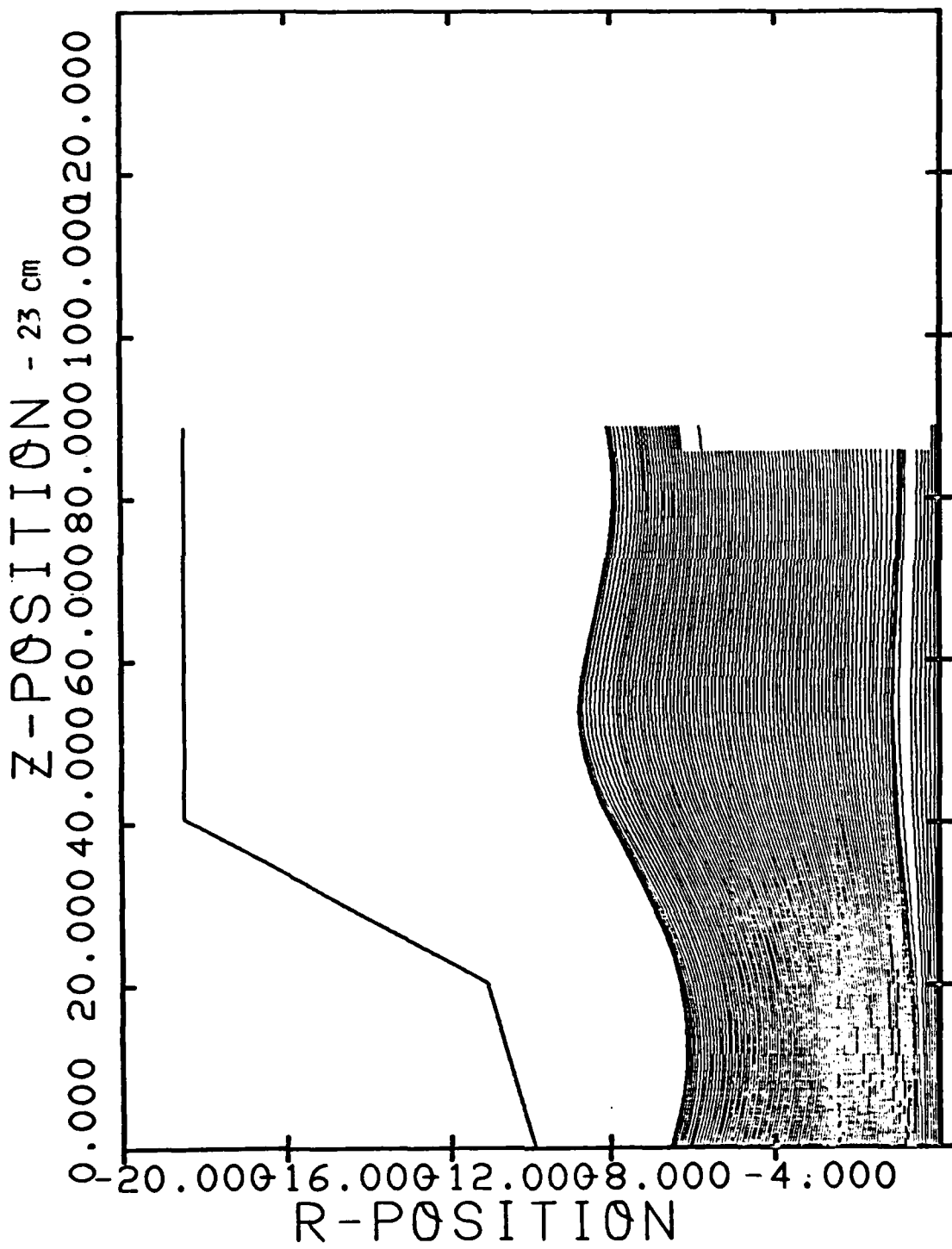


Figure 9. Stage 2 Beam Propagation

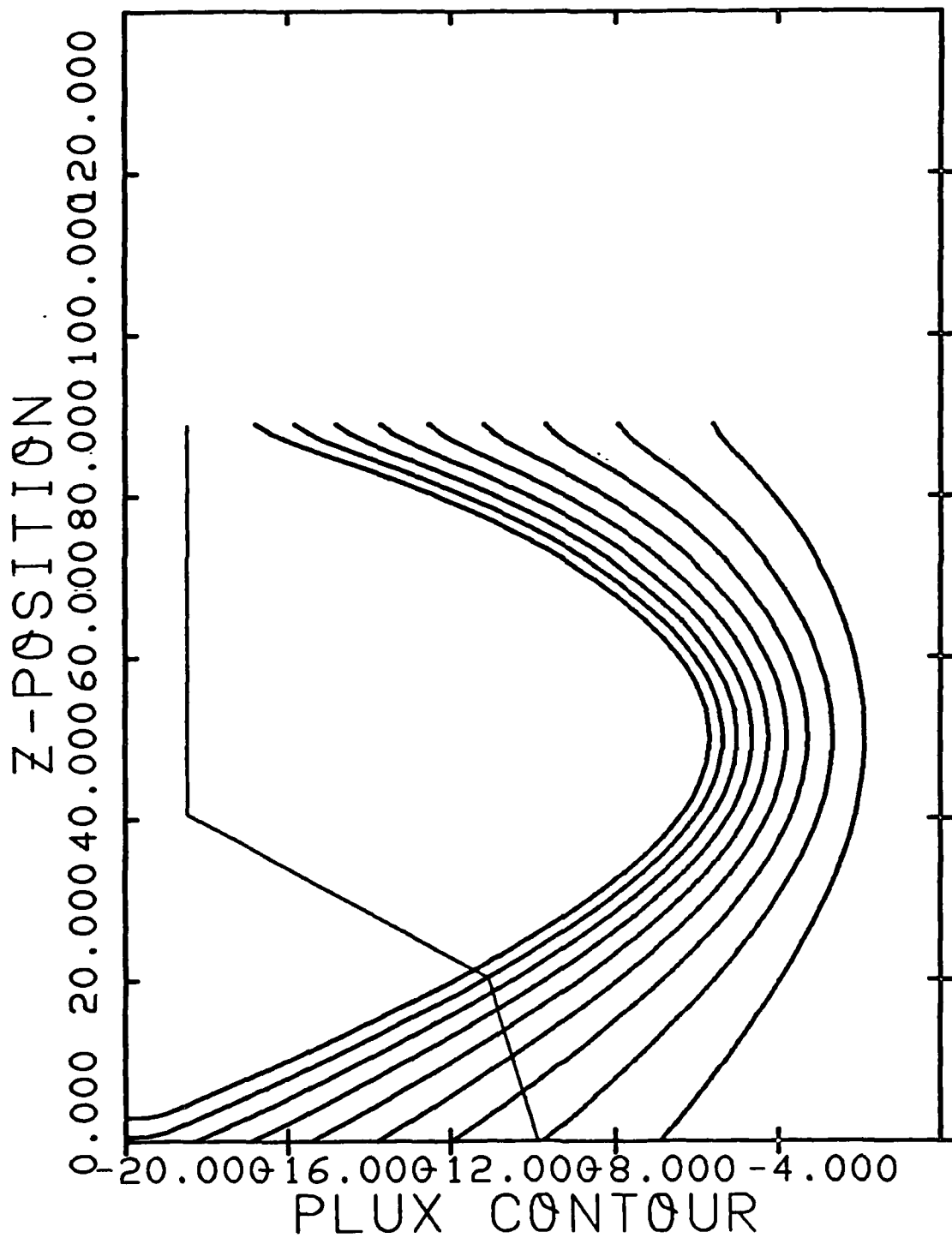


Figure 10. Magnetic Flux Contours in Stage 2

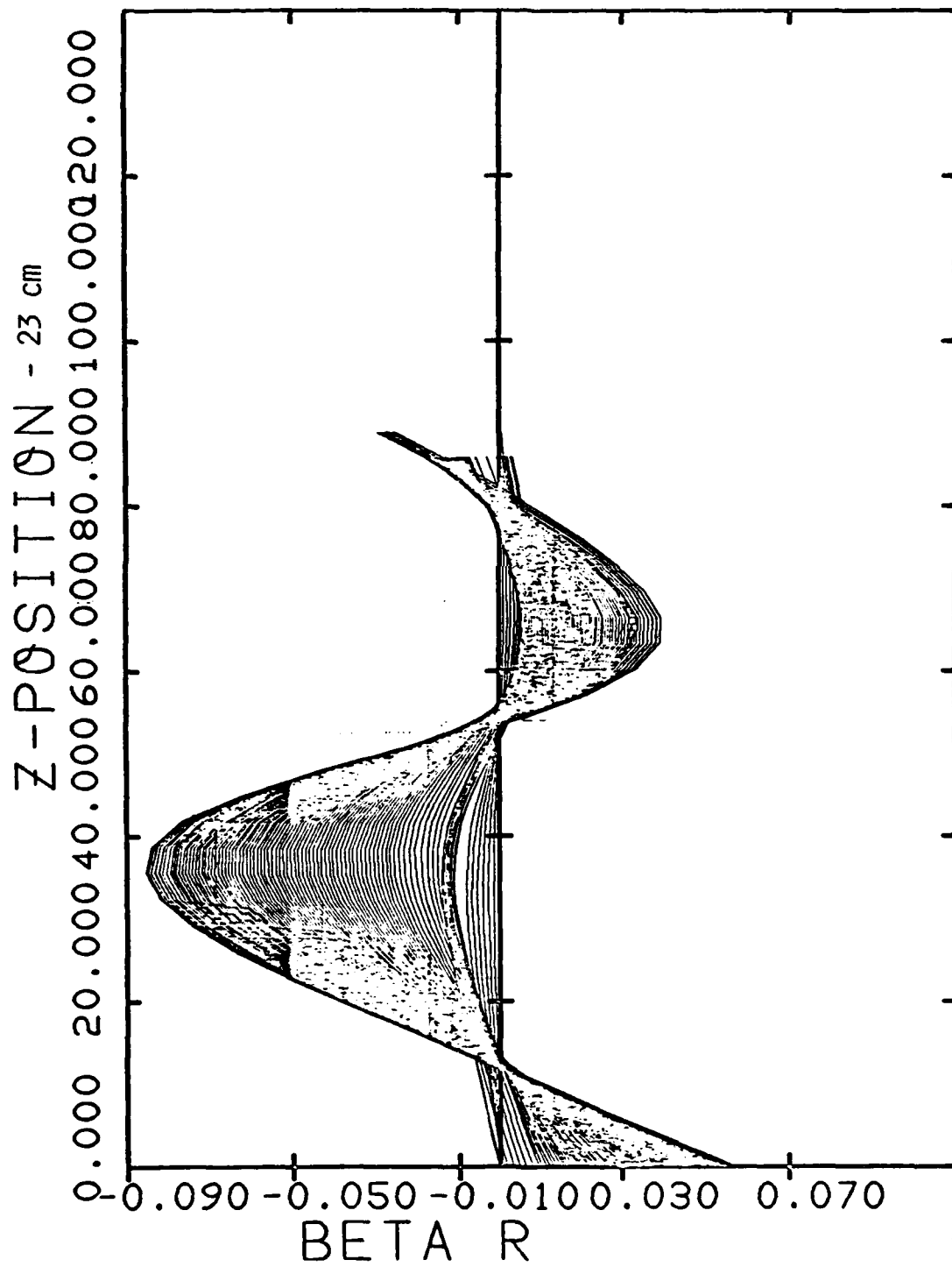


Figure 11. Radial Velocity in Stage 2

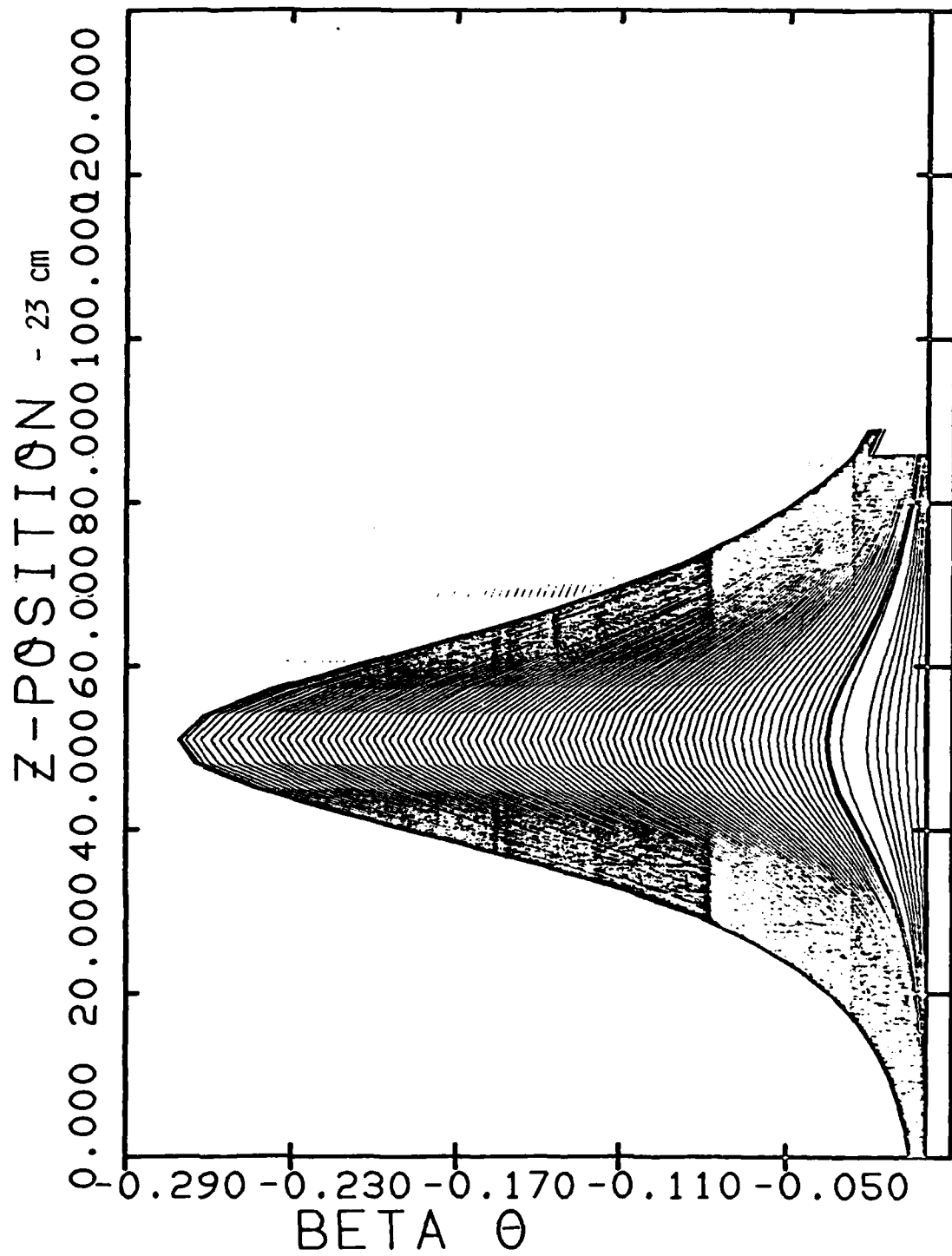


Figure 12. Azimuthal Velocity in Stage 2

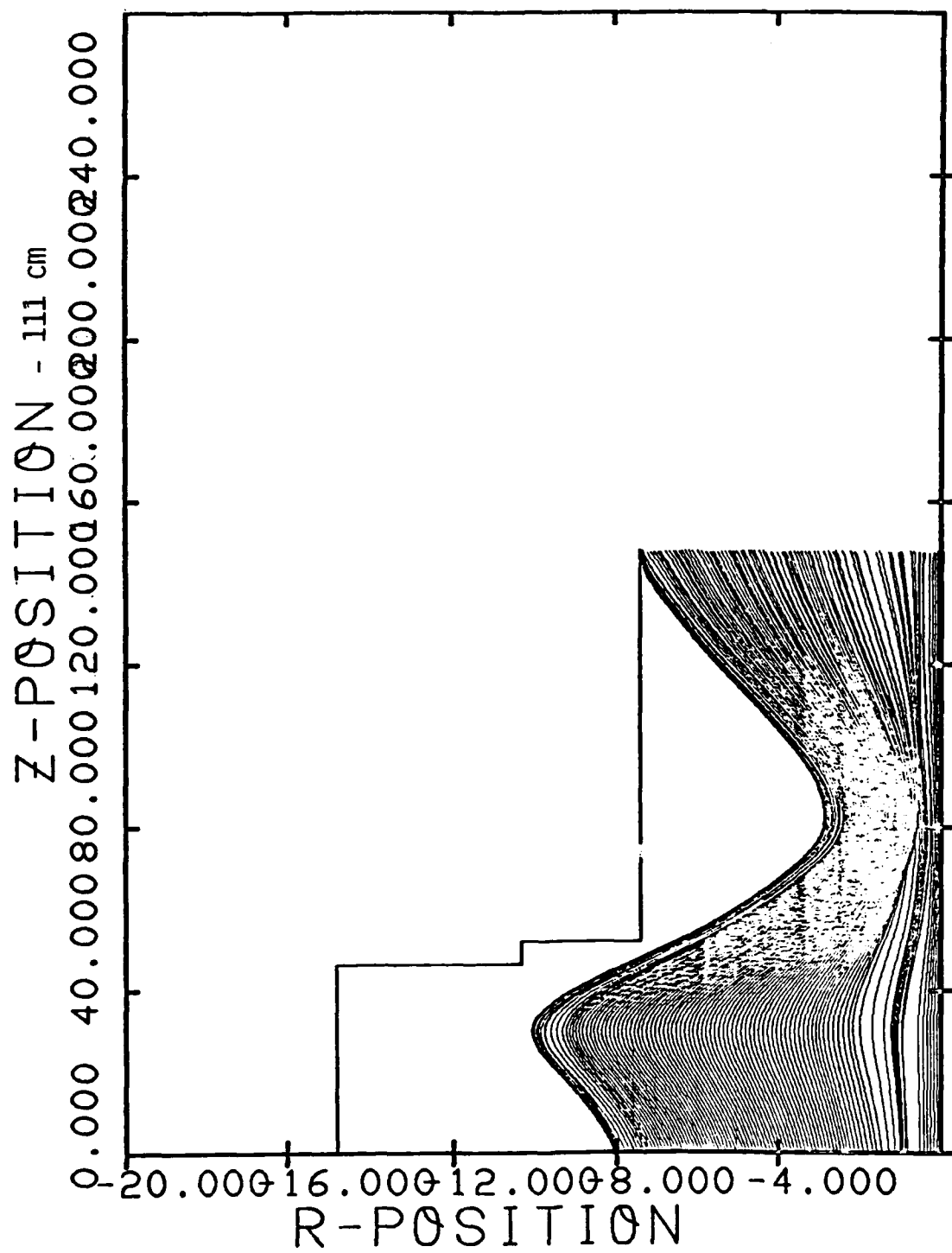


Figure 13. Stage 3 Beam Propagation Thru First Induction Gap

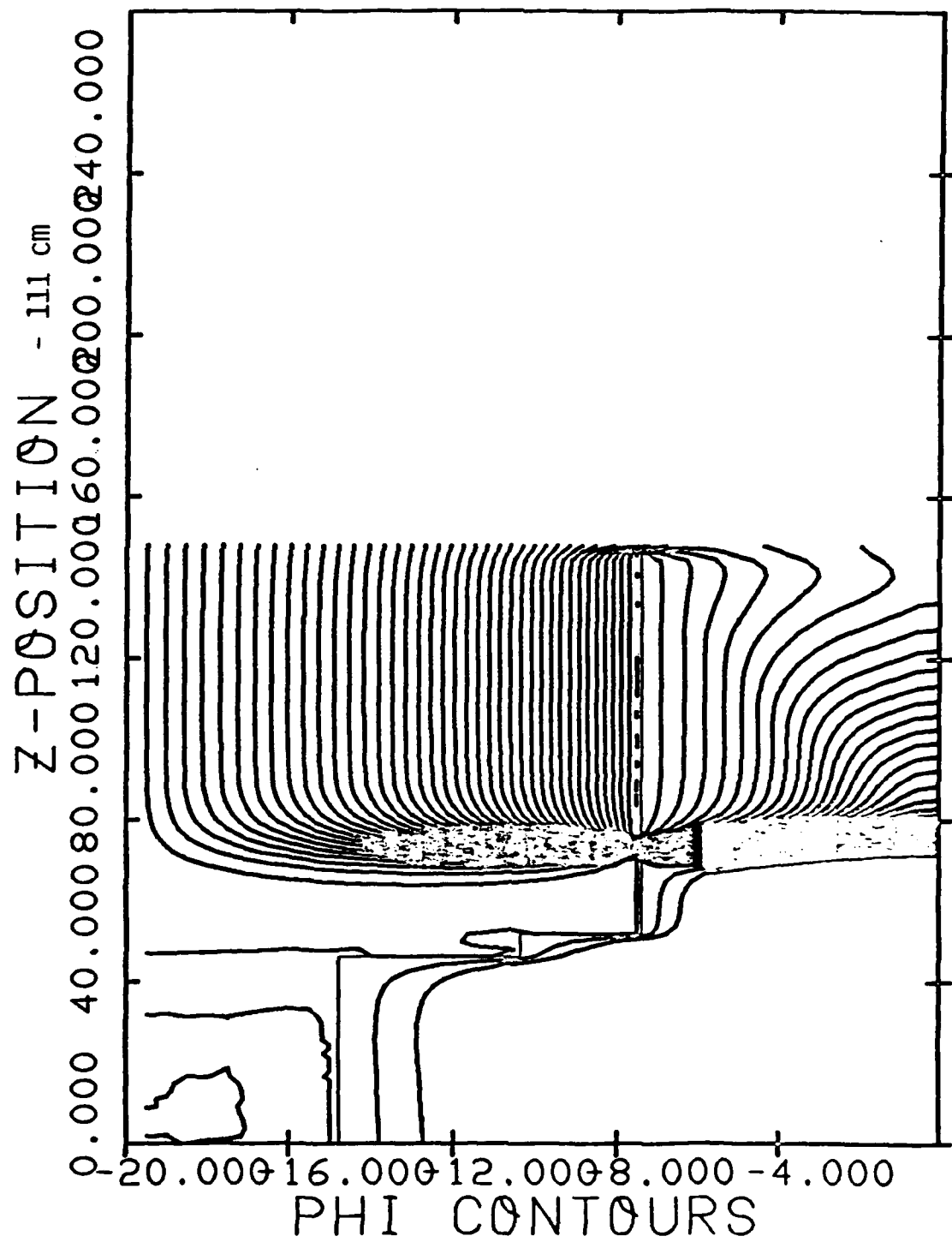


Figure 14. Equipotential Contours in Stage 3

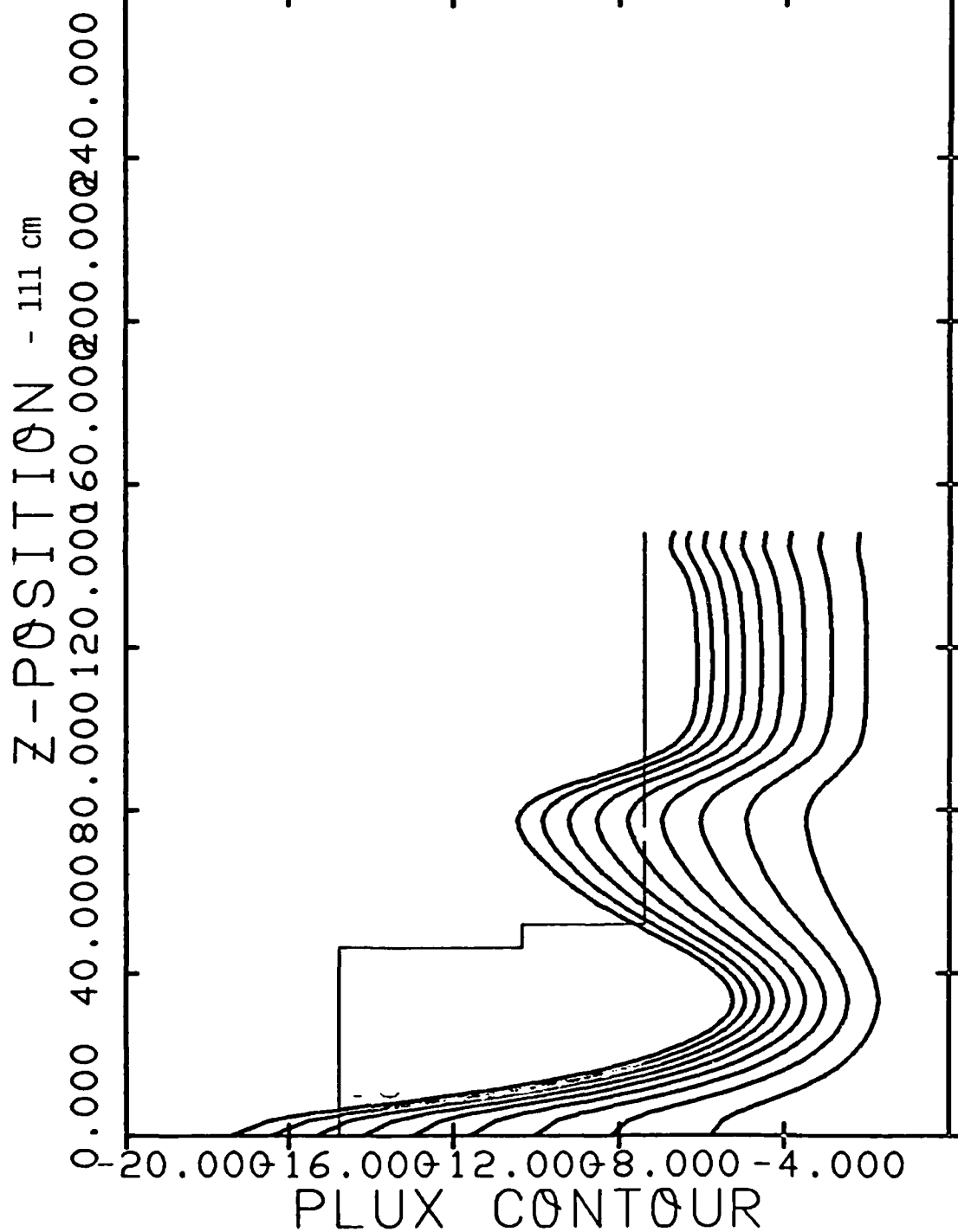


Figure 15. Magnetic Flux Contours in Stage 3

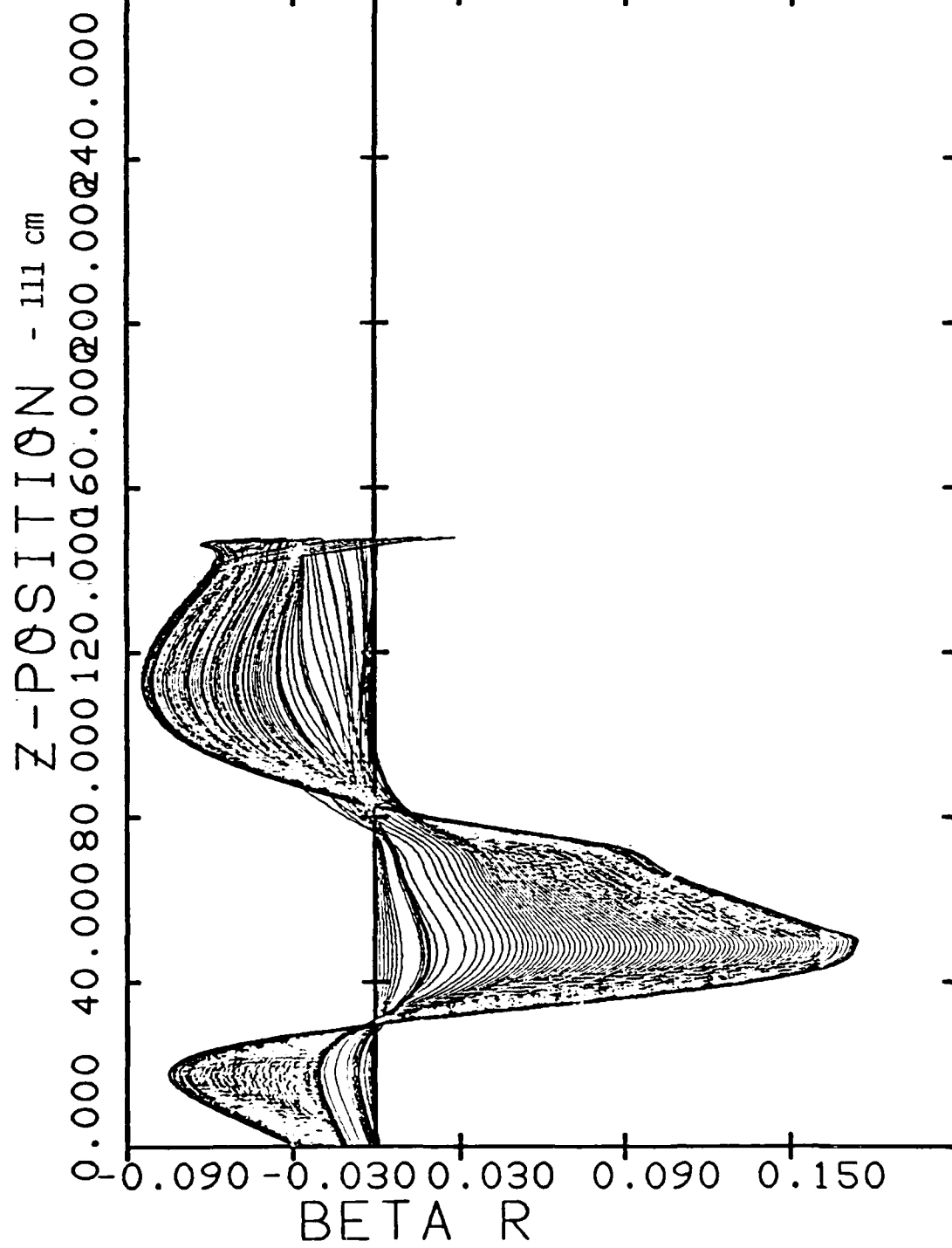


Figure 16. Radial Velocity in Stage 3

Z-POSITION - 111 cm
 0.000 40.000 80.000 120.000 160.000 200.000 240.000

BETA θ
 -0.380 -0.300 -0.220 -0.140 -0.060

Figure 17. Azimuthal Velocity in Stage 3

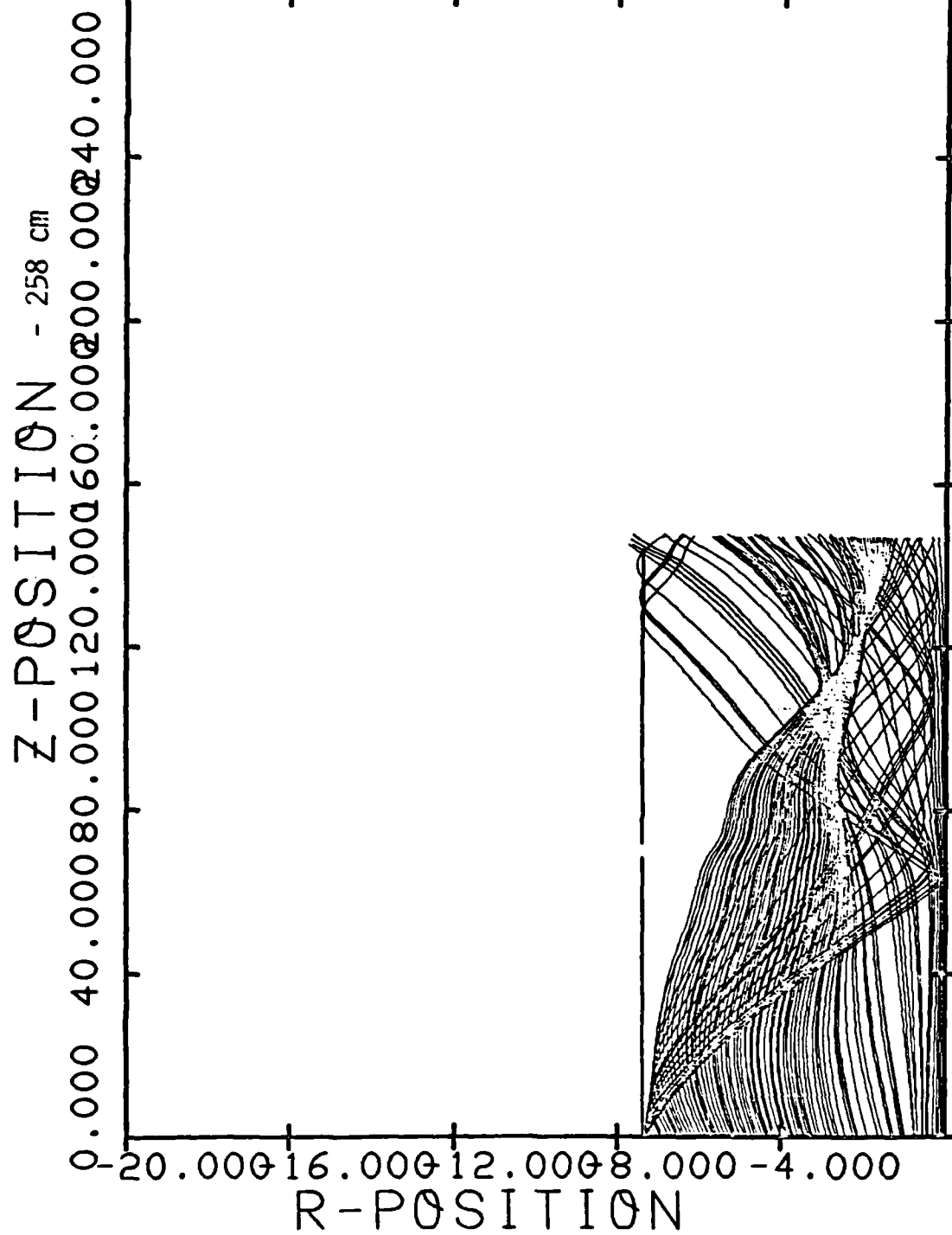


Figure 18. Stage 4 Beam Propagation Thru Second Induction Gap

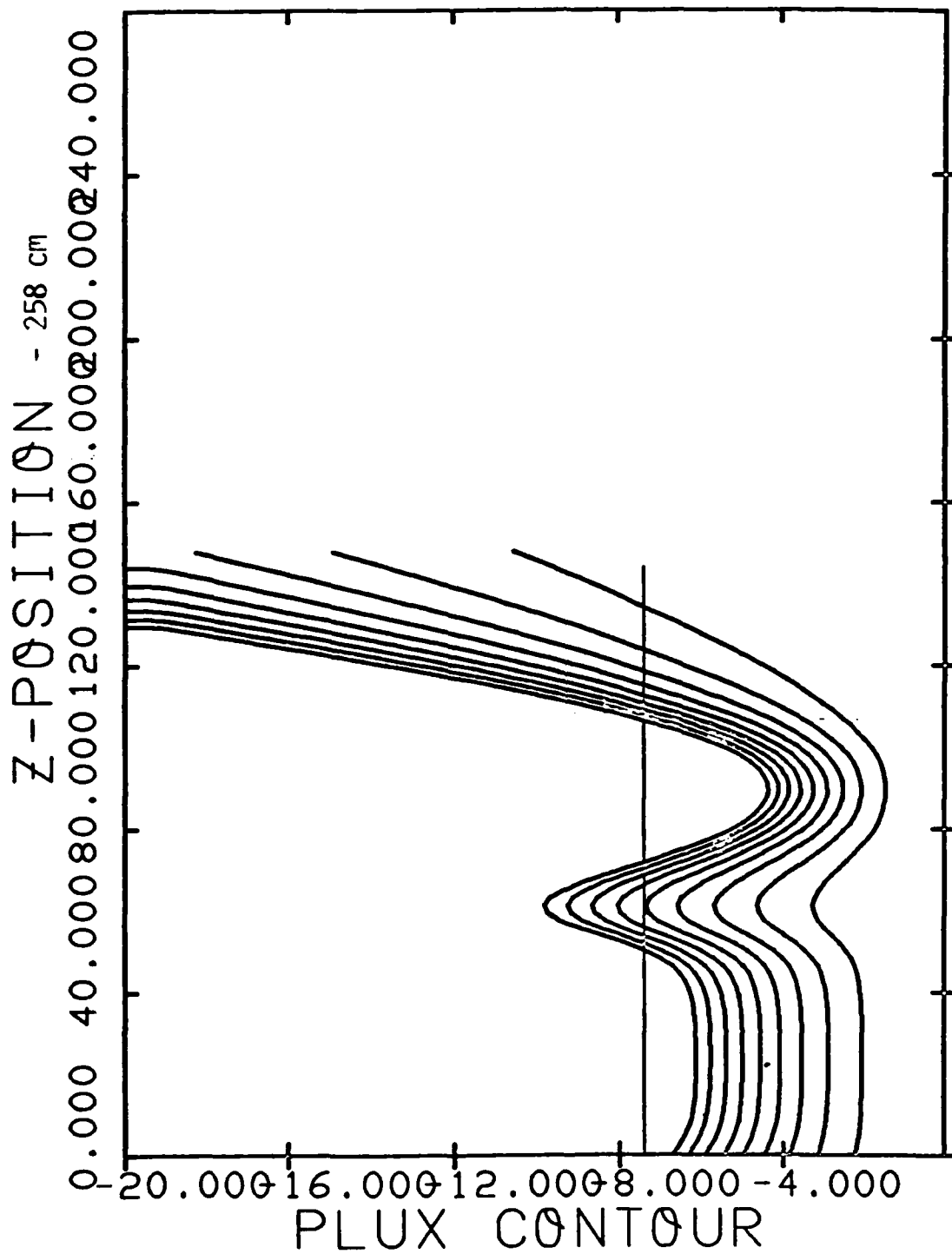


Figure 19. Magnetic Flux Contours in Stage 4

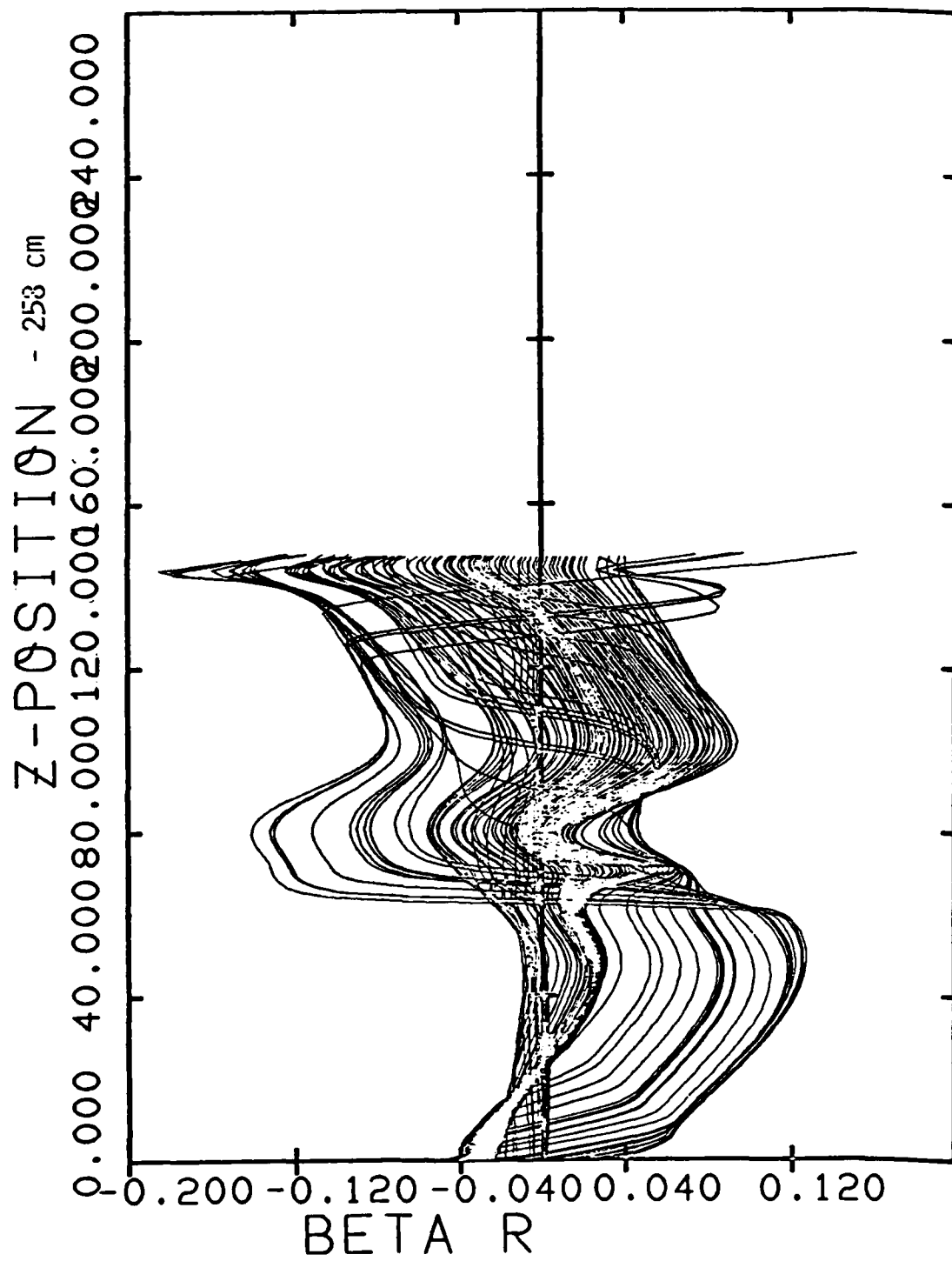


Figure 20. Radial Velocity in Stage 4

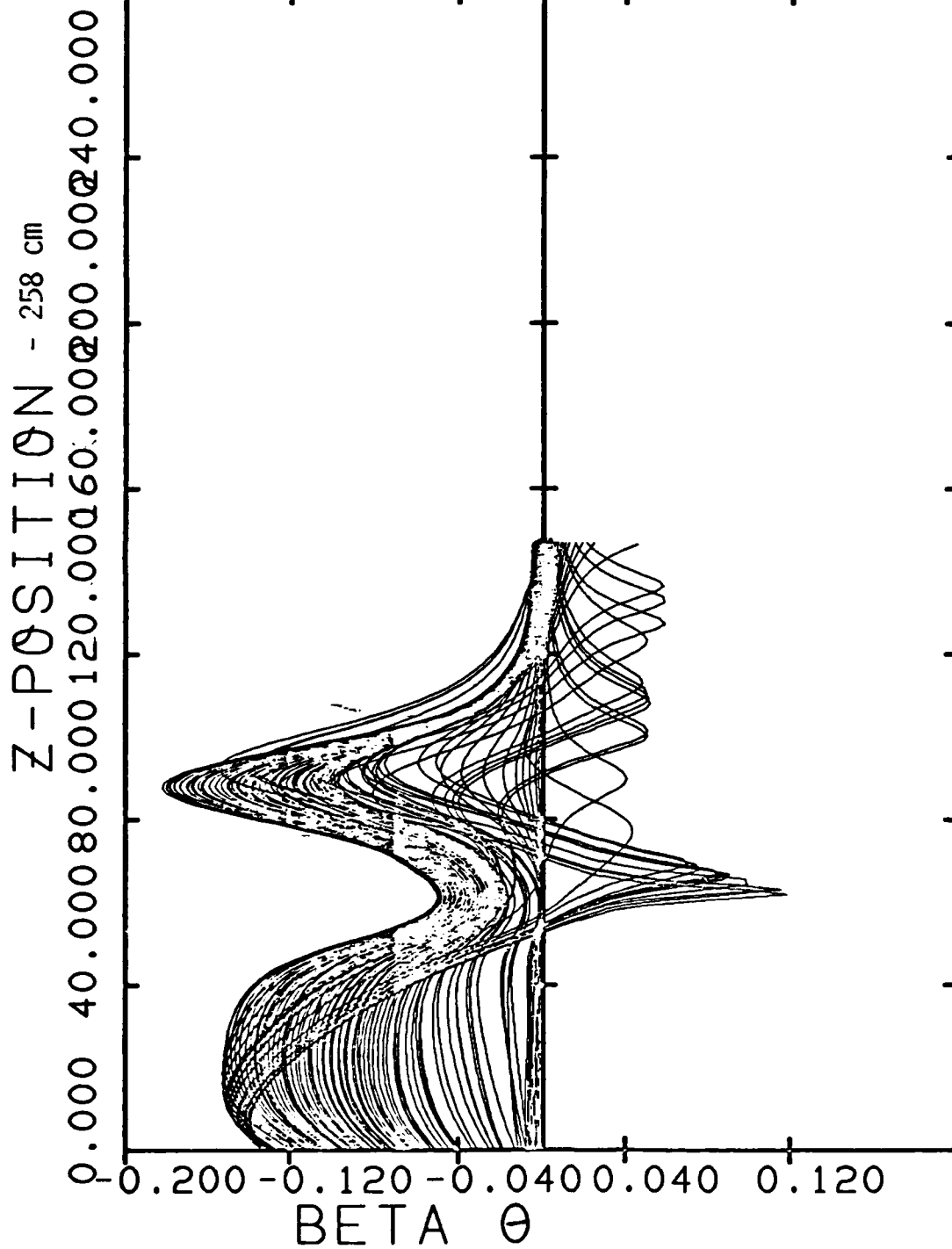


Figure 21. Azimuthal Velocity in Stage 4

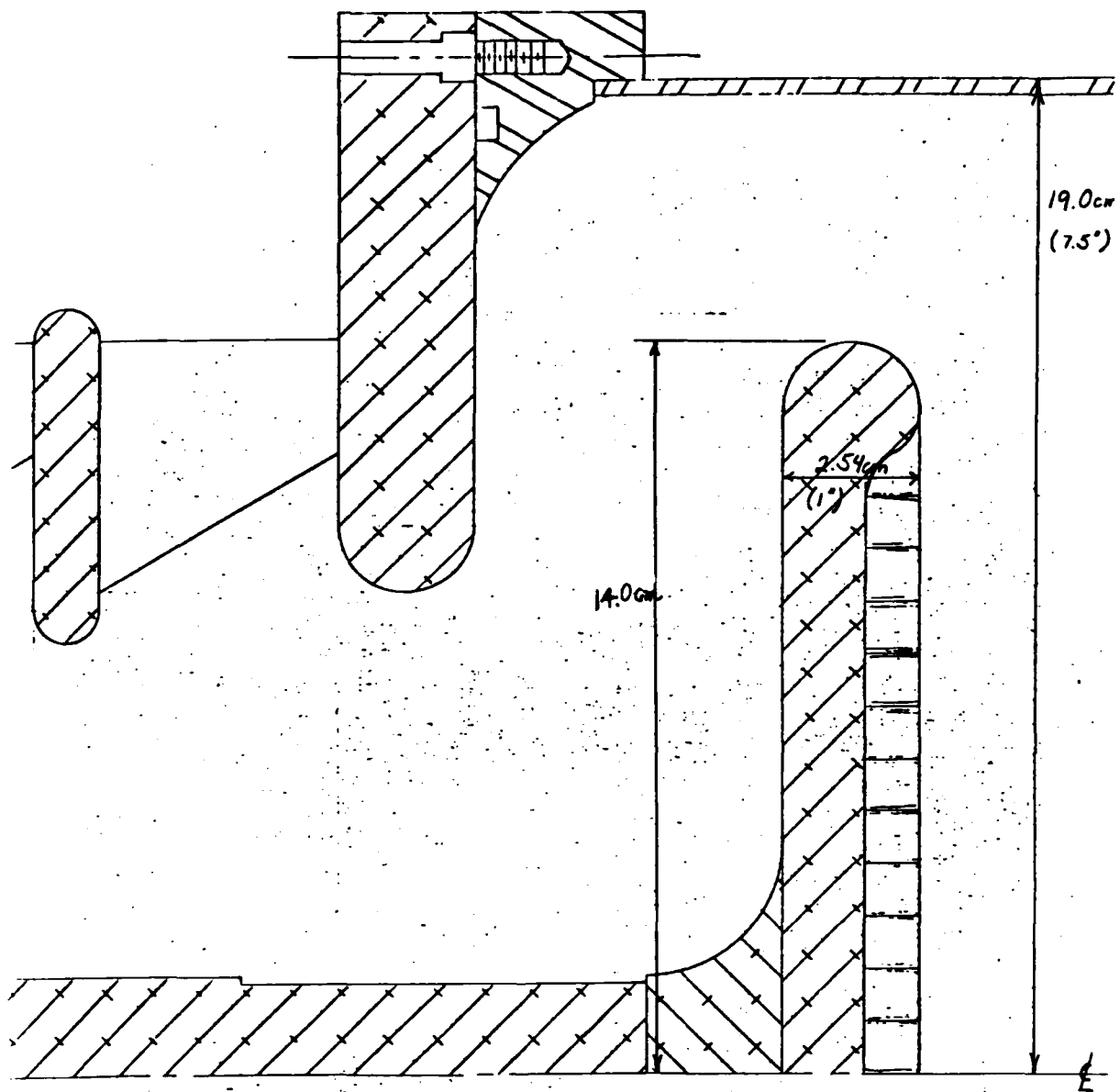


Figure 22. Proposed Diode Geometry

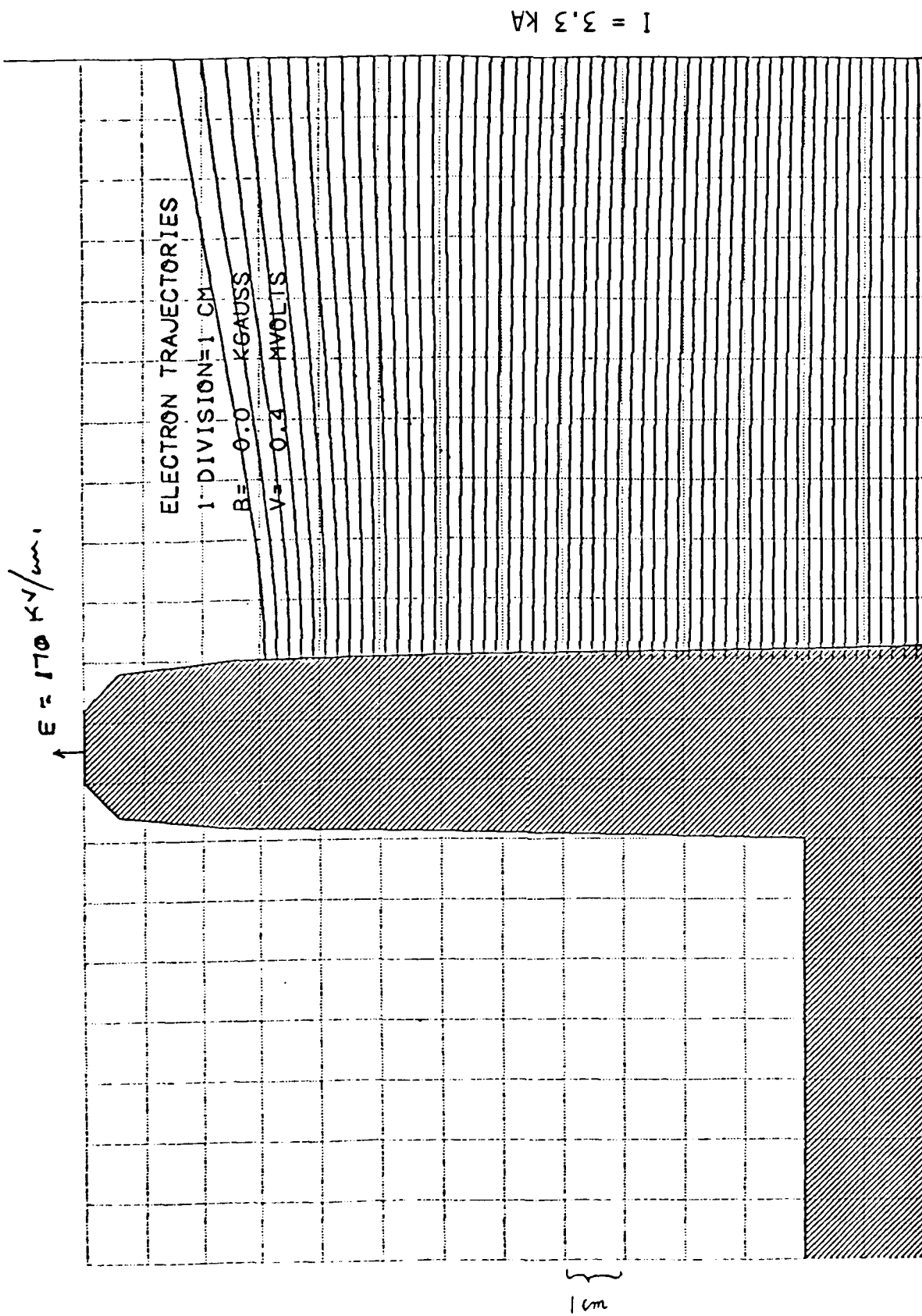


Figure 23. Electron Trajectories in Proposed Diode

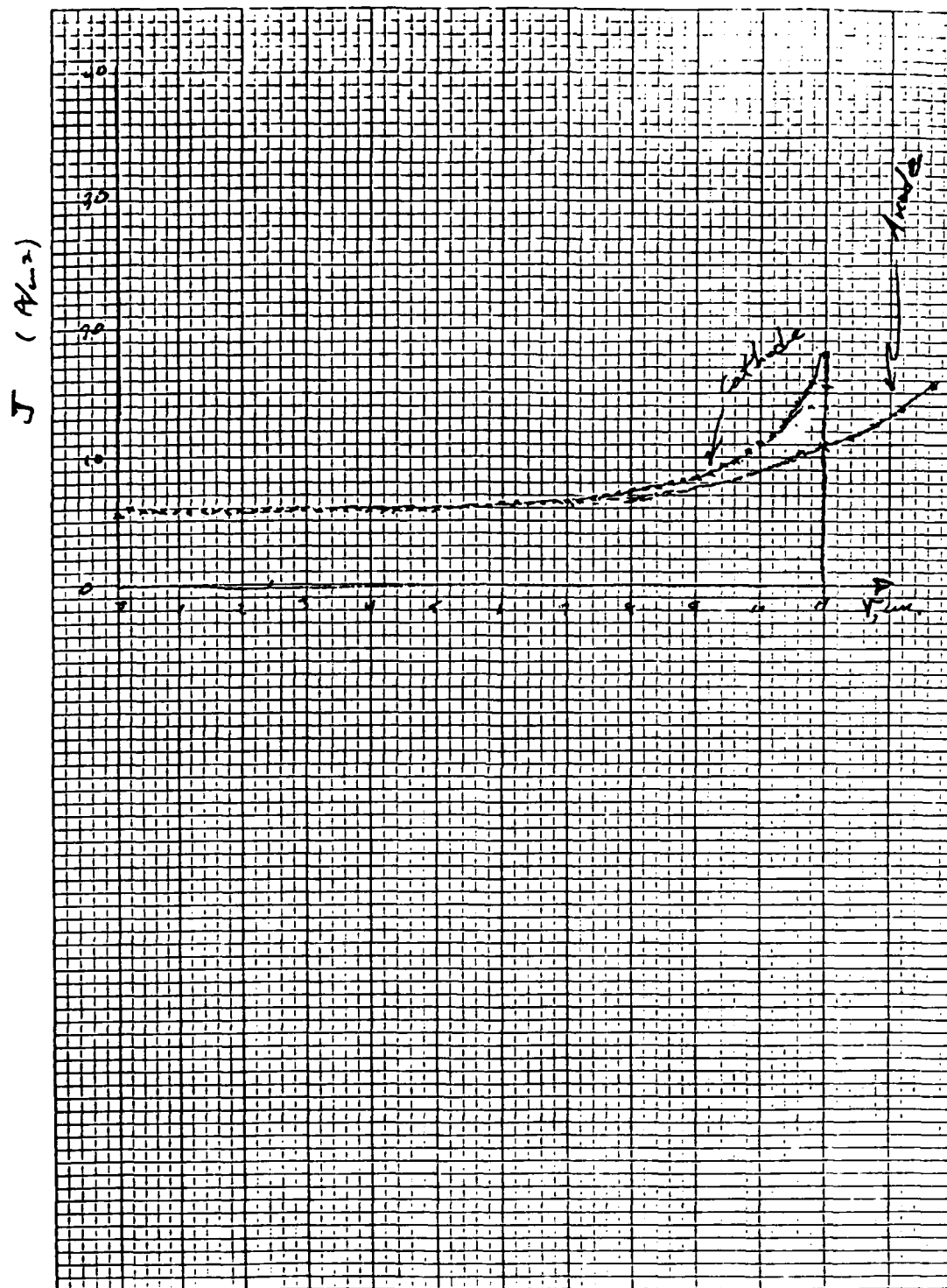


Figure 24. Current Density Profile in Proposed Diode

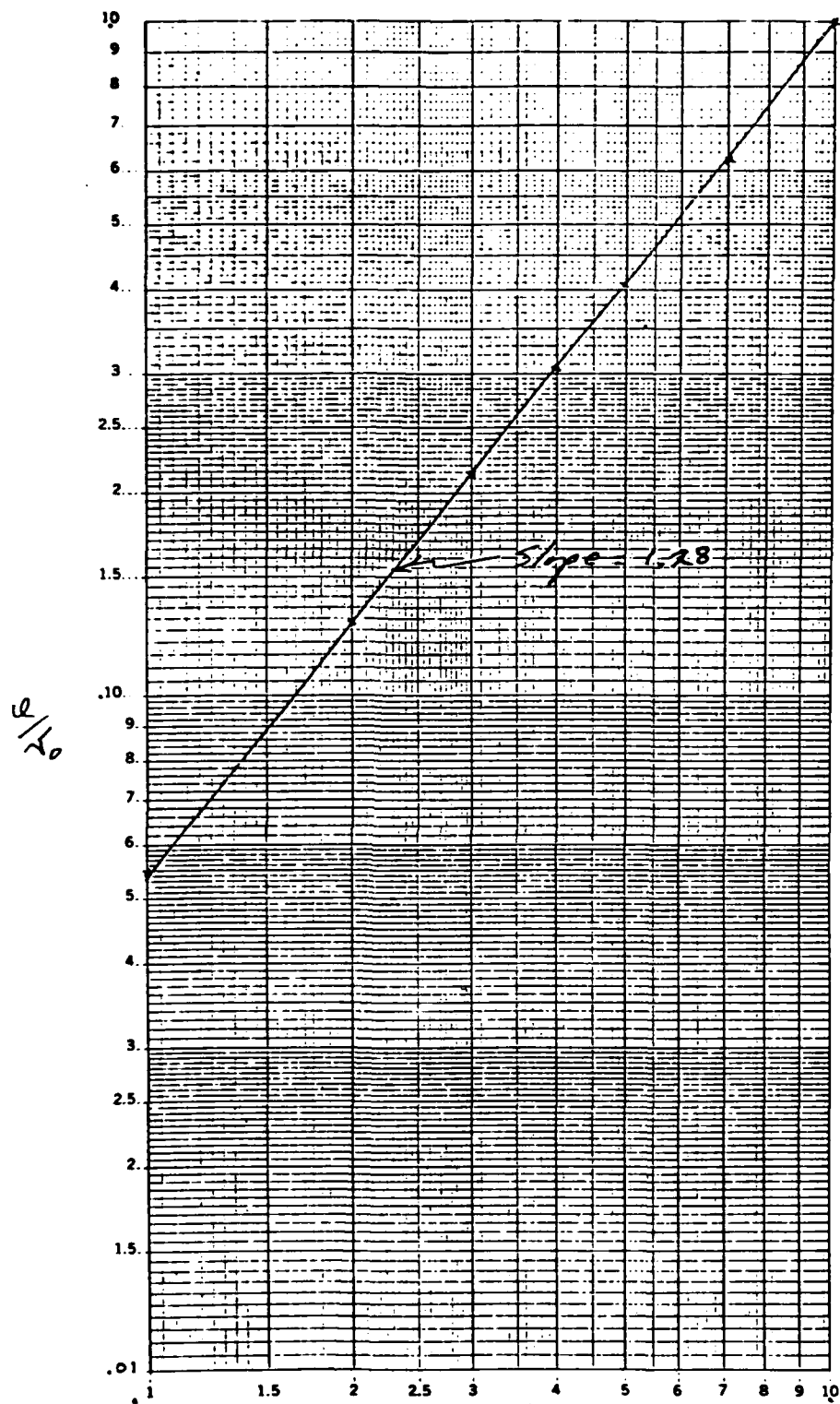


Figure 25. Axial Diode Potential Variation

A P P E N D I X B

Letter from Dr. James R. Thompson to Dr. C. W. Roberson,
dated April 27, 1982.

-- includes 24 figures

Austin Research Associates
1901 Rutland Drive-Austin, Texas 78758-Phone (512) 837-6623

April 27, 1982

Dr. C. W. Roberson
Plasma Physics Division, Code 4704
Naval Research Laboratory
4555 Overlook Avenue
Washington, D.C. 20375

Dear Chuck:

Enclosed is some more computer output to illustrate some of our recent calculations on beam transport through the first four meters of the NBS induction accelerator, including injection into the high field wiggler solenoid. I have numbered the figures and the following commentary is keyed to those numbers.

Figure 1 shows the magnetic field profile which we used for the transport calculations included herein. The wiggler magnetic field was assumed to be 2 kG, and at the end of our Stage 4, at $z = 406$ cm downstream of the cathode, B_z has risen to about 1.96 kG. This point is 26 cm into the throat of the wiggler solenoid.

Figures 2 through 5 show the flow patterns for a cool, laminar beam as it propagates through our Stages 1, 2, 3, and 4 in the presence of the magnetic field of Figure 1. Note that the axial scale varies from stage to stage, and the computer numbers are referenced to the beginning of each stage. In Figure 2, the $v_z B_\phi$ pinching in the diode is apparent, due to E_r being mostly shorted out there. At the end of Stage 3, in the center of the two induction modules, some electrons graze the wall and subsequently collapse to small radii in Stage 4. Near the end of Stage 4, in the region of strong magnetic compression, some electrons are spun up to high θ -velocities, and about 72 A of current is lost on the wall. However, about 780 A, or 92% of the current was successfully transmitted into the solenoid.

Figures 6 and 7 show B_r and B_θ in the Stage 4 flow. Strong zero frequency cyclotron oscillations are apparent in the region of the high field ramp. At this point, most of the transverse beam motion is still coherent, or sloshing, but some thermalization has clearly begun. If one assumes the worst, that all of this cyclotron motion will eventually thermalize, then the resulting beam emittance would be as follows:

Dr. C. W. Roberson
 Naval Research Laboratory
 April 27, 1982
 Page 2

$$\begin{aligned}
 \delta\beta_{\perp \text{ RMS}} &\approx 0.20 \\
 \text{outer beam radius} &= a \approx 1.10 \text{ cm} \\
 \text{RMS beam radius} &= R \approx \frac{a}{\sqrt{2}} = 0.78 \text{ cm} \\
 \gamma &= 2.57 \text{ (800 keV)} \\
 \text{normalized emittance} &= \frac{\epsilon_n}{\pi} = \gamma R \delta\beta_{\perp} \approx 400 \text{ mrad-cm} \\
 &\quad @ I = 780 \text{ A}
 \end{aligned}
 \left. \vphantom{\begin{aligned} \delta\beta_{\perp \text{ RMS}} &\approx 0.20 \\ \text{outer beam radius} &= a \approx 1.10 \text{ cm} \\ \text{RMS beam radius} &= R \approx \frac{a}{\sqrt{2}} = 0.78 \text{ cm} \end{aligned}} \right\} \text{ eyeball estimates}$$

This is considerably higher than the Stage 1 emittance for the laminar flow shown in Figure 2. There we estimate

$$\begin{aligned}
 \delta\beta_{\perp} &< 0.005 \\
 a &\approx 7.6 \text{ cm} \\
 R &\approx 5.37 \text{ cm} \\
 \gamma &\approx 1.78 \text{ (400 keV)} \\
 \frac{\epsilon_n}{\pi} &< 50 \text{ mrad-cm @ } I = 852 \text{ A}
 \end{aligned}$$

The reason for the much higher emittance in Stage 4 is of course the strong zero frequency oscillations which are excited as the beam is compressed.

Figures 8 and 9 show the equipotentials and the magnetic flux surfaces in Stage 4.

Figure 10 shows the Stage 1 diode flow, with a random angular scatter introduced at the location of the anode mesh. The RMS angular scatter was taken as 2.83° in the transverse plane. Figures 11 and 12 show β_r and β_θ for this scattered Stage 1 flow. The emittance just downstream of the anode mesh is as follows:

Dr. C. W. Roberson
Naval Research Laboratory
April 27, 1982
Page 3

$$\begin{aligned}\delta\beta_1 \text{ RMS} &\approx 0.041 \\ a &\approx 7.6 \text{ cm} \\ R &\approx 5.37 \text{ cm} \\ \gamma &\approx 1.78 \text{ (400 keV)} \\ \frac{\epsilon_n}{\pi} &\approx 392 \text{ mrad-cm @ } I = 858 \text{ A}\end{aligned}$$

Figure 13 shows the equipotentials in the diode region.

Figure 14 shows the Stage 2 flow pattern of the scattered beam, and Figures 15 and 16 show the corresponding β_r and β_θ .

Figure 17 shows the Stage 3 flow pattern, and Figures 18 and 19 show the corresponding β_r and β_θ . Stage 3 encompasses coil 2, coil 3, coil 4, the first induction gap, and the solenoidal coil 5. In this stage, a significant portion of the scattered beam is lost to the walls. About 135 A, or 16% of the beam current is lost at $z = 154$ cm at the entrance to the induction module. Another 349 A, or 41% of the beam current is lost between 20 cm and 70 cm downstream of the first induction gap, under the solenoidal coil 5. This leaves 374 A, or 44% of the beam current injected into stage 4. Figure 20 shows the Stage 3 equipotentials, including the strong gradients in the induction gap.

Figure 21 shows the Stage 4 flow pattern for the scattered beam, and Figures 22 and 23 show the corresponding β_r and β_θ . Stage 4 encompasses the second induction gap, and the magnetic field ramp into the wiggler solenoid. No further current is lost in Stage 4. The β_r and β_θ diagnostics again reveal strong zero frequency cyclotron oscillations. These have begun to thermalize somewhat, but are still largely coherent at the end of Stage 4. If we again assume that this cyclotron motion will eventually phase mix, the resulting emittance would be as follows:

Dr. C. W. Roberson
Naval Research Laboratory
April 27, 1982
Page 4

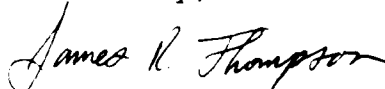
$$\left. \begin{aligned} \delta\beta_1 \text{ RMS} &\approx 0.20 \\ a &\approx 1.10 \text{ cm} \\ R &\approx 0.78 \text{ cm} \\ \gamma &\approx 2.57 \text{ (800 keV)} \\ \frac{\epsilon_n}{\pi} &\approx 400 \text{ mrad-cm @ } I = 374 \text{ A} \end{aligned} \right\} \text{ eyeball estimates}$$

The projected emittance for the scattered beam is thus the same as for the unscattered beam; however, since the transmitted current is much lower for the scattered beam, the scattered beam may be said to be hotter than is a corresponding amount of current in the unscattered beam. Likewise, for the 374 A transmitted, the emittance has grown significantly between Stages 1 and 4 due to the cyclotron motion excited in Stage 4.

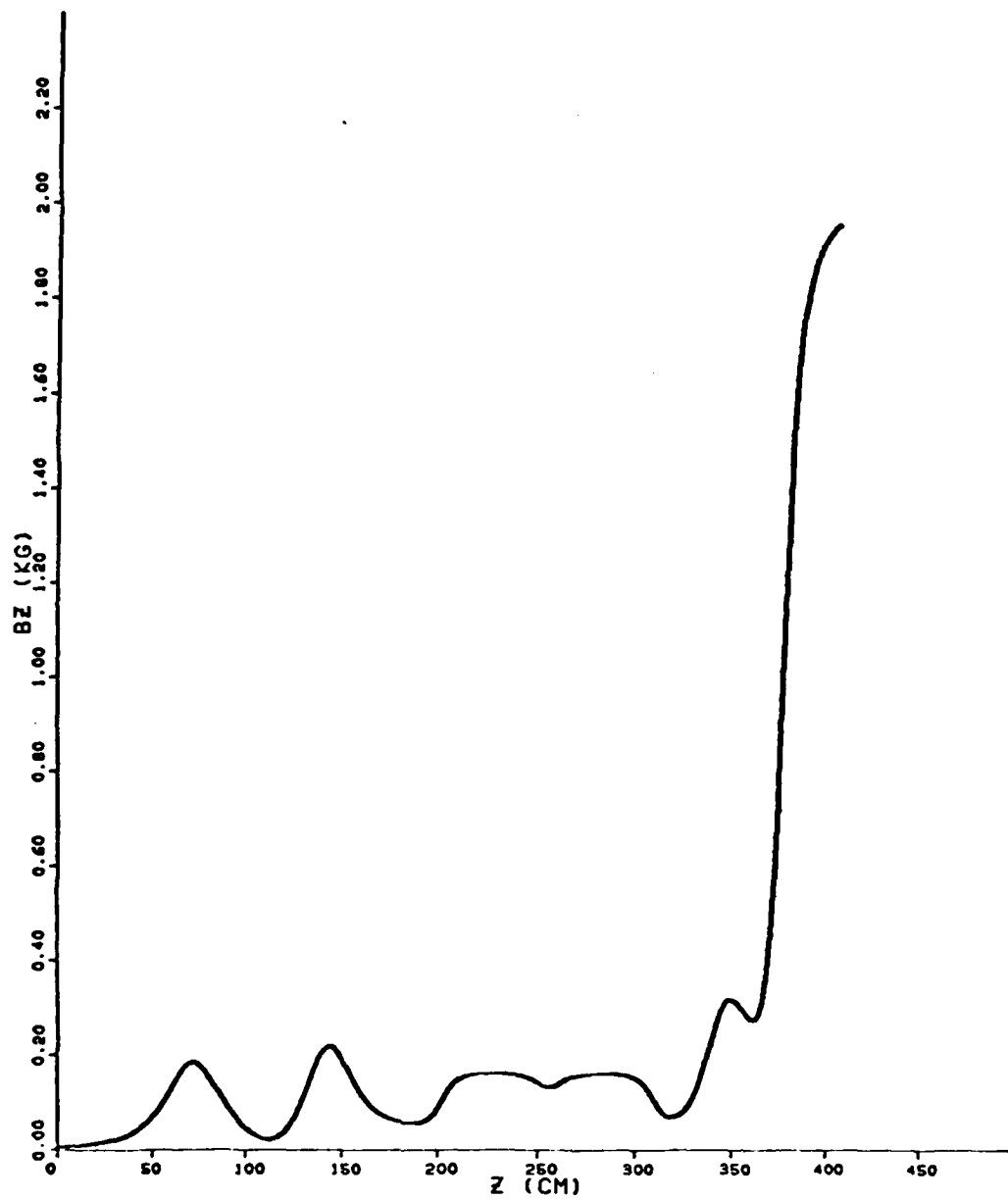
Figure 24 shows the magnetic flux contours for Stage 4. The inner contour drawn corresponds to $B_z r = 0.72 \text{ kG-cm}^2$. Hence it corresponds to the flux within $r = 0.6 \text{ cm}$ at $B_z = 2 \text{ kG}$, which are the desired final-state beam conditions. Unfortunately, Figure 21 reveals that the beam is well outside of this desired flux contour, despite carrying less current than desired into Stage 4. Producing the desired beam current density in the wiggler solenoid with $B_z = 2 \text{ kG}$ therefore remains a difficult challenge for our future work.

I am sorry for the delay of several days in getting these results into the mail. Also, we have recently noticed a peculiarity in the current diagnostic which appears to have some relation to the current lost in Stage 3. Until we get this sorted out, you should probably treat the figure of 374 A of transmitted current with a grain of salt.

Sincerely,



Bob Thompson



BZ VS Z

Figure 1. Transport Magnetic Field Profile with
Strong Wiggler Solenoidal Field

2-APR-82
12:20:30

(ara)

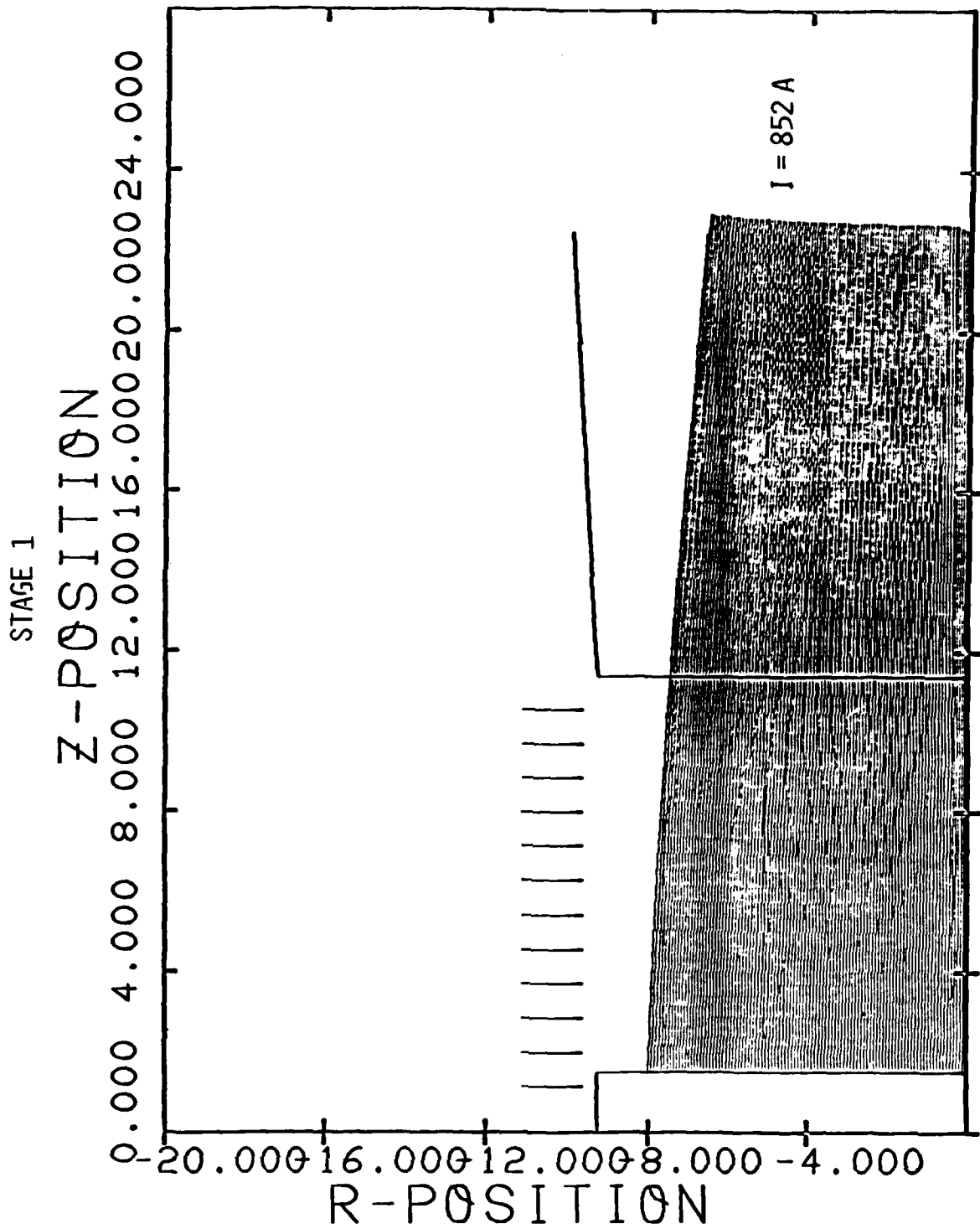


Figure 2. Laminar Beam Formation at Stage 1
Child-Langmuir Potential Grading

STAGE 2

Z-POSITION - 23 cm

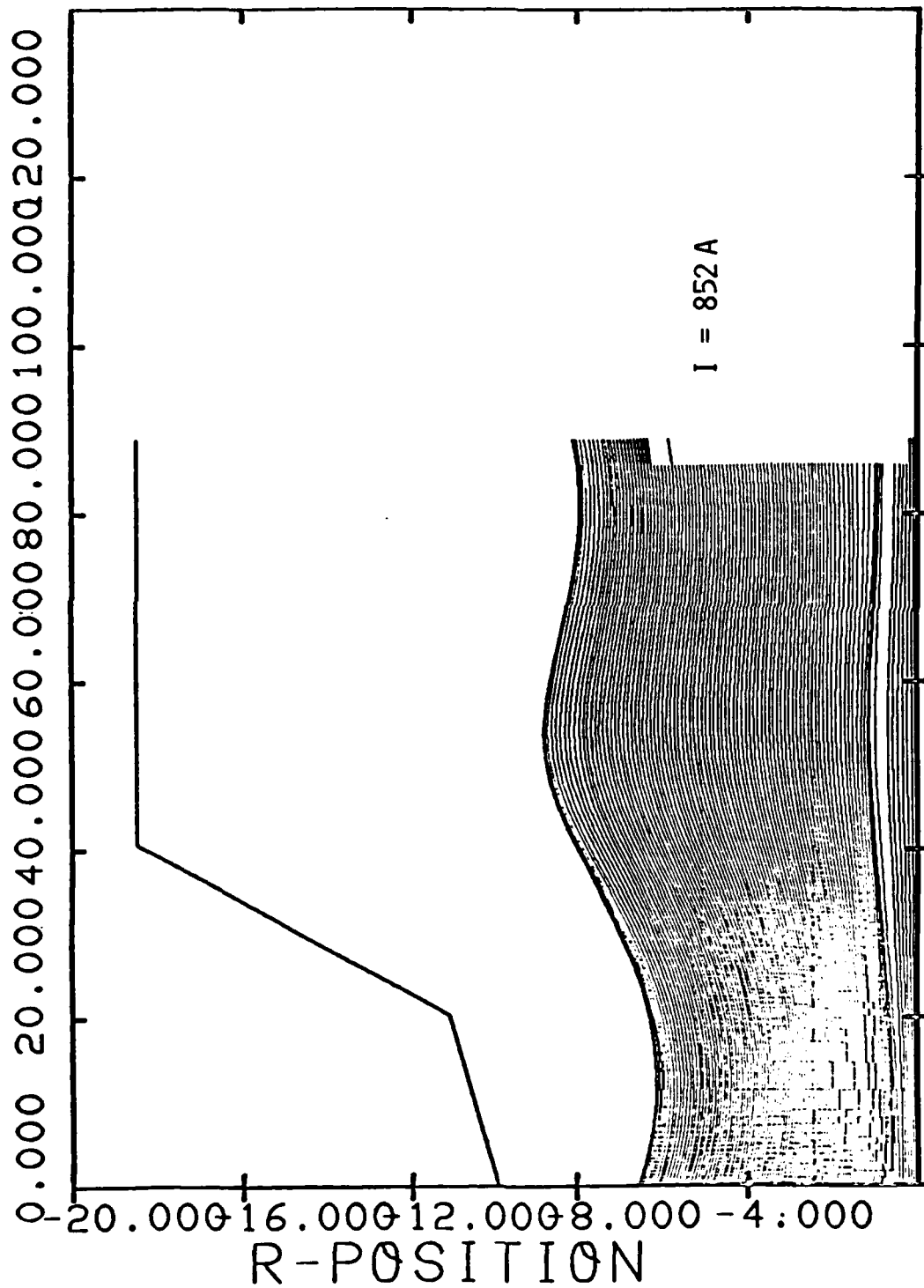


Figure 3. Laminar Beam Flow at Stage 2

STAGE 3

Z-POSITION - 111 cm

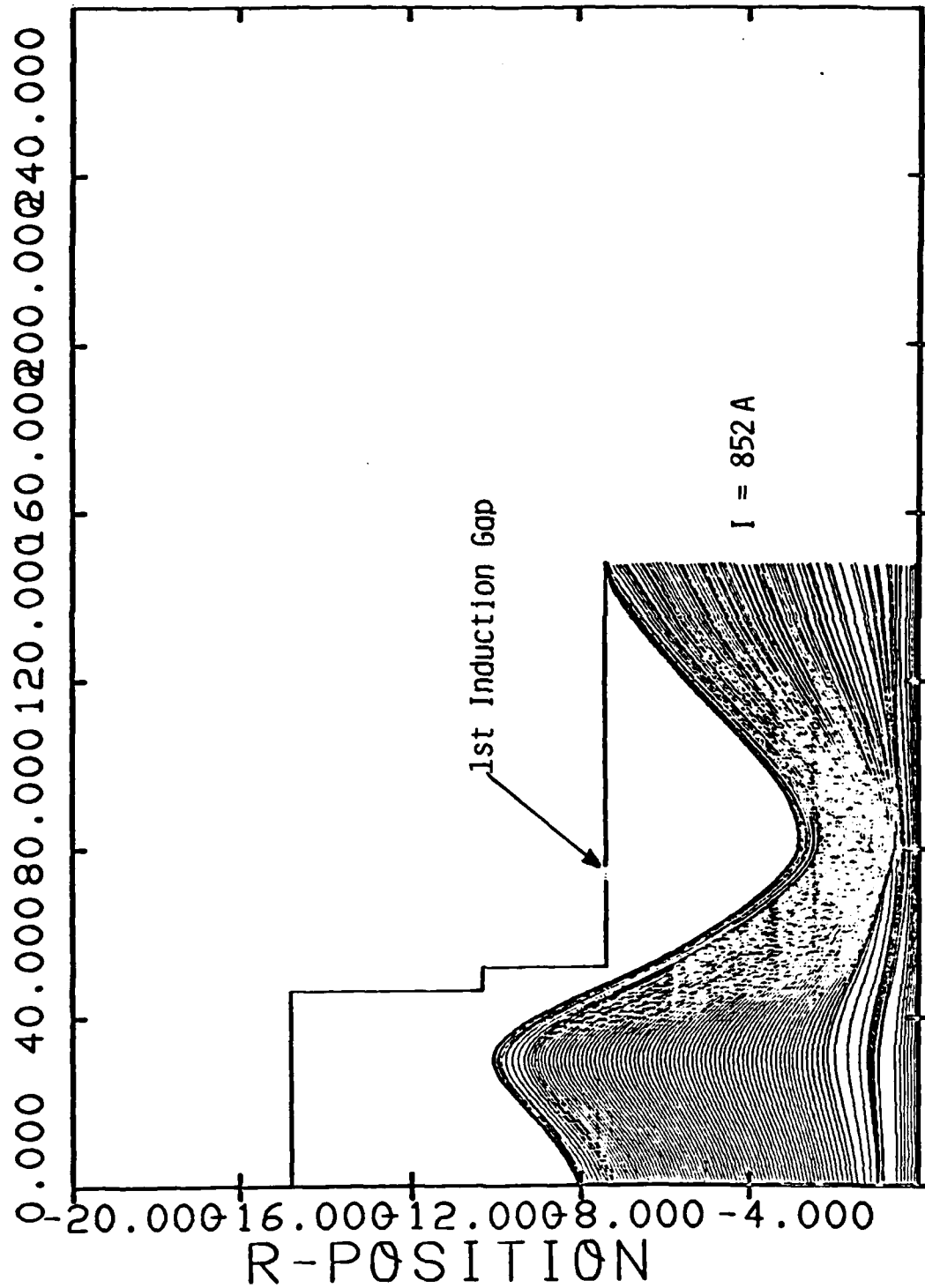


Figure 4. Laminar Beam Flow at Stage 3

STAGE 4

Z-POSITION - 258 cm

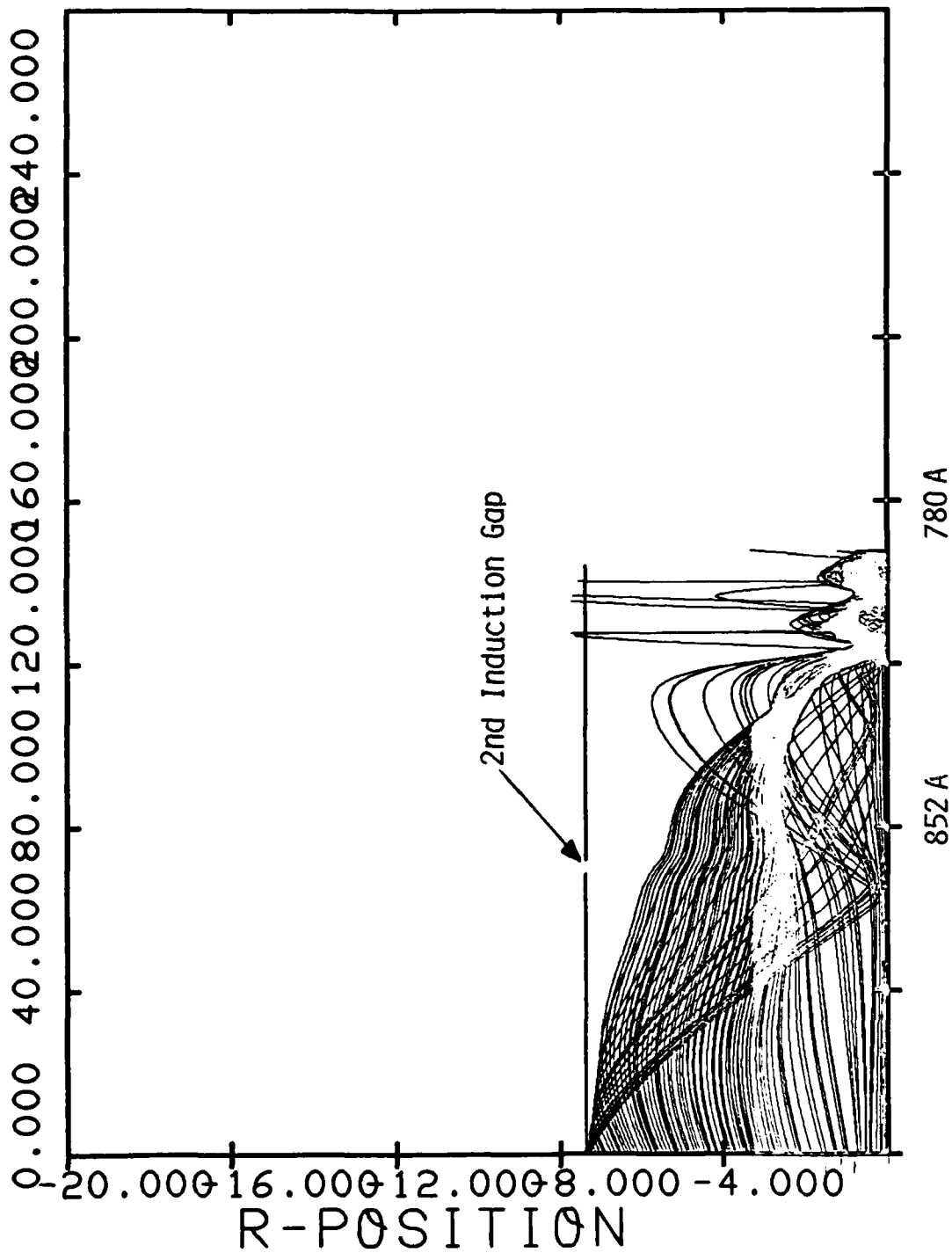


Figure 5. Compression of Laminar Beam at Stage 4

STAGE 4

Z-POSITION - 258 cm

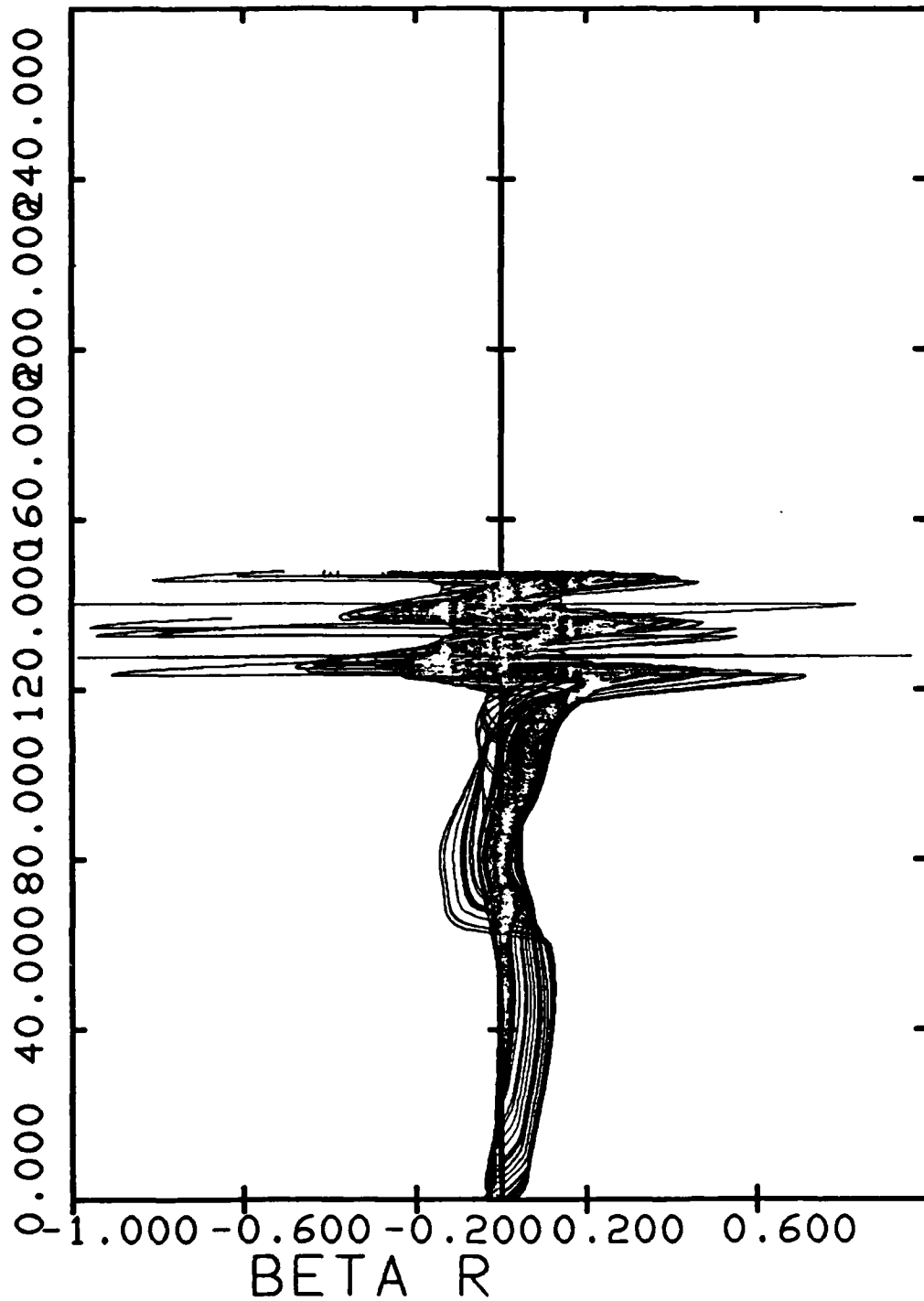


Figure 6. Compression of Laminar Beam at Stage 4

STAGE 4

Z-POSITION - 258 cm

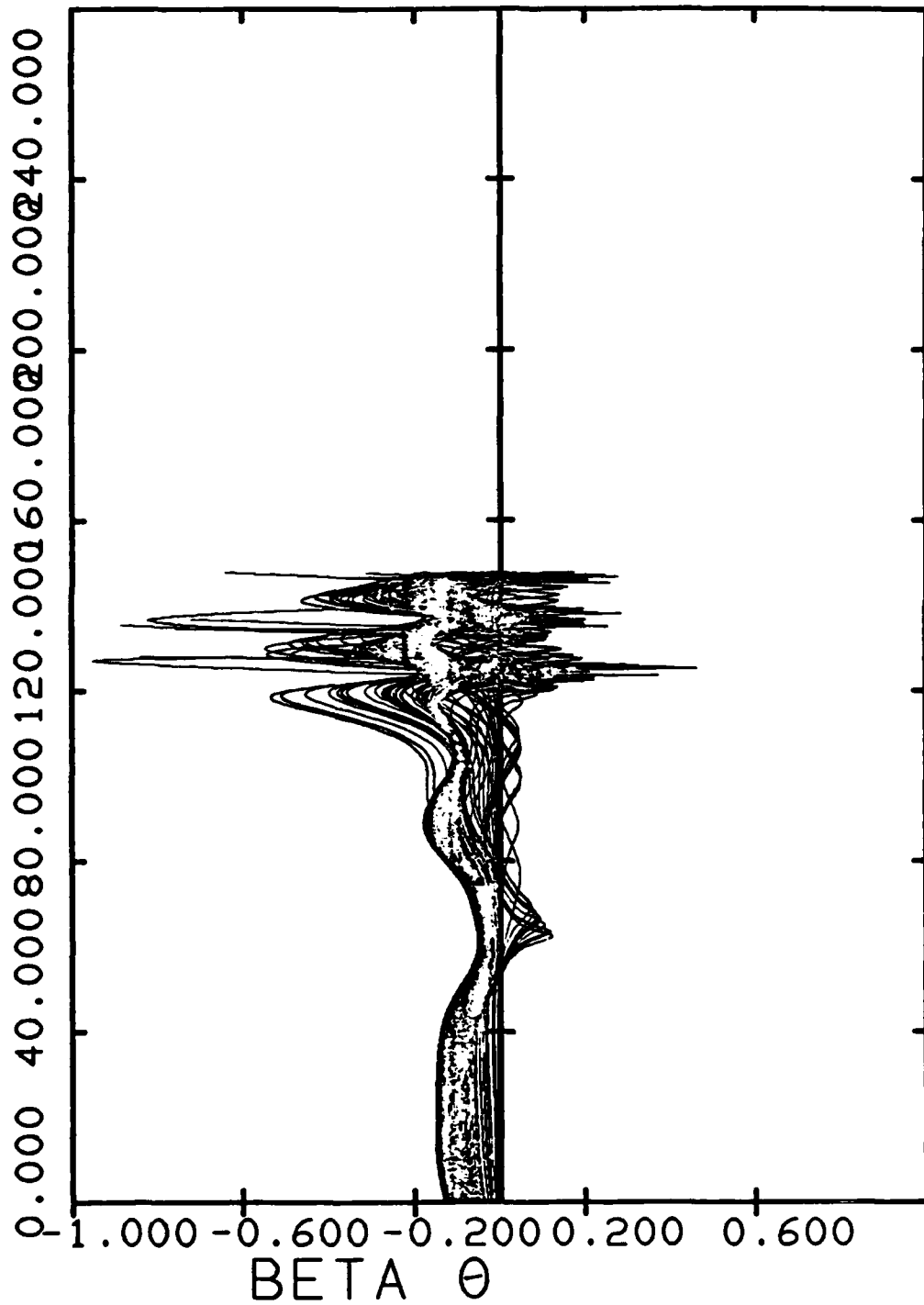


Figure 7. Compression of Laminar Beam at Stage 4

STAGE 4

Z-POSITION - 258 cm

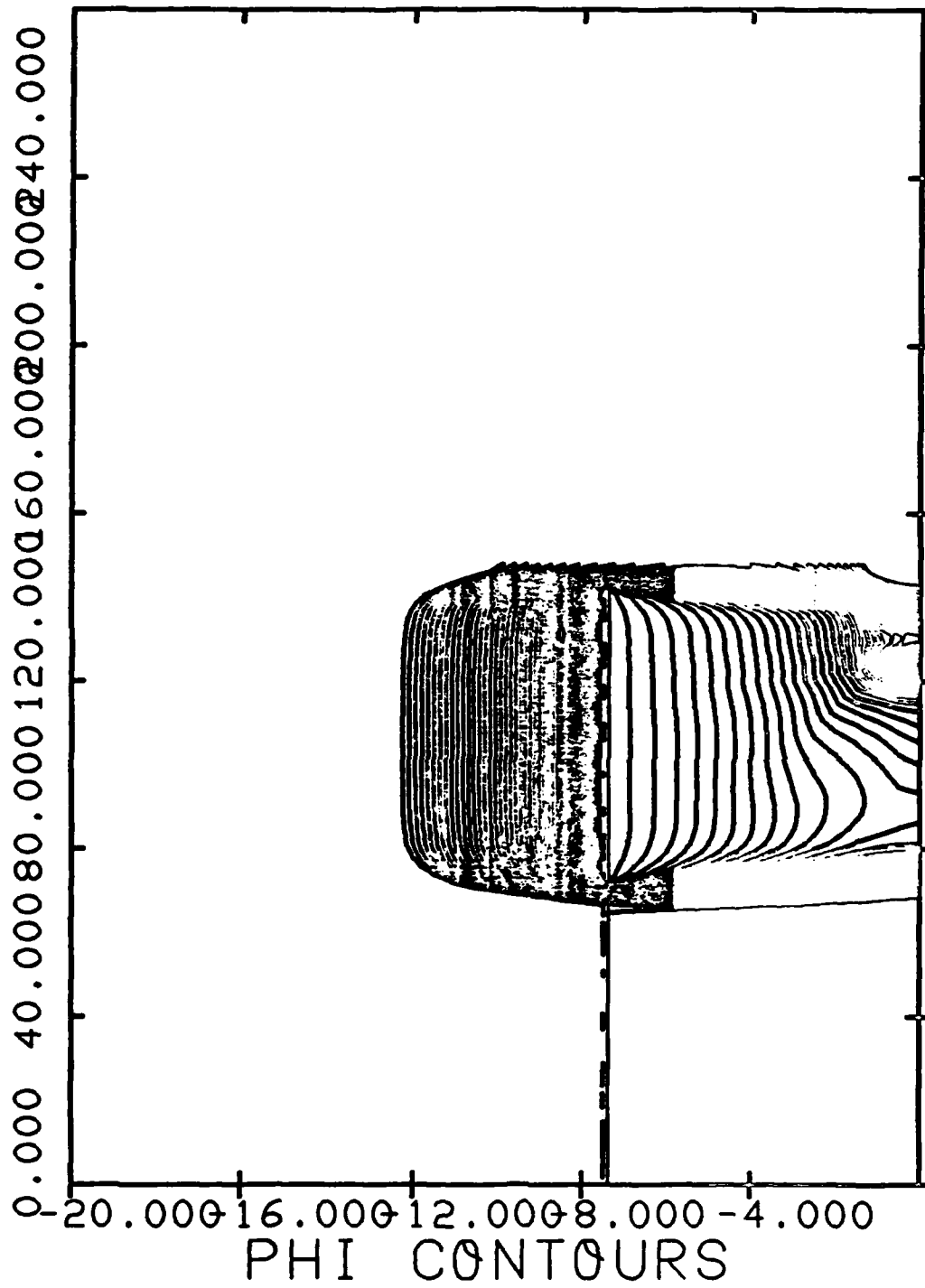


Figure 8. Equipotentials for Compression of
Laminar Beam at Stage 4

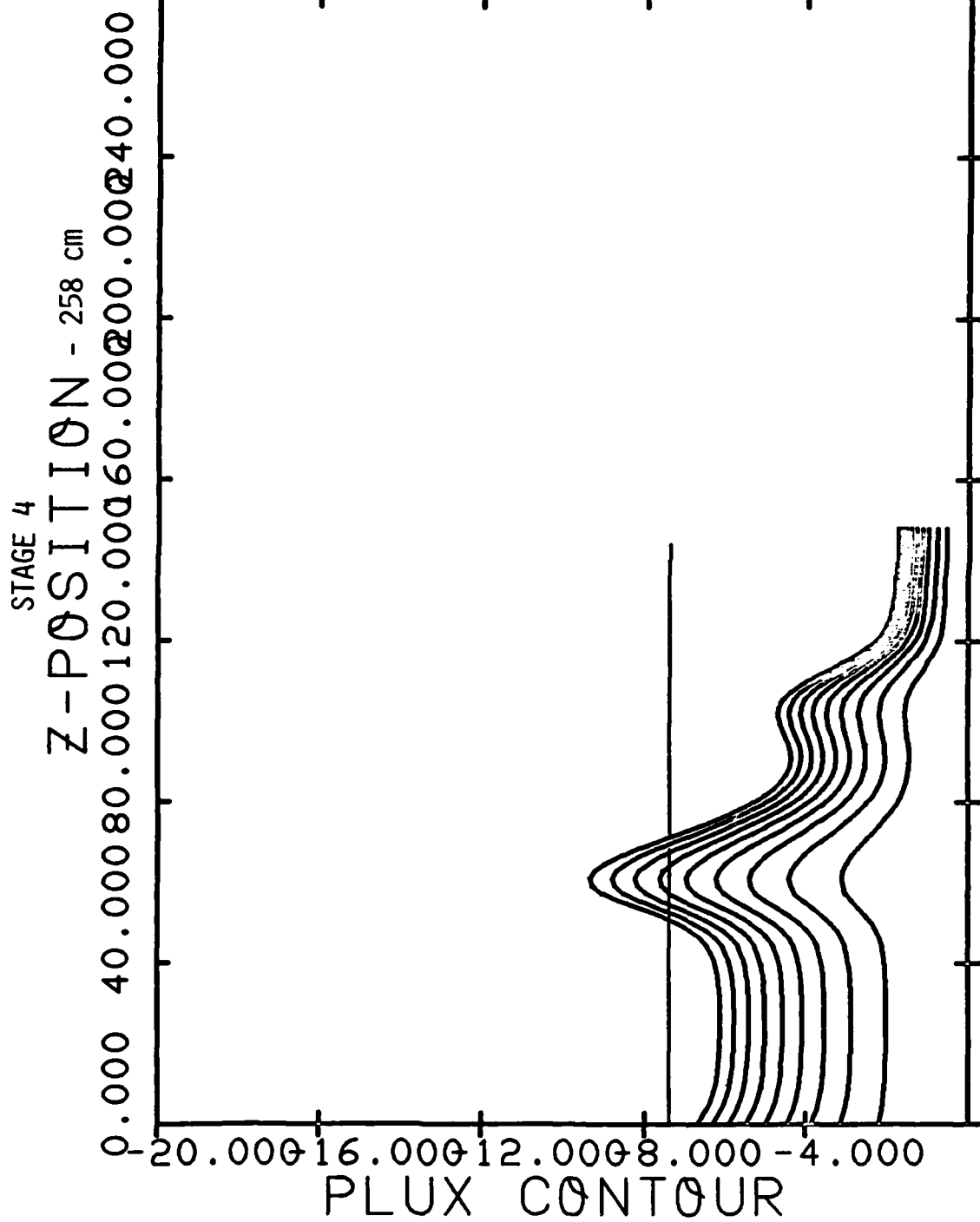


Figure 9. Flux Contours for Stage 4 Compression

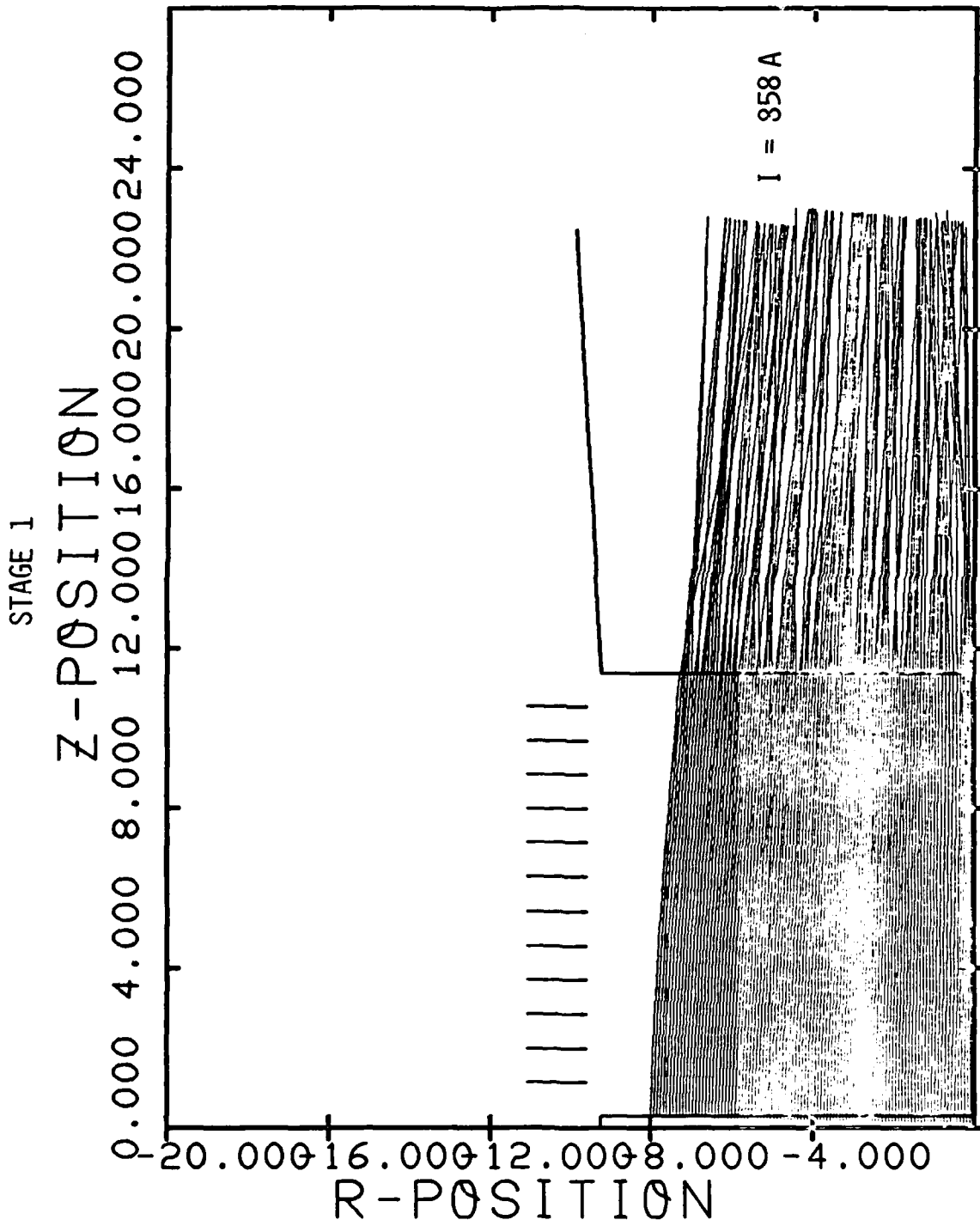


Figure 10. Laminar Diode Flow with Anode Mesh
Scattering of $\theta_{rms} \approx 2.83^\circ$

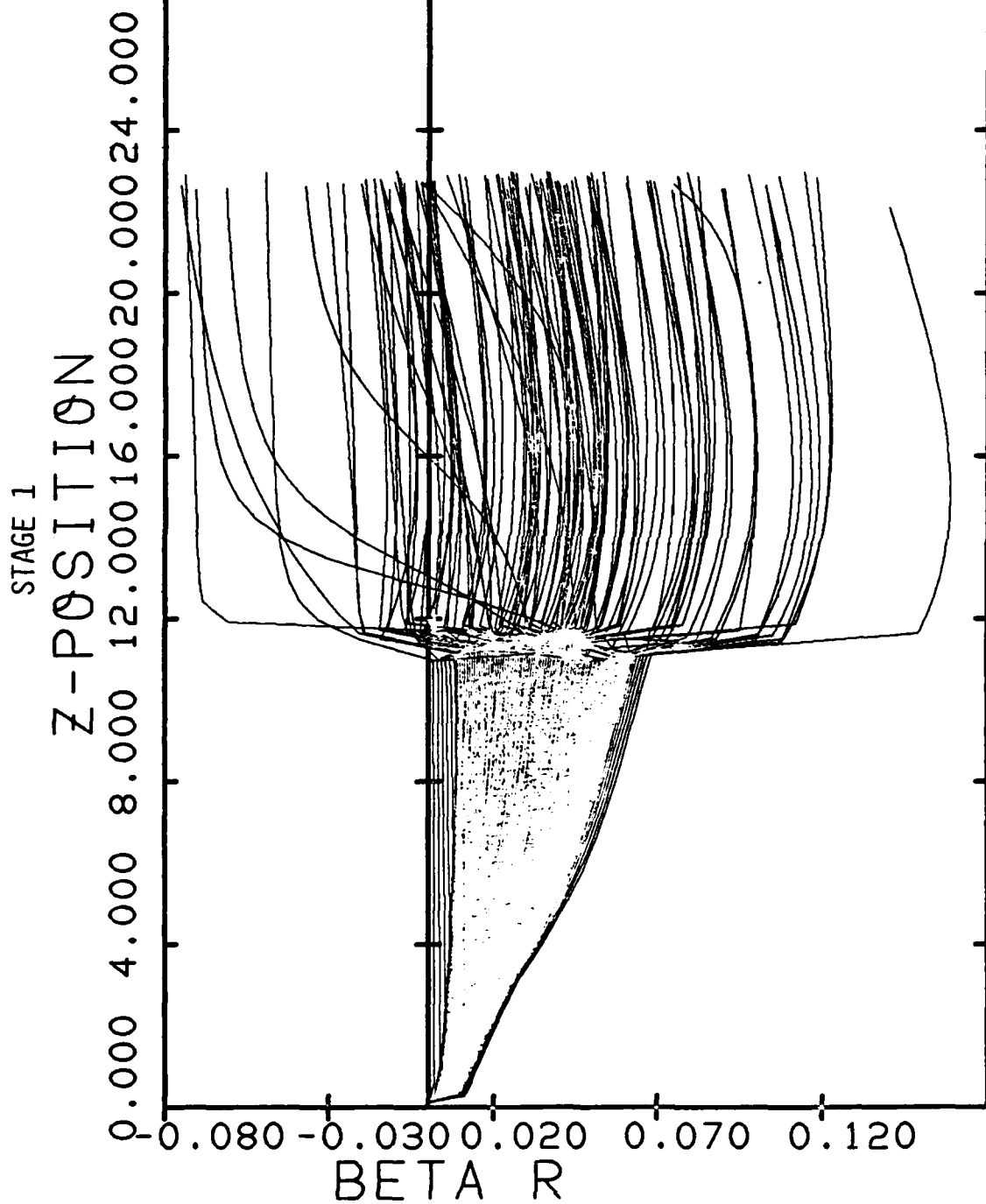


Figure 11. Stage 1 Mesh Scattering ($\theta_{rms} = 2.83^\circ$)

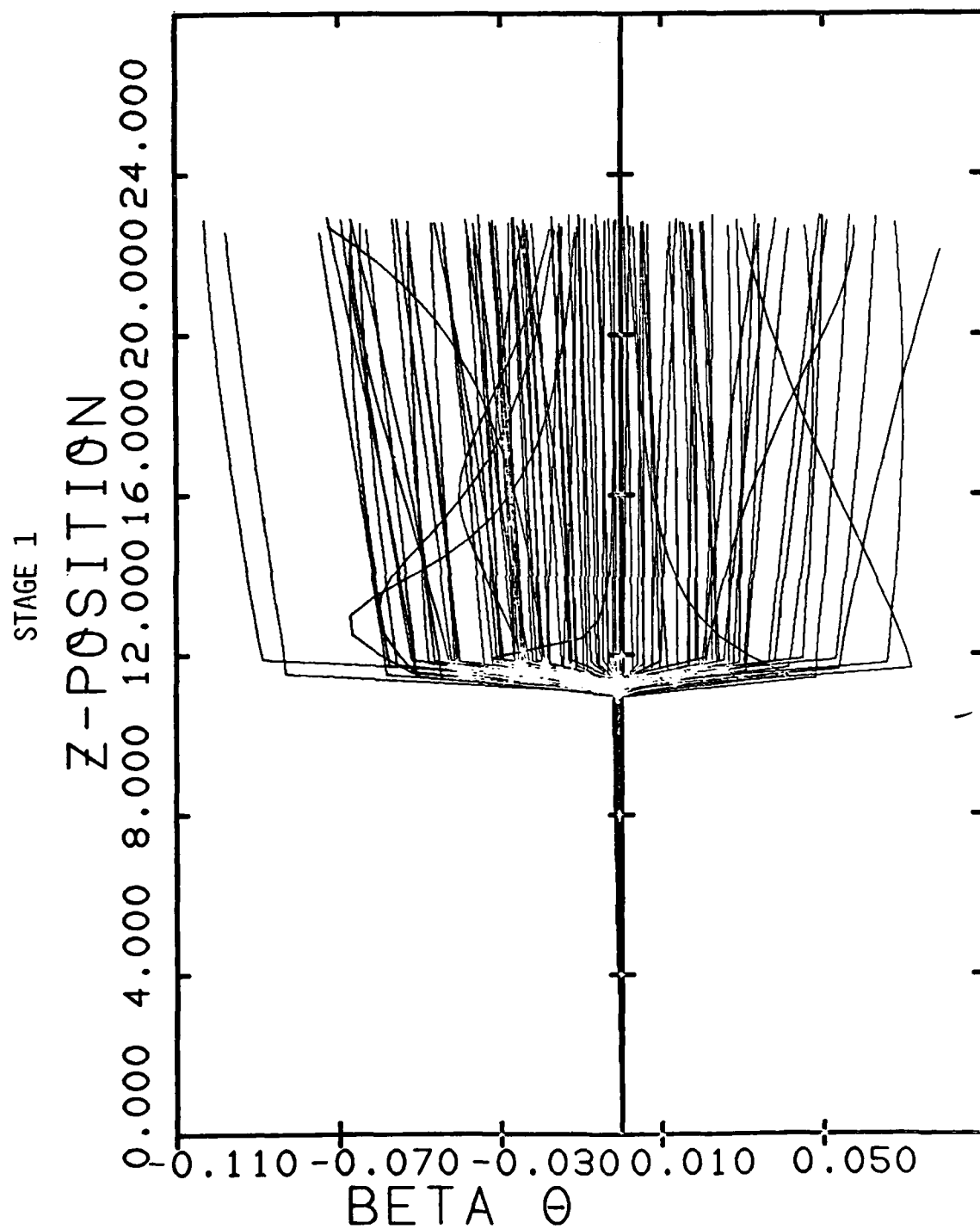


Figure 12. Stage 1 Mesh Scattering ($\theta_{\text{rms}} = 2.83^\circ$)

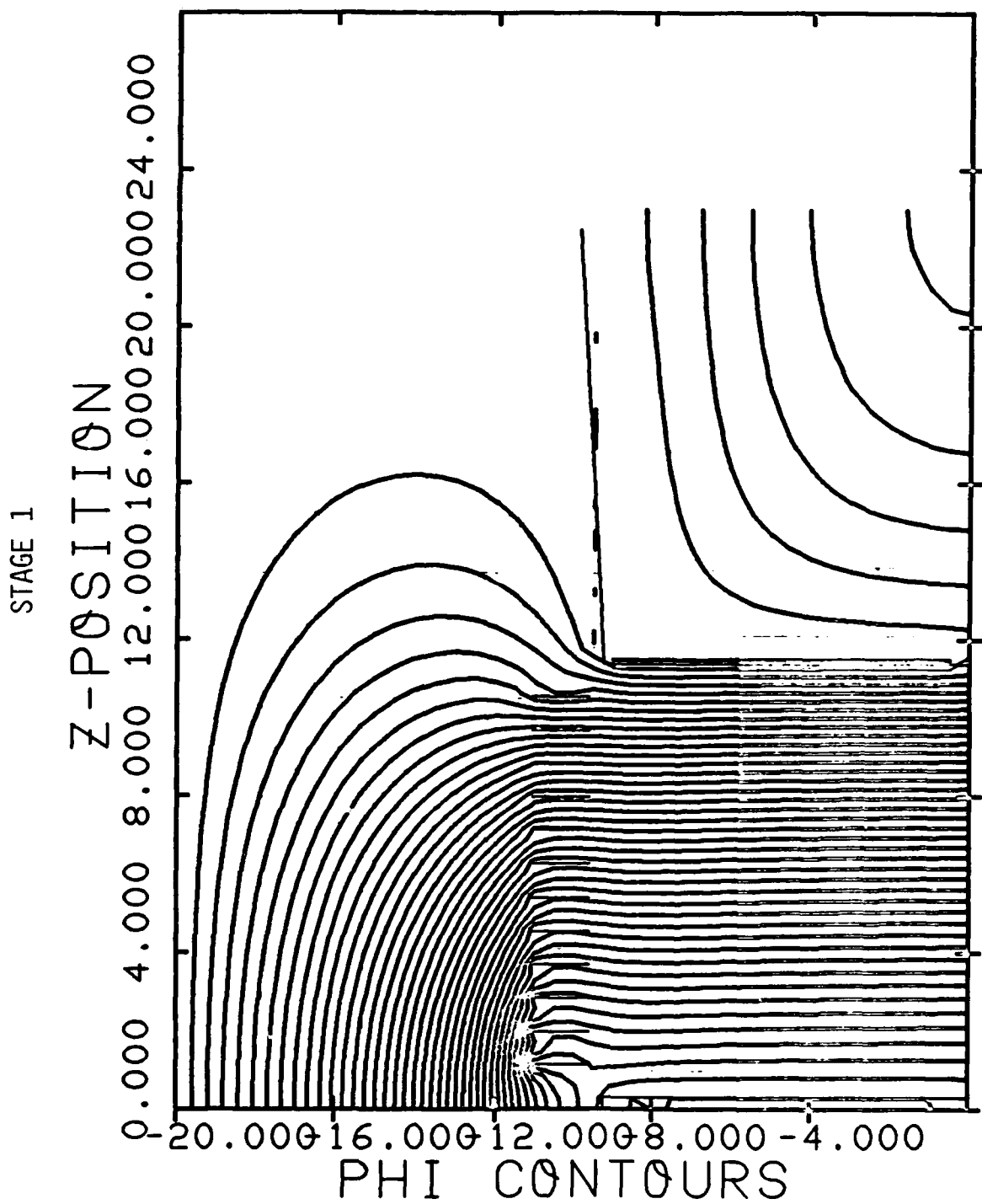


Figure 13. Stage 1 Equipotentials

STAGE 2

Z-POSITION - 23 cm

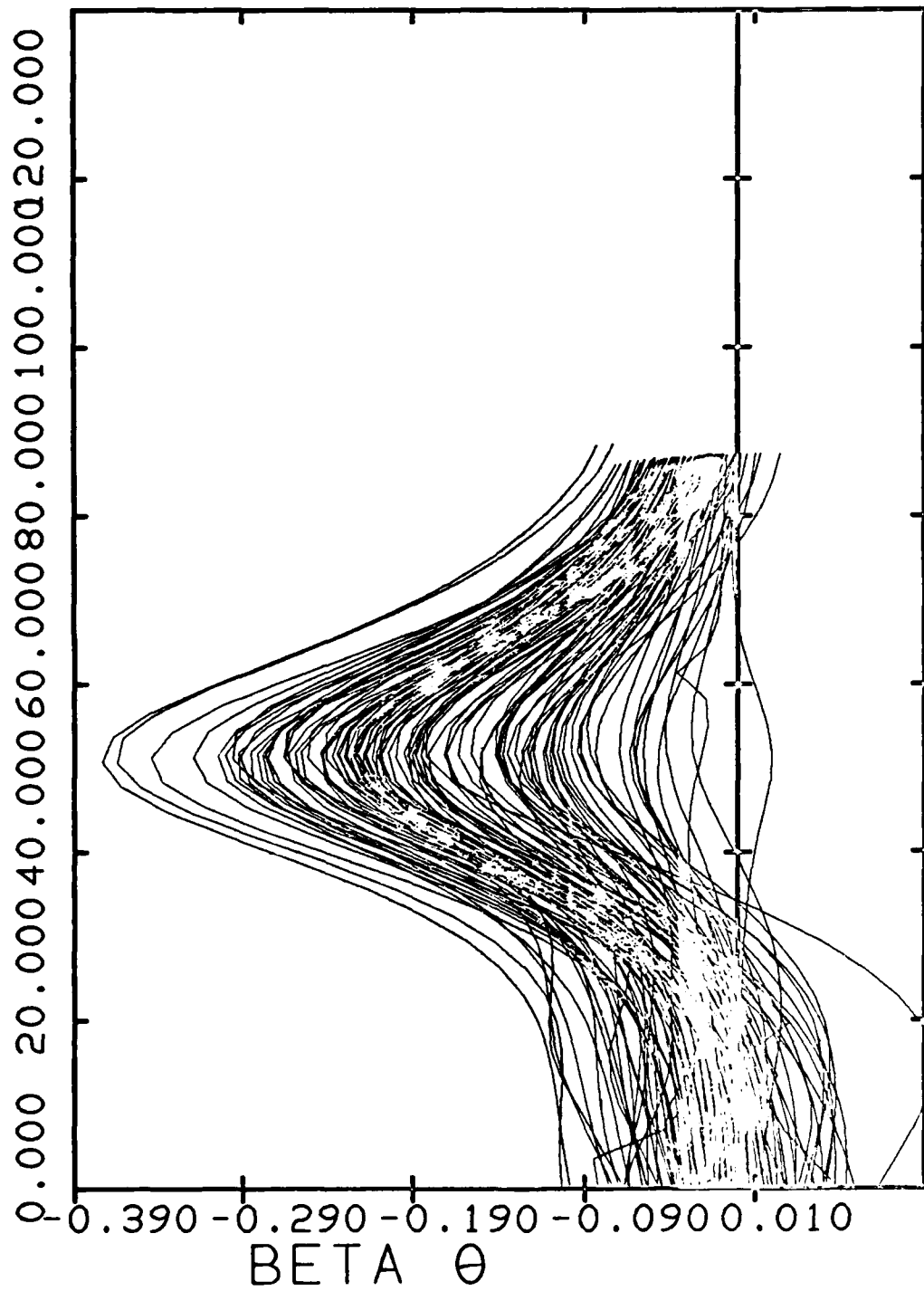


Figure 16. Scattered Flow at Stage 2

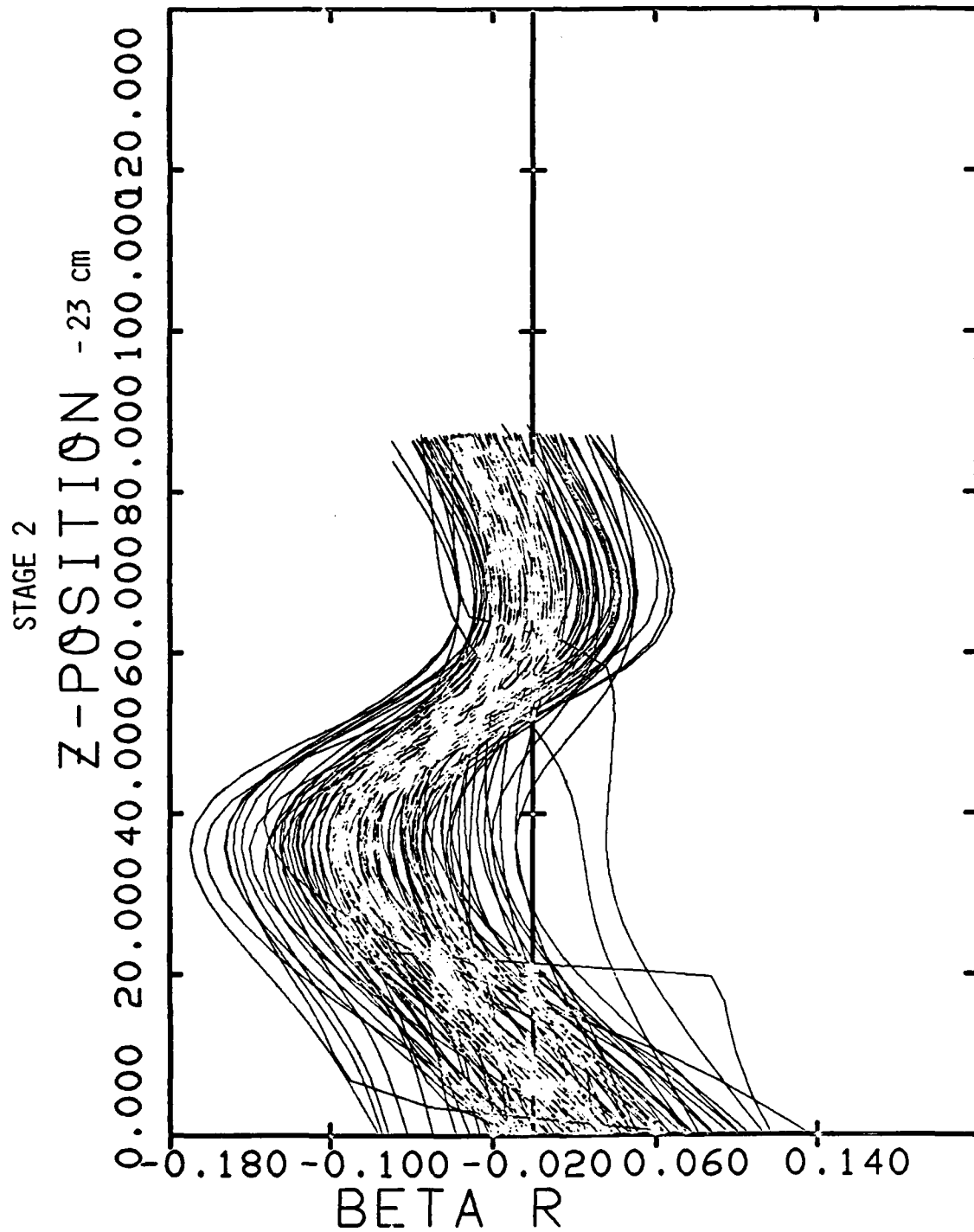


Figure 15. Scattered Flow a Stage 2

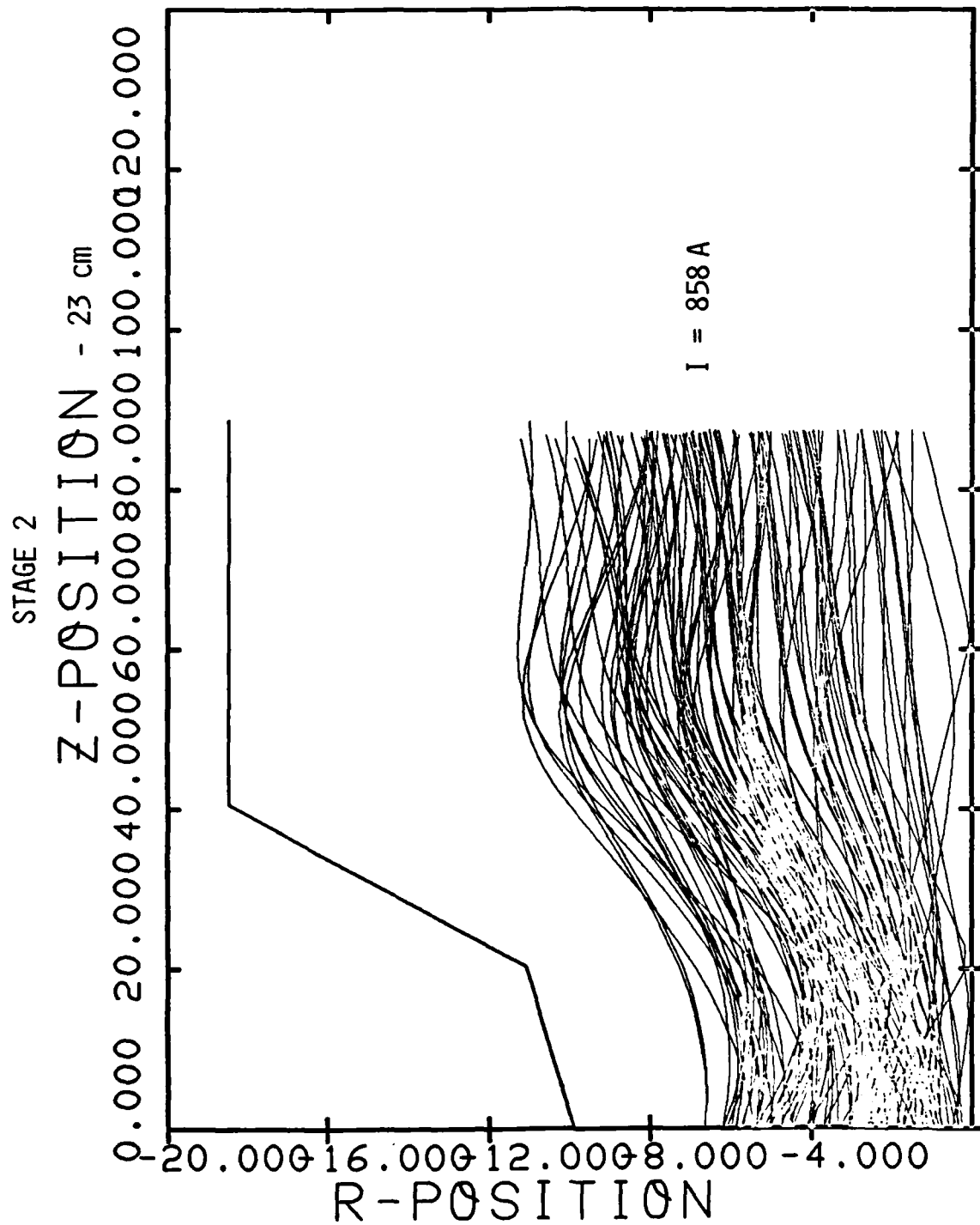


Figure 14. Scattered Flow a Stage 2

STAGE 3

Z-POSITION - 111 cm

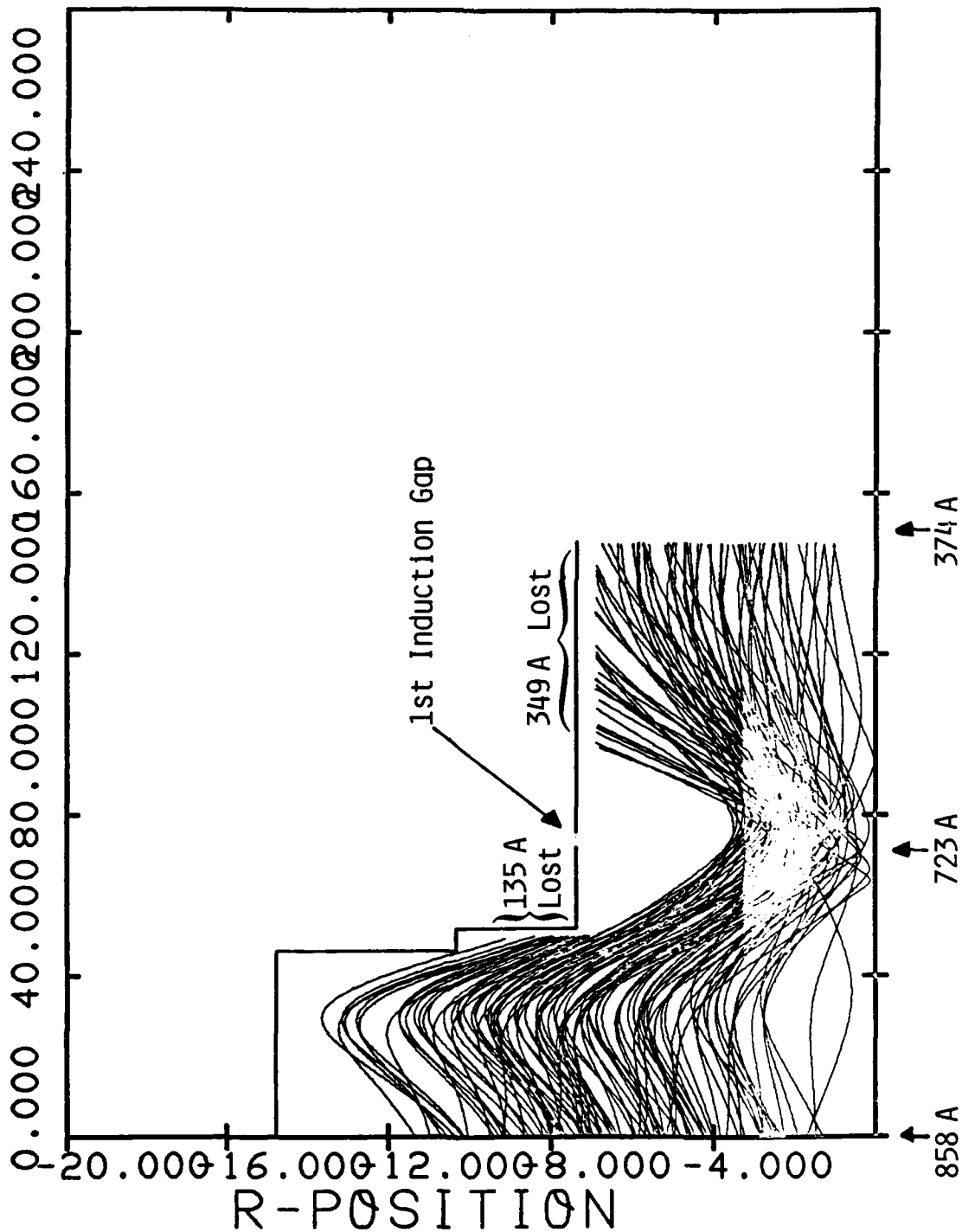


Figure 17. Scattered Flow Thru Stage 3, With Current Loss

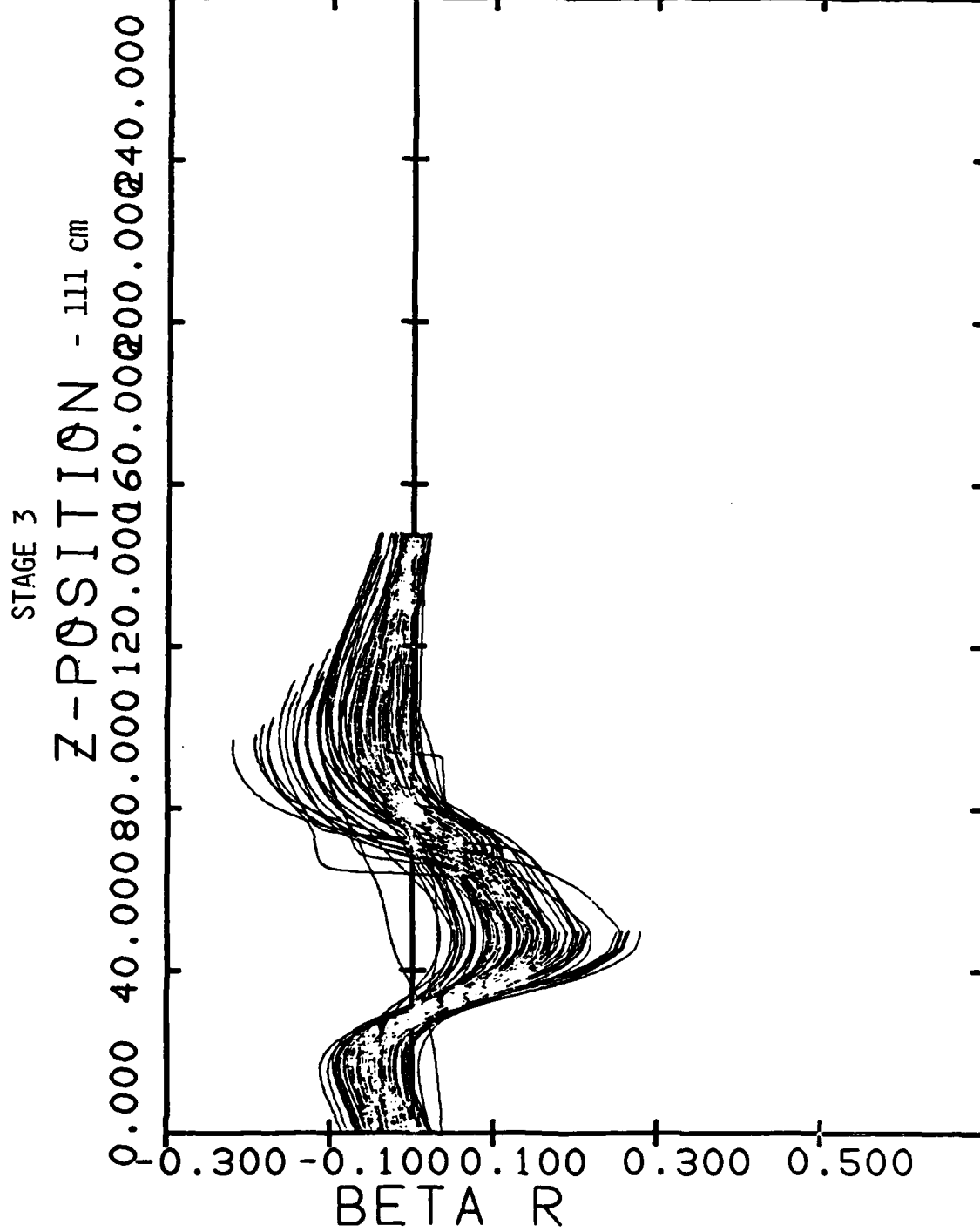


Figure 18. Scattered Flow Thru Stage 3

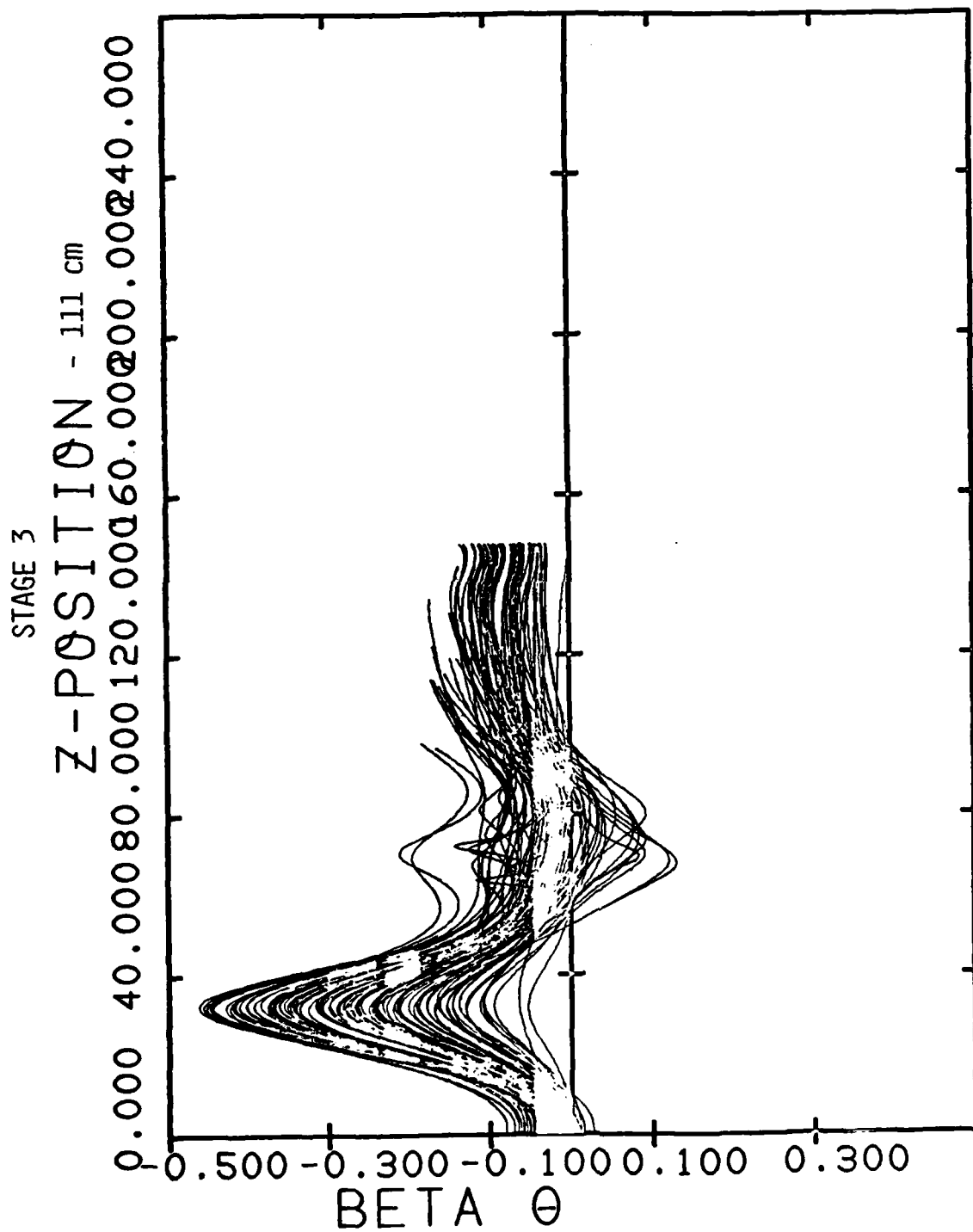


Figure 19. Scattered Flow Thru Stage 3

STAGE 3

Z-POSITION - 111 cm

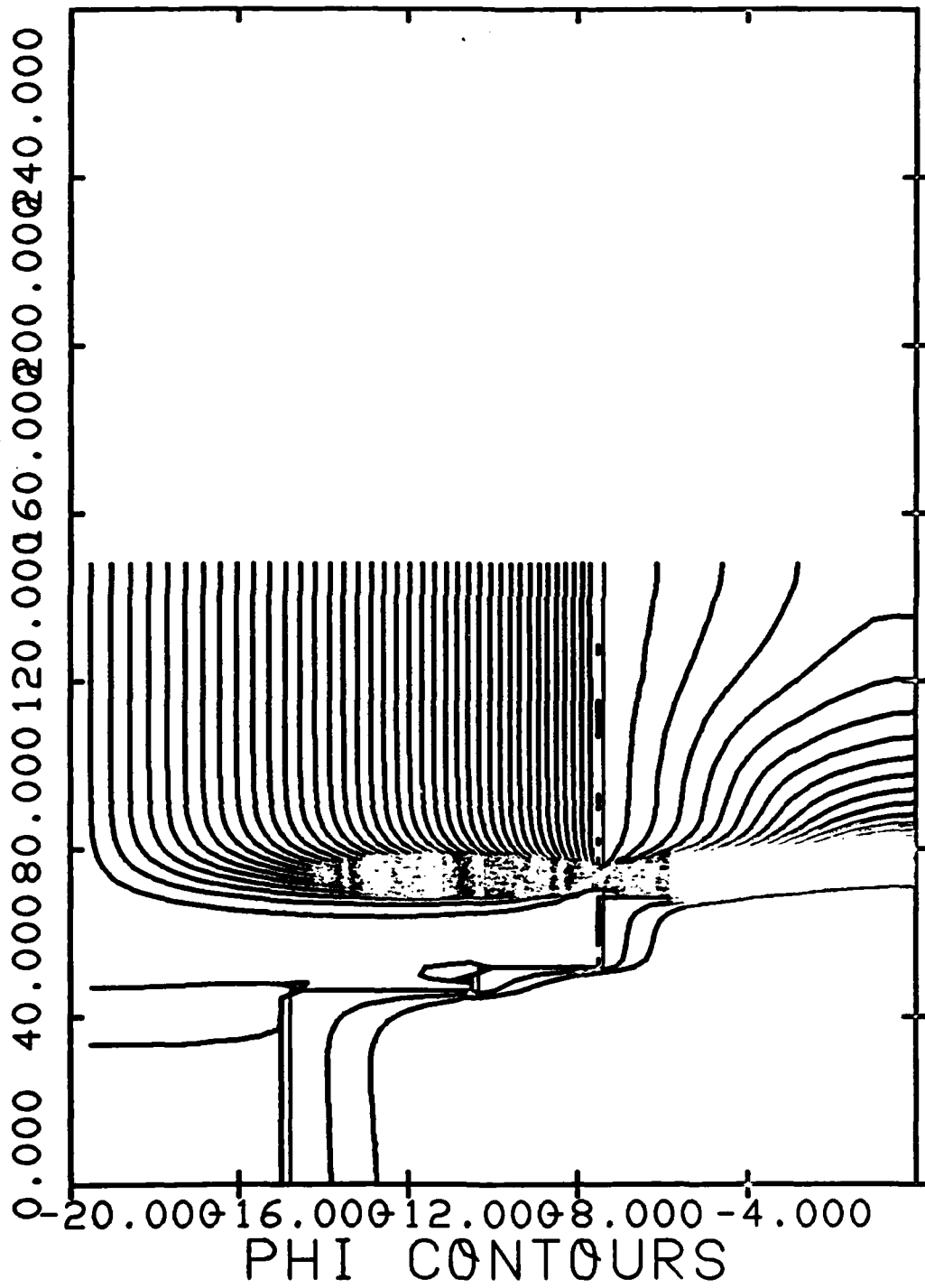


Figure 20. Equipotentials for Stage 3 Flow

STAGE 4

Z-POSITION - 258 cm

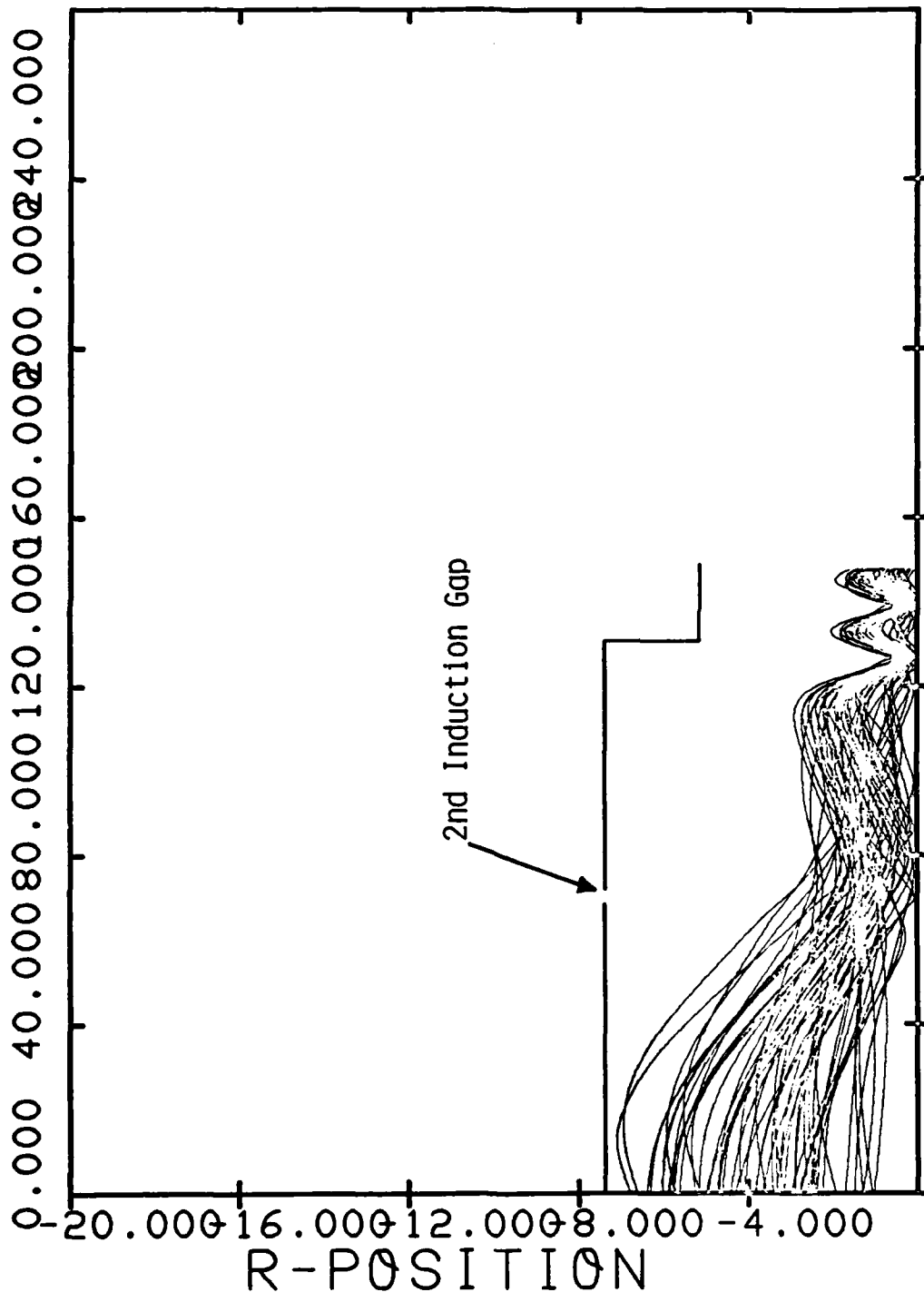


Figure 21. Transmission of Residual Scattered Current Thru Stage 4 Compression

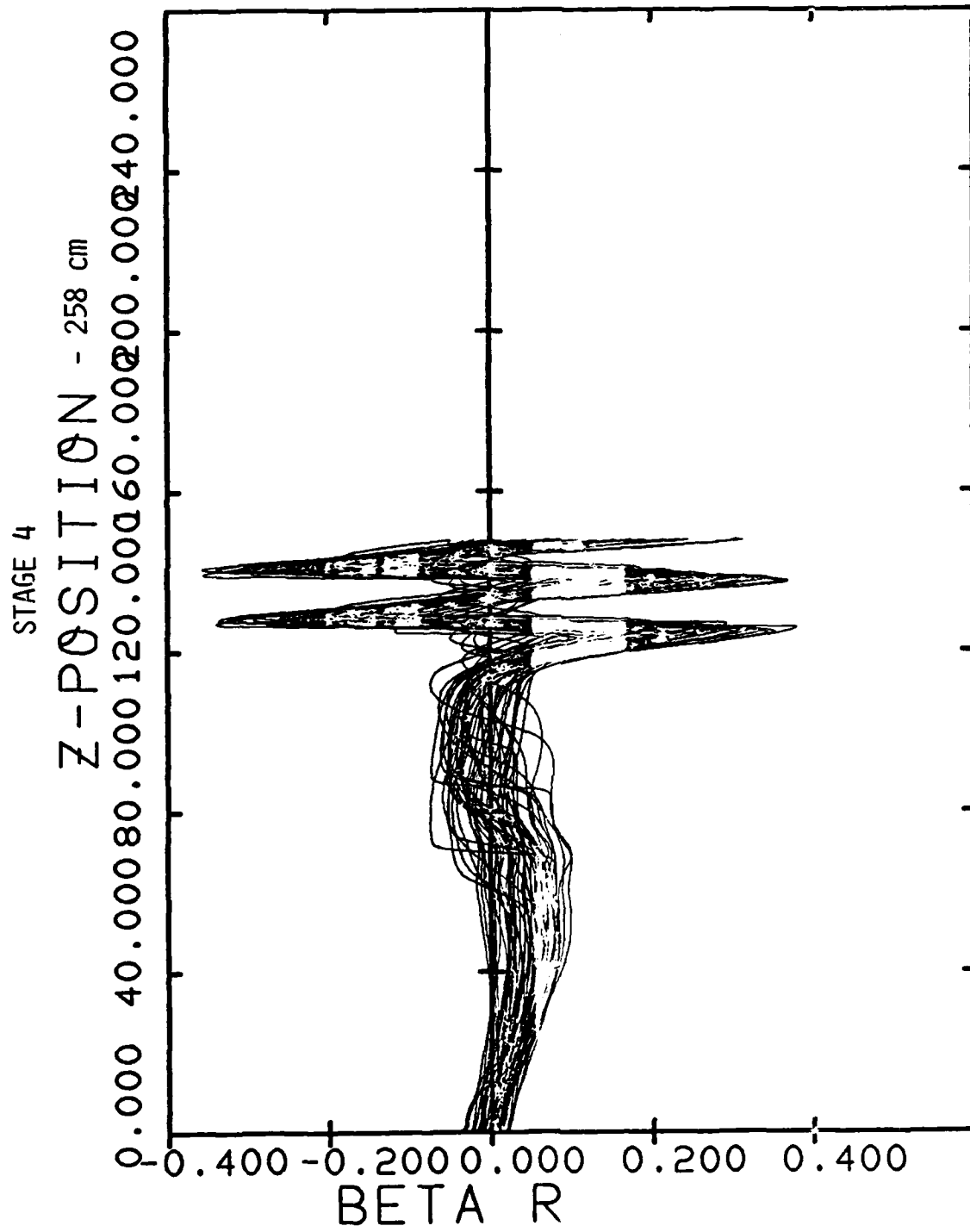


Figure 22. Compression of Scattered Beam Flow at Stage 4

STAGE 4

Z-POSITION - 258 cm

0.000 40.000 80.000 120.000 160.000 200.000 240.000

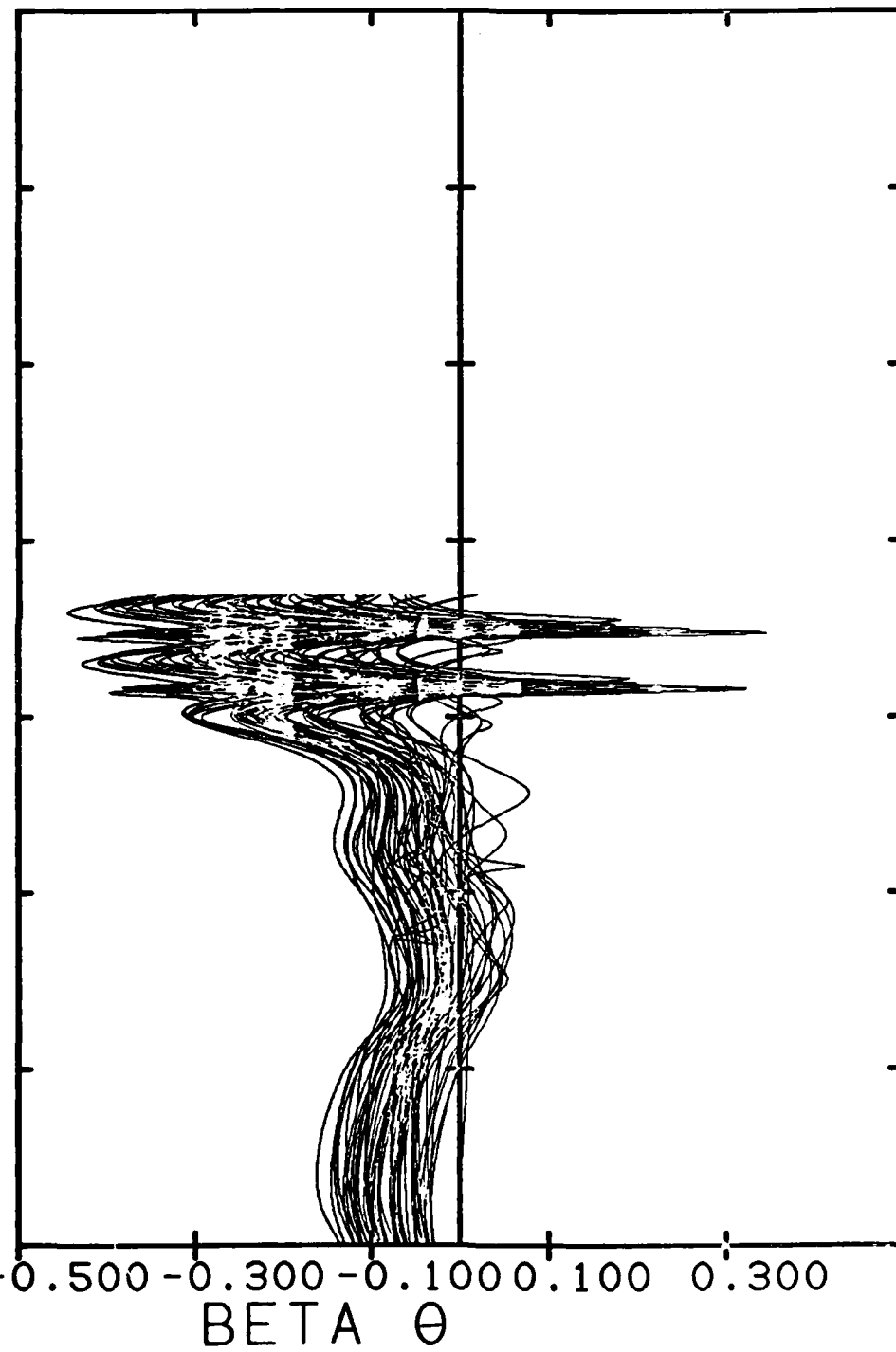


Figure 23. Compression of Scattered Beam Flow at Stage 4

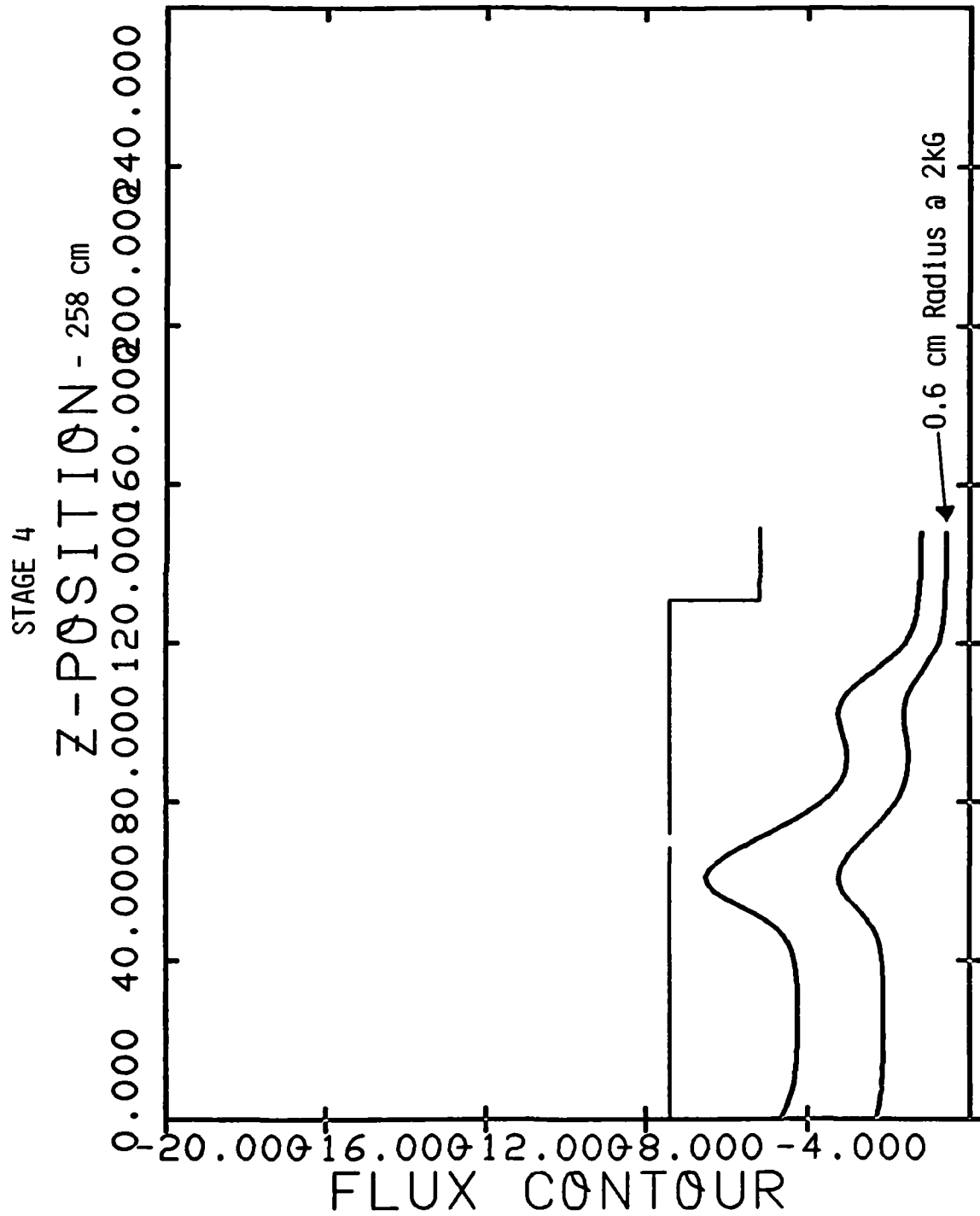


Figure 24. Flux Contours for Stage 4 Compression

A P P E N D I X C

Letter from Dr. James R. Thompson to Dr. C. W. Roberson,
dated May 13, 1982.

-- includes 30 figures

Austin Research Associates

1901 Rutland Drive-Austin, Texas 78758-Phone (512) 837-6623

May 13, 1982

Dr. C. W. Roberson
1908 Tollbridge Court
Alexandria, Virginia 22308

Dear Chuck:

Enclosed is the latest batch of copies of our computer output, to illustrate our recent progress in calculating diode flow and beam transport through the first four meters of the NBS induction accelerator. I have numbered these figures and the following commentary is keyed to those numbers.

We have done a series of diode calculations, to determine the effect of various alternative potential gradings of the ring electrodes in the anode-cathode gap on the beam formation and on the subsequent transport. Figure 1 illustrates the four different gradings which we have considered. The "design" and the "modified design" cases correspond to the two sets of numbers on the engineering drawing of the electrode geometry. Notice that the linear grading produces stronger electric fields near the cathode than does Child-Langmuir grading, while the design grading produces weaker electric fields. As expected, the extracted current is ordered in the same way as the electric field stresses.

Figure 2 shows the diode flow for linear grading; 1.24 kA current is extracted. Figure 3 shows the cathode current density profile for this case. Because of the high electric field stresses, the current density is peaked at the edge of the beam. The diode flow is also slightly divergent near the beam edge.

Figure 4 reviews the r-z transport geometry, and shows the locations of our computer stage break-points. Figure 5 reviews the magnetic field profile which is based upon the data that you gave us in December, 1981, and which we have been using until very recently.

Figures 6 through 9 illustrate the transport of the beam formed in a linearly graded diode (see Figures 2 and 3), and propagated along the system shown in Figures 4 and 5. No anode mesh scattering was introduced. Out of 1,260 amperes initially extracted from the cathode, 720 amperes are lost in Stage 3 just

Dr. C. W. Roberson
May 13, 1982
Page 2

beyond the first induction gap. The remaining 540 amperes (43% of the current) are then well compressed in Stage 4.

Figures 10 and 11 show the transverse velocities in the Stage 4 compression to $B_z \approx 2$ kG. Assuming as usual that the cyclotron oscillations will eventually phase mix, the resulting emittance would be as follows:

$$\begin{aligned}\delta\beta_{\perp \text{ RMS}} &\approx 0.07 \\ a &\approx 0.52 \text{ cm} \\ R &\approx a/\sqrt{2} \approx 0.37 \text{ cm} \\ \gamma &\approx 2.57 \text{ (800 keV)} \\ \frac{\epsilon_n}{\pi} &\approx 66 \text{ mrad-cm @ } I = 540 \text{ A}\end{aligned}$$

This residual beam is of high quality, and the Figure 9 flow pattern may be seen to be compressed within the desired inner flux contour of Figure 12.

Figure 13 shows the diode flow pattern for a Child-Langmuir potential grading. The beam is slightly convergent, and the current density profile is only slightly peaked on edge, as shown in Figure 14. Figures 15 through 22 review previous transport calculations for Child-Langmuir potential grading. However, for these previous transport studies, the cathode current density profile was assumed uniform in radius: the slight peak shown in Figure 14 was omitted. Likewise, the current was only about 850 A rather than 900 A as in Figures 13 and 14.

Figures 15 through 18 show the transport without anode mesh scattering. Figures 19 through 22 show the same transport with 2.83° of RMS scattering at the anode mesh. This is a fairly large amount of mesh scattering. Figure 21 shows that 135 A were lost at the entrance to the first induction solenoid. Although this case does not correspond closely with the experimental cases, this location is where you have apparently been losing a lot of current also in your experimental runs. An additional 349 A were lost downstream of the first induction gap, where you have also been losing a smaller amount of current experimentally.

Dr. C. W. Roberson
May 13, 1982
Page 3

Figure 23 shows the diode flow for the design potential grading, which is a sub-Child-Langmuir grading. For this case, we allowed the cathode to emit all the way out to the tip, to see how much additional current might be produced. We got 820 A, with a current density profile peaked on axis as shown in Figure 24.

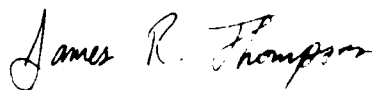
Figure 25 shows the diode flow for the set of parameters that you recently gave us. We used the modified potential grading, and the most up-to-date geometrical dimensions. The cathode emission extended to $r = a = 8.0$ cm. The leakage magnetic fields from coil #1 were 5.7 gauss at the cathode and 8.6 gauss at the anode mesh. The flow is fairly strongly convergent, and 720 A were extracted, which is some 10% lower than you observe. Figure 26 shows that the cathode current density is peaked on axis and declines to about 85% of the peak value at the edge of the beam.

We have just started a transport calculation for the beam. We are using the magnetic field profile shown in Figure 27, based upon the coil settings which we obtained from you during our February, 1982 visit. We are again assuming 2 kG in the wiggler solenoid.

Figure 28 shows the Stage 1 diode flow for this beam. We have introduced anode mesh scattering of $\theta_{rms} \approx 0.28^\circ$, which is much less than for our previous scattering runs, but which we believe may be more realistic. The modified design for the sub-Child-Langmuir potential grading has been used. Figures 29 and 30 show the perpendicular velocities for the Stage 1 flow. At this point the beam flow is still extremely laminar.

Our computer is presently chewing on the transport through Stages 2, 3, and 4. I hope to have some of these results to send to you tomorrow, or at least to relate over the telephone. I'll also try to get busy on our renewal proposal. Hope that you have a good meeting.

Sincerely,



Bob Thompson

AD-A174 586

CALCULATIONS OF THE FORMATION AND TRANSPORT OF HIGH
QUALITY HIGH CURRENT (U) AUSTIN RESEARCH ASSOCIATES TX
J R THOMPSON ET AL OCT 86 I-ARR-86-U-44

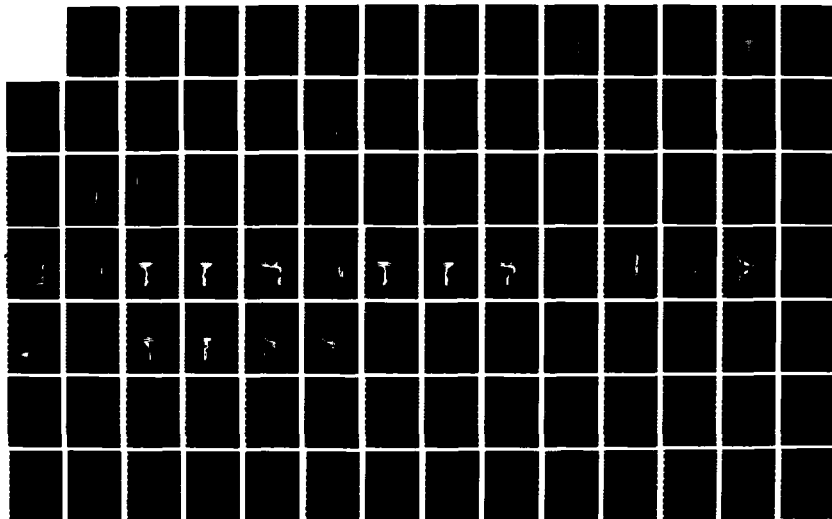
2/3

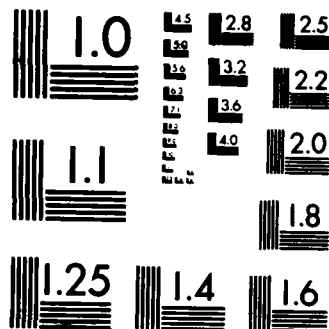
UNCLASSIFIED

N00014-81-C-0704

F/G 20/7

NL





MICROCOPY RESOLUTION TEST CHART
NATIONAL BUREAU OF STANDARDS-1963-A

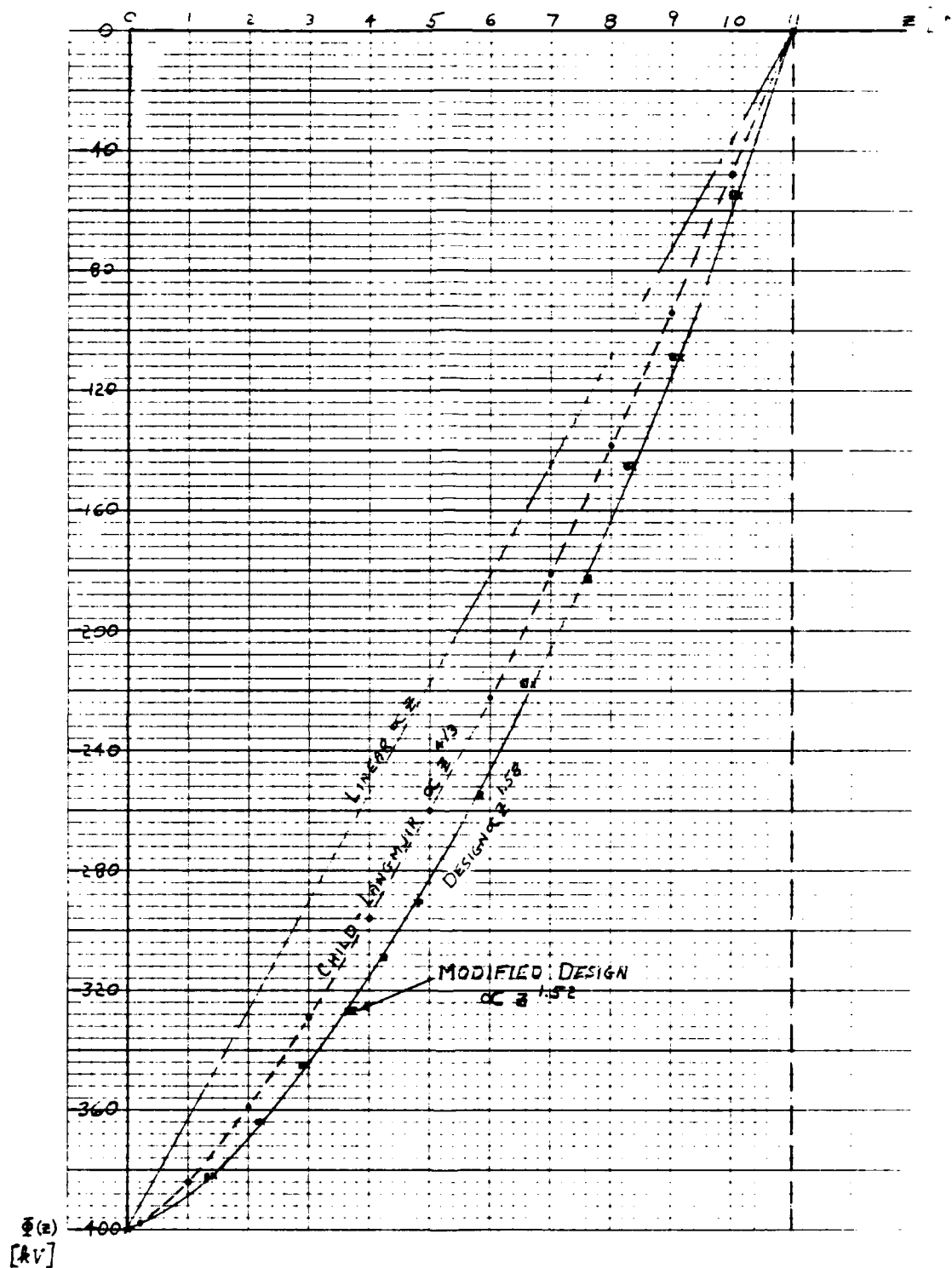


Figure 1. Diode Potential Grading

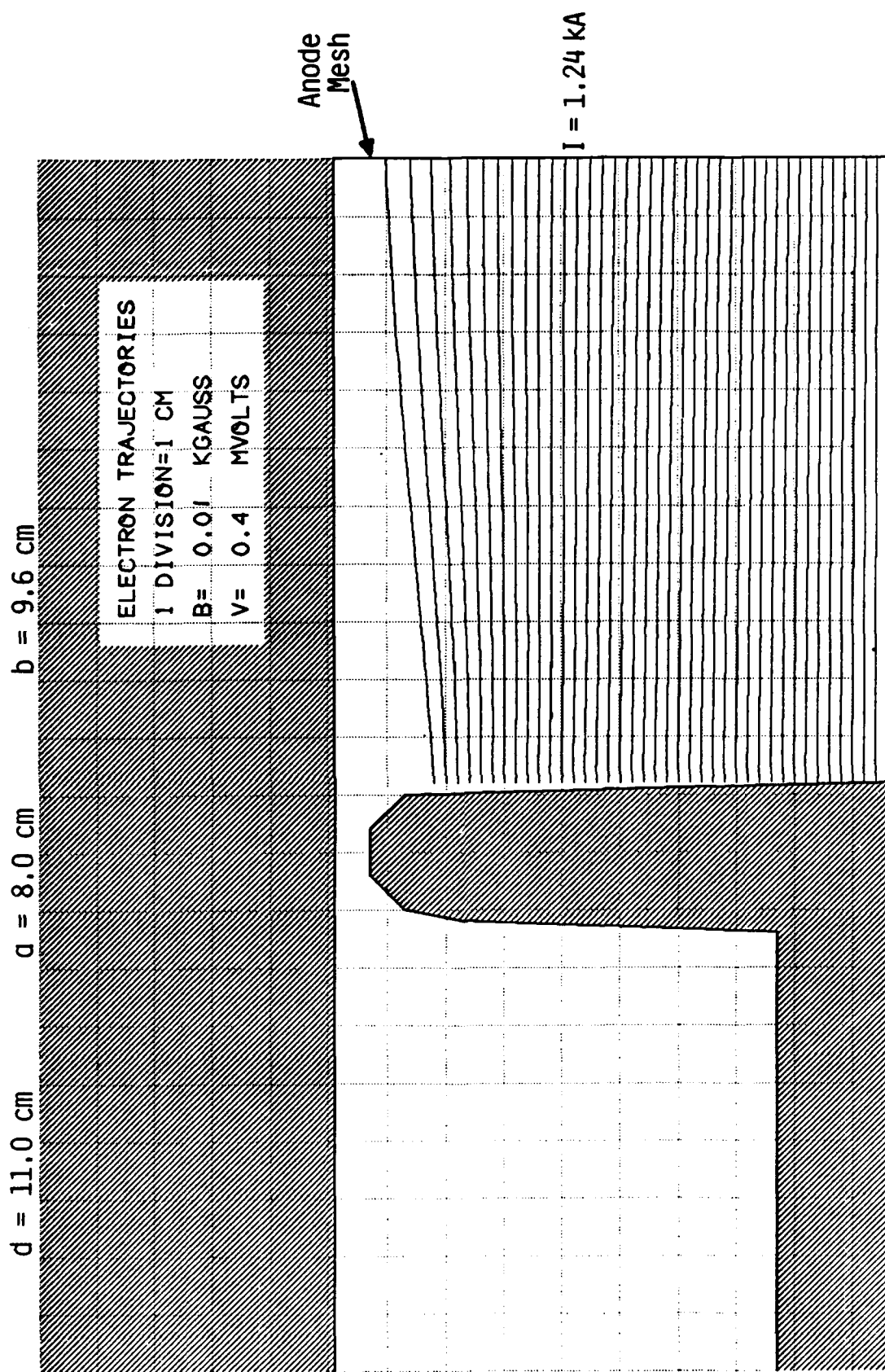


Figure 2. Cold Cathode with Linear Potential Grading: $\Delta \phi(b, z) = 0.4 (z/d)$ MV

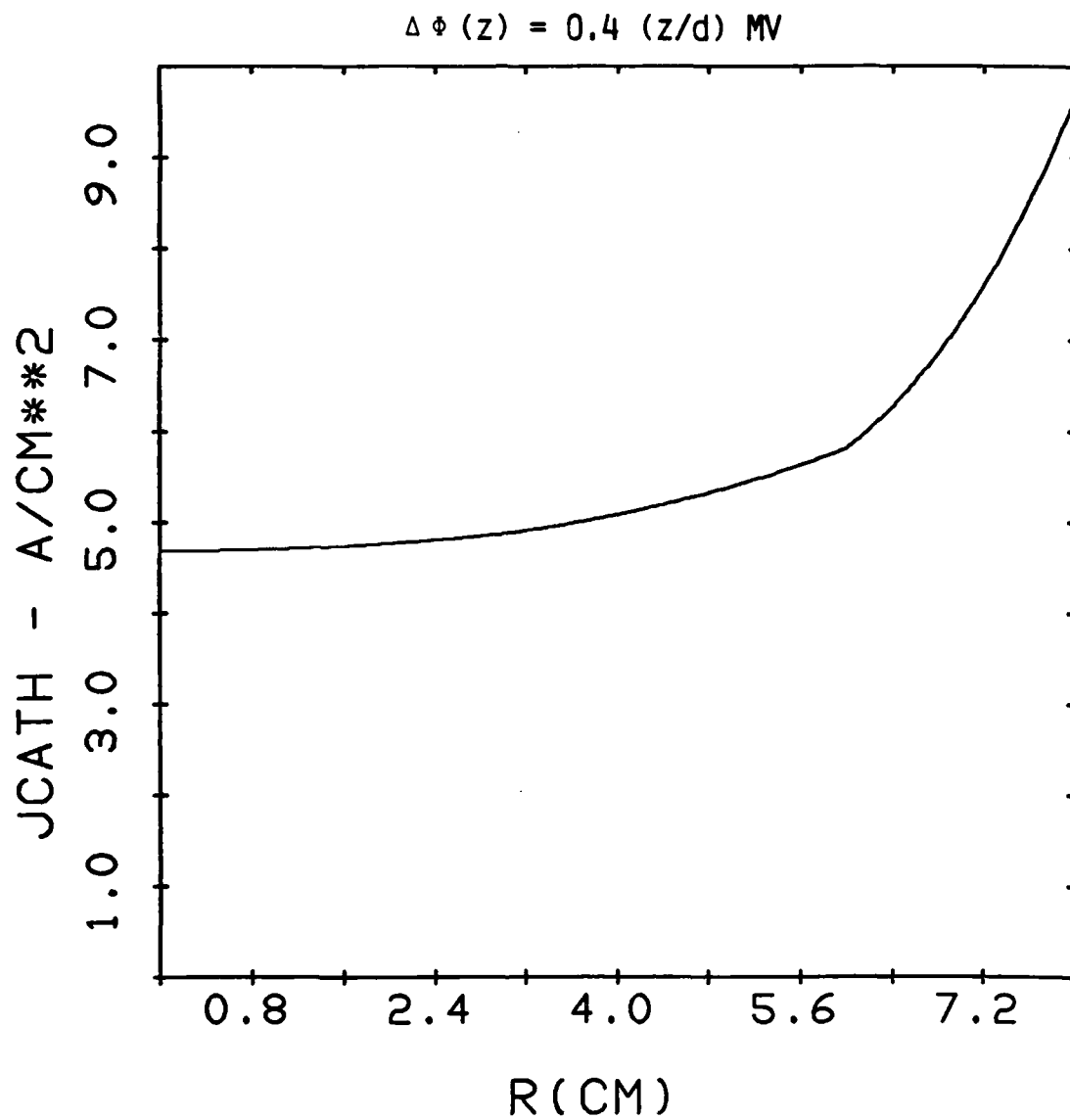


Figure 3. Current Density Profile @ Cathode
for Linear Potential Grading

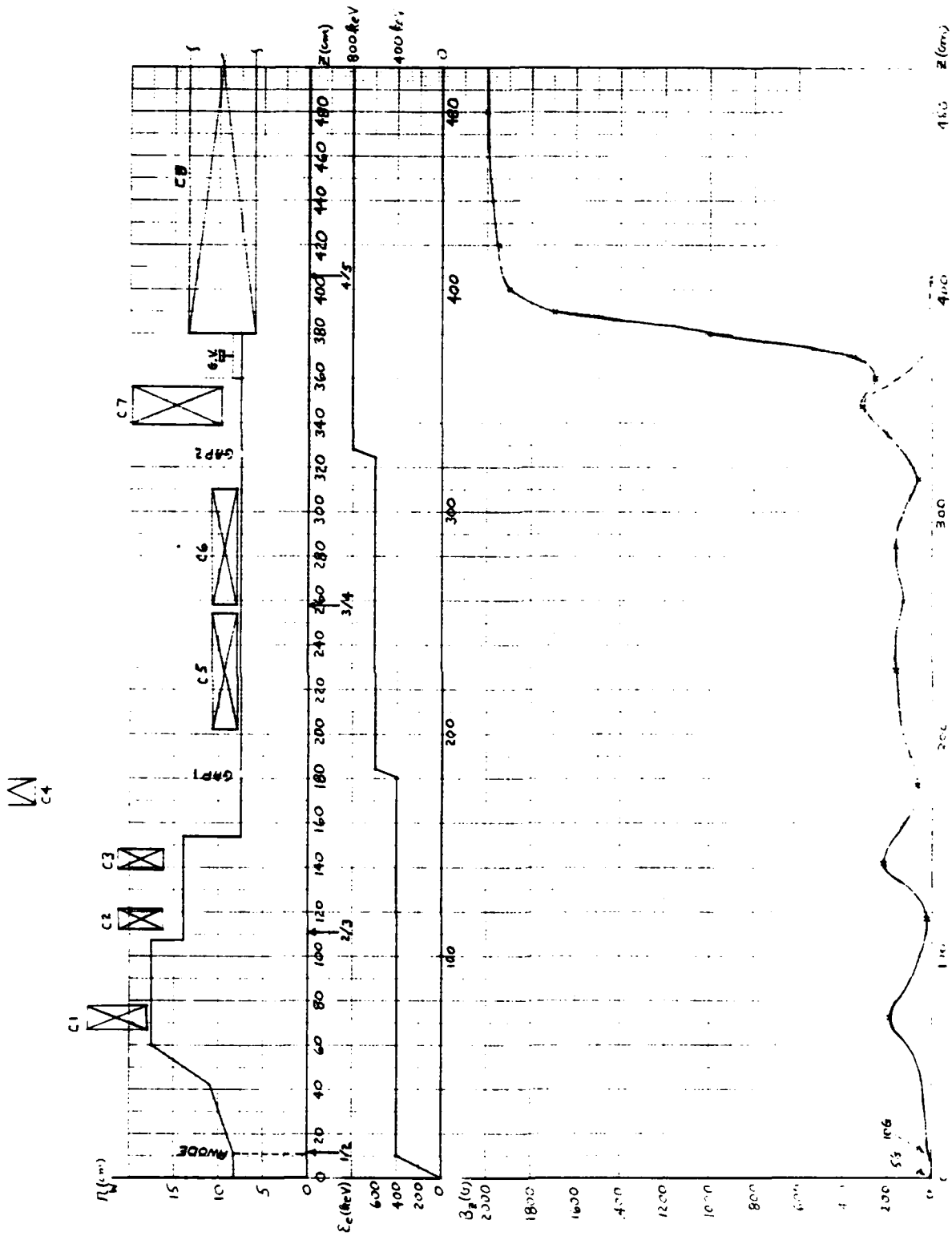
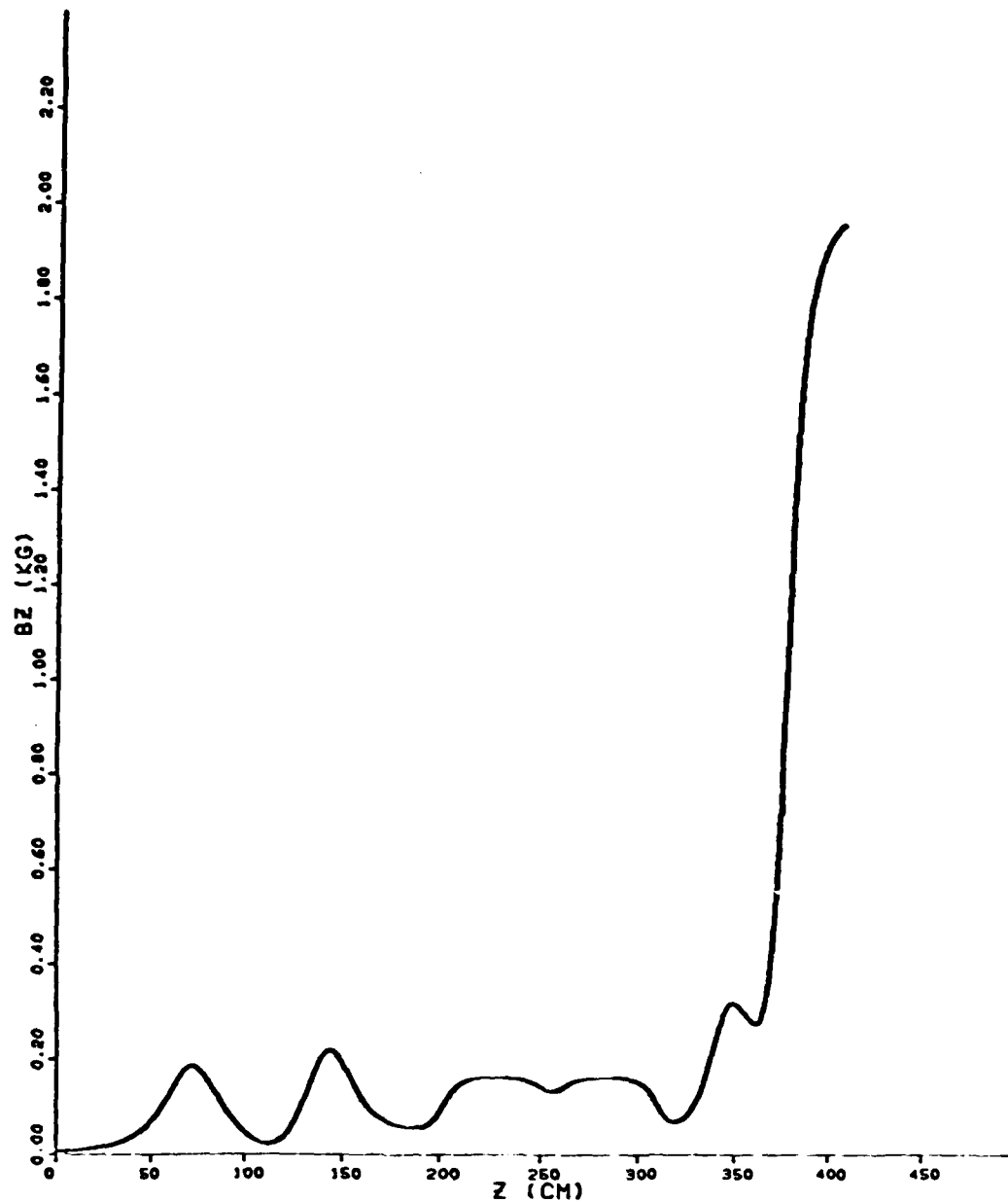


Figure 4. NBS Induction Accelerator



BZ VS Z

Figure 5. Magnetic Field Profile from Dec. 1981 Data

2-APR-82
12:20:30

(ara)

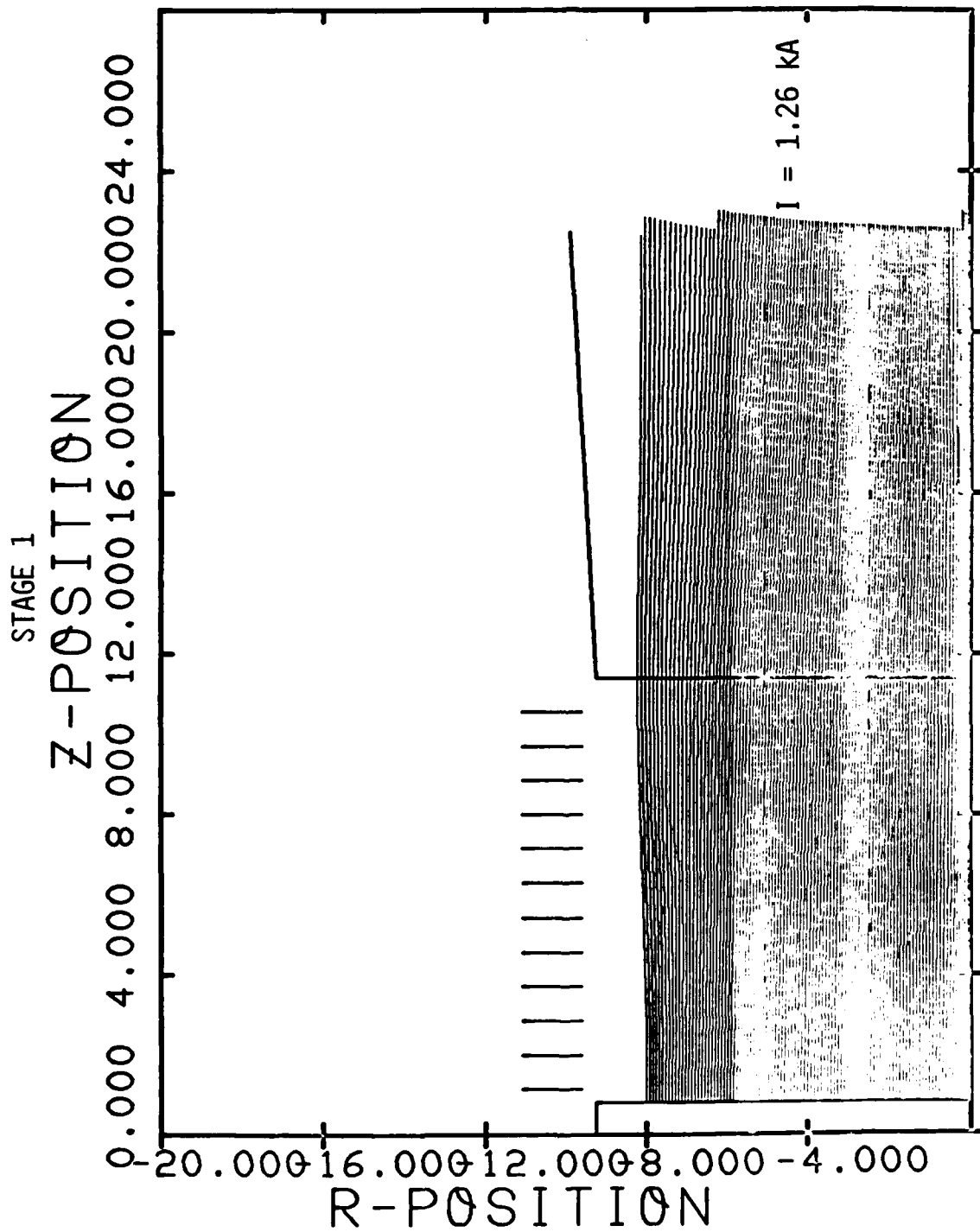


Figure 6. Laminar Beam Formation a Stage 1, with Linear Potential Grading [0 to 400 kV], Edge-Peaked $J_z(r)$

STAGE 2

Z-POSITION - 23

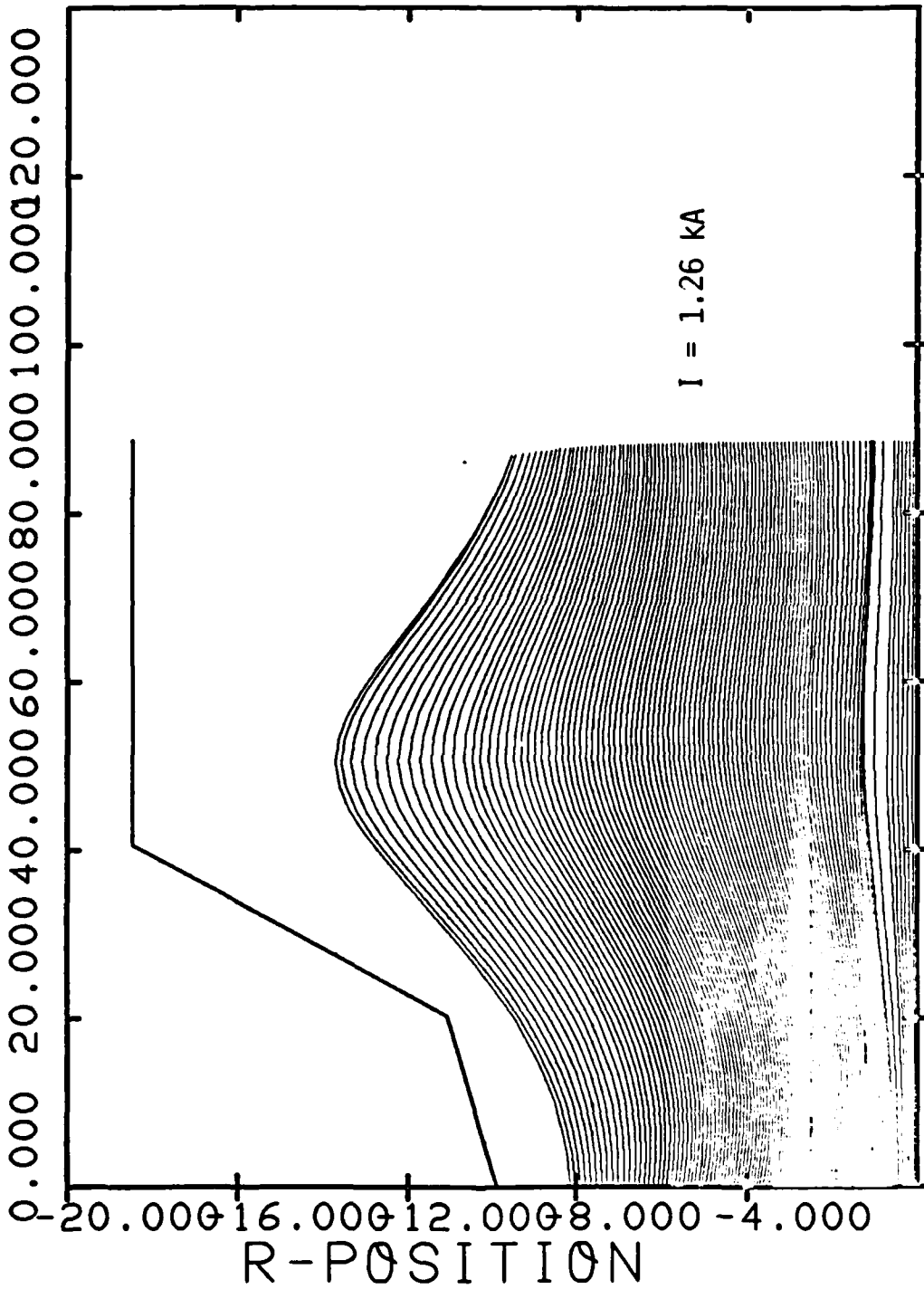


Figure 7. Laminar Flow a Stage 2

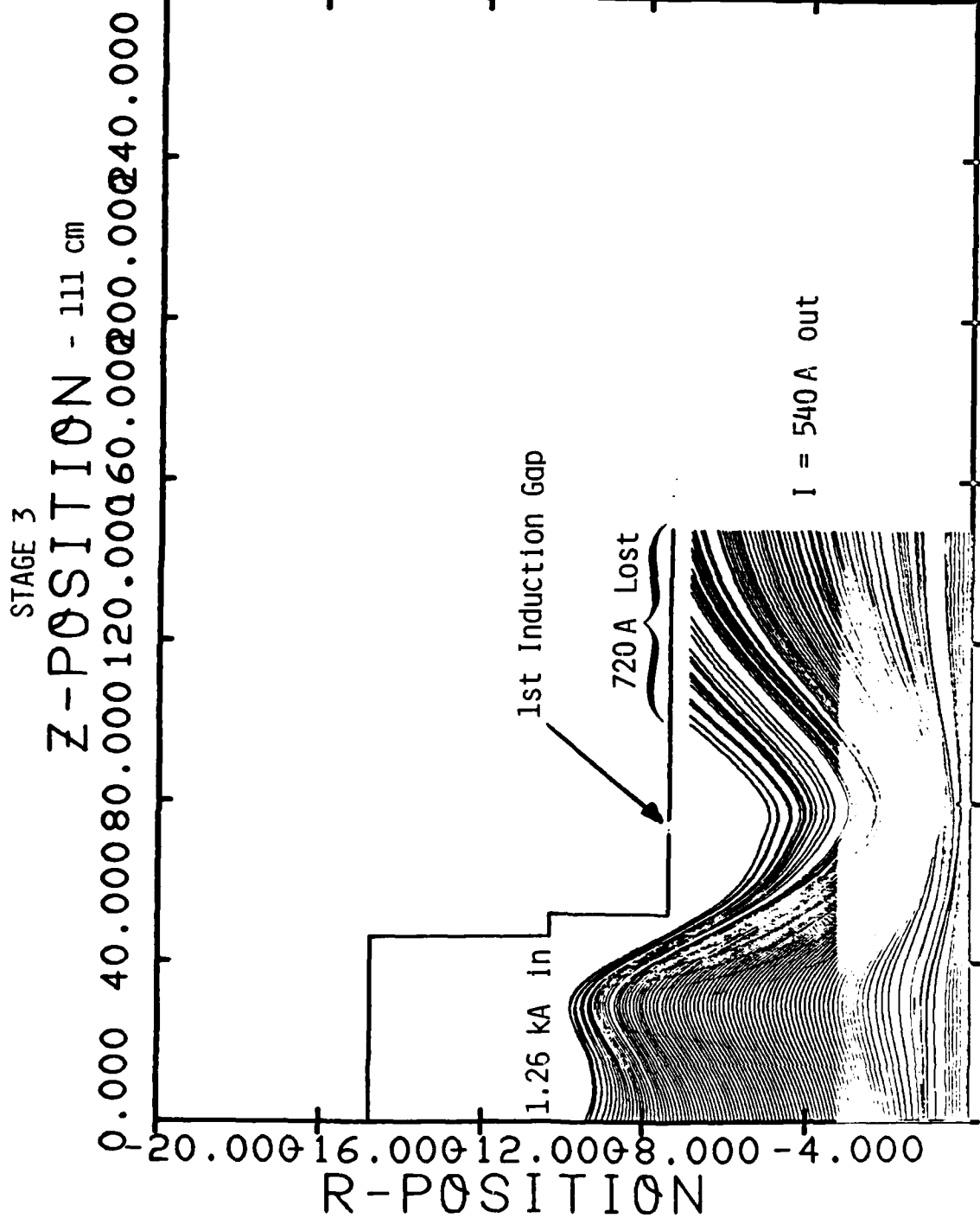


Figure 8. Transport Thru Stage 3, with Current Loss to Walls

STAGE 4

Z-POSITION - 253 cm

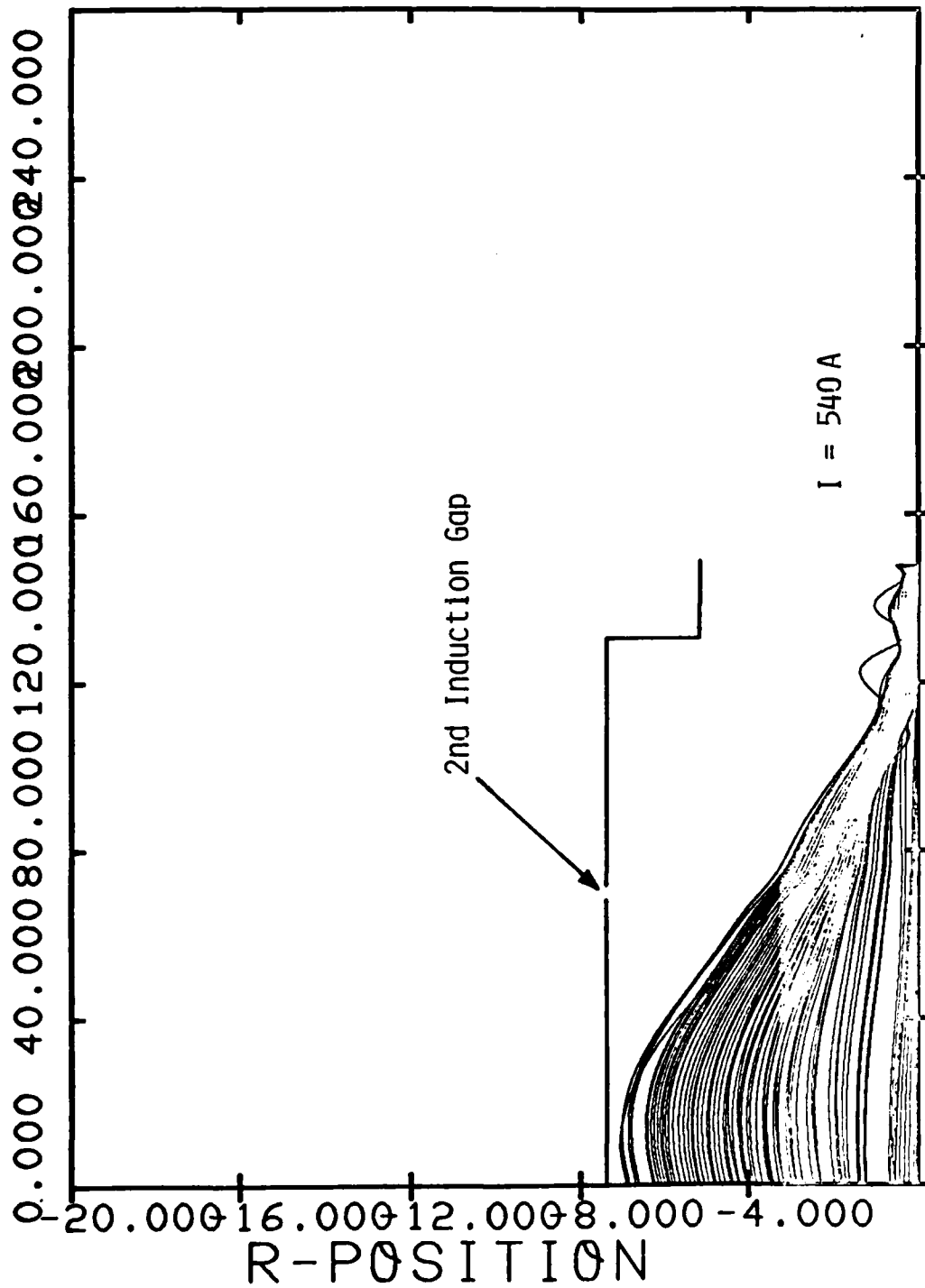


Figure 9. Transport of Residual Current Thru Stage 4 Compression

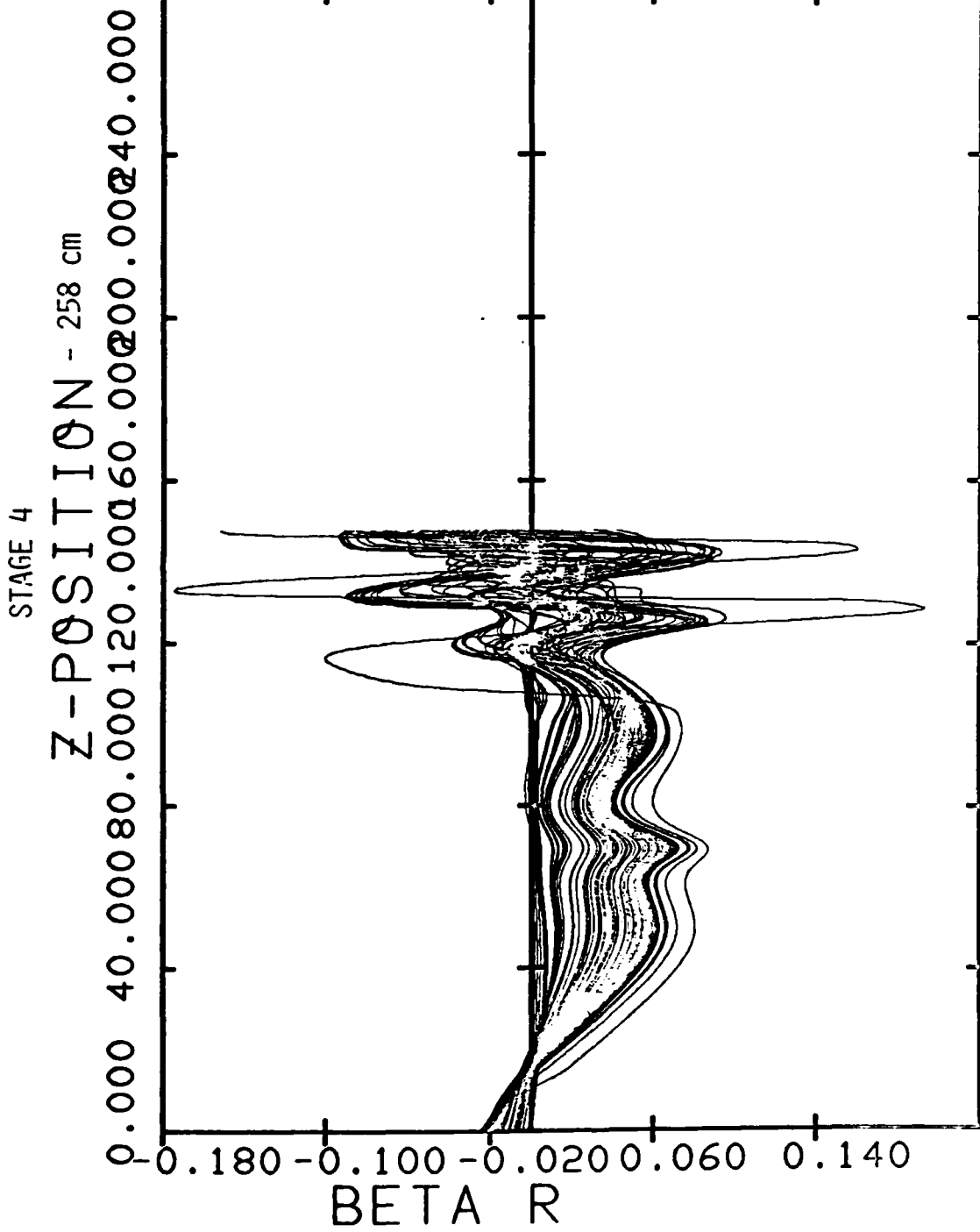


Figure 10. Compression of Residual Beam Flow at Stage 4

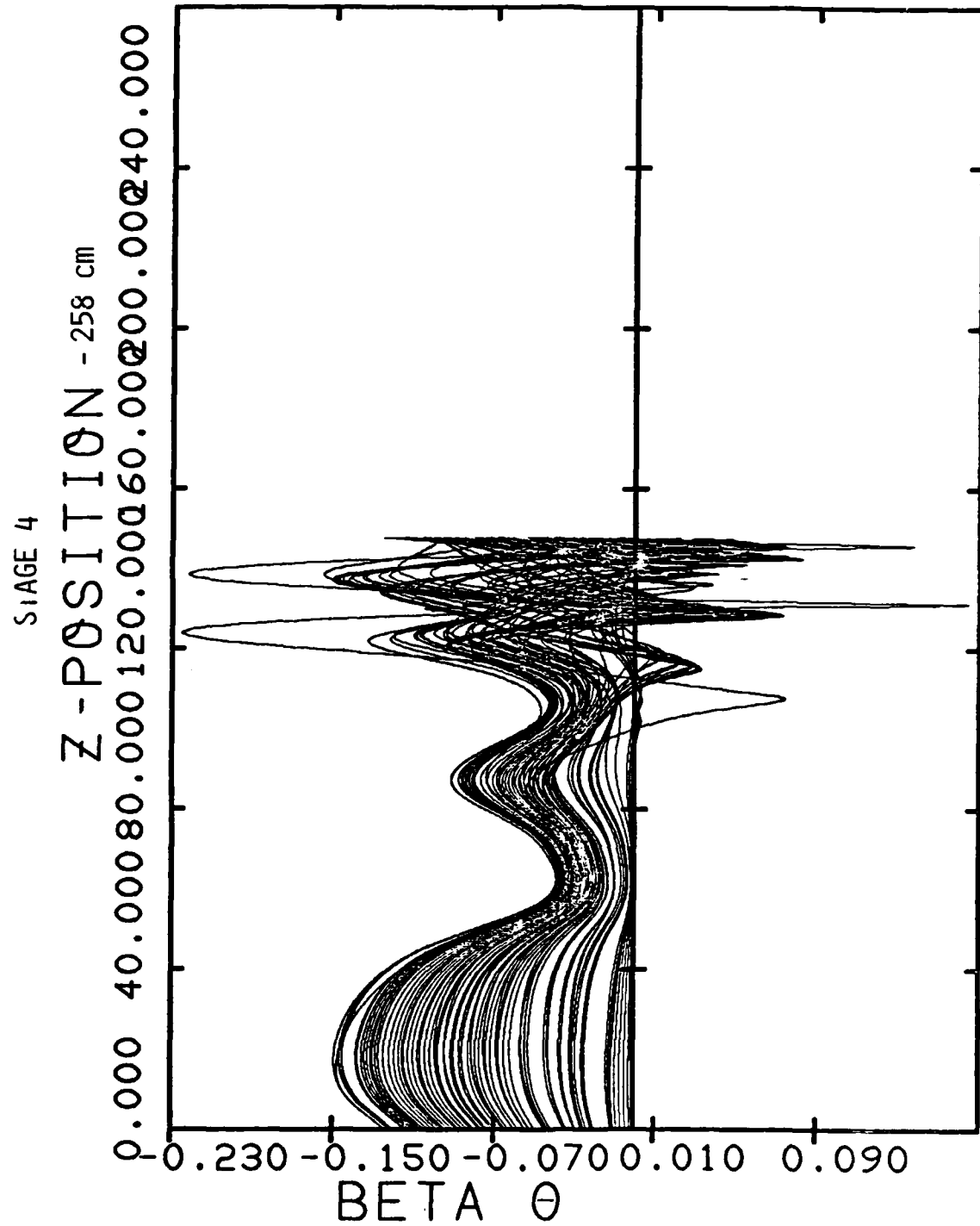


Figure 11. Compression of Residual Beam Flow at Stage 4

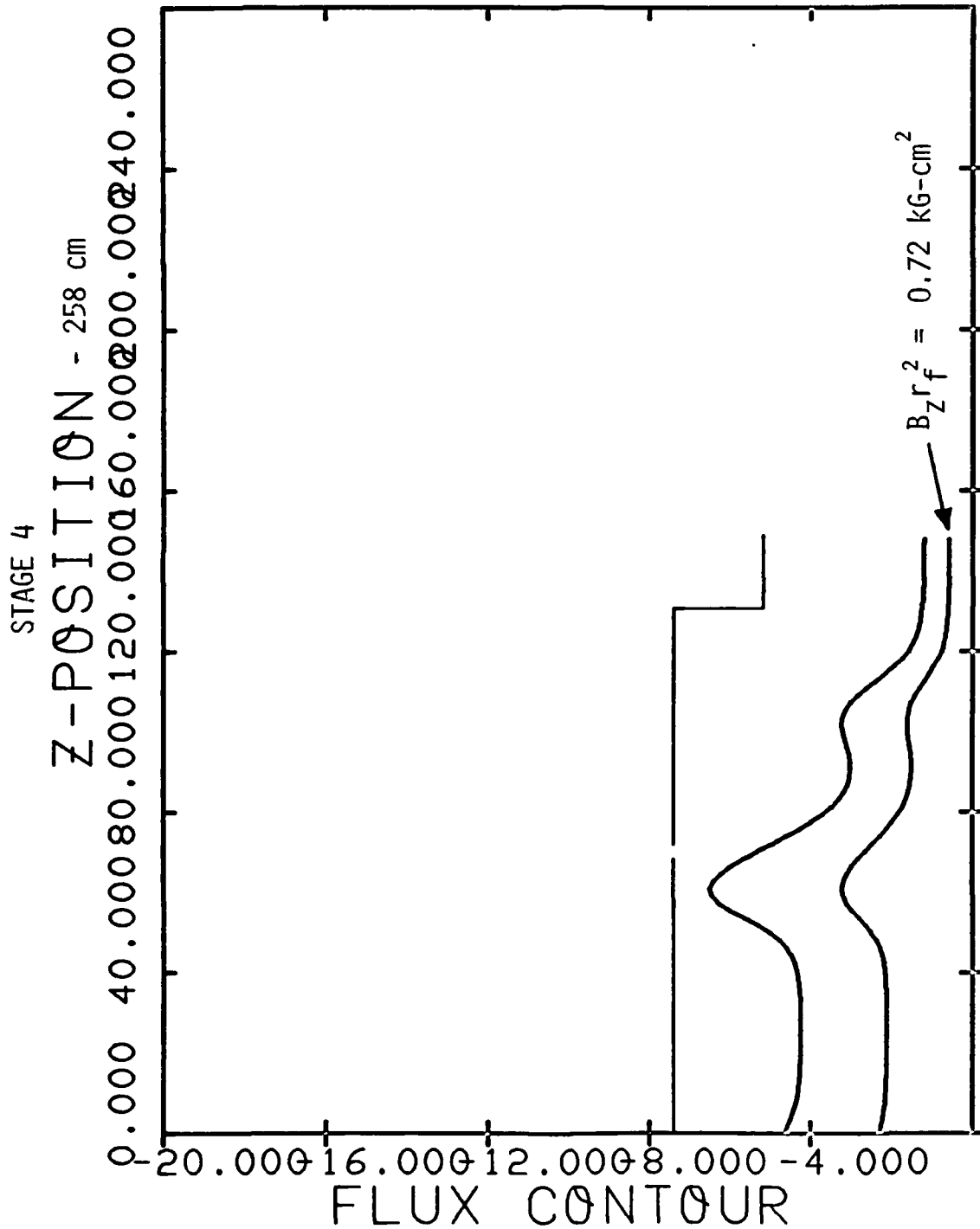


Figure 12. Flux Contours for Stage 4 Compression

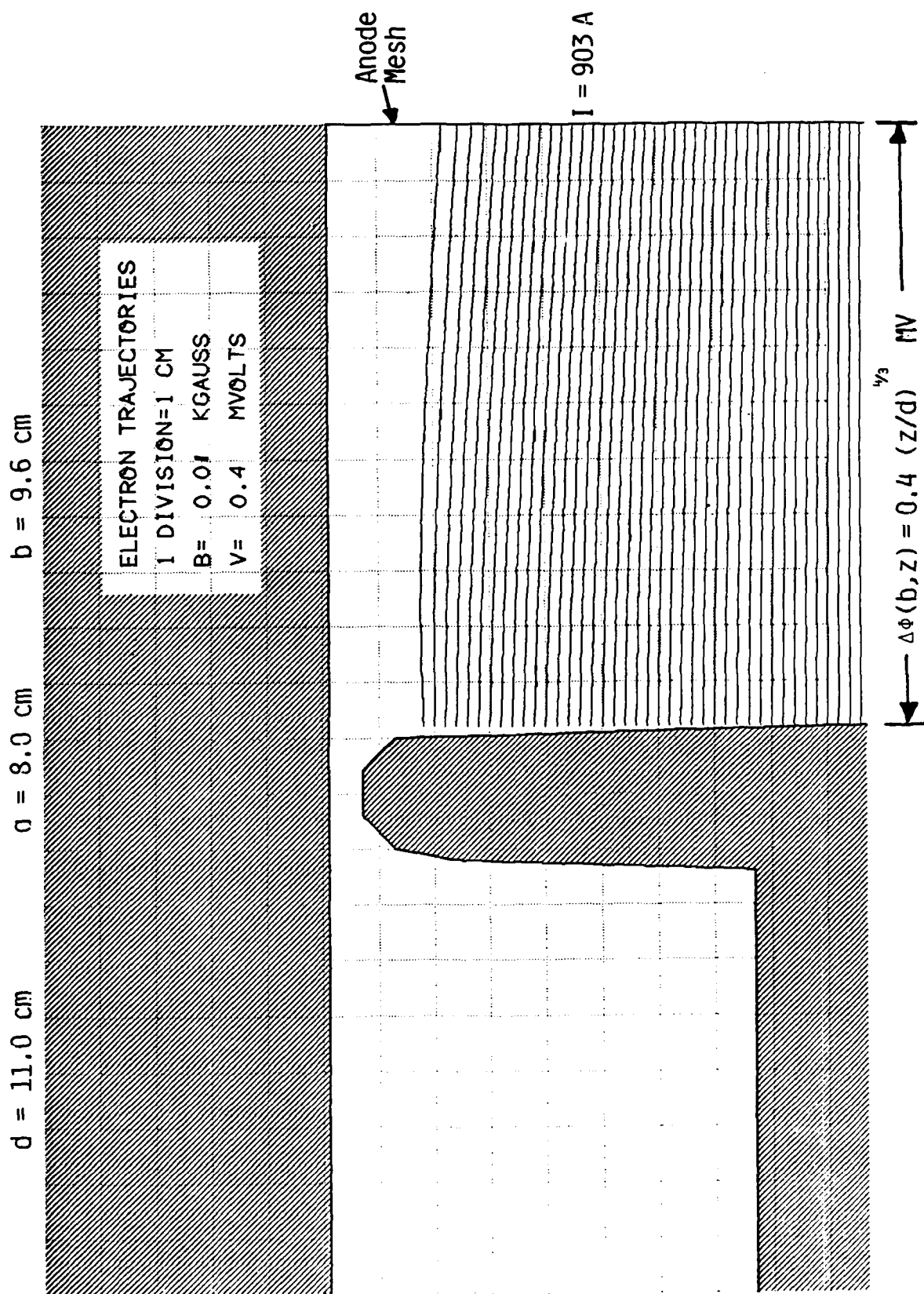


Figure 13. Cold Cathode with Child-Langmuir Potential Grading

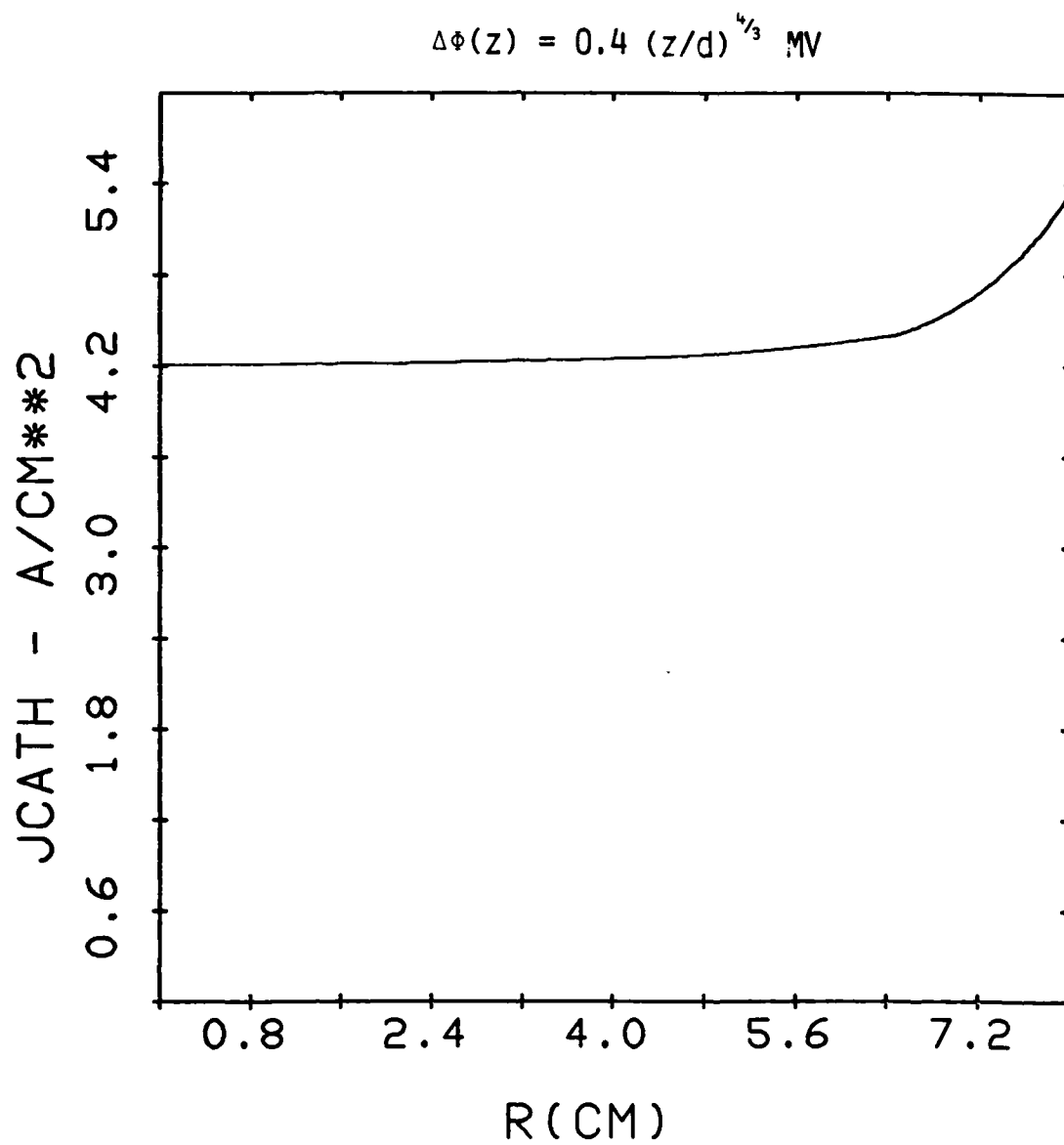


Figure 14. Current Density Profile @ Cathode
for Child-Langmuir Potential Grading

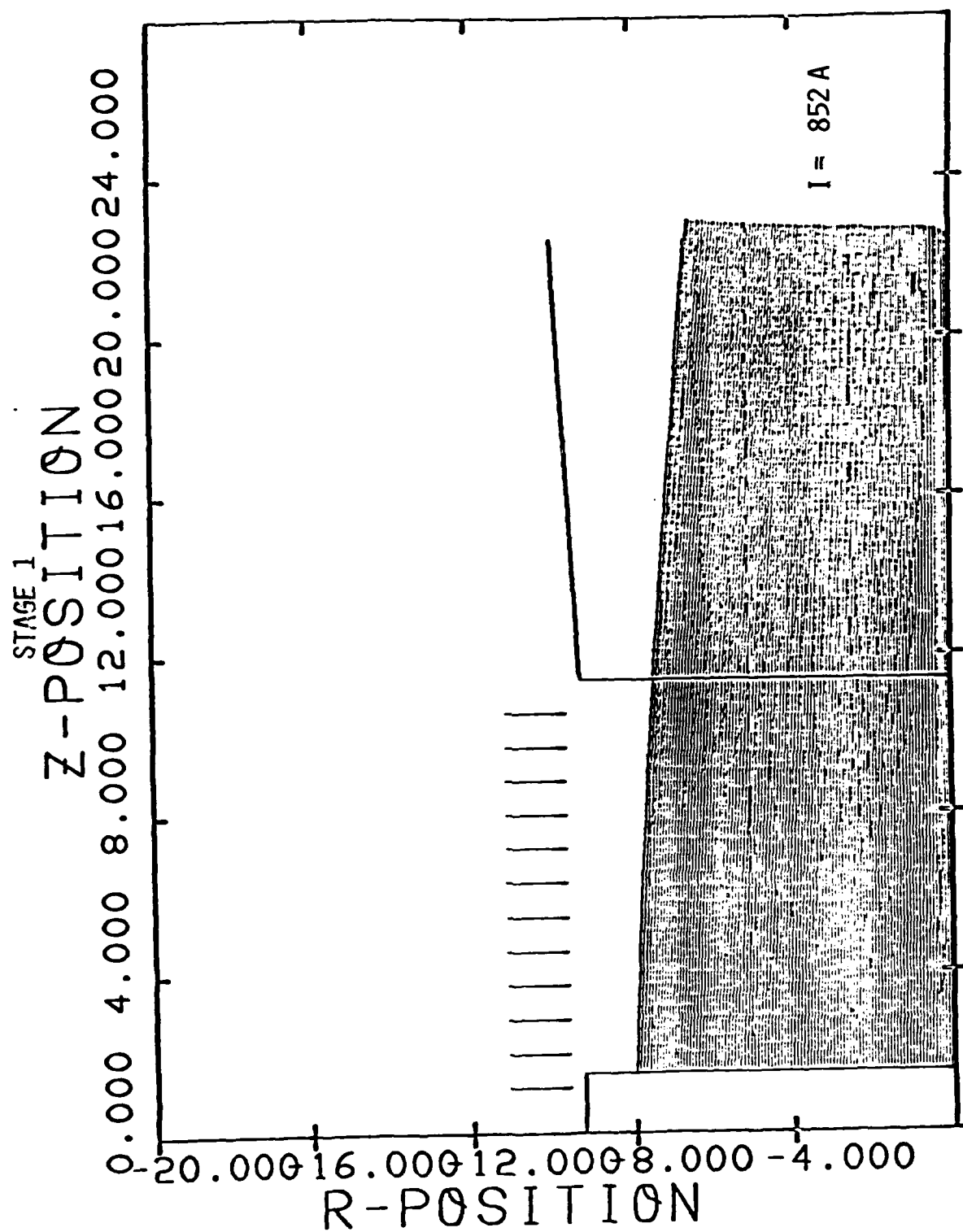


Figure 15. Laminar Beam Formation a Stage 1
Child-Langmuir Potential Grading

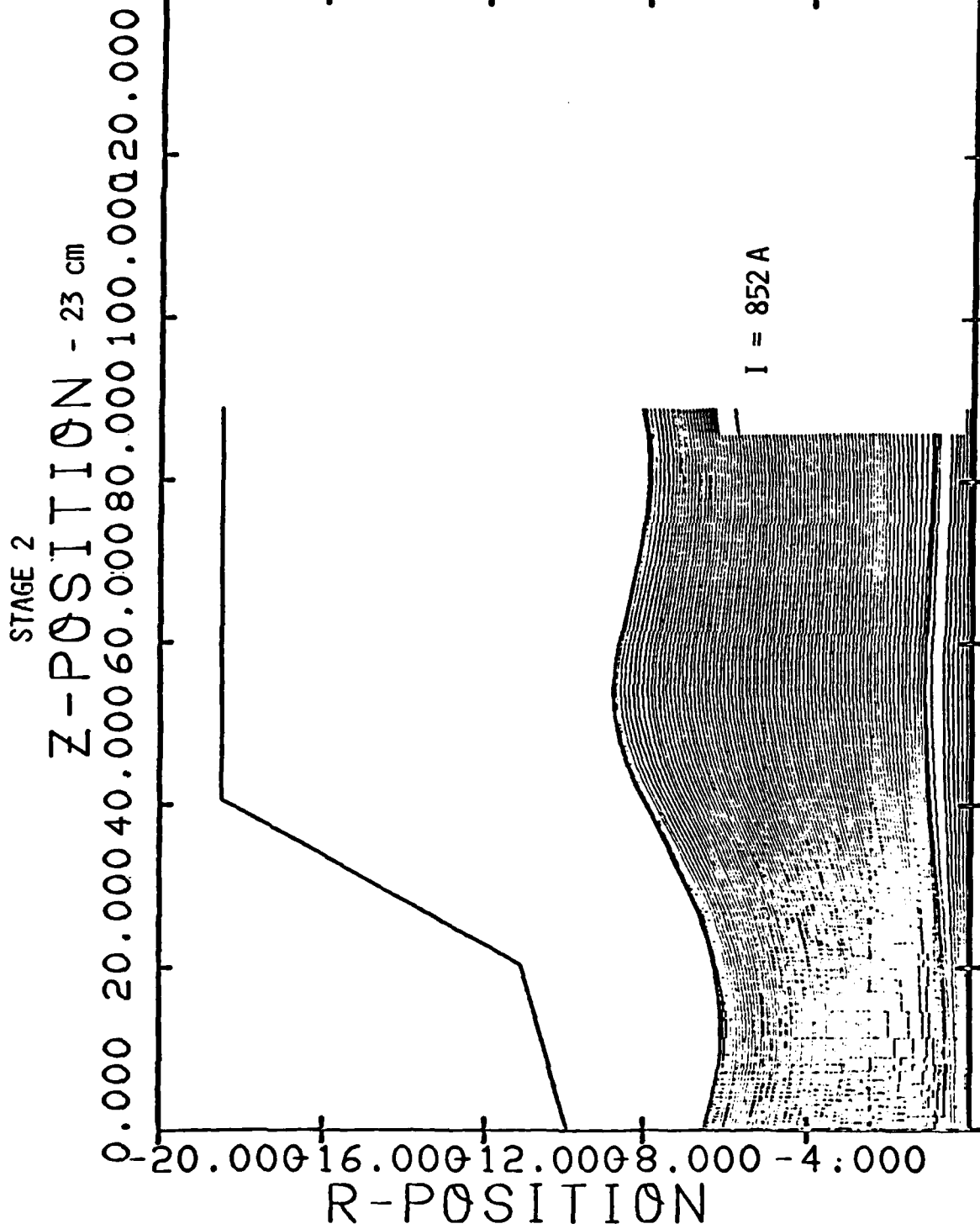


Figure 16. Laminar Beam Blow a Stage 2

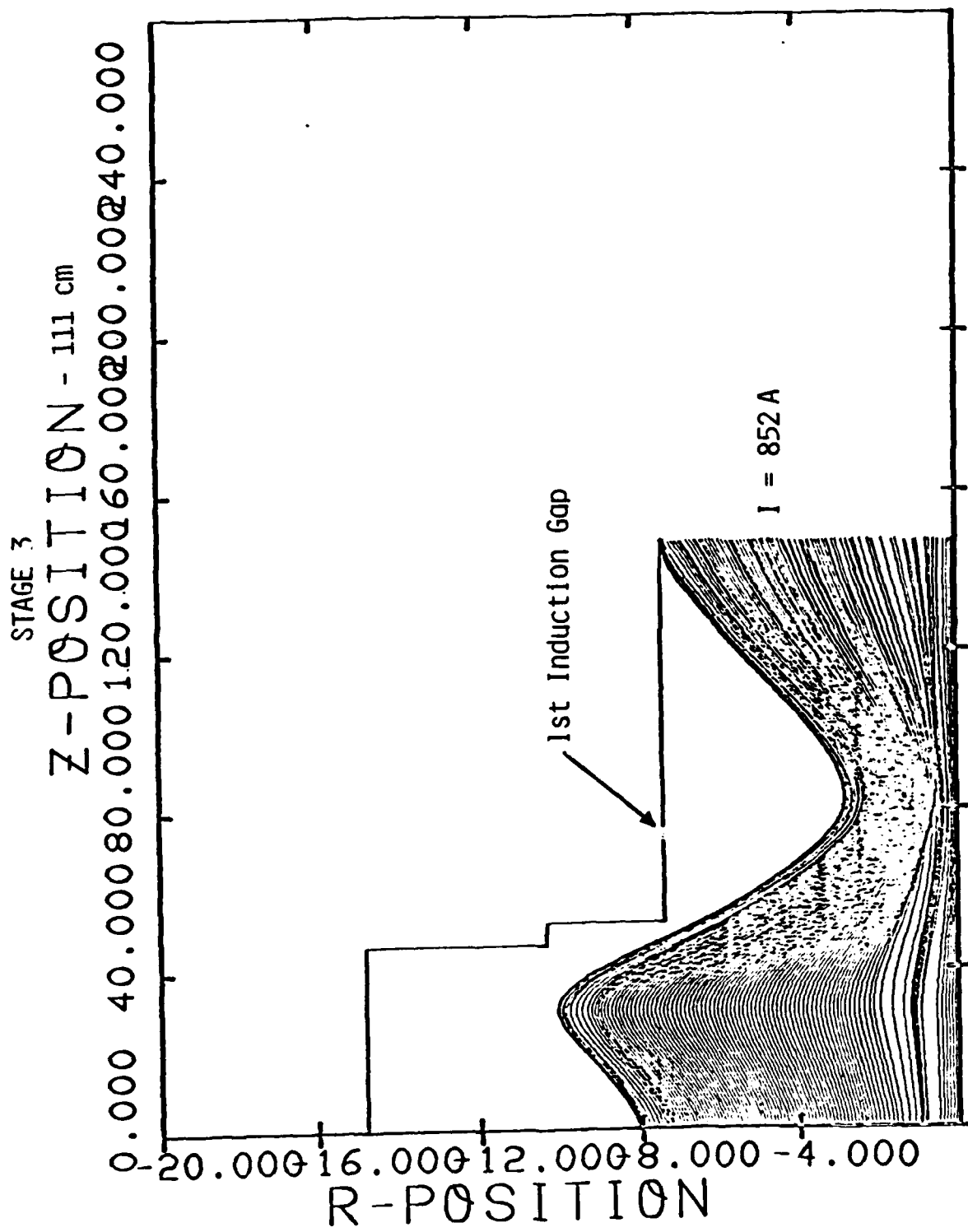
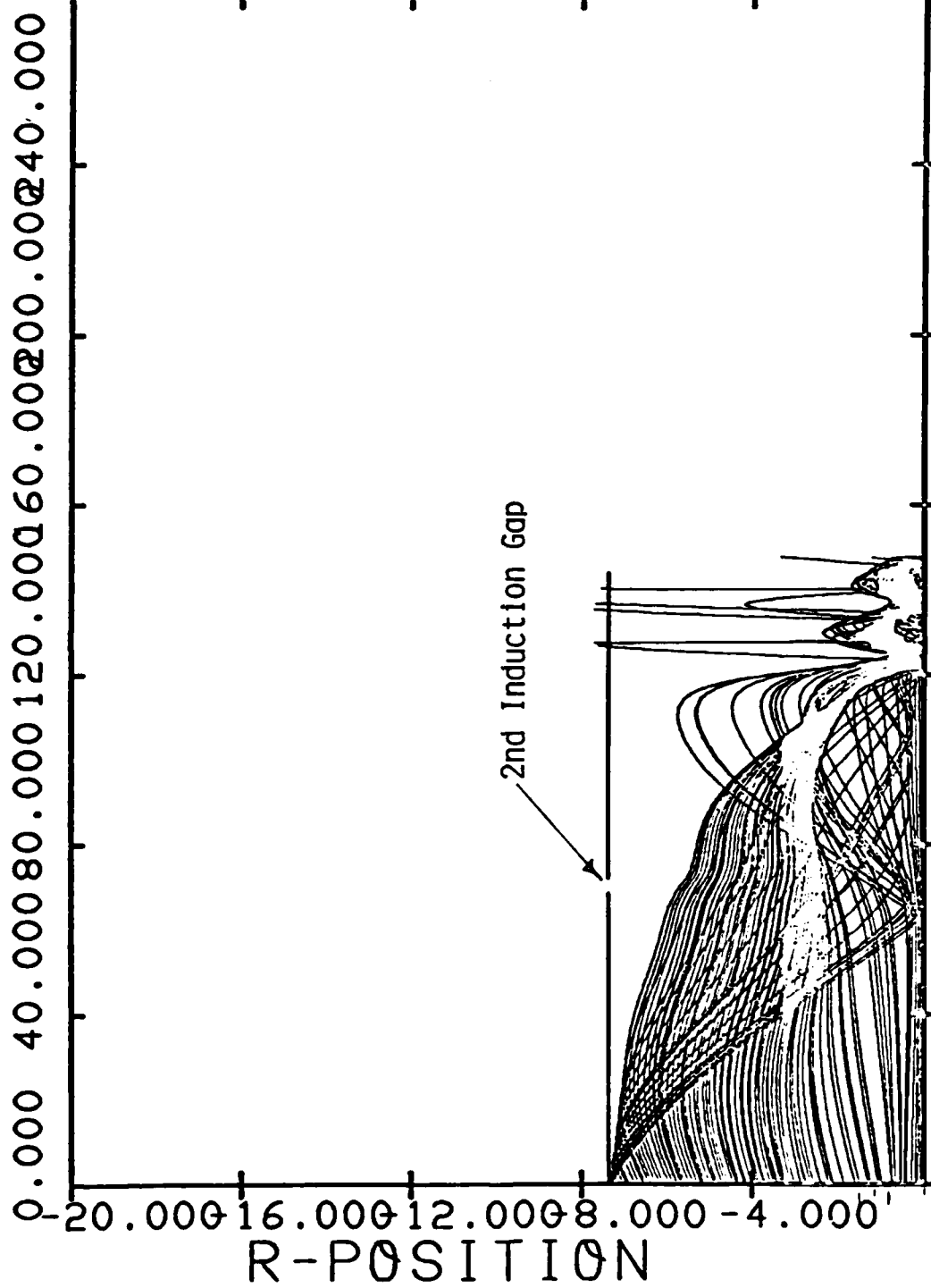


Figure 17. Laminar Beam Flow at Stage 3

STAGE 4

Z-POSITION - 258 cm



852 A

730 A

Figure 18. Compression of Laminar Beam at Stage 4

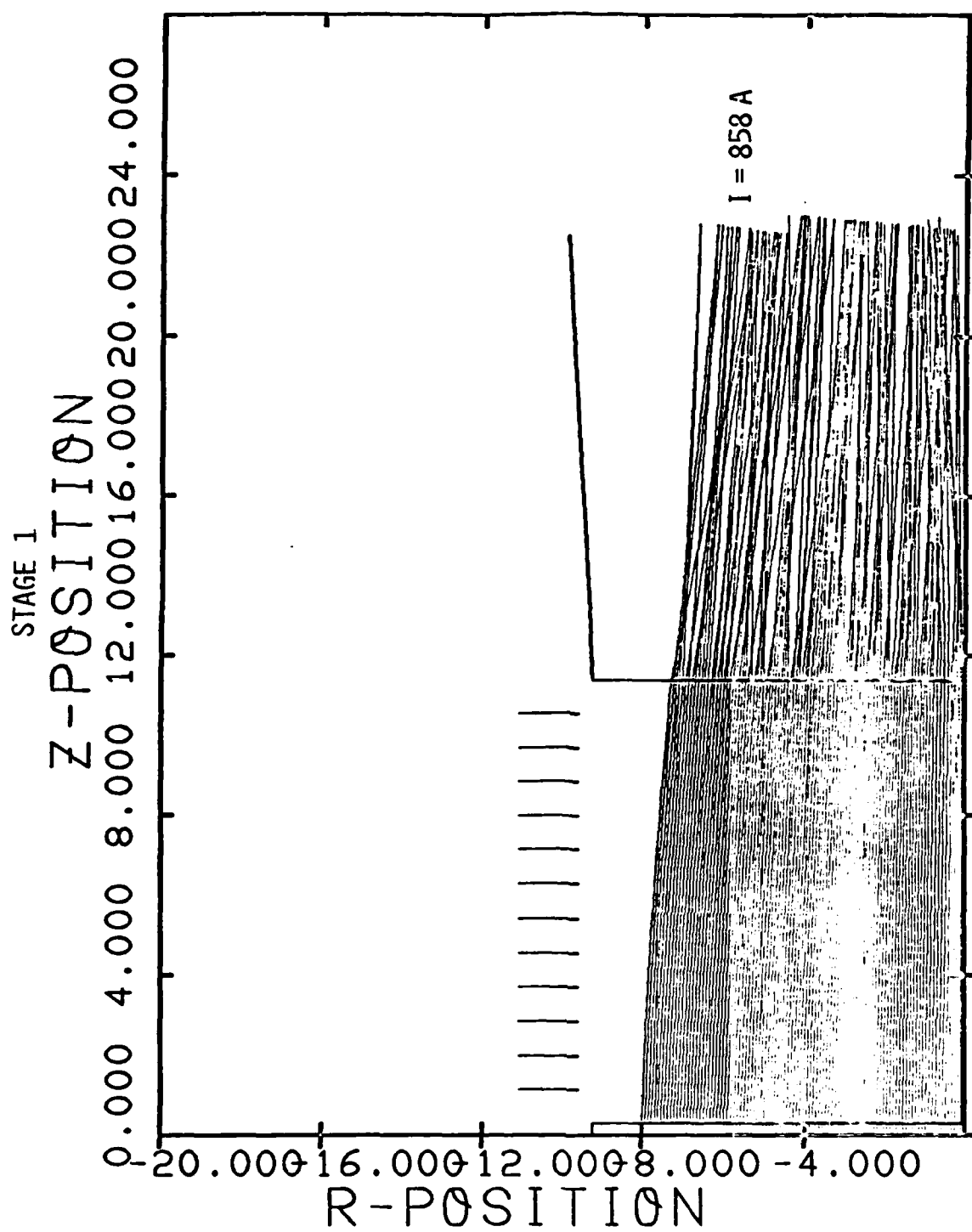


Figure 19. Laminar Diode Flow with Anode Mesh Scattering of $\theta_{\text{RMS}} \approx 2.93^\circ$

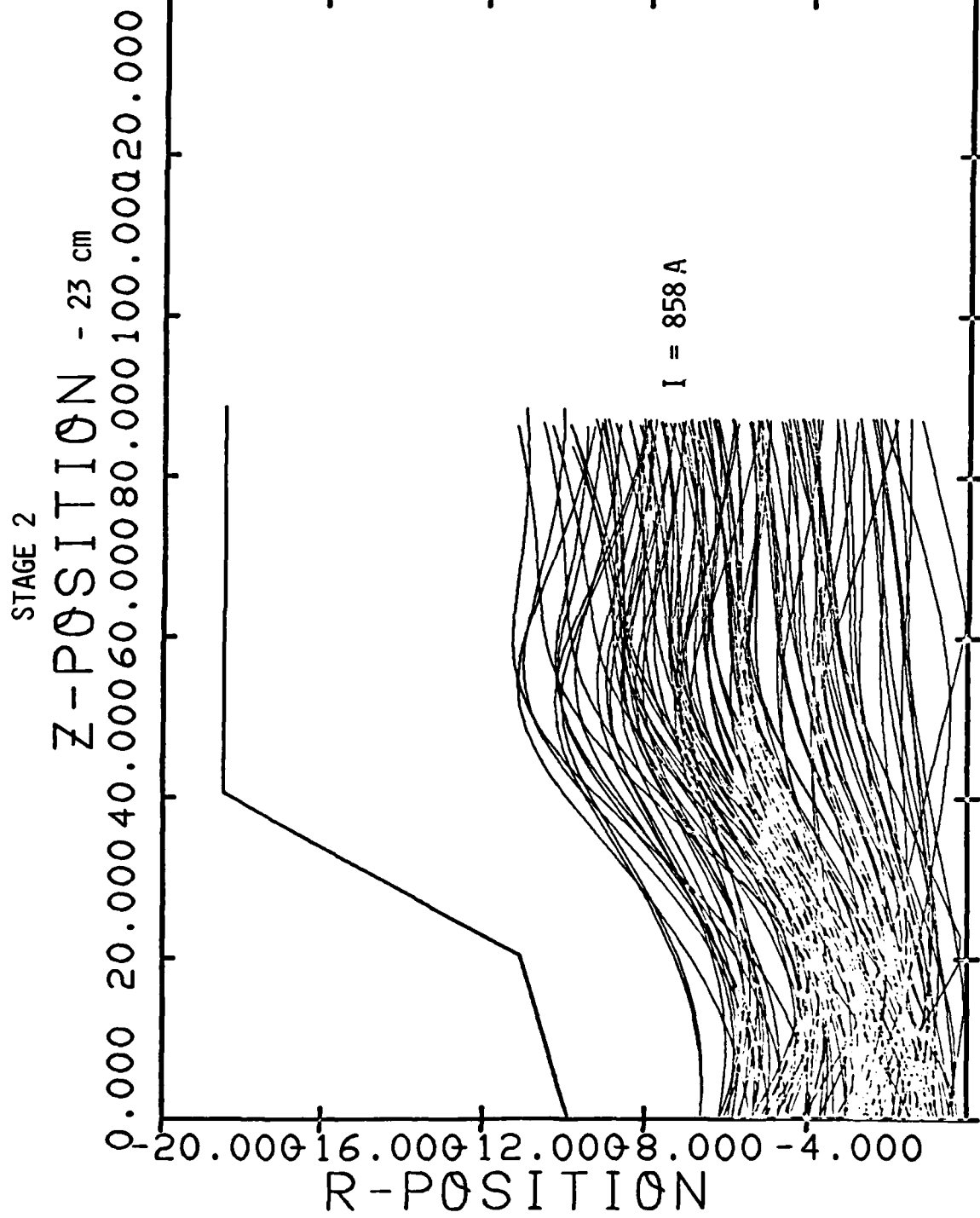


Figure 20. Scattered Flow at Stage 2

STAGE 3

Z-POSITION - 111 cm

0.000 40.000 80.000 120.000 160.000 200.000 240.000

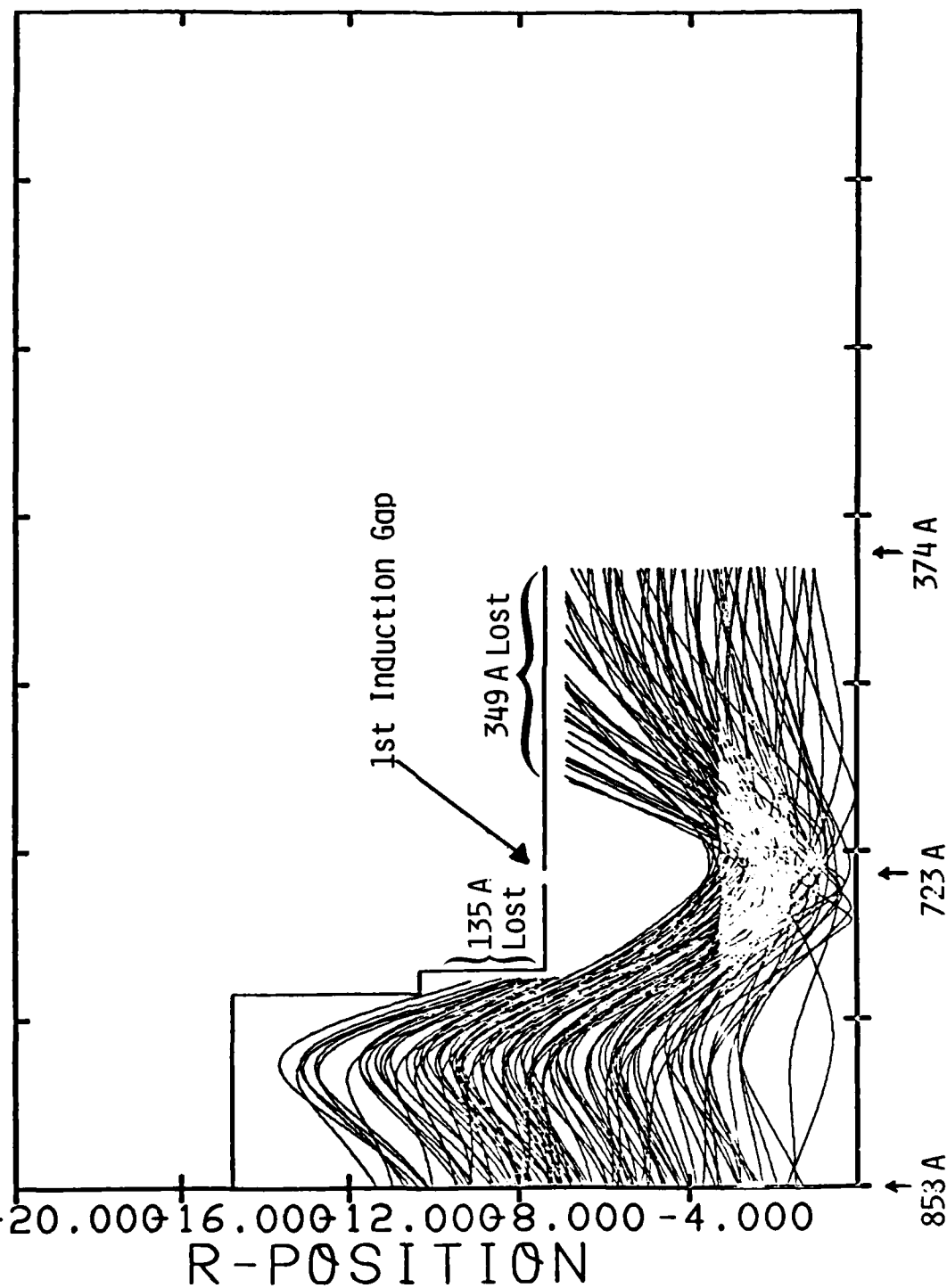


Figure 21. Scattered Flow Thru Stage 3, with Current Loss

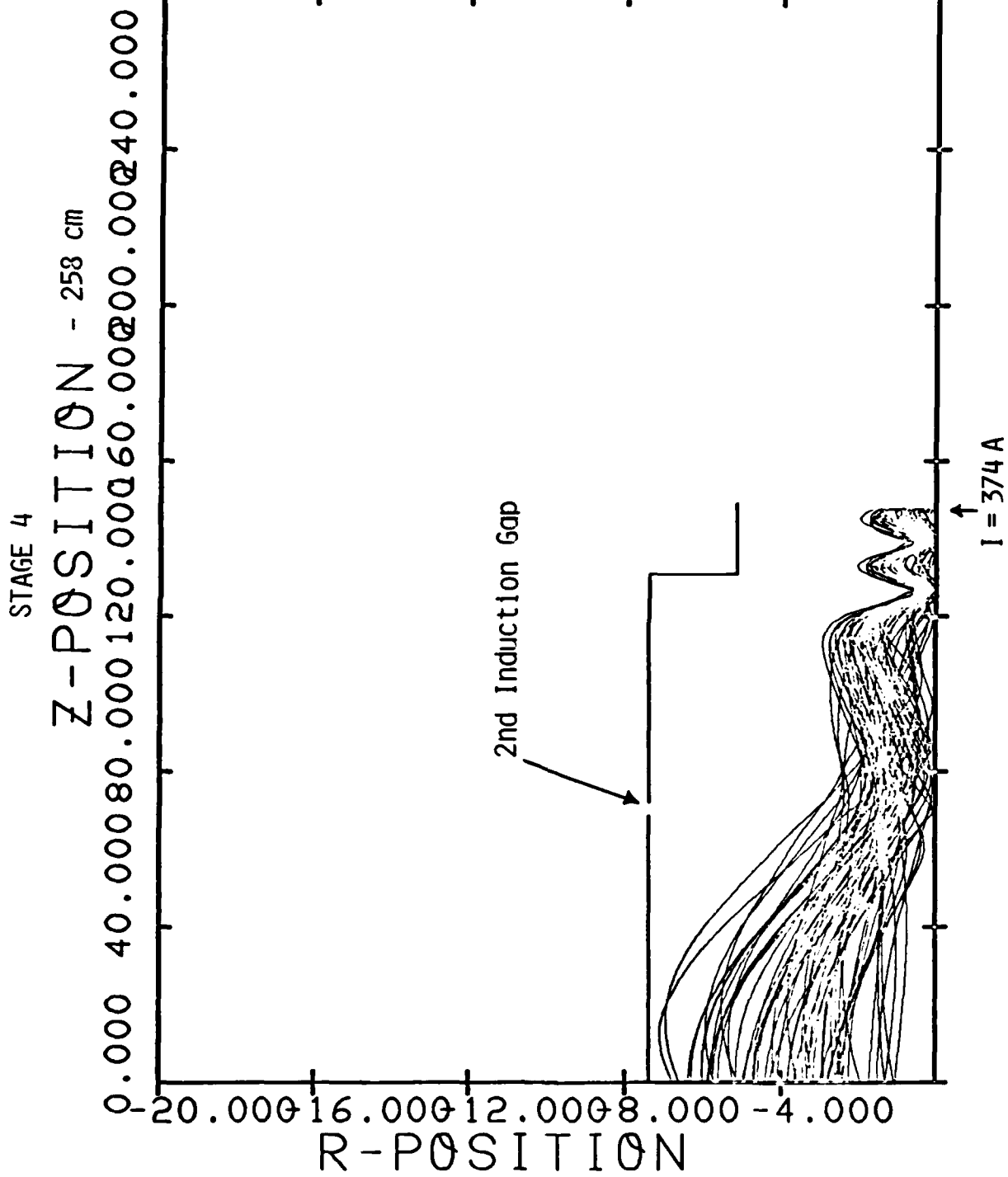


Figure 22. Transmission of Residual Scattered Current Thru Stage 4 Compression

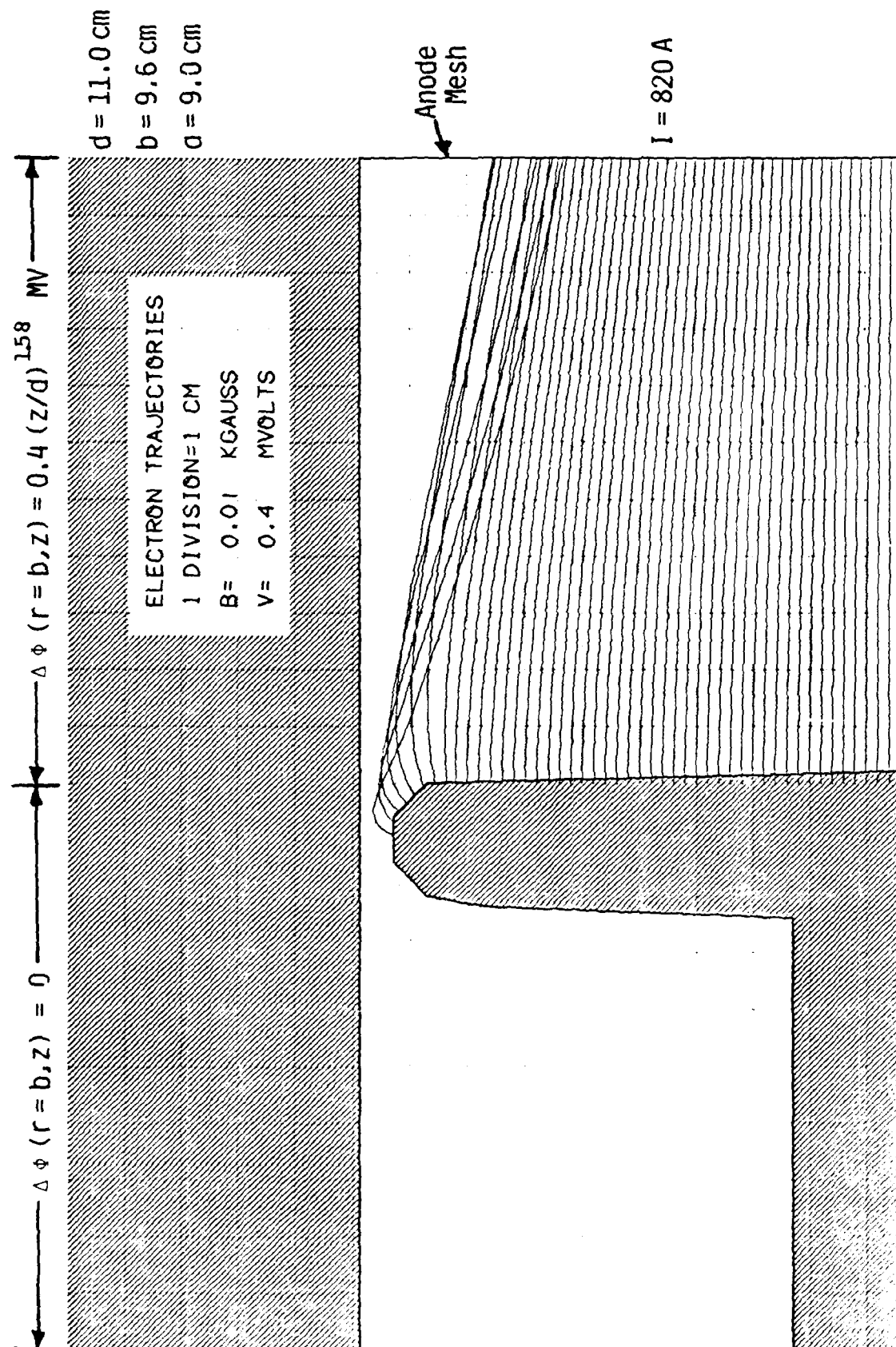


Figure 23. Cathode with Sub-Child-Langmuir Potential Grading and Emission to Top of Cathode.

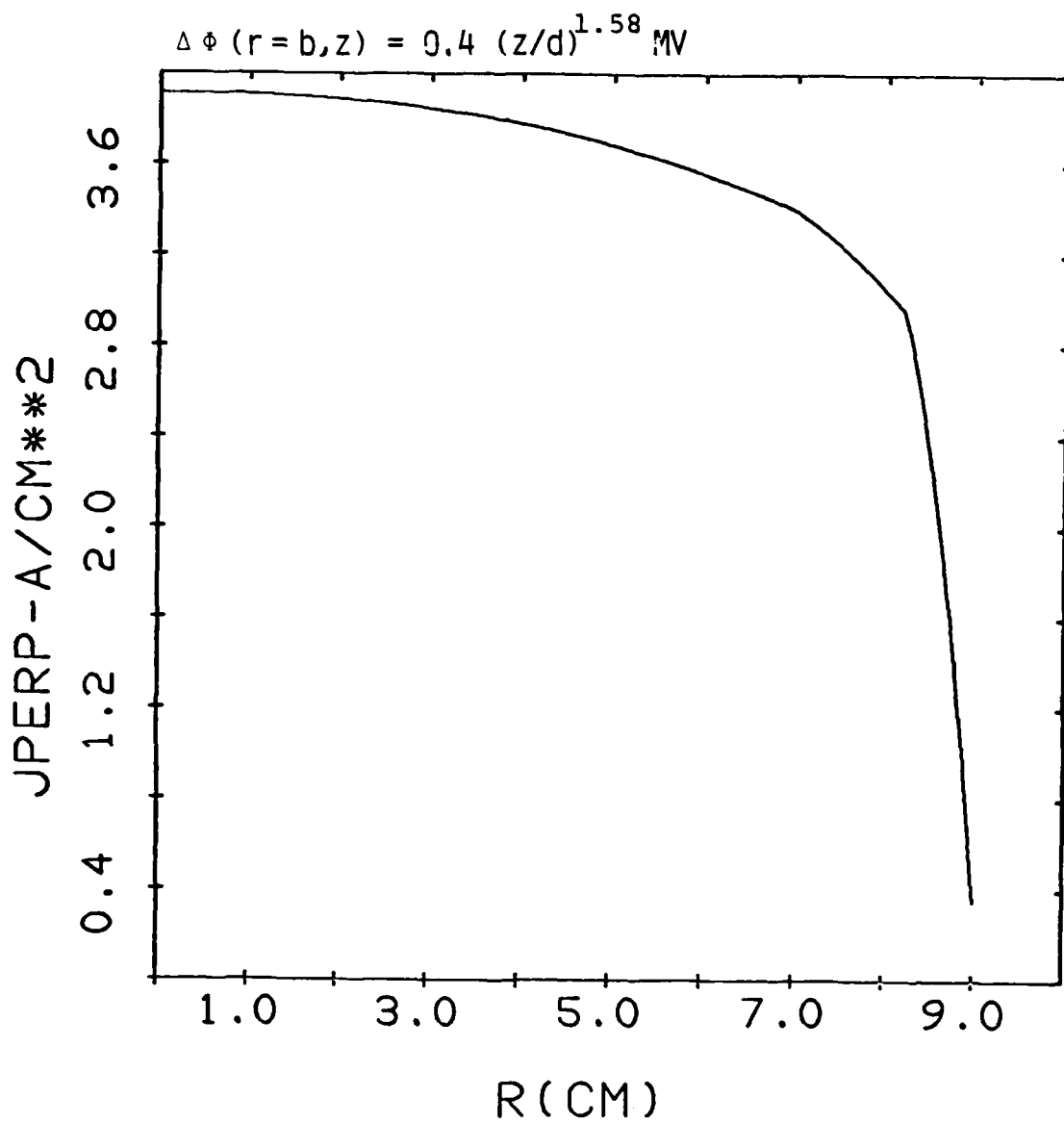


Figure 24. Current Density Profile @ Cathode for Sub-Child-Langmuir Potential Grading

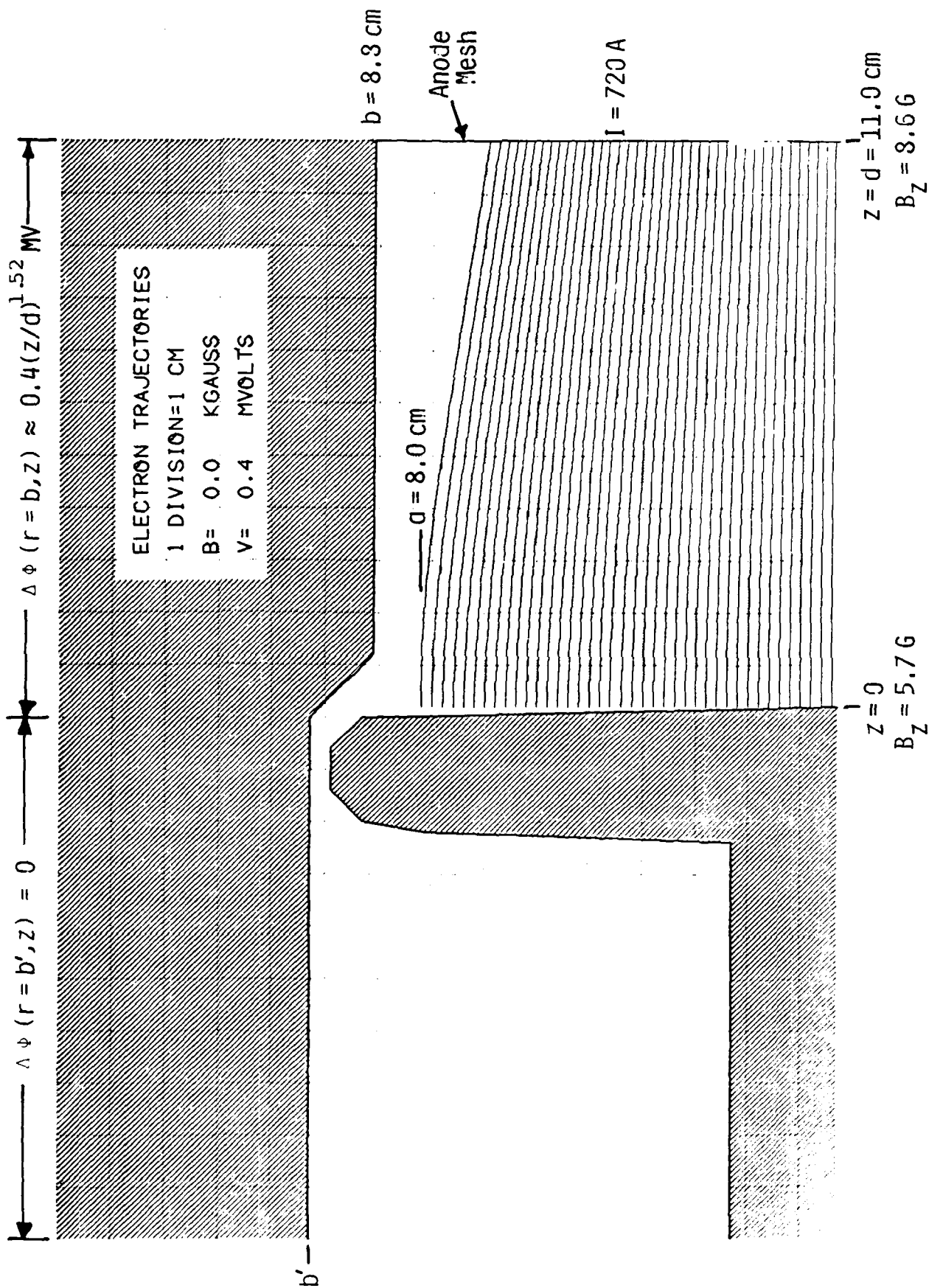
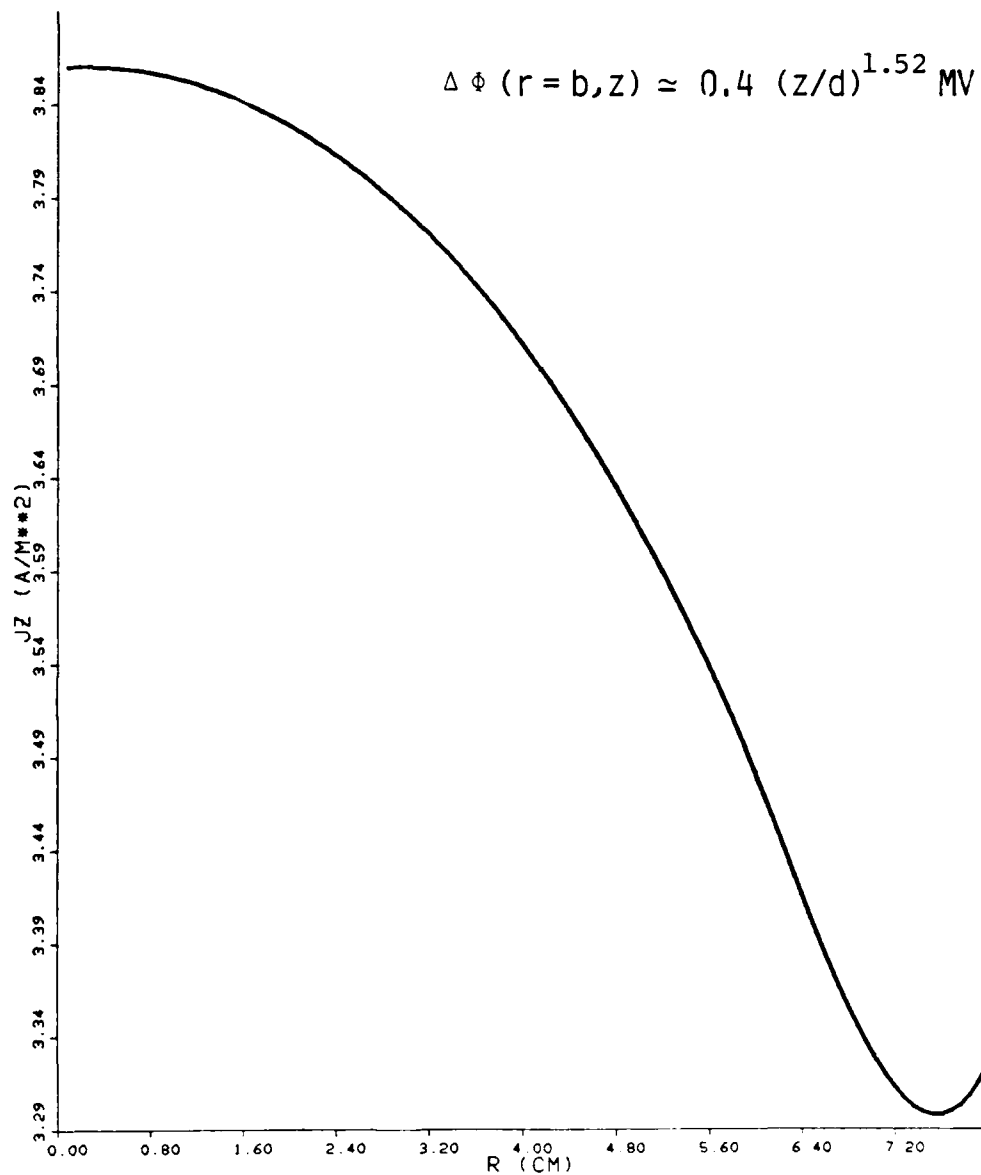


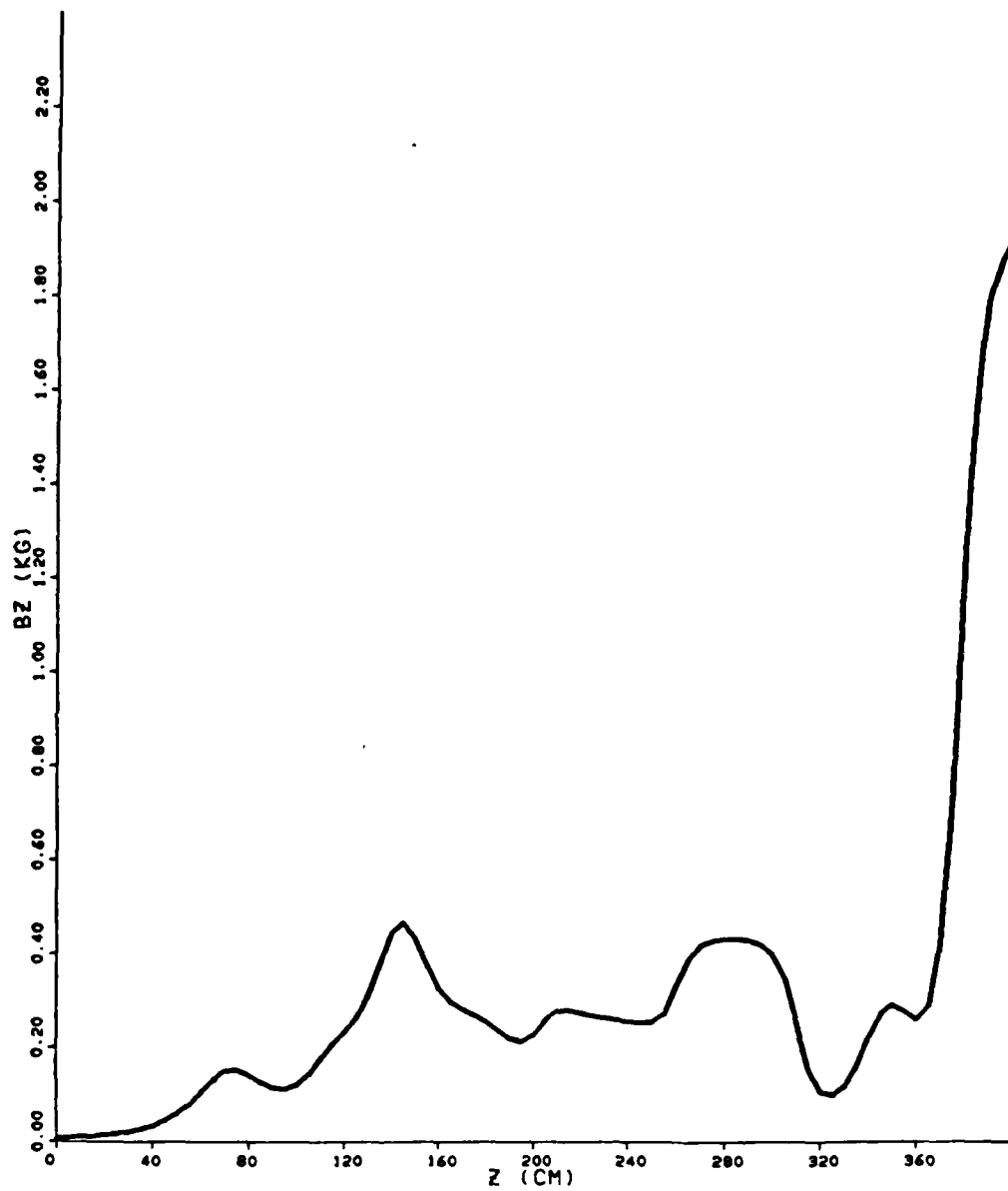
Figure 25. Cold Cathode with Sub-Child-Langmuir Potential Grading



JZ VS R

Figure 26. Current Density Profile a Cathode for Sub-Child-Langmuir Potential Grading (Modified Design)

13-MAY-82
06:42:45



BZ VS Z

Figure 27. Magnetic Field Profile from Feb. 1982 Data

7-MAY-82
11:17:59

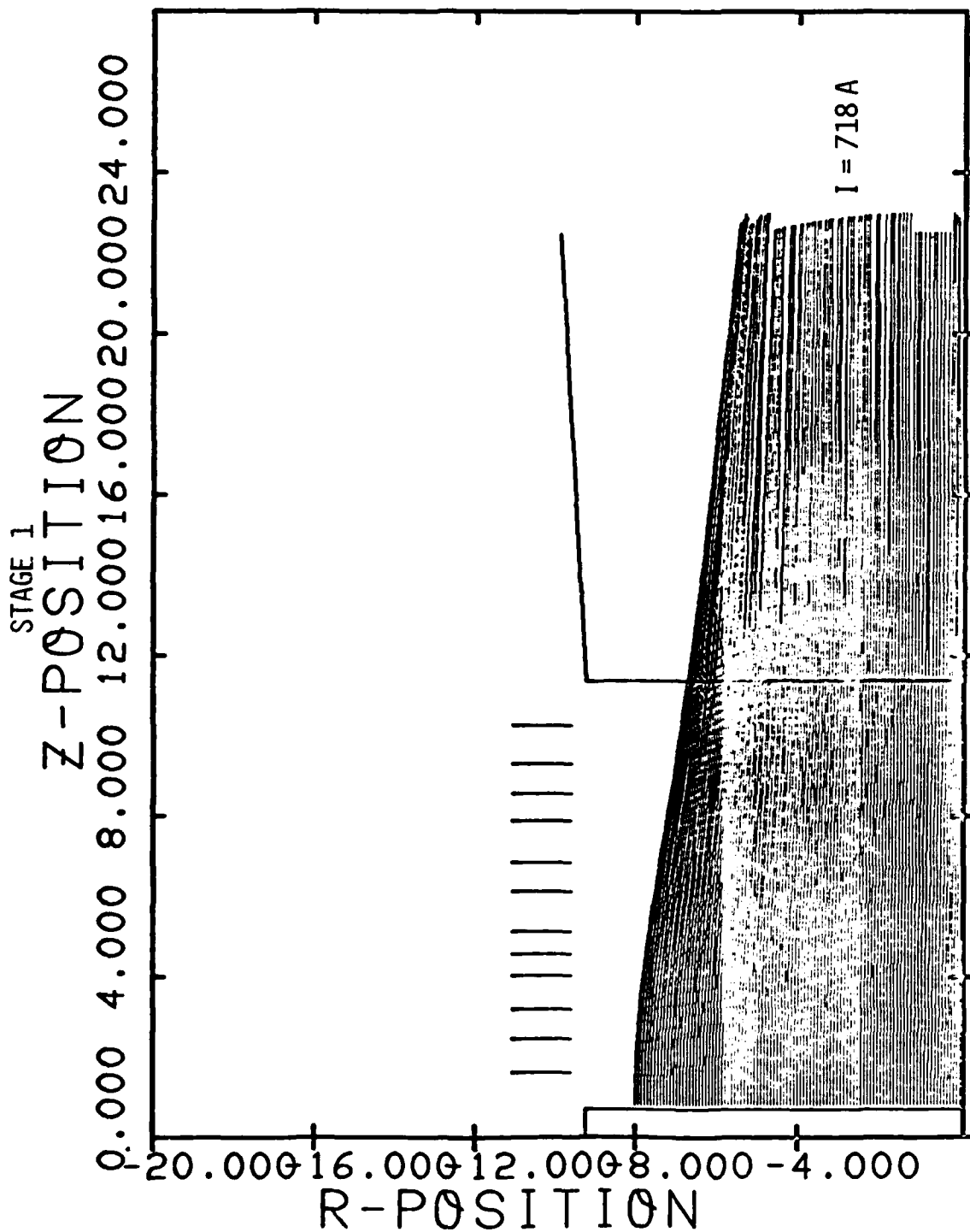


Figure 28. Cold Cathode Beam Formation at Stage 1, with Sub-Child-Langmuir Potential Grading (Modified Design) & Anode Mesh Scattering of $\theta_{\text{RMS}} \approx 0.28^\circ$

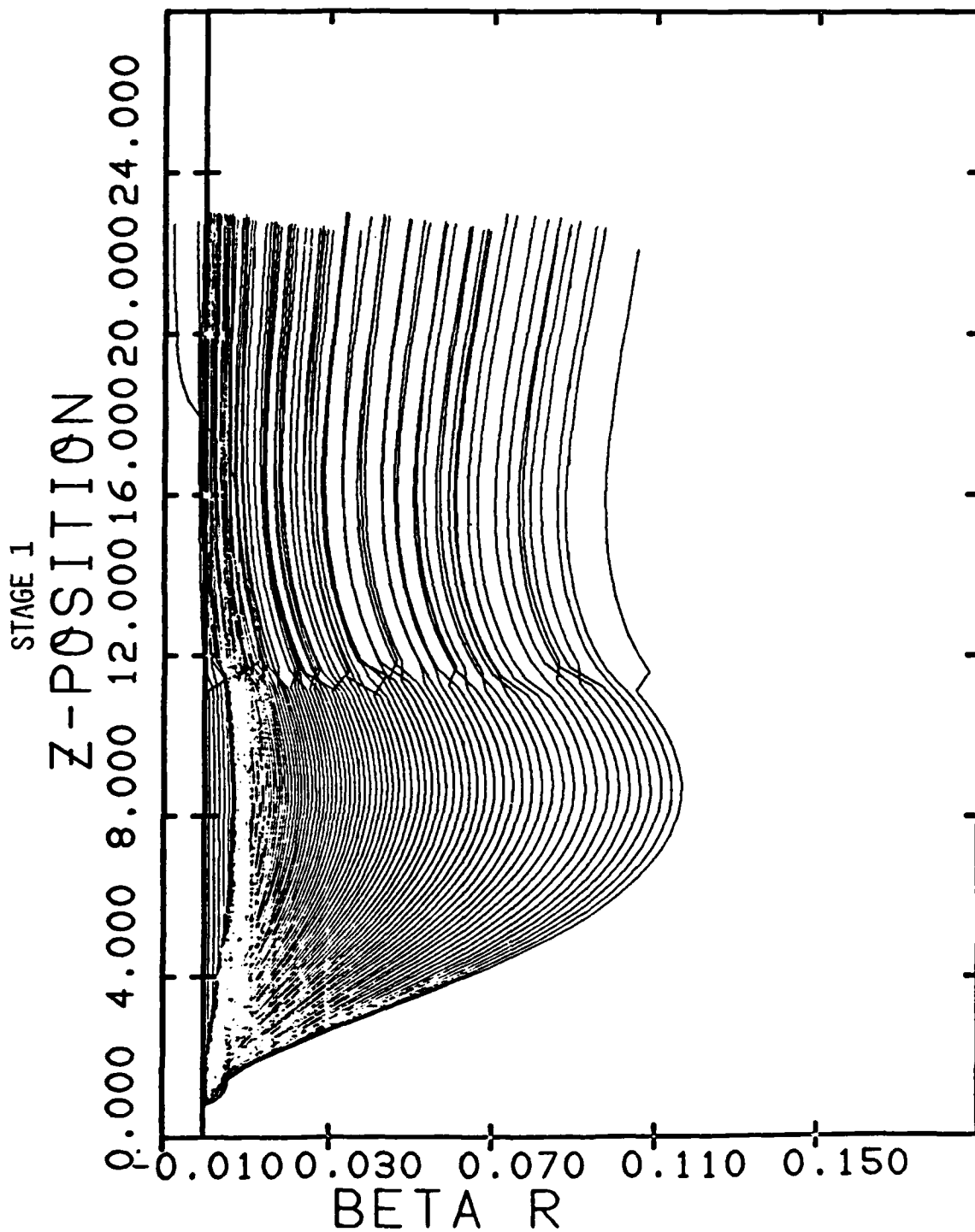


Figure 29. Stage 1 with Mesh Scattering $\theta_{\text{RMS}} = 0.28^\circ$

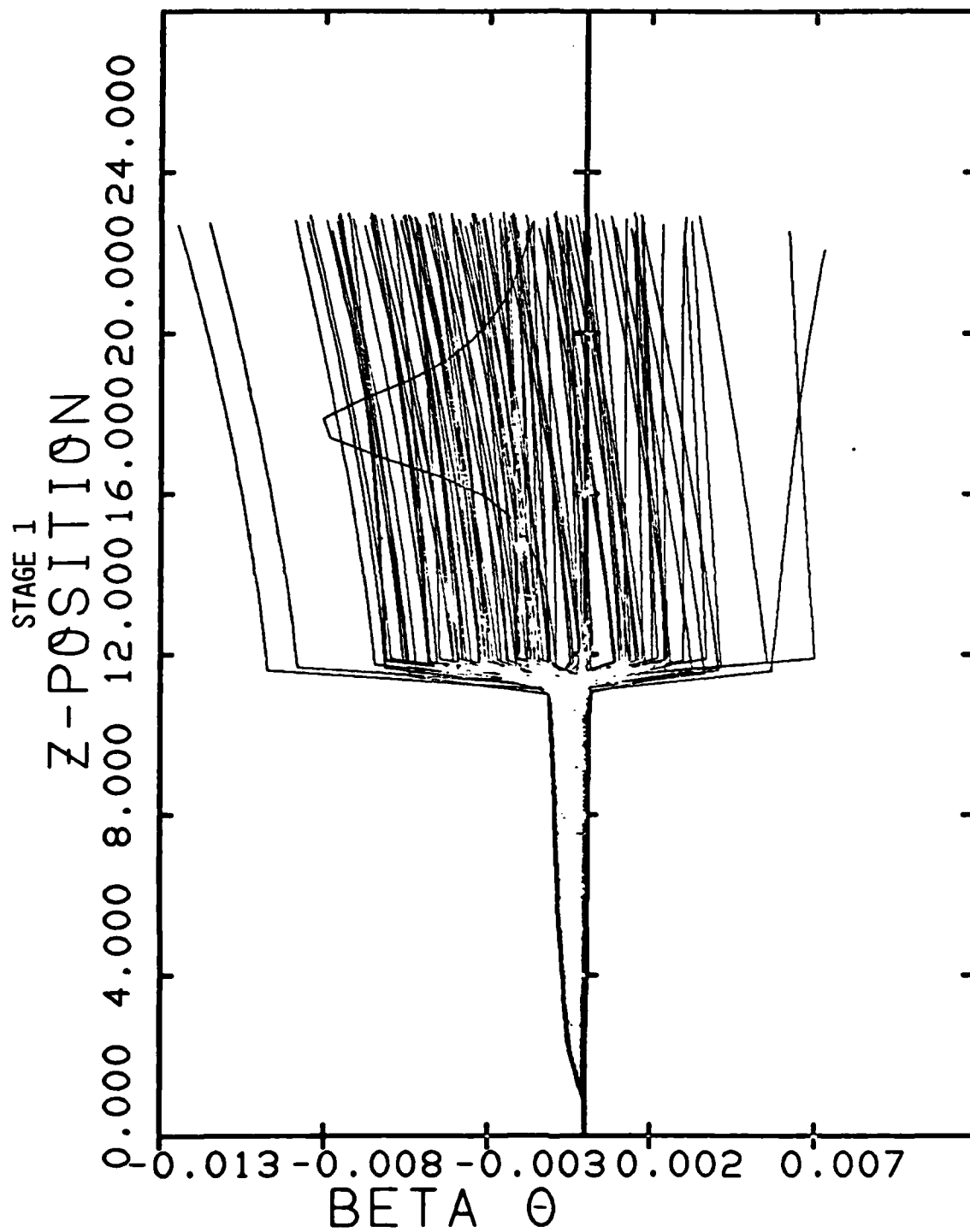


Figure 30. Stage 1 with Mesh Scattering $\theta_{\text{RMS}} = 0.28^\circ$

A P P E N D I X D

Letter from Dr. Barry N. Moore to Dr. C. W. Roberson,
dated June 29, 1982.

-- includes 25 figures

Austin Research Associates
1901 Rutland Drive-Austin, Texas 78758-Phone (512) 837-6623

June 29, 1982

Dr. C. W. Roberson
Plasma Physics Division, Code 4704
Naval Research Laboratory
4555 Overlook Avenue
Washington, D.C. 20375

Dear Chuck:

Enclosed is computer output from two more series of calculations of beam transport through the first four meters of the long pulse induction linac. I have numbered these figures and the following commentary is keyed to those numbers.

The first series of runs, in Figures 1-14, simulates transport of a cold cathode beam, with 1.4° of rms angular scattering introduced at the anode mesh to mock up the emittance generated at the hairbrush cathode face. Figure 1 shows the magnetic field profile which was used for these transport studies. Figure 2 shows the computed beam flow in the diode, using the experimental sub-Child-Langmuir potential grading. We find that 720 amperes of current is extracted, peaked slightly on axis as shown in Figure 3. The current density near the beam edge is about 85% of the central current density. Figure 4 shows the convergent beam flow through Stage 1, including the anode mesh scattering. Figure 5 shows the transport through Stage 2, and Figure 6 shows the beam focusing and injection into the first induction module in Stage 3. It may be seen that about 135 amperes or 19% of the beam current is lost to the walls just downstream of the first induction gap. In Figure 7, the beam transport through Stage 4 is shown, for a case where the second induction module has been turned off. The strong compression of the residual current by the 2 kG wiggler magnetic guide field is evident near the end of Stage 4. Figures 8 and 9 show the transverse velocity modulations of the beam particles in Stage 4, while Figure 10 shows the γ_z factors for the beam electrons in Stage 4. The strong cyclotron oscillations of the beam near the end of Stage 4, at the entrance of the wiggler solenoid, may be seen to extract energy from the directed

Dr. C. W. Roberson
Naval Research Laboratory
June 29, 1982
Page 2

z-motion and to convert it to \hat{r} , $\hat{\theta}$ motion. It appears that the rms beam radius, averaged over the cyclotron wave, is about $R \approx 1.2$ cm. The rms value of β_{\perp} , averaged over the cyclotron wave, appears to be $\beta_{\perp \text{ rms}} \approx 0.39$. Since $\gamma \approx 2$, the normalized emittance is about

$$\frac{\epsilon_n}{\pi} \approx \gamma R \beta_{\perp \text{ rms}} \approx 940 \text{ mrad-cm}$$

after the cyclotron wave phase mixes. The residual beam current for this case is 583 amperes. It may be noticed that there is a considerable spread in the γ_z values at the entrance to the wiggler, since the outer electrons have considerably more transverse cyclotron motion than the inner electrons do. The median value of γ_z appears to be about 1.61 at the entrance to the wiggler for this case.

In Figures 11-14, the Stage 4 transport was recomputed with the second induction gap turned on. The higher beam energy created may be seen to lengthen the cyclotron wavelength, as expected. In this case, it appears that $R \approx 1.3$ cm, $\beta_{\perp \text{ rms}} \approx 0.40$, $\gamma \approx 2.4$, $(\epsilon_n/\pi) \approx 1260$ mrad-cm and $\gamma_z\text{-median} \approx 1.76$.

In Figures 15-25, we have repeated a transport calculation for a high current, warm cathode beam. However, we applied the December 1981 scaling factors to the coil currents rather than to the fields themselves, yielding the magnetic field profile shown in Figure 15. The magnetic field goes slightly negative between 105 cm and 125 cm from the cathode, reaching perhaps -32G under the second focusing coil. This implies two weak magnetic cusps located at 105 cm and 125 cm.

Figure 16 shows the hot cathode beam formation in Stage 1; it was assumed that 858A were emitted. The experimental sub-Child-Langmuir potential grading was used, with uniform current density profile. Figure 17 shows the beam transport in Stage 2, through the first magnetic cusp at $z = 105$ cm. As the beam approaches the magnetic cusp, its radius increases somewhat, but its azimuthal velocity

Dr. C. W. Roberson
Naval Research Laboratory
June 29, 1982
Page 3

returns to zero and goes slightly negative as shown in Figure 18. The azimuthal velocity is low near the cusp, since the beam was born in a weak field region. Because of the large beam radius acquired in Stage 2, the beam cannot be sufficiently compressed in Stage 3 to avoid the loss of significant current at the entrance to the first induction module. In Figure 19 it may be seen that 600A or 70% of the beam current is lost, and only 258A or 30% of the current is injected through the induction module. Figure 20 shows the electron γ_z factors in Stage 3; the loss of the outer, transversely excited electrons, and the acceleration of the central core of the beam is apparent. Figure 21 shows the transport of this residual beam current through Stage 4, and the beam compression at the entrance to the wiggler solenoid. Figures 22 and 23 show the transverse beam velocity components in Stage 4, while Figures 24 and 25 show β_z and γ_z in Stage 4. In this case, the cyclotron wave amplitude is much less than before, but there is still an appreciable spread in γ_z due to the cyclotron motion. From Figures 21-25, we estimate

$$R \approx 0.6 \text{ cm}$$

$$\beta_{\perp \text{ rms}} \approx 0.21$$

$$\frac{\epsilon_n}{\pi} \approx 310 \text{ mrad-cm}$$

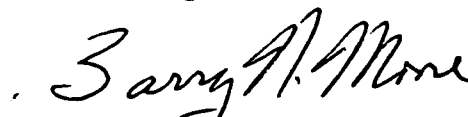
$$\gamma_{z\text{-median}} \approx 2.2 \quad .$$

Of course, the transmitted current of 258A is much lower for this case than for the cold cathode case discussed earlier.

Dr. C. W. Roberson
Naval Research Laboratory
June 29, 1982
Page 4

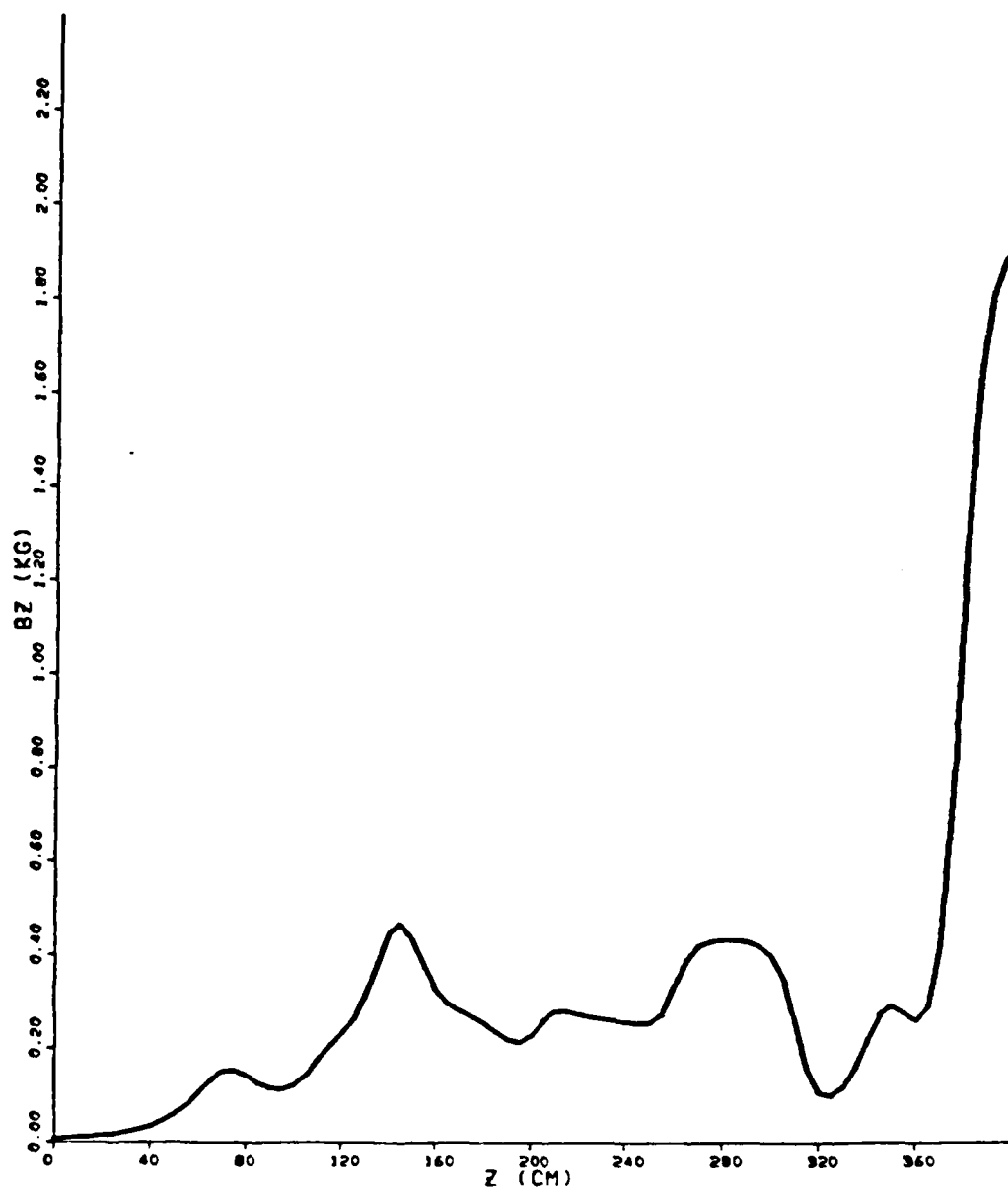
We are proceeding with envelope equation studies and with studies of emittance generation by the cold, hairbrush cathodes. Of course, it should be recognized that the envelope equations will be of limited usefulness, since they cannot represent the effects of radial gradients, such as in $\gamma(r)$. We will keep you informed of our progress.

Sincerely,


Barry N. Moore

BNM:kft

Enclosures: As noted above.



BZ VS Z

Figure 1. Magnetic Field Profile from Feb. 1982 Data

7-MAY-82
11:17:59

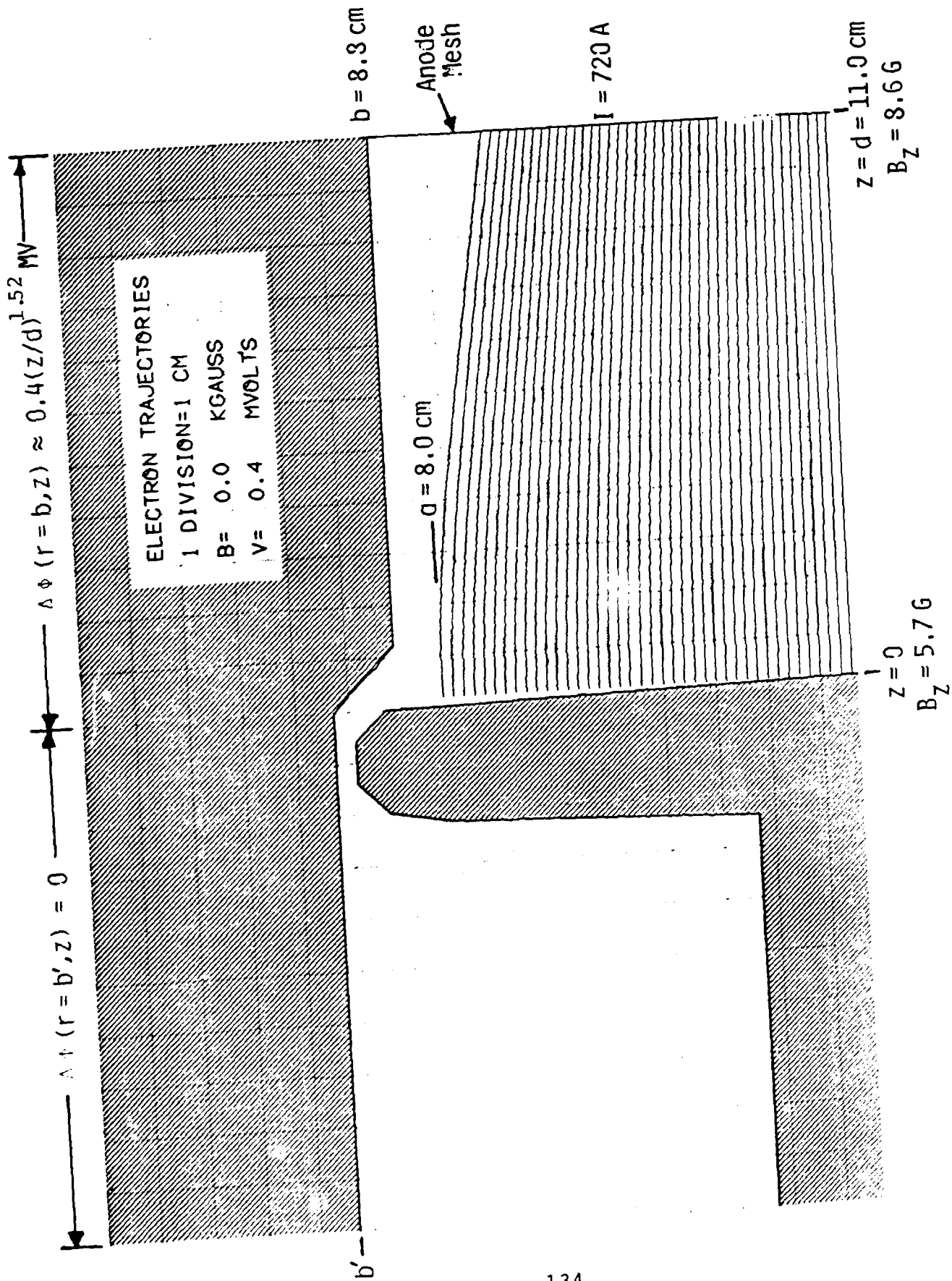
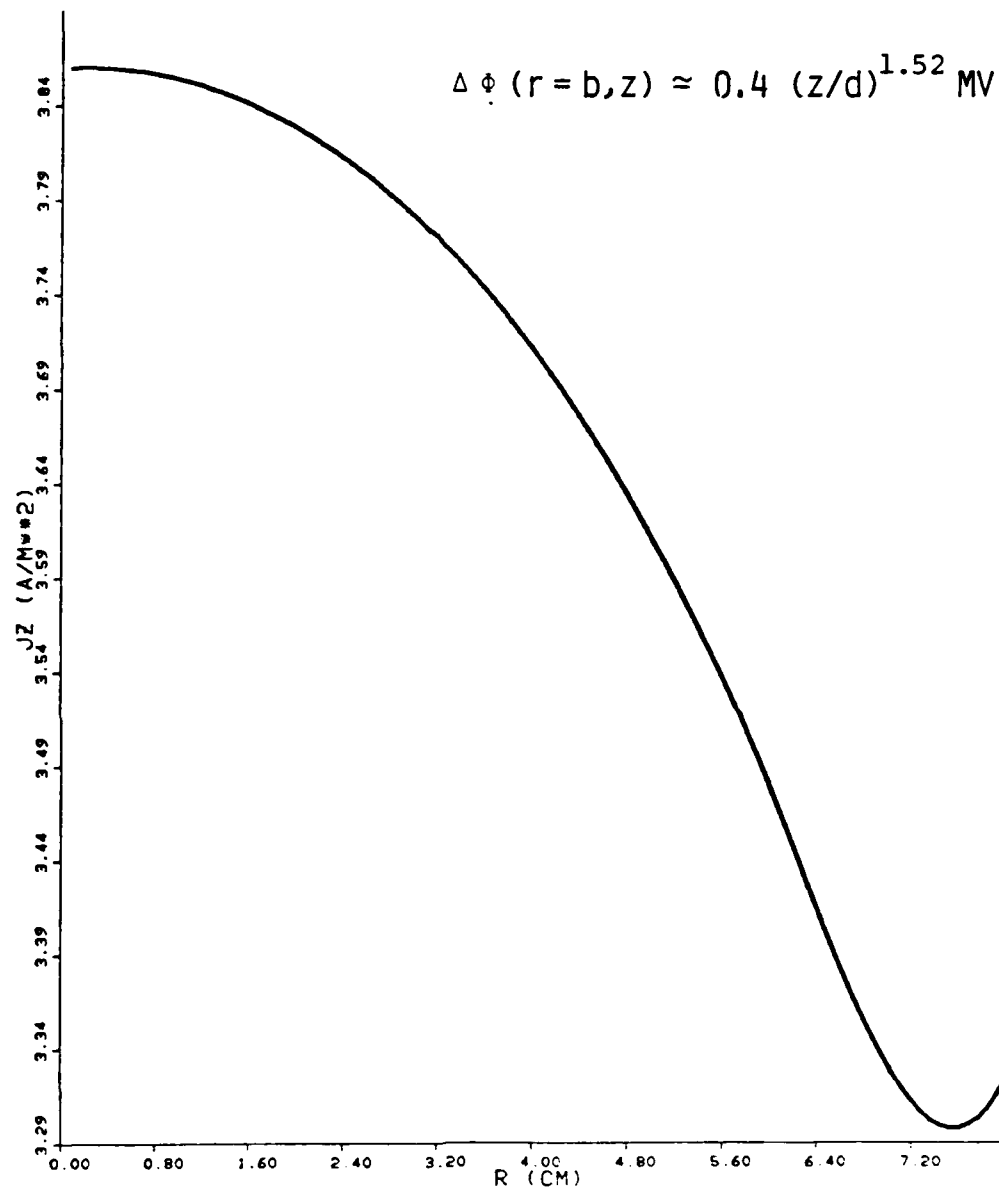


Figure 2. Cold Cathode with Sub-Child-Langmuir Potential Grading



JZ VS R

Figure 3. Current Density Profile @ Cathode for Sub-Child-Langmuir Potential Grading (Modified Design)

13-MAY-82

06:42:45

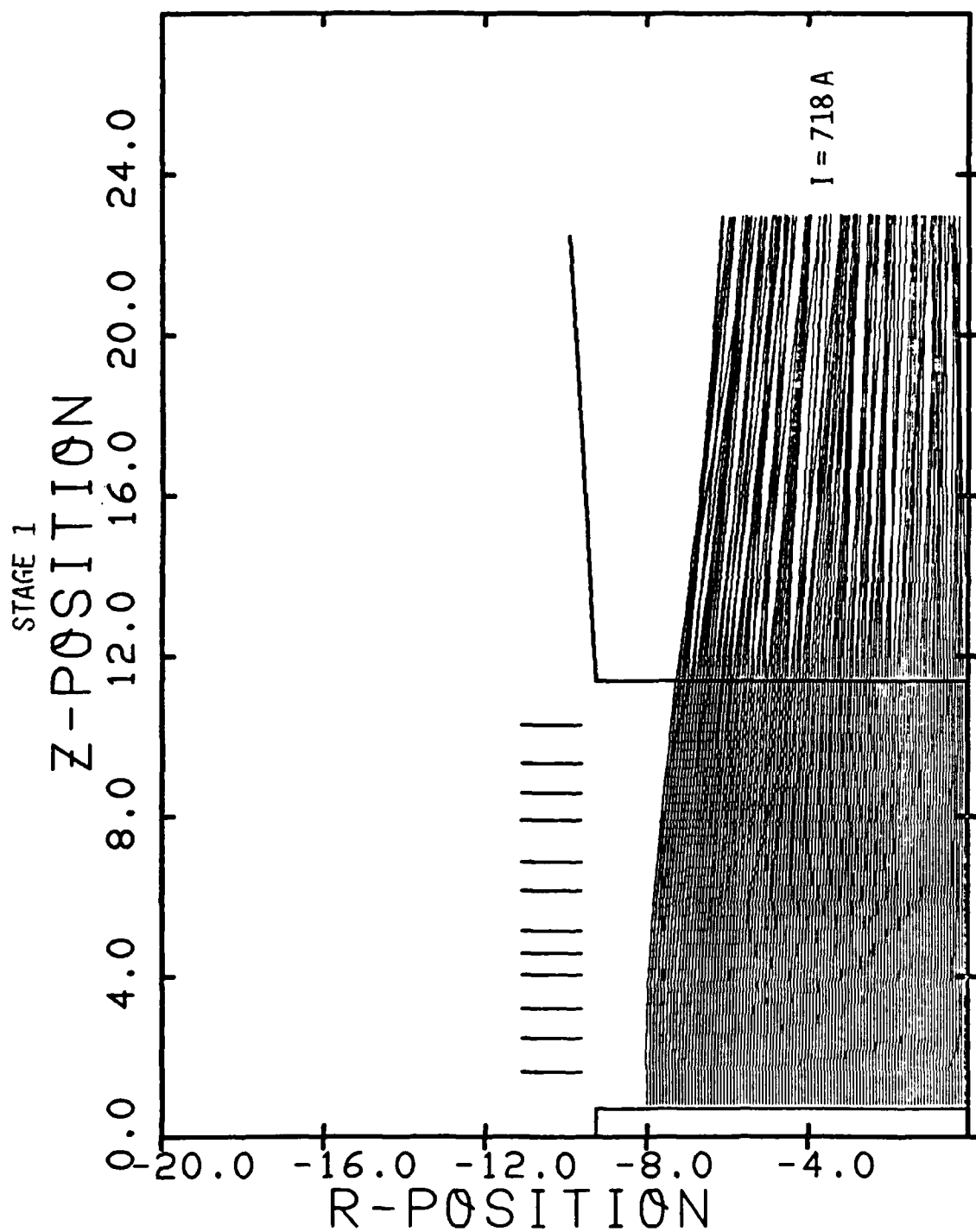


Figure 4. Cold Cathode Beam Formation in Stage 1, with Sub-Child-Langmuir Potential Grading (Modified Design) and Anode Mesh Scattering of $\theta_{\text{RMS}} = 1.4^\circ$

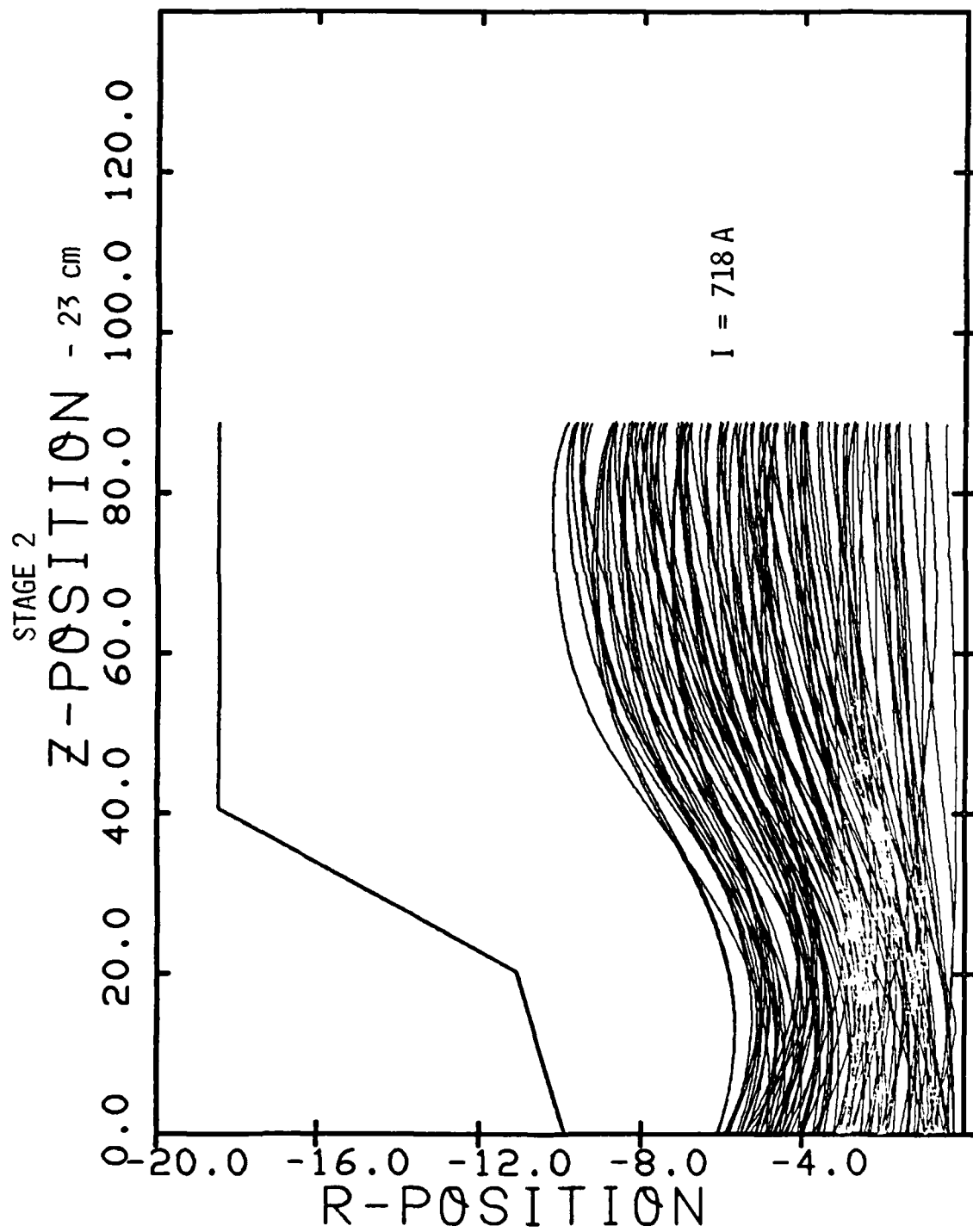


Figure 5. Scattered Beam Flow in Stage 2

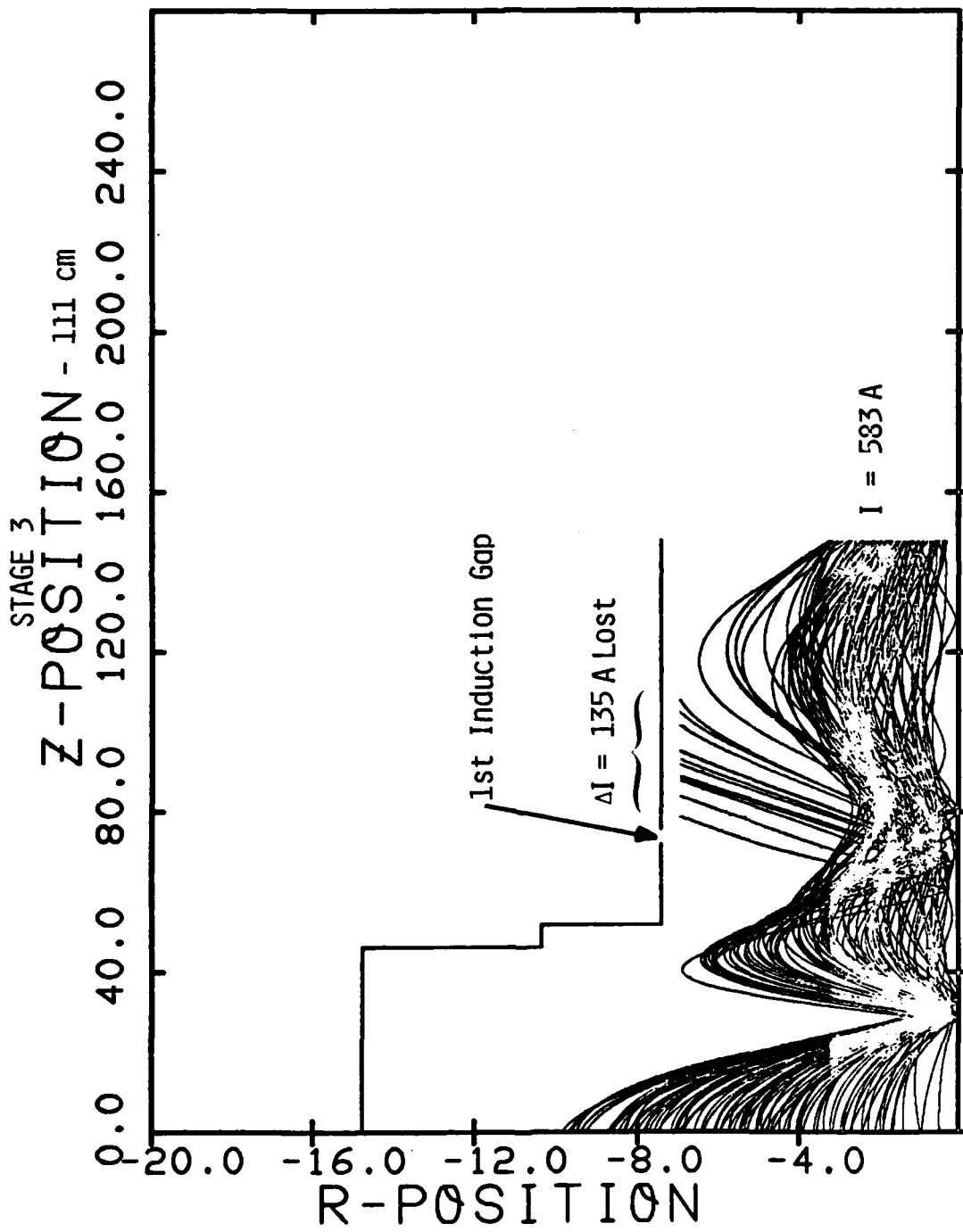


Figure 6. Scattered Beam Flow with Current Loss in Stage 3

STAGE 4

Z-POSITION - 258 cm
0.0 40.0 80.0 120.0 160.0 200.0 240.0

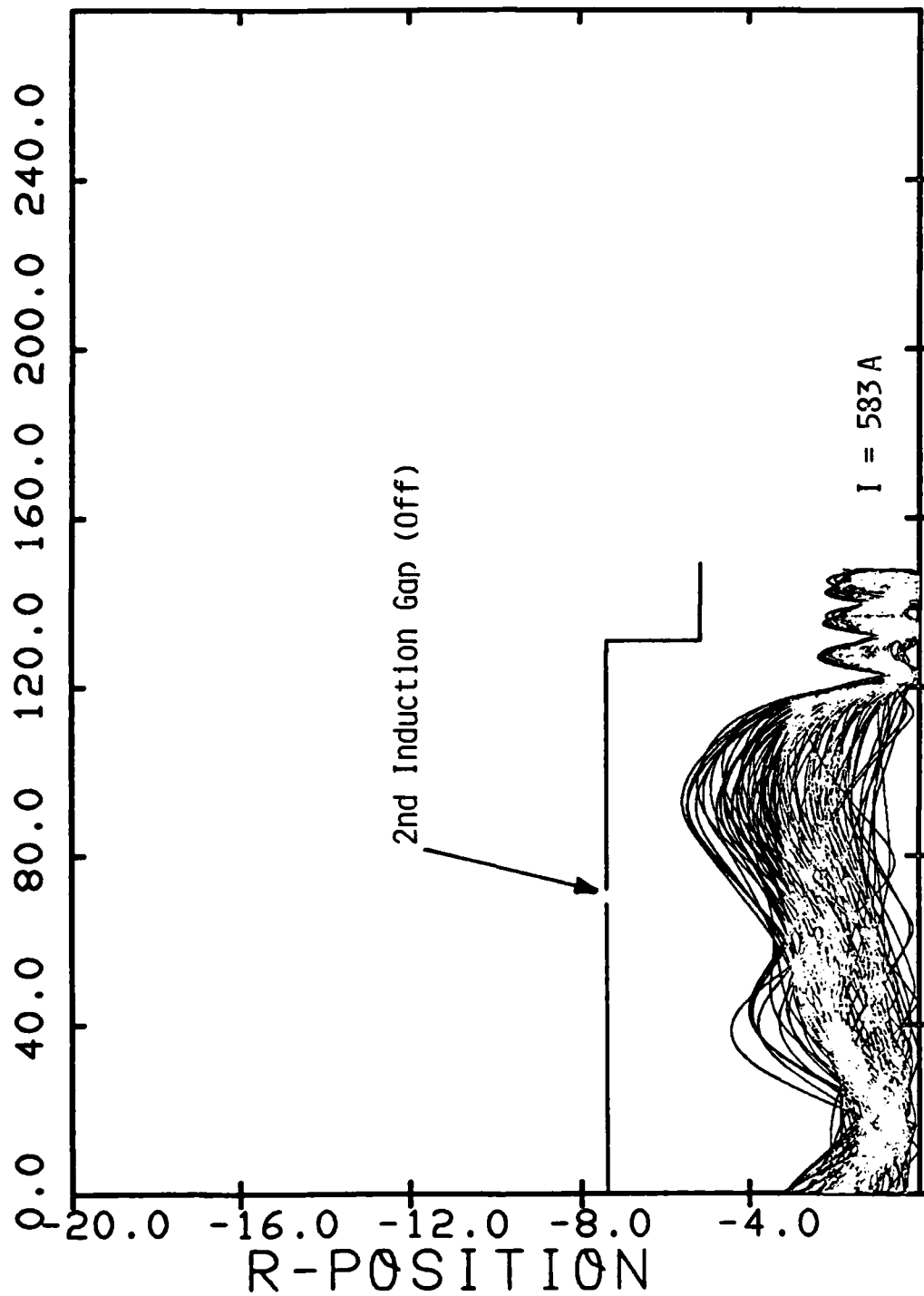


Figure 7. Transmission of Residual Scattered Current Thru Stage 4 Compression

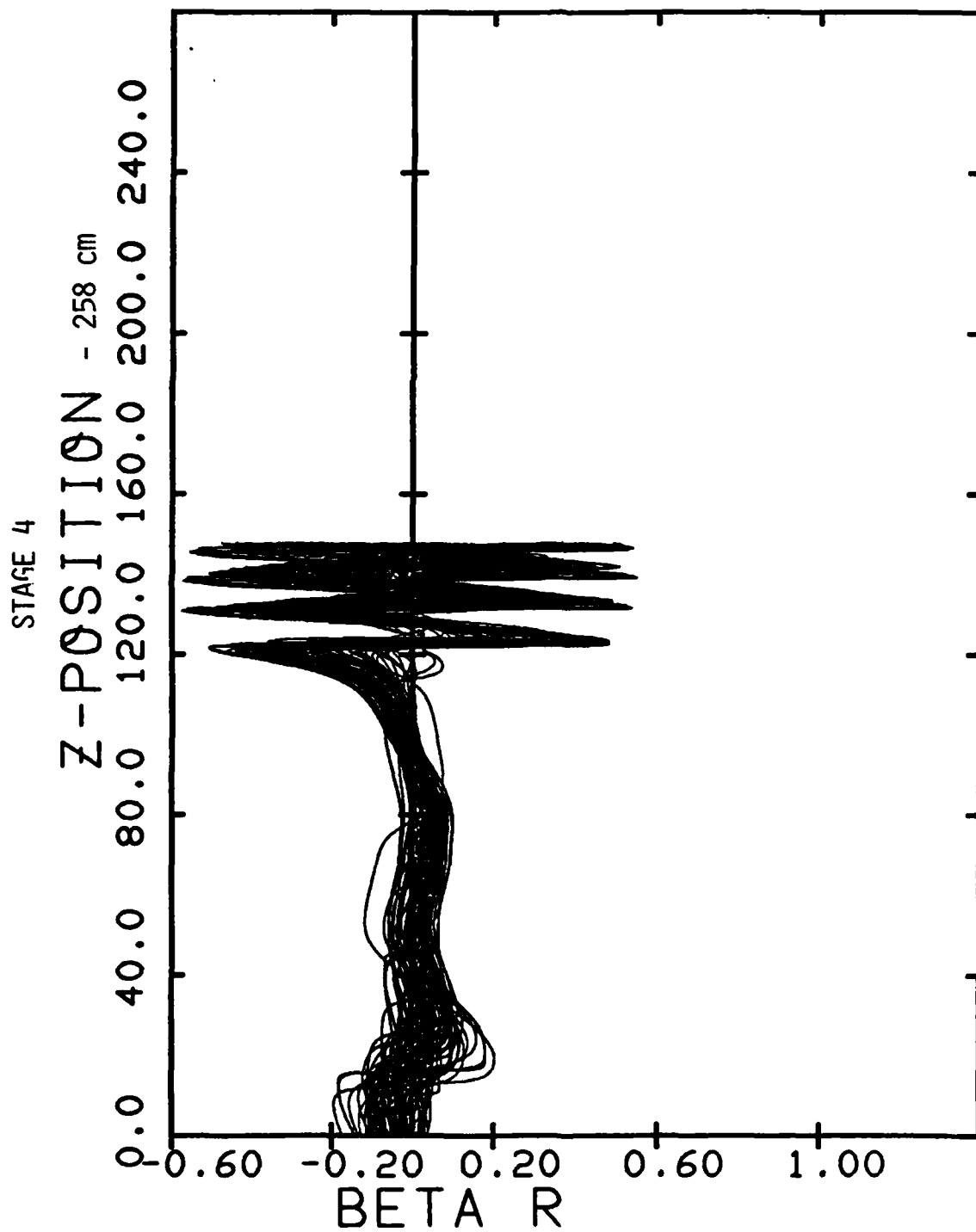


Figure 8. Compression of Scattered Beam Flow in Stage 4 with 2nd Induction Gap Off

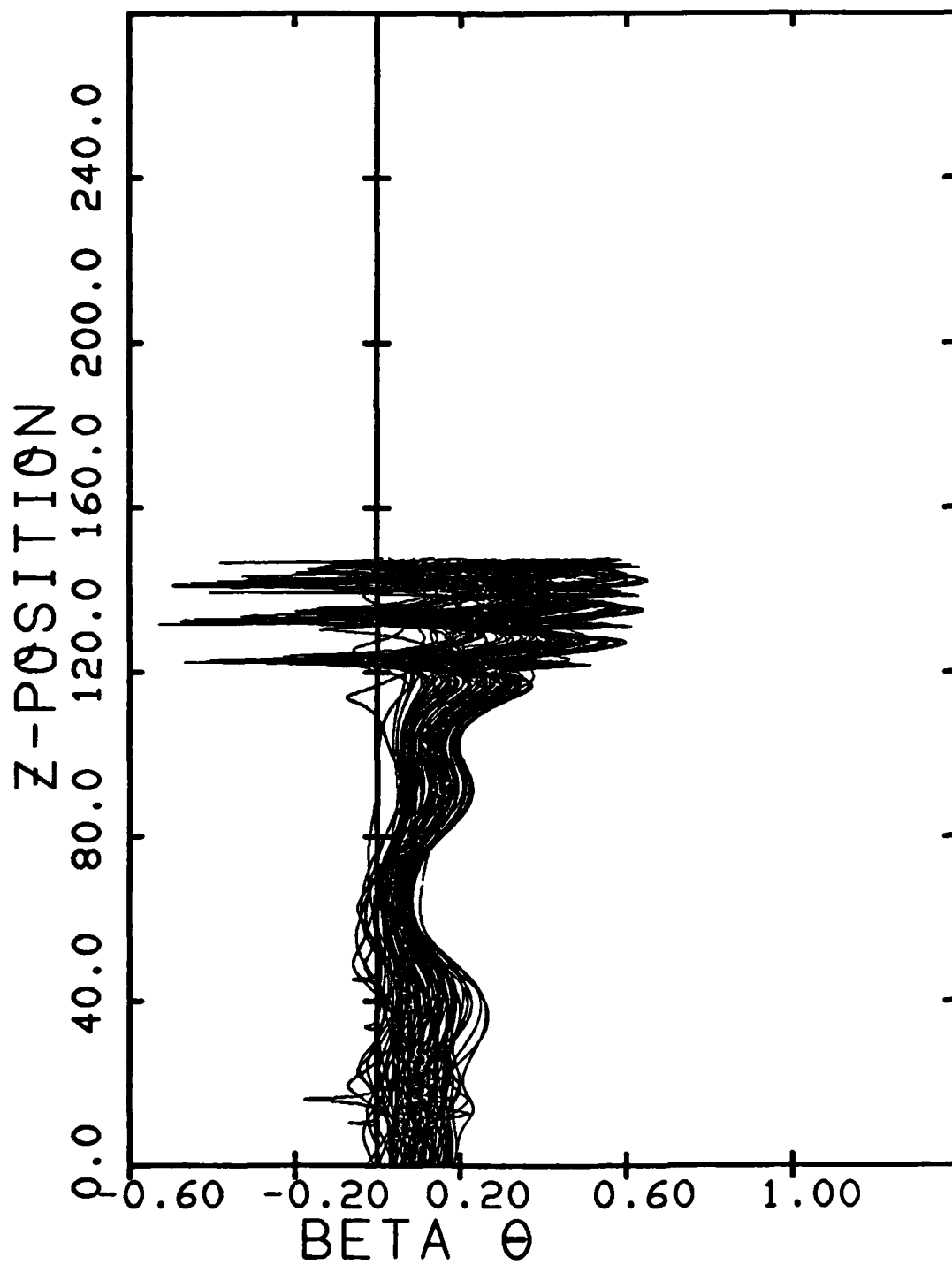


Figure 9. Compression of Scattered Beam Flow in Stage 4
with 2nd Induction Gap Off

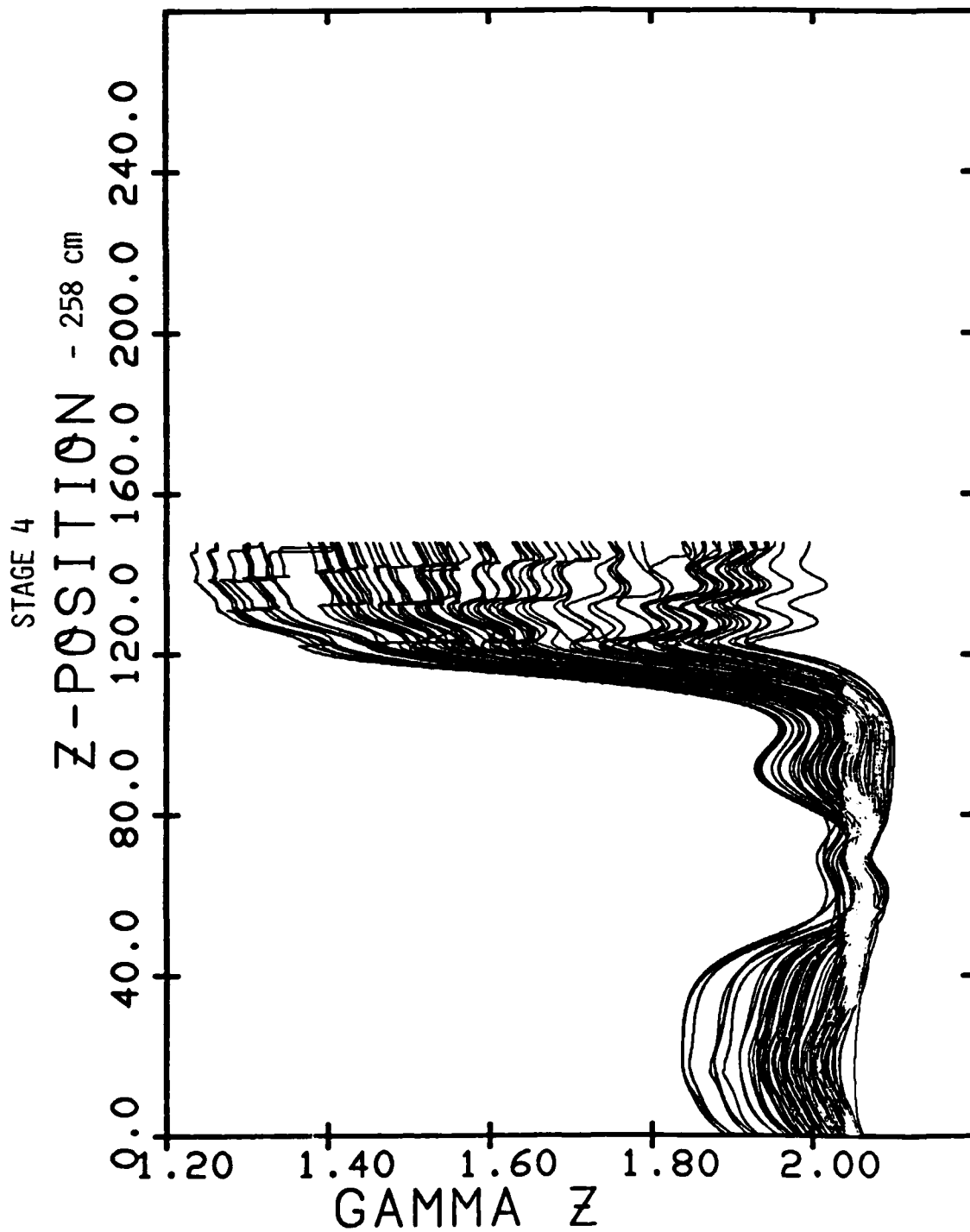


Figure 10. Compression of Scattered Beam Flow in Stage 4 with 2nd Induction Gap Off

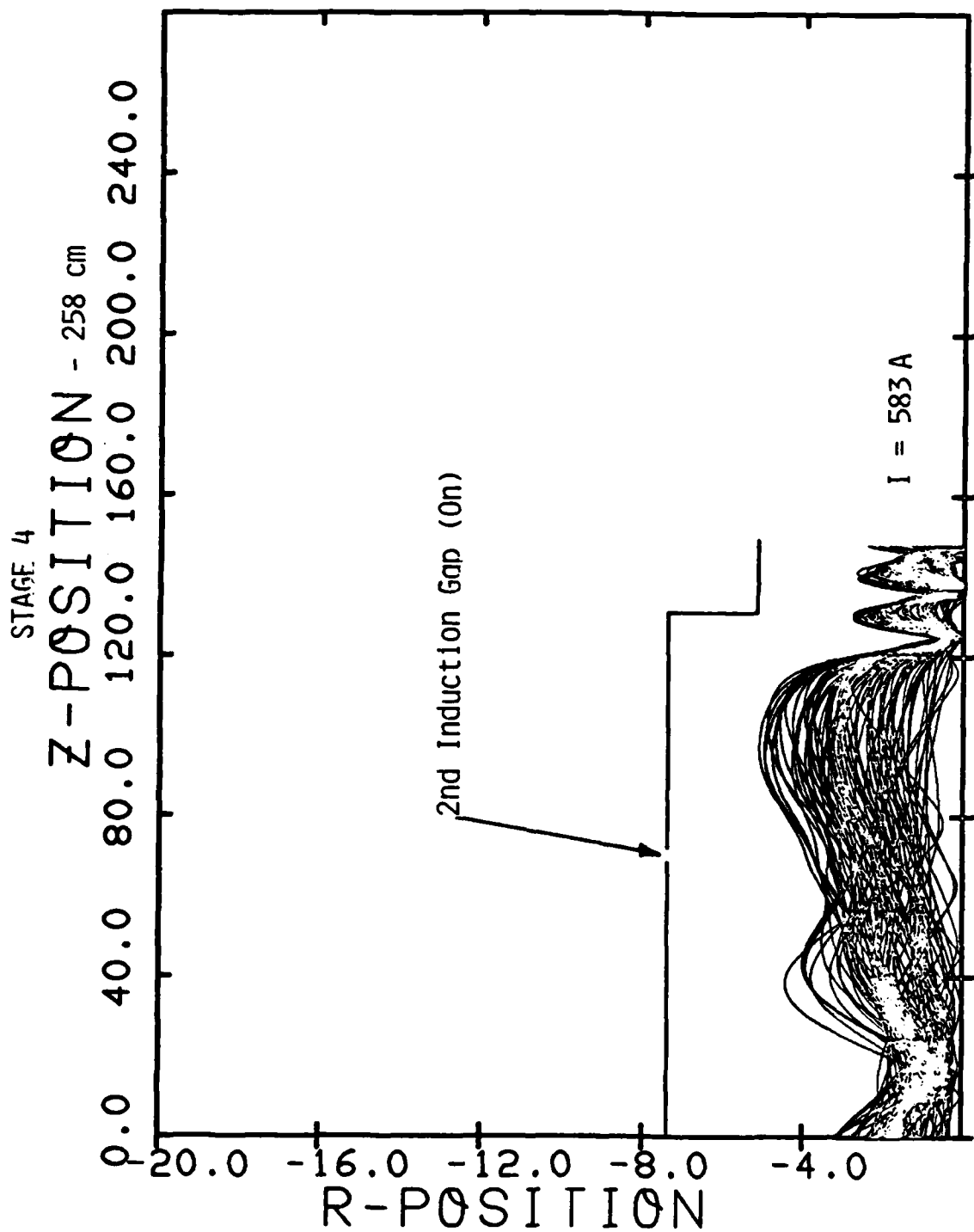


Figure 11. Transmission of Residual Scattered Current Thru Stage 4 Compression

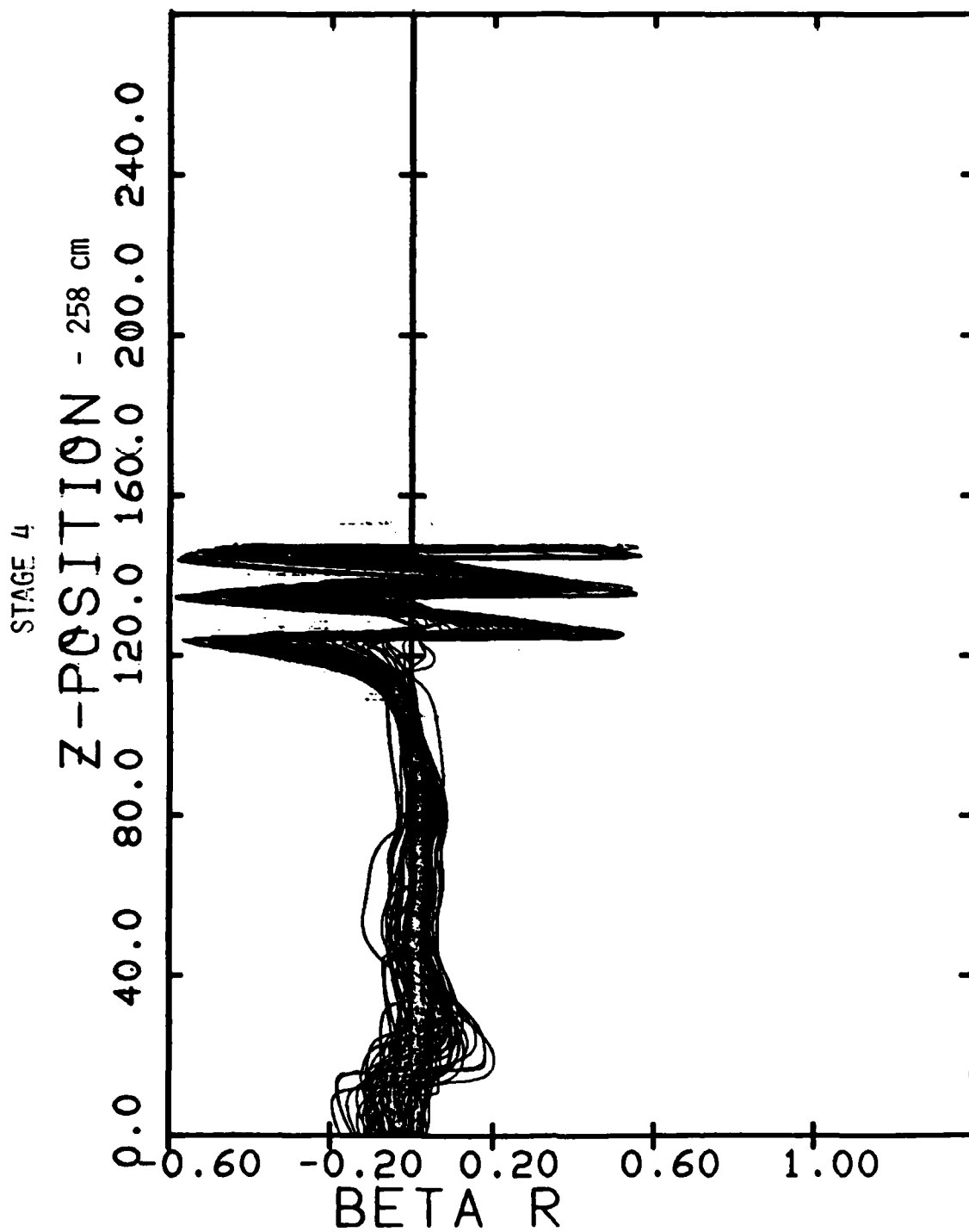


Figure 12. Compression of Scattered Beam Flow in Stage 4 with 2nd Induction Gap On

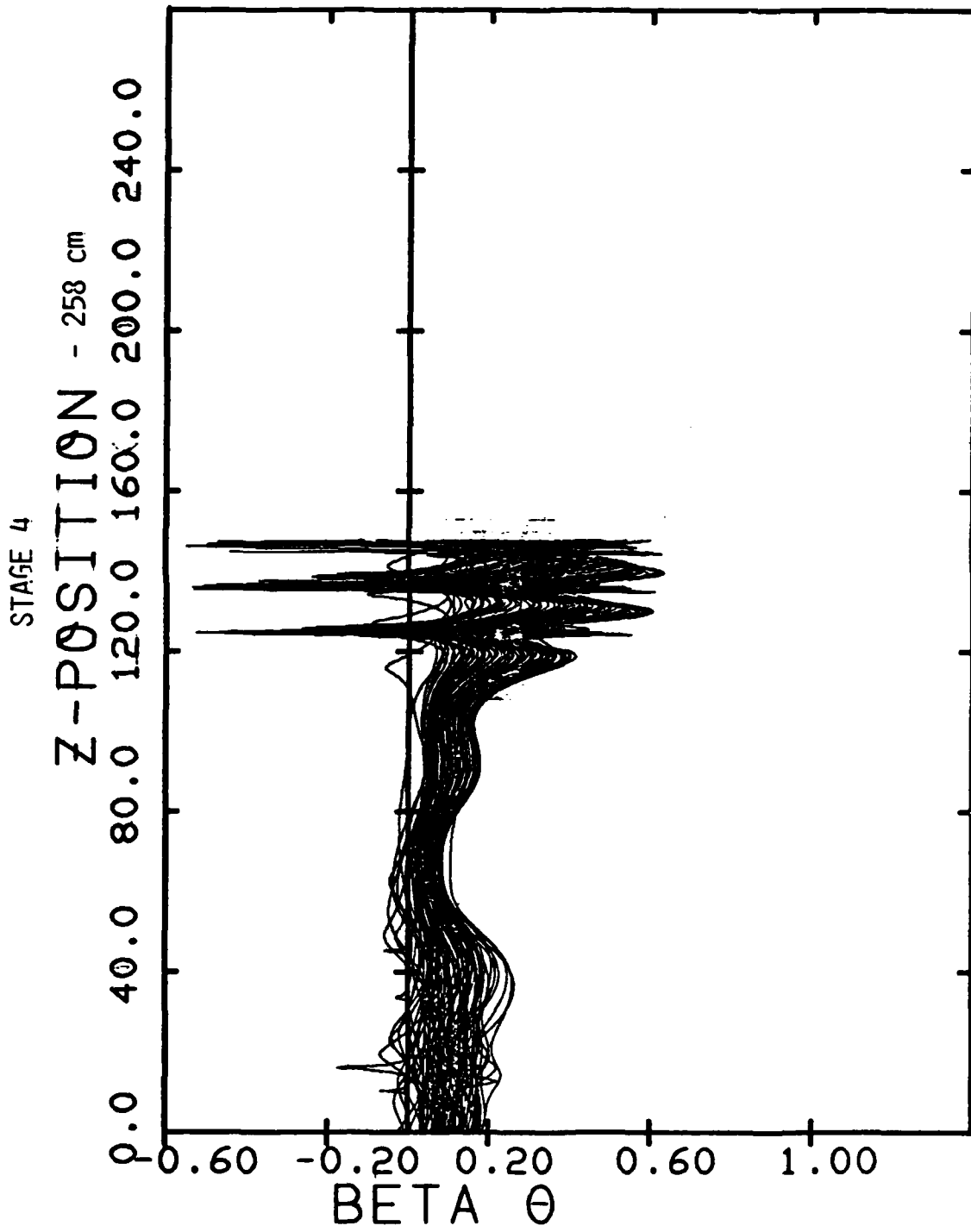


Figure 13. Compression of Scattered Beam Flow in Stage 4 with 2nd Induction Gap On

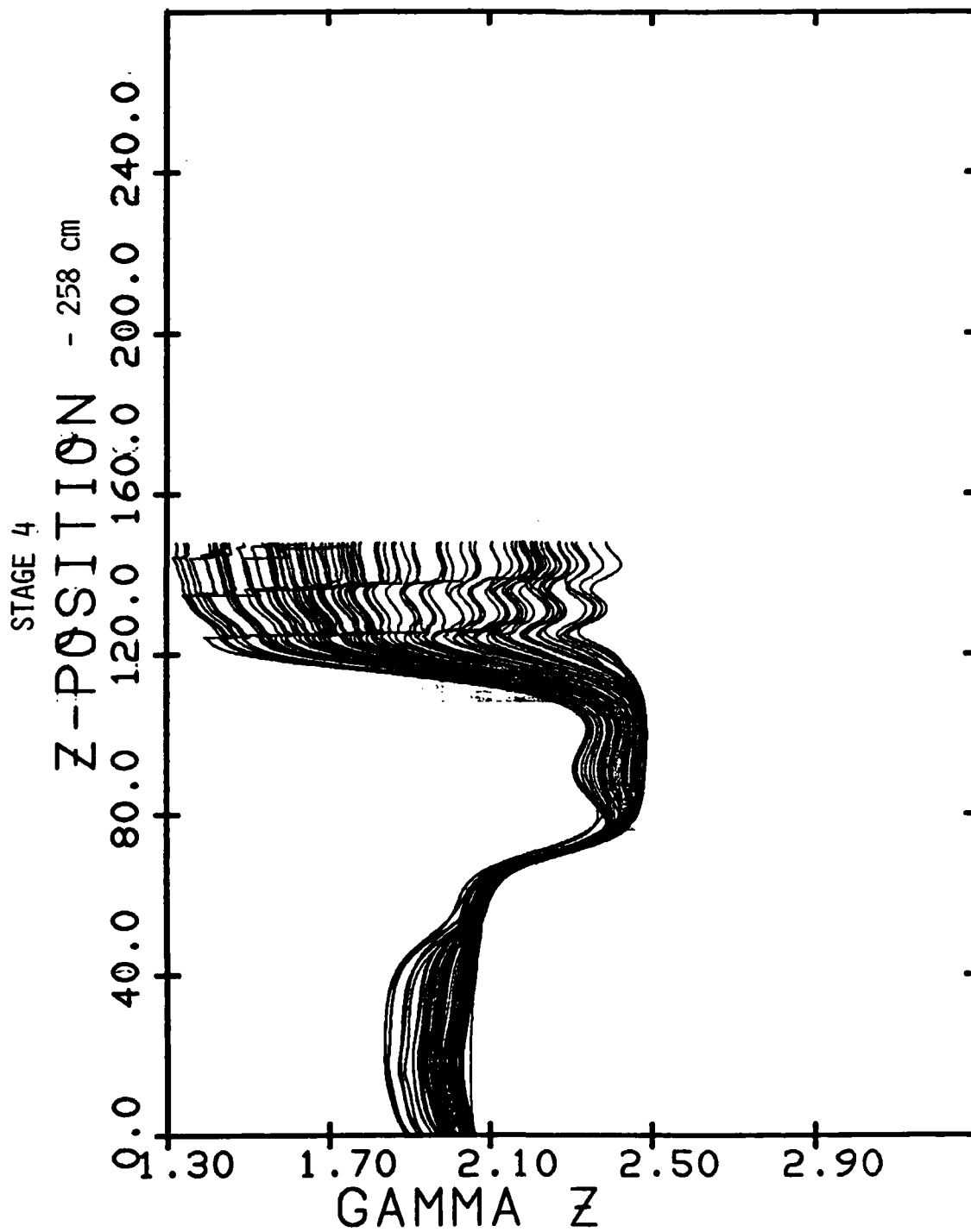
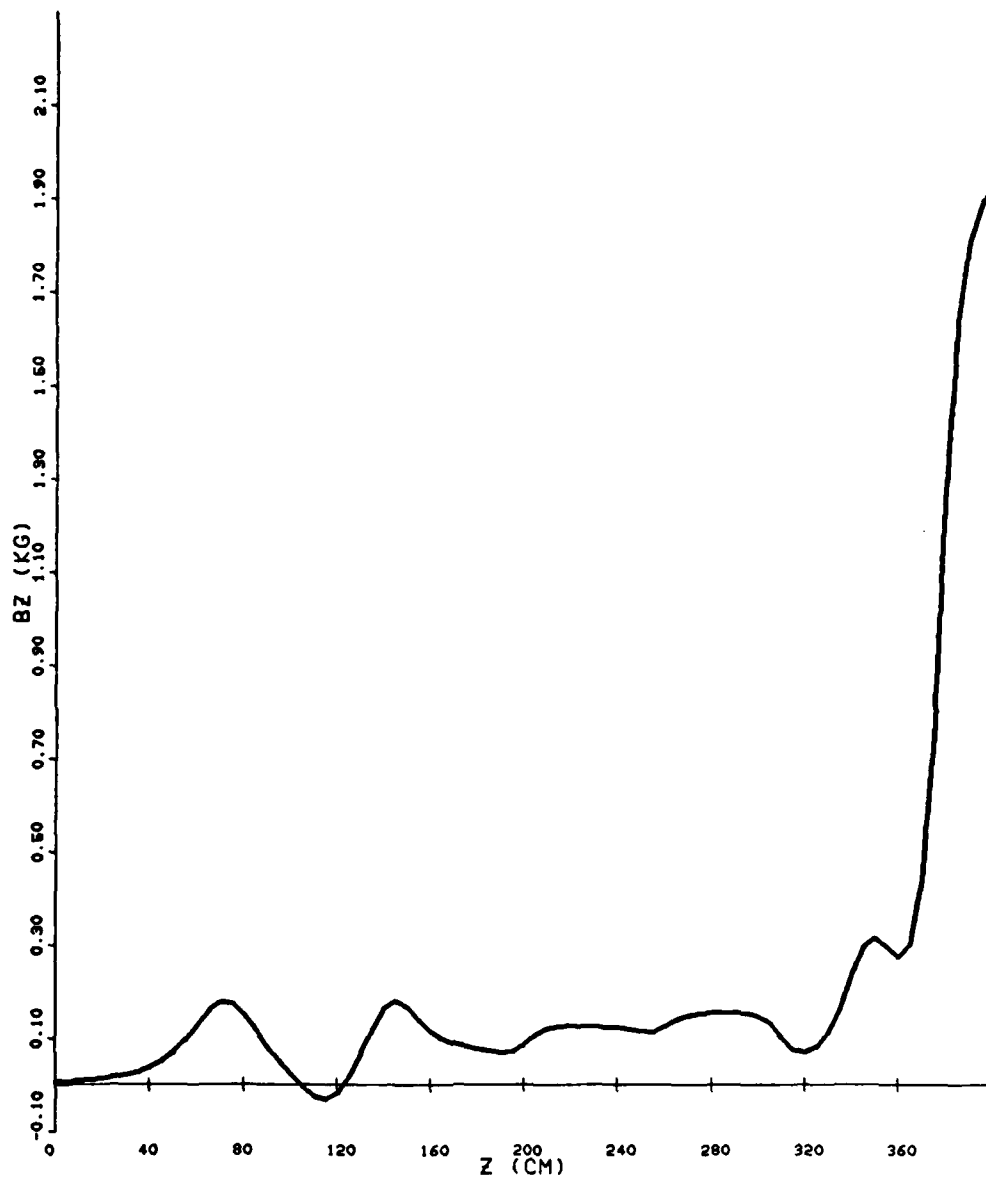


Figure 14. Compression of Scattered Beam Flow in Stage 4 with 2nd Induction Gap On



BZ VS Z

Figure 15. Magnetic Field Profile from Dec. 1981 Data
with Scaled Coil Currents

11-JUN-82
14:34:58

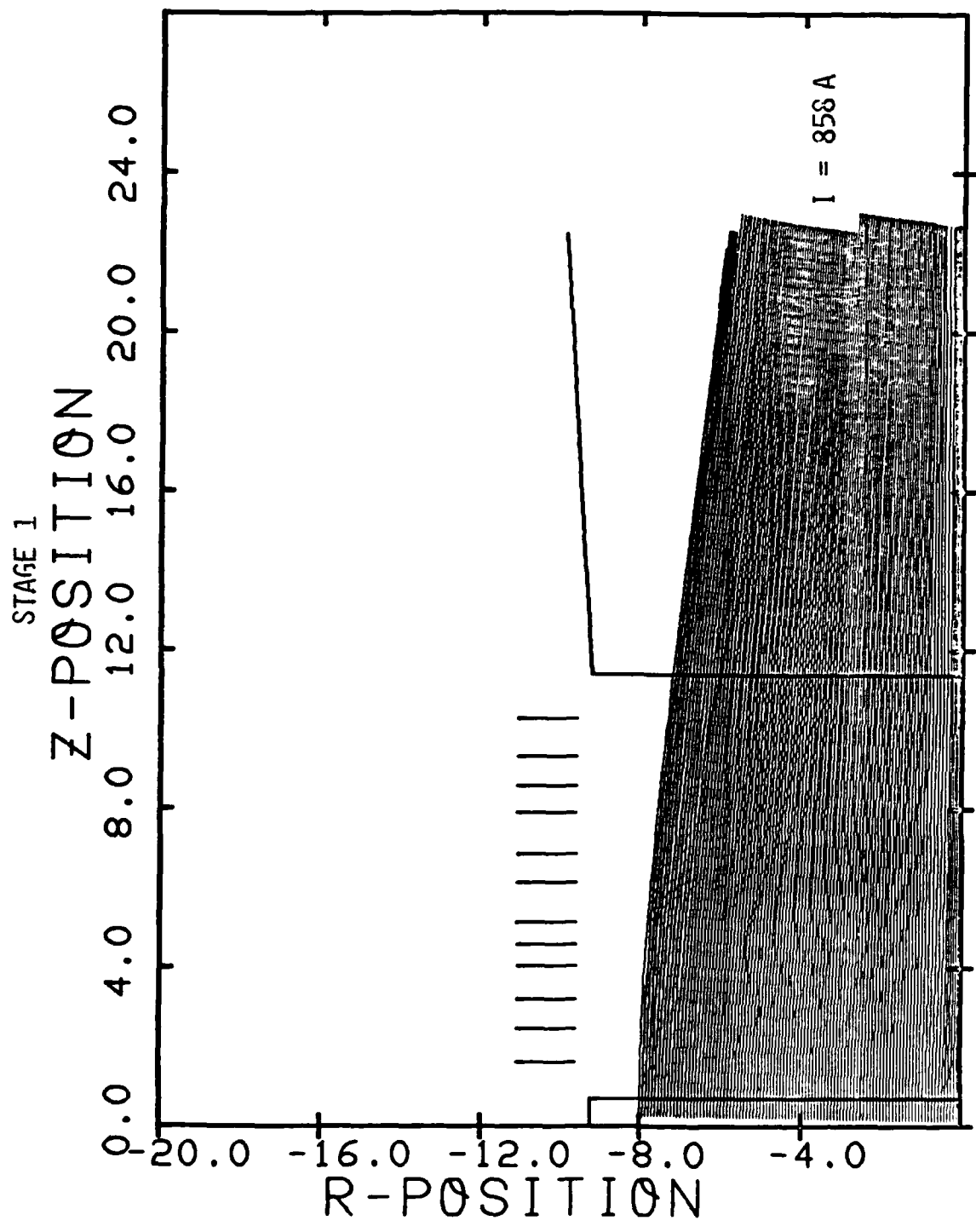


Figure 16. Hot Cathode Beam Formation in Stage 1, with Sub-Child-Langmuir Potential Grading (Modified Design), and Uniform Current Density Profile

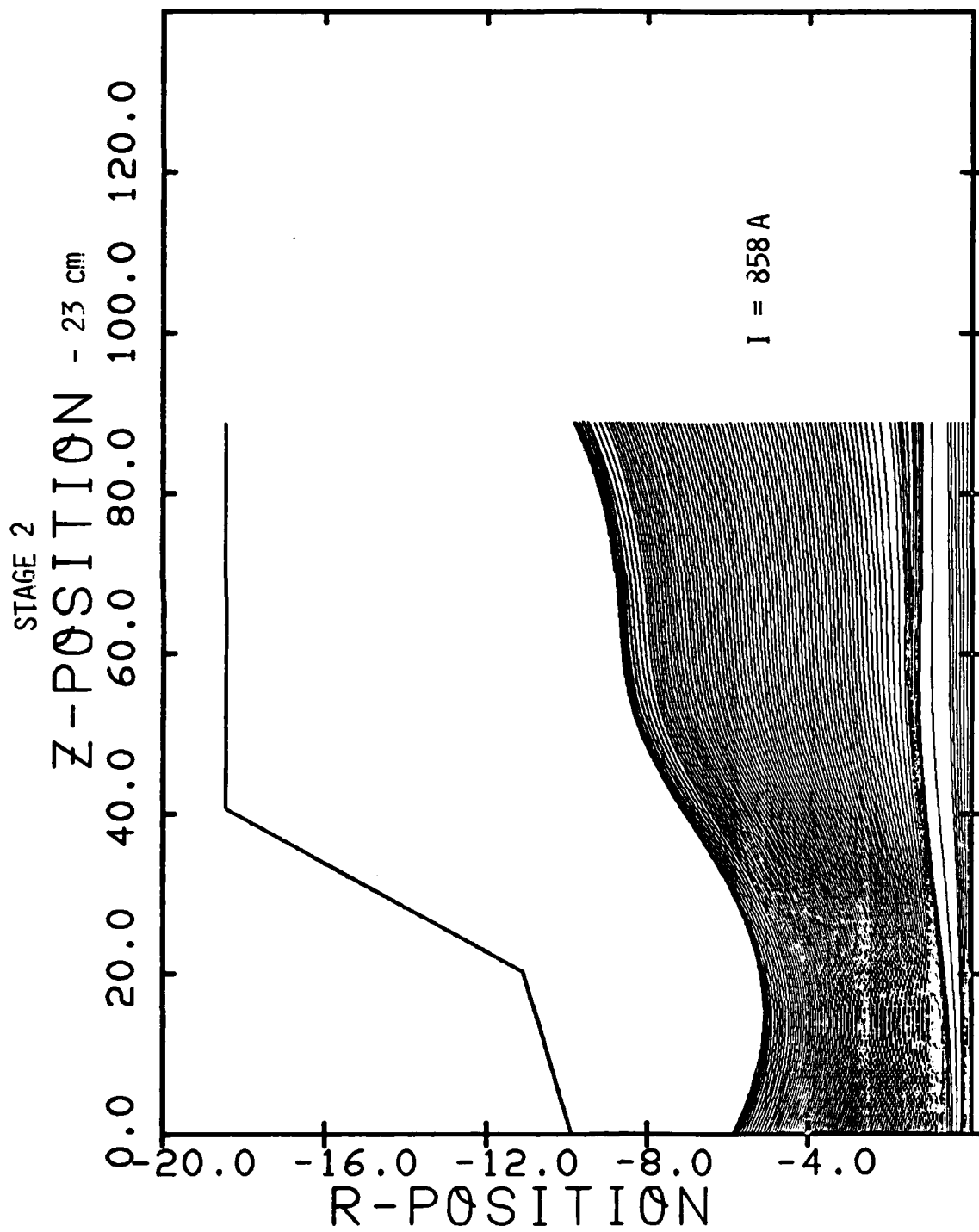


Figure 17. Laminar Beam Flow in Stage 2, Passing Through a Weak Magnetic Cusp

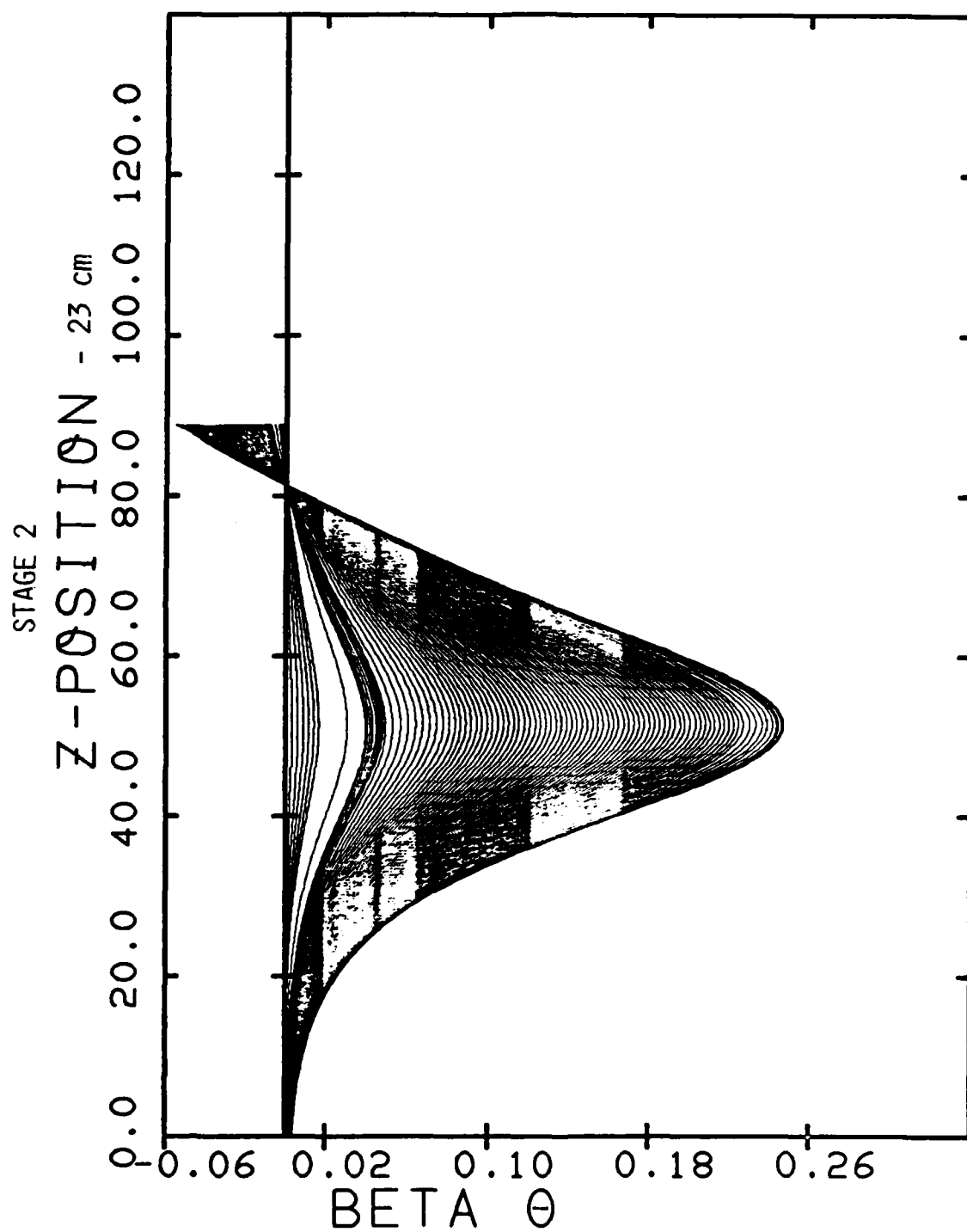


Figure 18. Laminar Beam Rotational Velocity in Stage 2, as
Beam Passes Through a Weak Magnetic Cusp

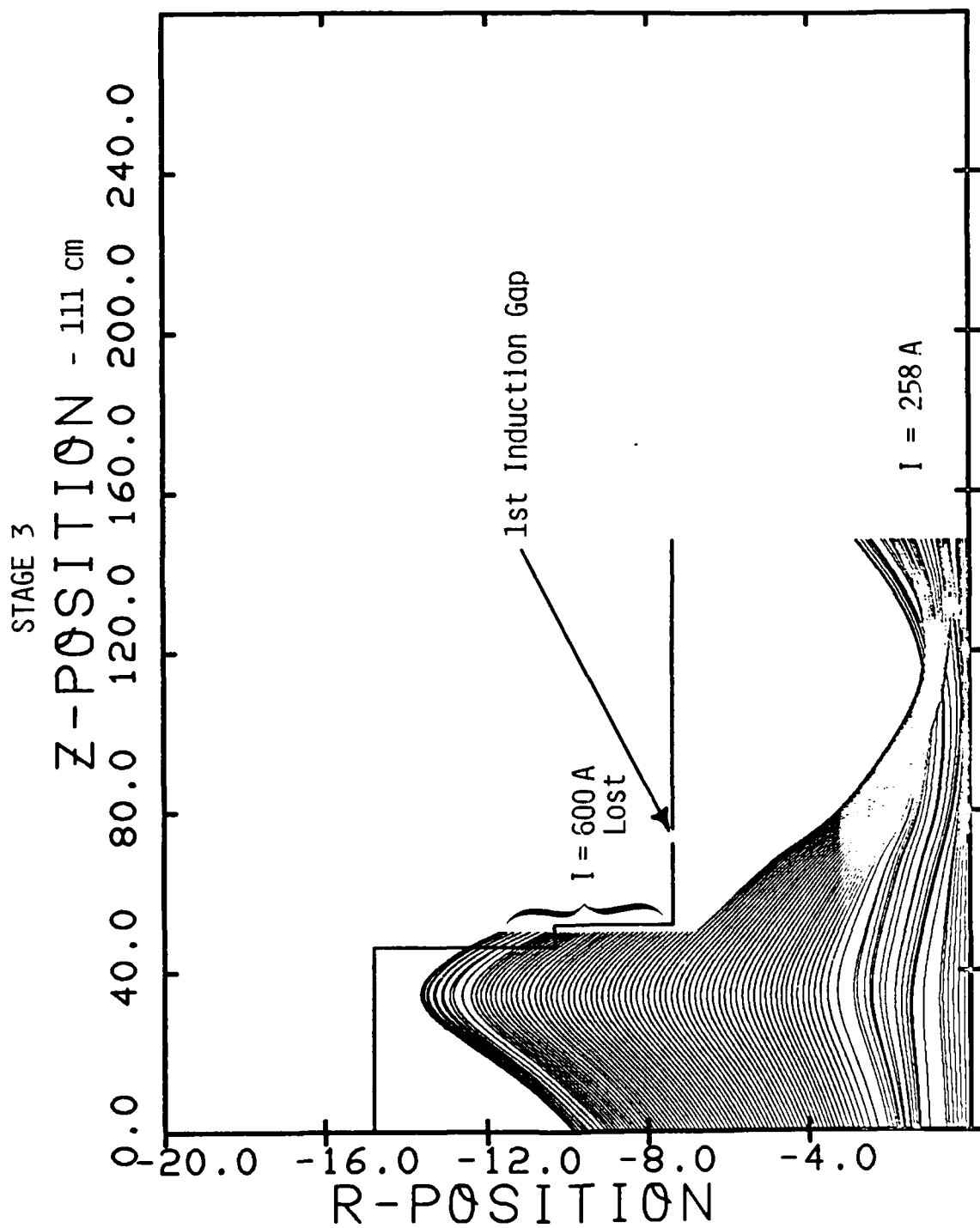


Figure 19. Hot Cathode, Laminar Beam Flow with Current Loss in Stage 3

STAGE 3

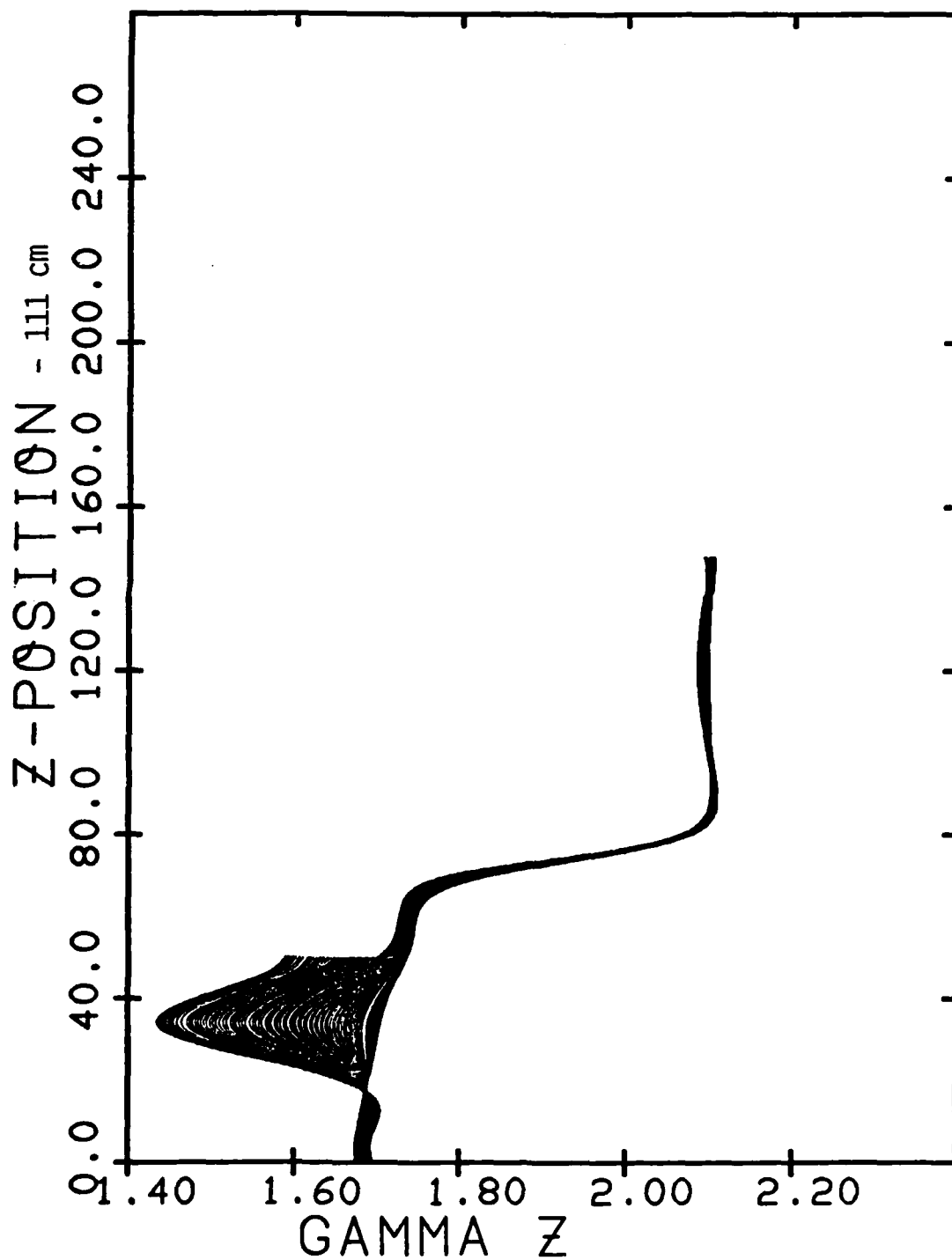


Figure 20. Axial Energy Variation as Laminar Beam is Injected into Induction Module, with Current Loss at Entrance, and Subsequently Accelerated

STAGE 4

Z-POSITION - 258 cm
0.0 40.0 80.0 120.0 160.0 200.0 240.0

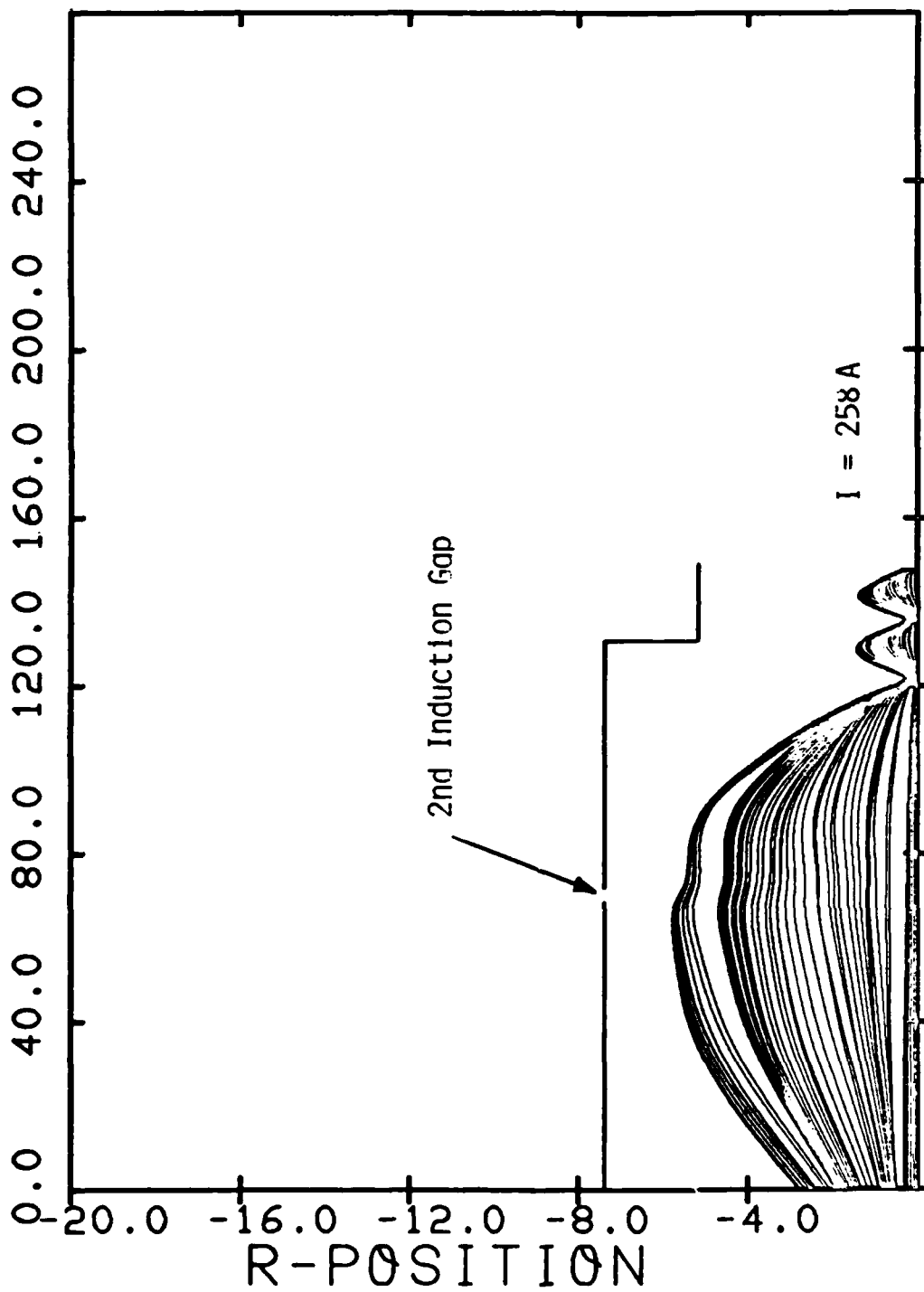


Figure 21. Transmission of Residual Beam Flow Through
Stage 4, with Strong Magnetic Compression

STAGE 4

Z-POSITION - 258 cm

0.0 40.0 80.0 120.0 160.0 200.0 240.0

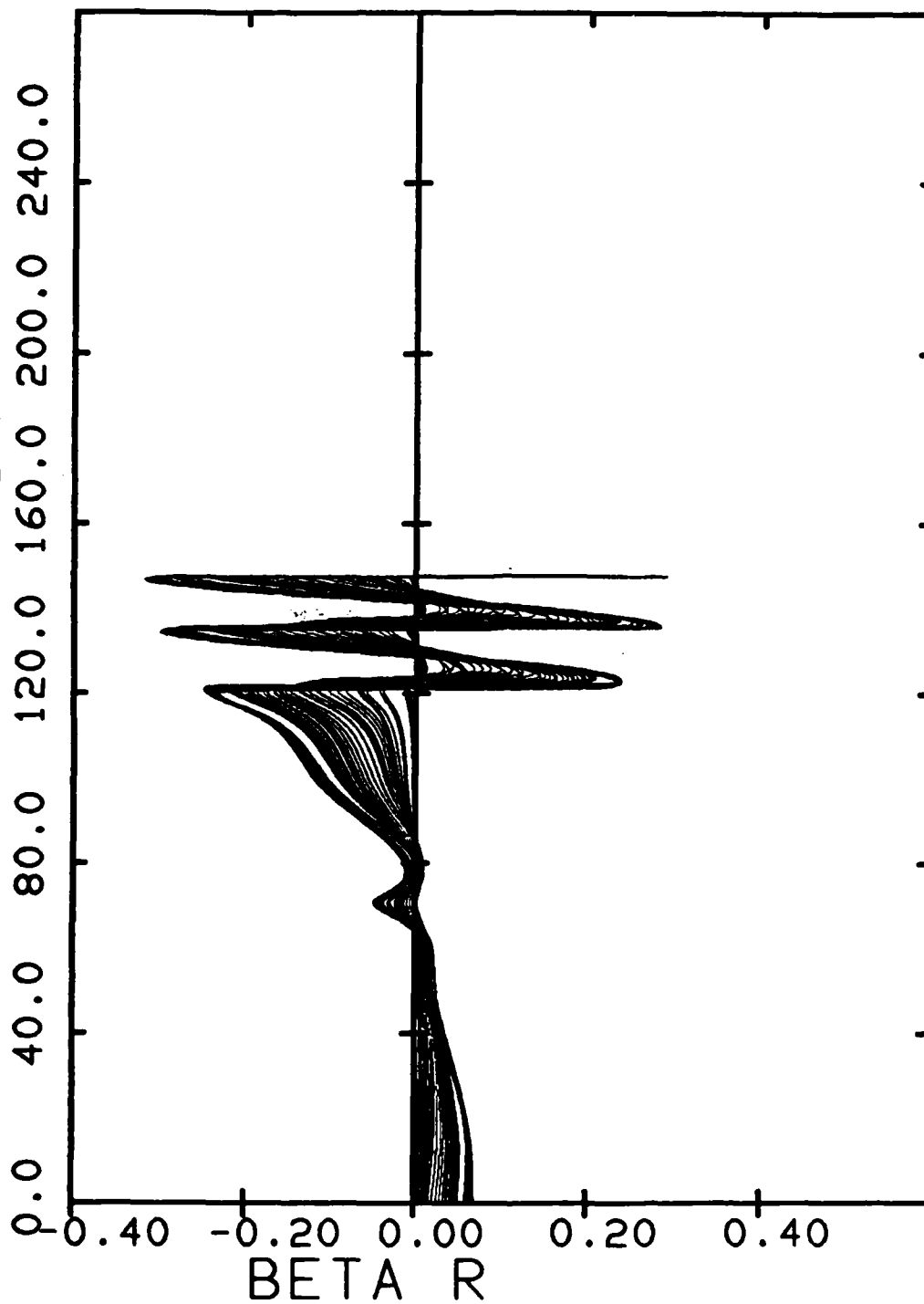


Figure 22. Compression of Residual Beam Flow in Stage 4

STAGE 4

Z-POSITION - 258 cm

0.0 40.0 80.0 120.0 160.0 200.0 240.0

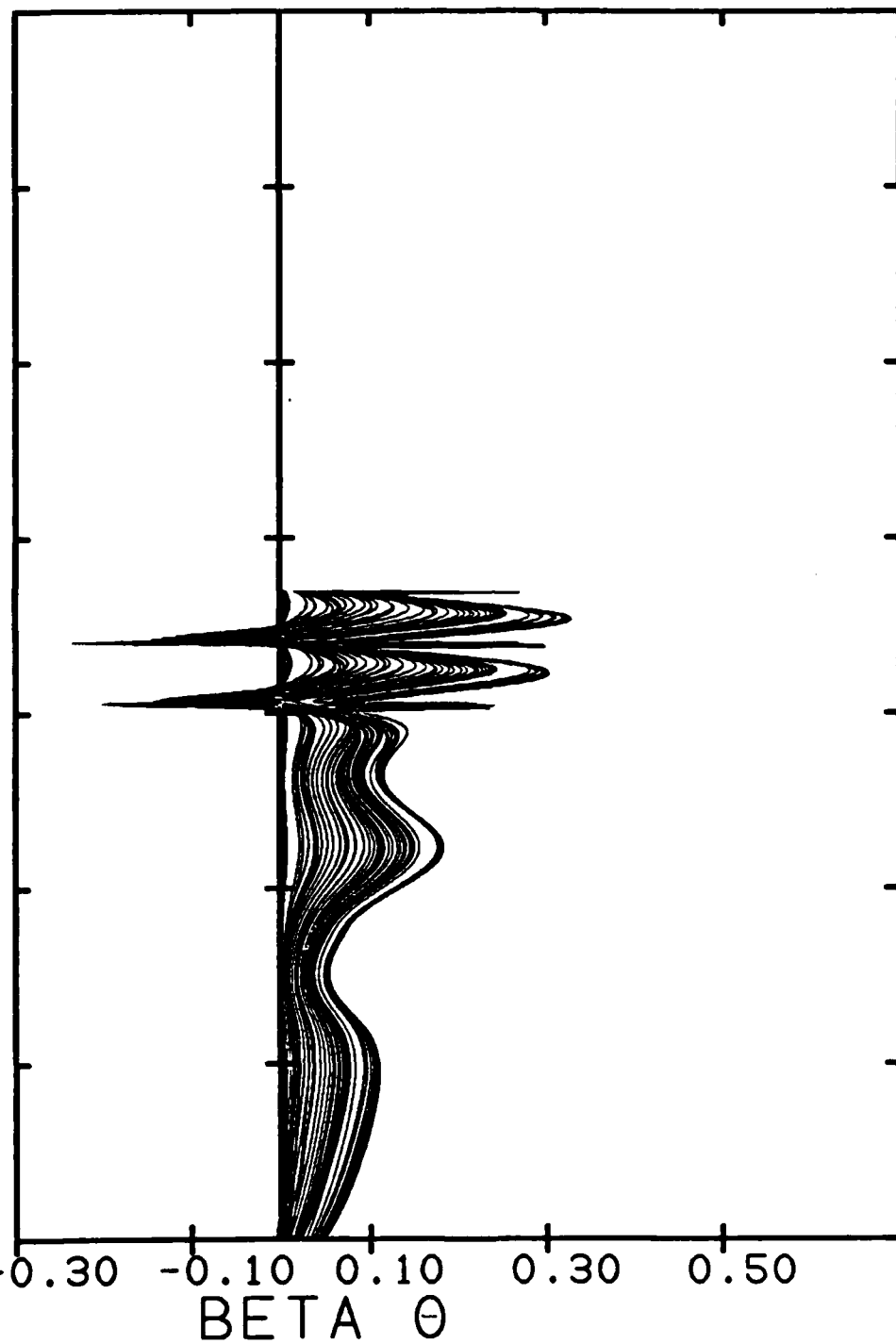


Figure 23. Compression of Residual Beam Flow in Stage 4

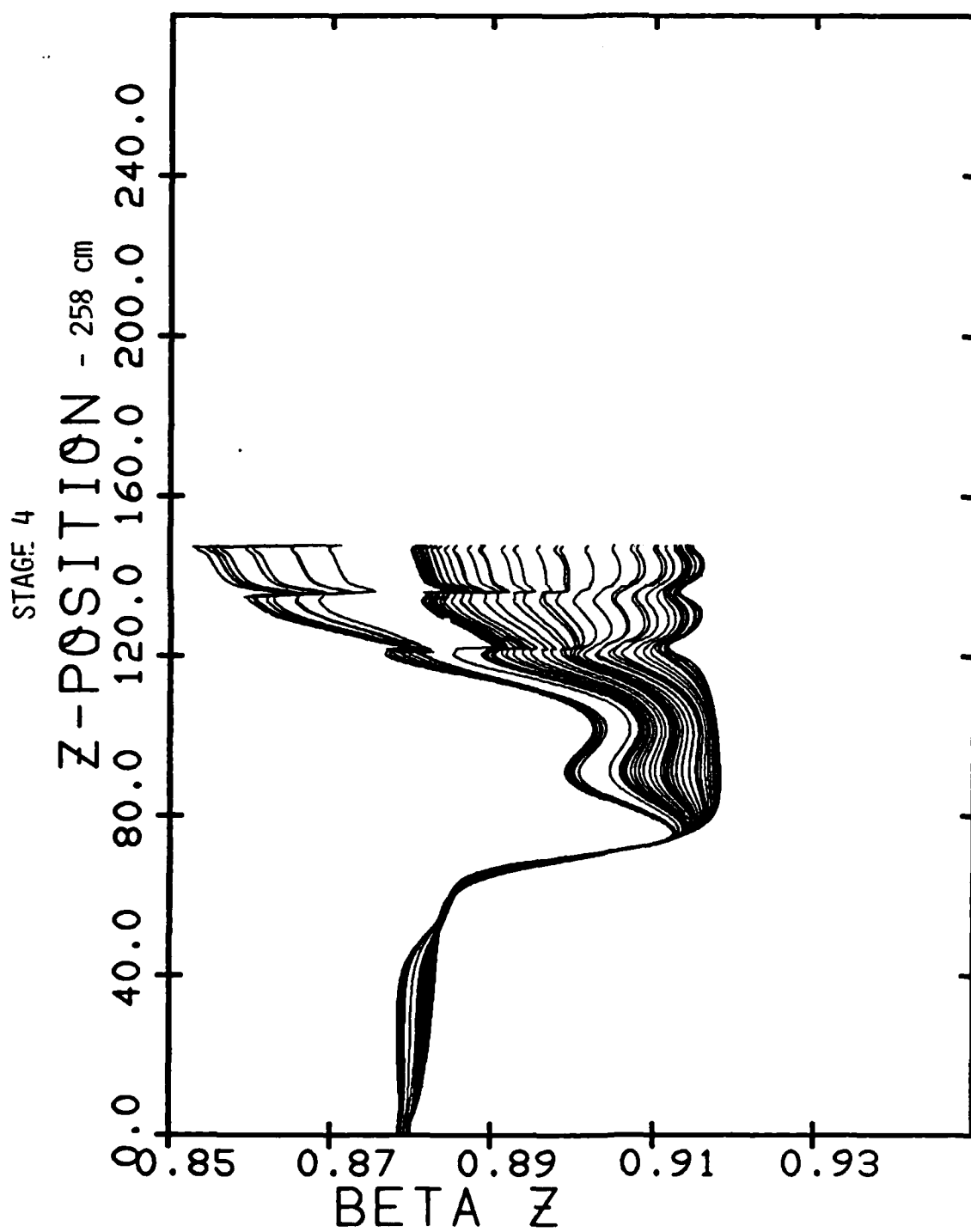


Figure 24. Acceleration and Compression of Residual Beam Flow in Stage 4

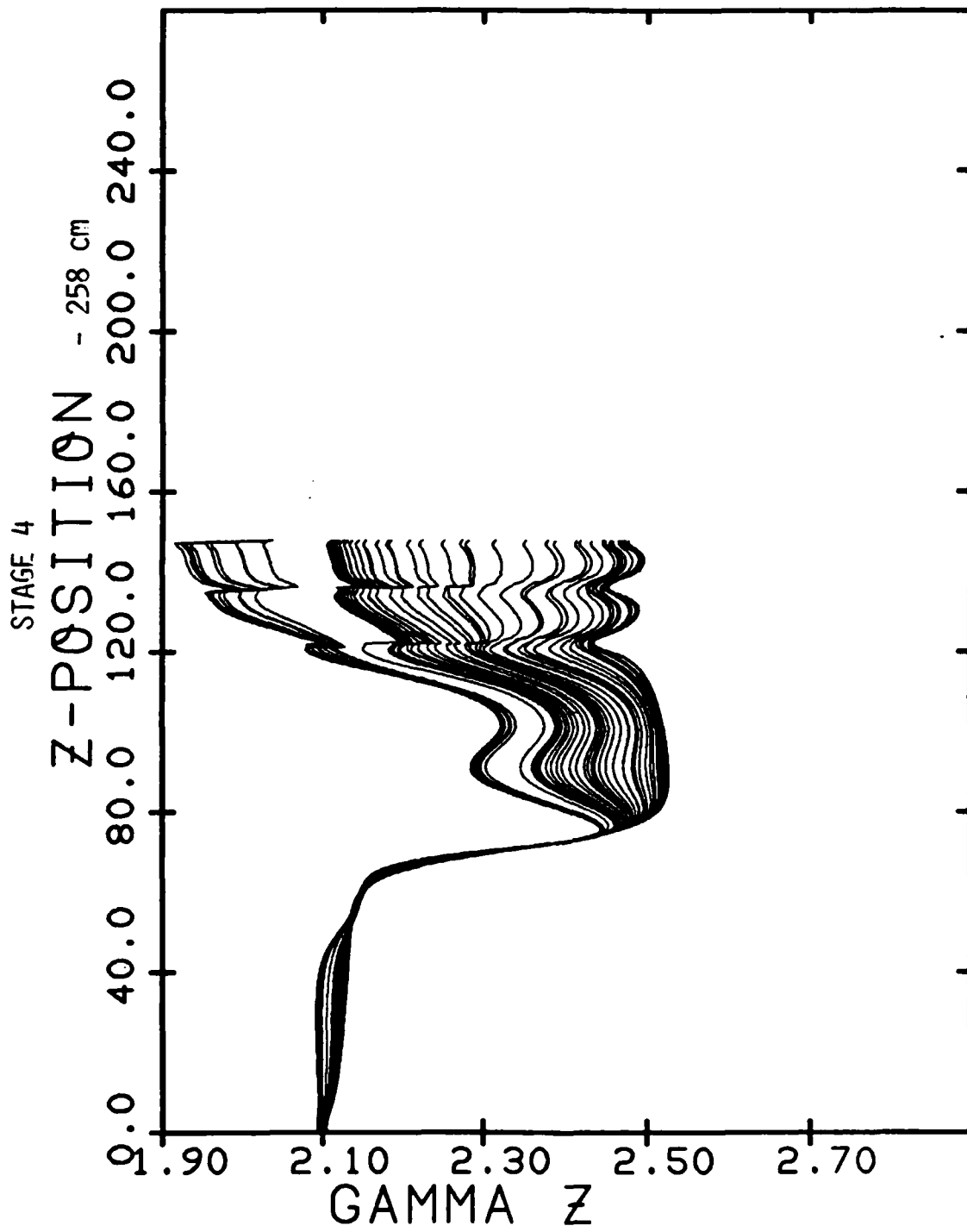


Figure 25. Acceleration and Compression of Residual Beam Flow in Stage 4

A P P E N D I X E

Review of Beam Formation and Transport Through an Induction Linac

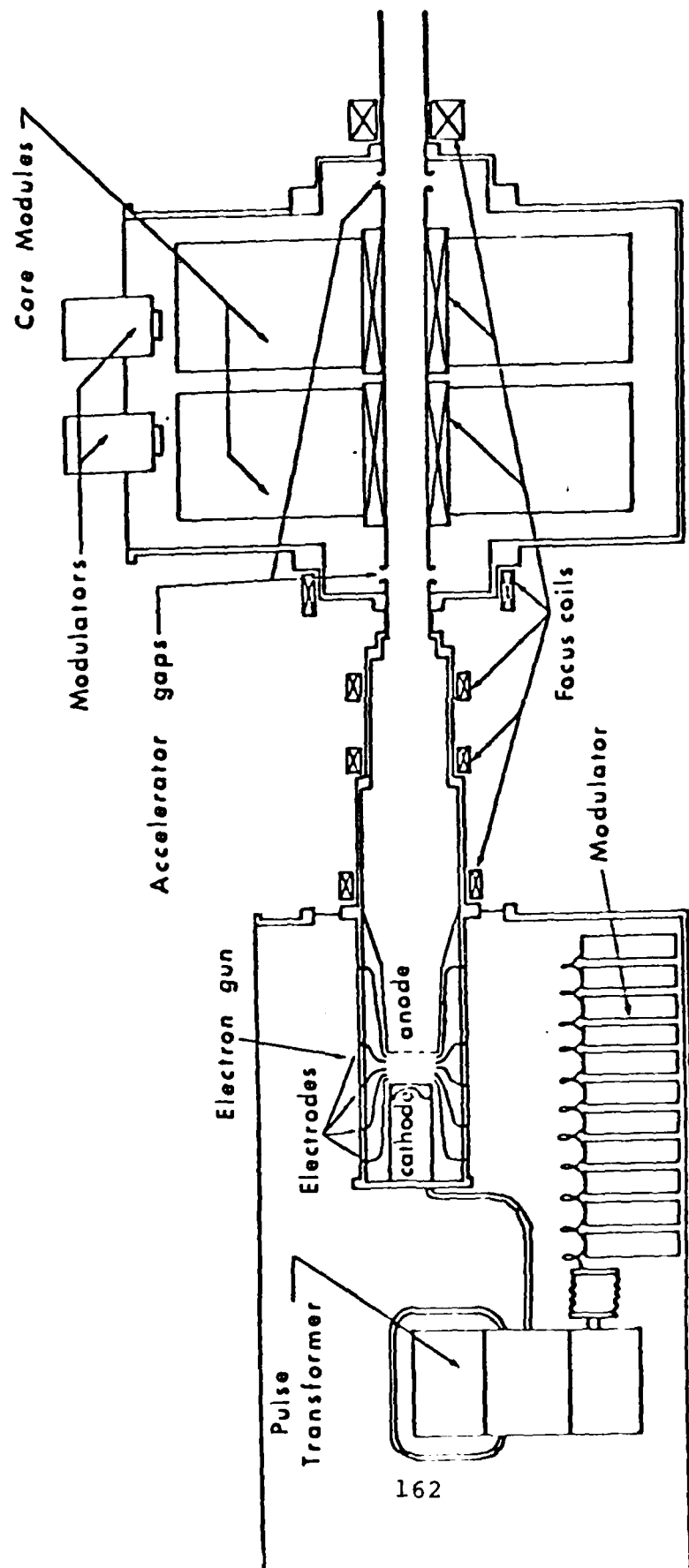
Section II of Renewal Proposal No. I-ARA-82-U-56 (ARA-454),
"Computational and Theoretical Studies of the Formation and
Transport of High Quality, High Current Electron Beams for Use
as Free Electron Laser Drivers," May 1982.

REVIEW OF BEAM FORMATION AND TRANSPORT THROUGH AN INDUCTION LINAC

Results of our calculations of beam formation and transport through the system illustrated in Figure 1 have previously been discussed during one site trip to the Naval Research Laboratory and in three letter progress reports,¹ and will be briefly reviewed herein.

Beam formation in the injector has been studied by using the REEFER code² to compute steady state diode flow patterns. One design with a cantilevered button field emission cathode of 14 cm radius, 2.5 cm thickness, and -400 kV potential inside a grounded cylindrical housing of 19 cm radius with a grounded anode mesh located 10 cm downstream was evaluated. However, the pre-breakdown electric field stresses were found to be above 170 kV/cm on the cathode tip, which would lead to complete breakdown of the cathode surface, a current density profile highly peaked on edge, some 5 kA of emitted current, and an expanding flow pattern in the anode-cathode gap in the absence of a strong magnetic guide field. This beam was judged unacceptable, inasmuch as its size (>14 cm) was so much greater than the desired downstream beam radius in the wiggler (<0.6 cm), the flow was expansive in the diode--making laminar compression difficult downstream, and the current was well above the

Figure 1. INDUCTION LINAC



$N \sim 10^{16}$ particles

$\tau \sim 2.0 \mu s$

$\frac{\Delta V}{V} \sim 3 \%$

$V = 0.8 \text{ MV}$

$I = 0.8 \text{ kA}$

nominal design value of ~ 1 kA. Consequently, the remainder of our diode studies have contemplated the use of either warm or cold cathodes, with emission out to ~ 8 cm radius controlled by the presence of fibers, and with annular electrode rings in the anode-cathode gap to provide a graded potential axially through the diode, and to reduce the pre-breakdown stresses on the cathode surface.

The following general theoretical considerations reveal the principal constraints which govern the diode and beam transport design. First, the phenomenon of diode closure, at velocities of ~ 2 cm/ μ sec during the 1-2 μ sec pulse time of the beam, leads to the necessity for an anode-cathode gap spacing d of at least 10 cm to avoid excessive changes in the beam impedance.

Second, it is necessary that the diode operate at a current density below the Child-Langmuir limit. For a "parallel-plate" diode, which the resistively graded electrode rings simulate to some extent, one has

$$J = \frac{I}{\pi a^2} \leq \frac{mc^3/e}{8\pi d^2} \left[\int_0^{\gamma_0^{-1}} \frac{dy}{(2y+y^2)^{1/4}} \right]^2$$

where $mc^3/e = 17$ kA. For a 400 kV injector,

$$\gamma_0^{-1} \approx 0.783, \quad \int_0^{\gamma_0^{-1}} dy (2y+y^2)^{-1/4} \approx 0.86,$$

and one finds that the beam current density J must not exceed about 5 A/cm^2 for $d \geq 10 \text{ cm}$. Therefore, in order to produce 1,000 amperes of current, the emitting radius of the cathode must exceed about 8 cm.

Third, the requirement that the electron beam should eventually be compressed to a radius of about 0.6 cm in the wiggler solenoid places a very high premium on techniques for beam convergence. It is easy to see that complete reliance on magnetic compression to achieve this hundredfold increase in the beam current density is hardly feasible. In order for the beam to be magnetically compressed, it must first be well tied to the field lines, which roughly occurs when

$$1 \gg \frac{2\omega_p^2}{\gamma^2 \Omega^2} = \frac{I(\text{kA})}{.73\gamma\beta B_z^2(\text{kG}) a^2(\text{cm})}$$

where ω_p, Ω are the relativistic plasma and cyclotron frequencies. This tying requirement would require hundreds of gauss in order to be obeyed in the diode region. Then if the beam were to be magnetically compressed by an order of magnitude in radius while tied to the flux surface $B_z a^2 = \text{constant}$, the magnetic field would have to be increased to some tens of kilogauss in the wiggler solenoid. Judging this to be technologically infeasible or too

expensive, we conclude that the beam convergence must be achieved electrostatically in part, while the magnetic field is weak, leaving a lesser amount of compression to be achieved magnetically.

Electrostatic beam convergence is possible either through the use of Pierce electrode geometry or in a graded potential parallel plate geometry. We have concentrated on this latter possibility, which is built into the existing long pulse induction linac. Diode parameters for this injector, which we have adopted for our computational studies as well, are

anode-cathode gap spacing = $d = 11.0$ cm

cathode emission radius = $a = 8.0$ cm

cathode potential = $-\Delta\phi = -400$ kV.

The resistively graded electrodes lead to a radial boundary condition in the anode-cathode gap which may be modeled as

$$\frac{\phi(r=b, z) - \phi_{\text{cathode}}}{\Delta\phi} = \left(\frac{z}{d}\right)^p$$

We have considered computationally three alternative cases:

- (i) $p = 1$, linear grading
- (ii) $p = 4/3$, Child-Langmuir grading
- (iii) $p \approx 1.52$, sub-Child-Langmuir experimental grading.

The computed diode flow patterns and the current density profiles at the cathode surface are illustrated for these three cases in Figures 2 through 7. A grounded anode mesh was placed at $z = d = 11$ cm, to conform to the experimental situation. The axial magnetic field was varied in the range 0-10 G, commensurate with the magnitude of the initial experimental magnetic fields, and the diode flow was found to be insensitive to B_z in this range. Just as the electric field stresses in the vicinity of the cathode are strongest for $p = 1$ and weakest for $p \approx 1.52$, the current extracted was found to be highest for $p = 1$ ($I = 1.24$ kA) and lowest for $p = 1.52$ ($I = 0.72$ kA). It is also found that for the linear grading ($p = 1$), the current density was strongly peaked at the edge of the beam and the outer flow was somewhat divergent. For the intermediate Child-Langmuir grading ($p = 4/3$), the current density is only slightly peaked at the edge of the beam and the flow is slightly convergent. (The computed current of $I = 0.90$ kA is also in close agreement with the theoretical Child-Langmuir prediction of 0.89 kA.) Finally, for the sub-Child-Langmuir

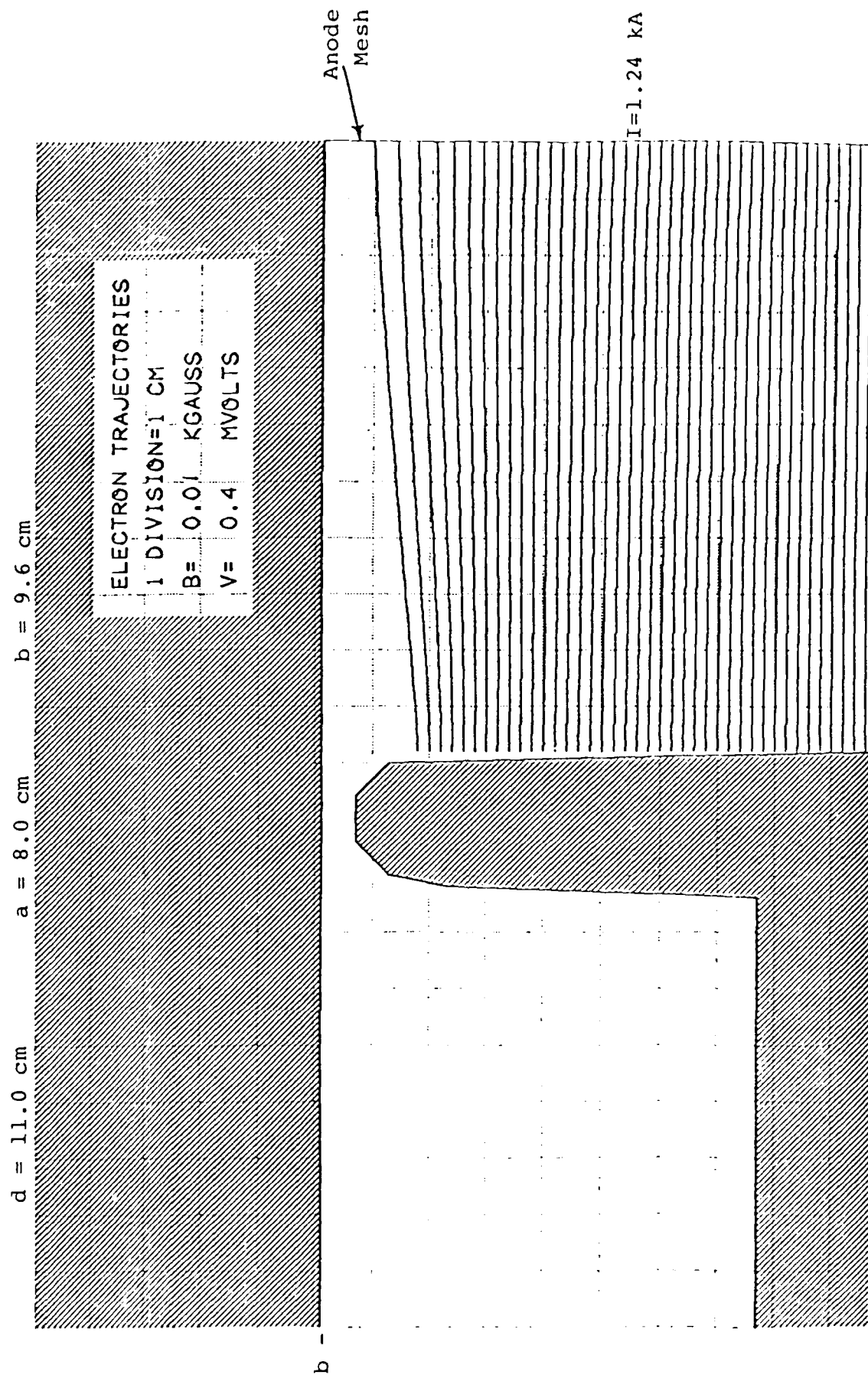


Figure 2. Cold Cathode with Linear Potential Grading; $\Delta \phi(b, z) = 0.4 (z/d) \text{ MV}$

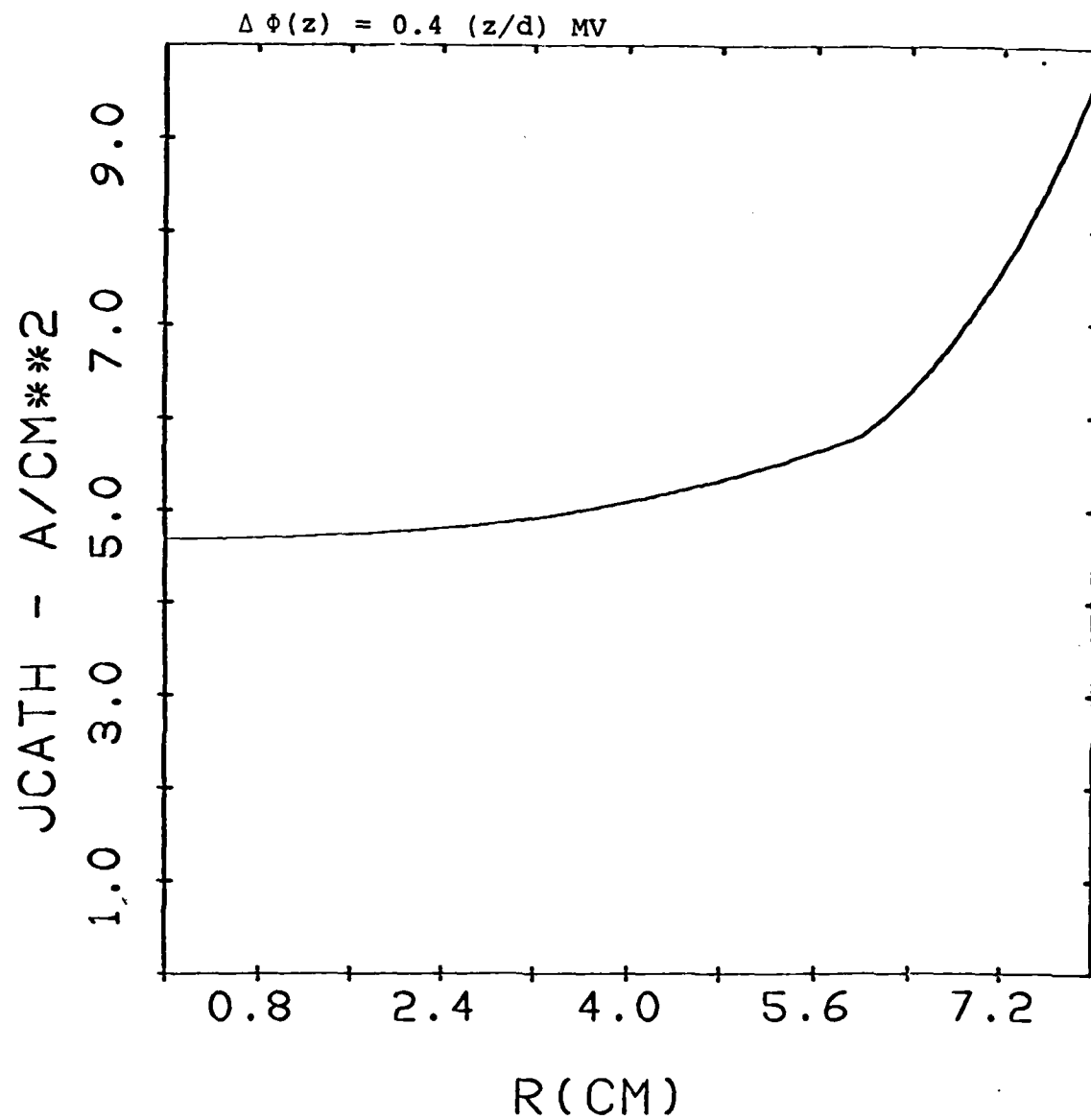


Figure 3. Current Density Profile @ Cathode
for Linear Potential Grading

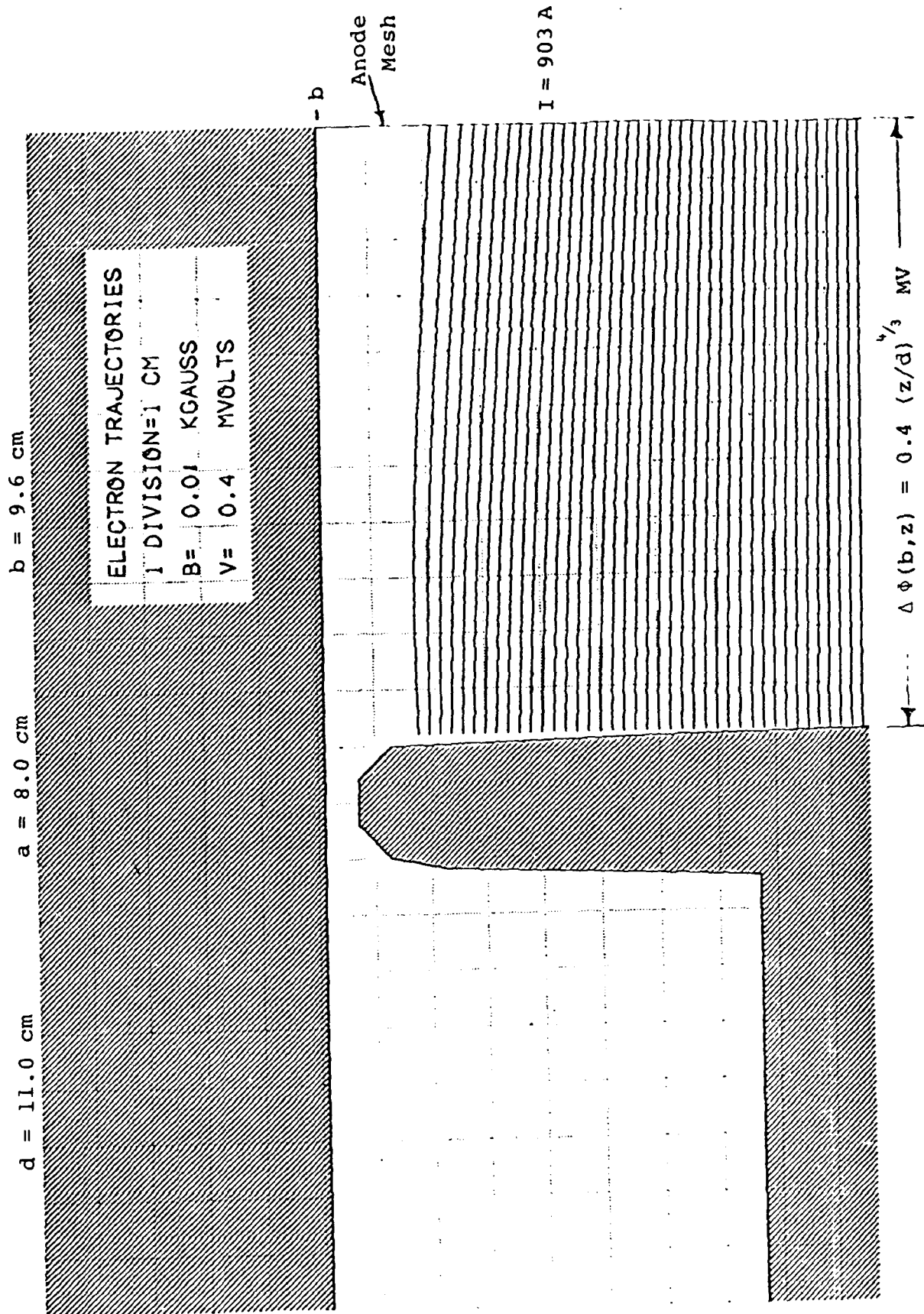


Figure 4. Cold Cathode with Child-Langmuir Potential Grading

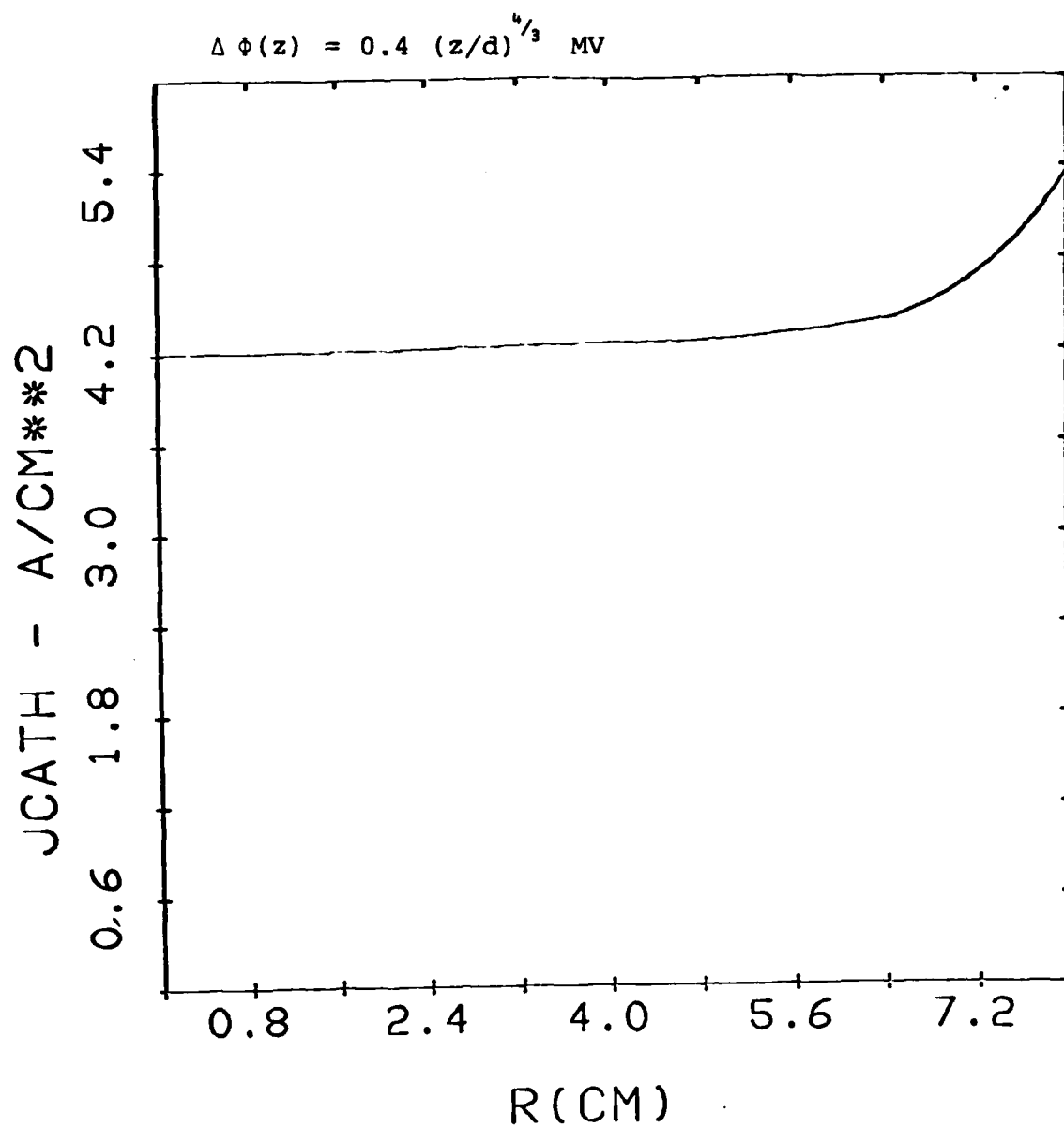


Figure 5. Current Density Profile @ Cathode
for Child-Langmuir Potential Grading

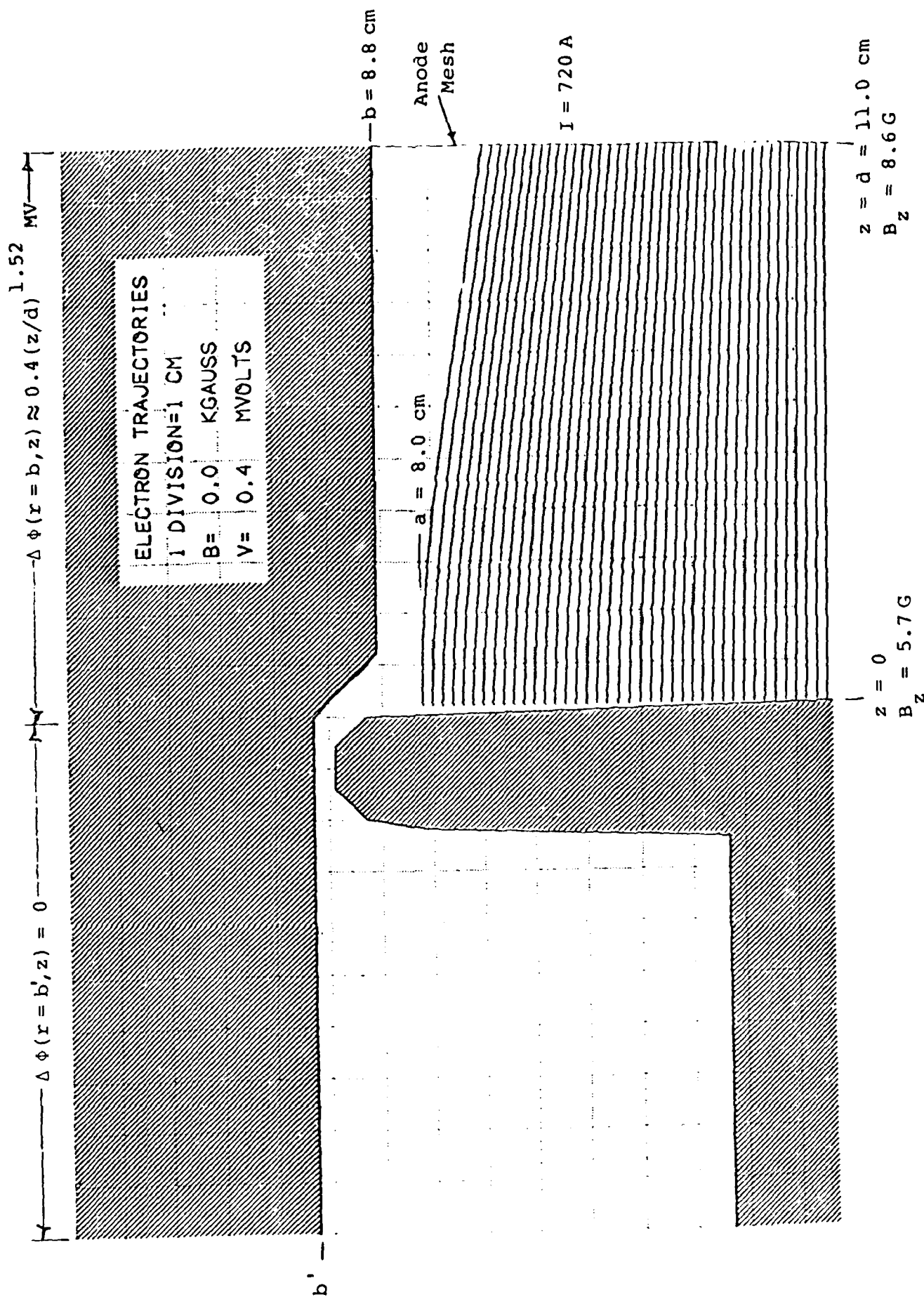
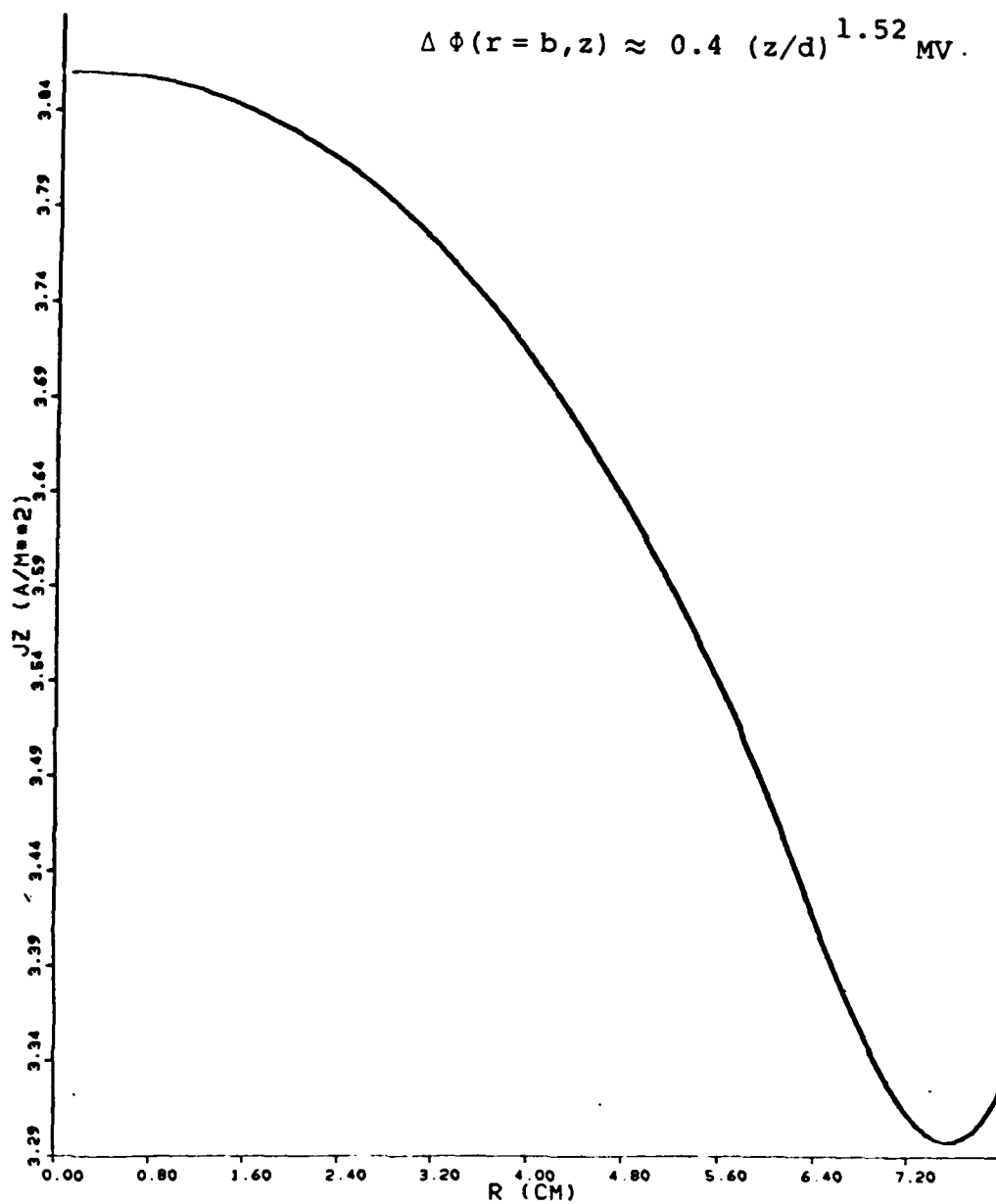


Figure 6. Cold Cathode with Sub-Child-Langmuir Potential Grading



JZ VS R

Figure 7. Current Density Profile @ Cathode for Sub-Child-Langmuir Potential Grading (Modified Design)

13-MAY-82

05:42:45

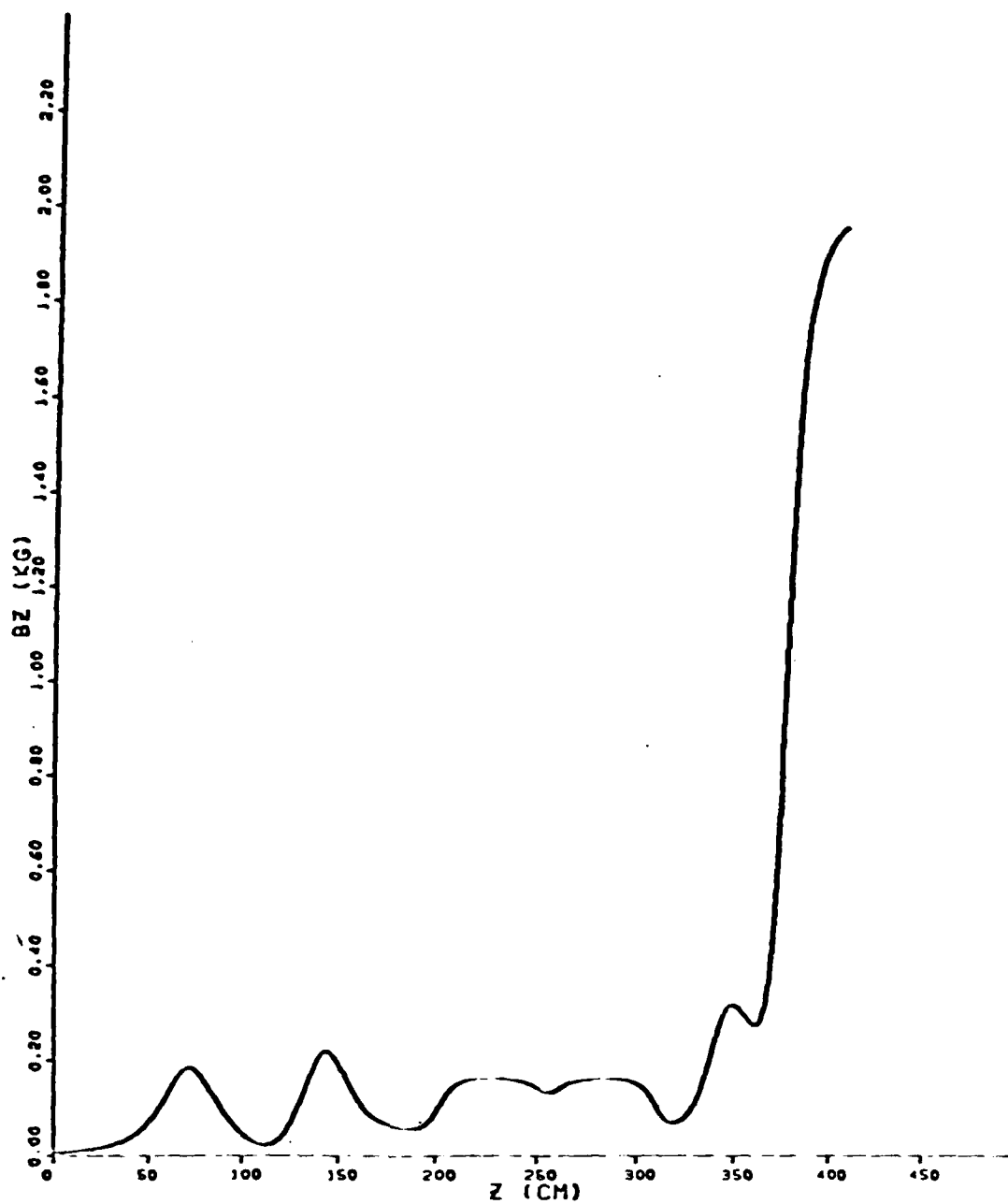
grading ($p \approx 1.52$), the current density is slightly peaked on axis and the flow pattern is strongly convergent, as illustrated in Figure 6. The convergent beam flow results from the graded electrode structure tending to short out the radial electric fields normally associated with the electron beam space charge such that the $v_z \times B_\theta$ pinch force is left to compress the beam radially.

As shown in Figure 1, the electron beam, once formed, must be transported through a complex array of magnetic field coils and radially varying conducting boundaries, and through two accelerating gaps in the induction module before being finally compressed and injected into the wiggler solenoid, which begins 380 cm downstream of the cathode surface.

In order to study this challenging transport problem, Austin Research Associates has further extended and developed a steady state, fully relativistic particle simulation code named STAGEN. This code retains all three components of velocity and of the electric and magnetic fields, but is restricted to the two spatial coordinates r, z as independent variables, appropriate to situations which are symmetric in the azimuthal coordinate θ . In order to reduce the computing requirements to a manageable level, the axial transport is divided into four "stages." The first stage extends to $z = 23$ cm, encompassing the

11 cm length of the anode-cathode region plus 12 cm beyond the anode mesh. The flow is initiated from an equipotential near but not on the cathode surface--typically $\phi - \phi_{\text{cathode}} \leq 20$ kV. Stage 2 extends from $z = 23$ cm to $z = 111$ cm, encompassing the initial focusing coil and the conductor wall flaring out to a radius of 17.5 cm. Stage 3 extends from $z = 111$ cm to $z = 258$ cm, and encompasses three more focusing coils, the first induction accelerating gap (of 200kV), and the first induction solenoid. Stage 4 extends from $z = 258$ cm to $z = 406$ cm, and encompasses the second induction solenoid, the second induction accelerating gap (also of 200 kV), another focusing coil, and the first 26 cm of the wiggler solenoid.

Under this contract, STAGEN has been exercised repeatedly to examine the beam transport through the first four meters of the long pulse induction linac for all three of the diode potential gradings discussed previously, and for several magnetic field configurations. We have also developed the capability of introducing scattering into the beam flow as it passes through the anode mesh. To illustrate these transport calculations, Figure 8 displays one magnetic field configuration based upon some December 1981 coil settings, and including the magnetic ramp into the 2 kG wiggler solenoid. For this magnetic field configuration and for the Child-Langmuir potential grading of Figure 4, the



BZ VS Z

Figure 8. Magnetic Field Profile from
December 1981 Data

2-APR-82
12:20:30

(ara)

beam transport is shown in Figures 9 through 12 for Stages 1 through 4. Figure 9 shows the slightly convergent diode flow, with rms mesh scattering of 2.83° introduced. A current of 858 A was followed in this series of runs, which is slightly below the 900 A given by the diode calculations. This current is transported into Stage 3, but there 135 A (or 15.7%) of the current is lost at the entrance to the induction module, while an additional 349 A (or 40.7%) of the current is lost downstream of the first induction gap, as shown in Figure 11. The remaining 374 A (or 43.6%) of the current is transported through Stage 4 and injected into the wiggler solenoid without further loss, as shown in Figure 12. The r and θ velocity flow patterns of the compressed Stage 4 flow are shown in Figures 13 and 14. It is apparent that strong zero frequency cyclotron oscillations have been excited in the magnetic compression to 2 kG. These cyclotron oscillations have begun to phase mix and will continue to thermalize further downstream in the wiggler. From these flow diagnostics, the eventual beam emittance may be estimated as follows:

$$\text{RMS transverse velocity}/c = \delta\beta_{\perp} \approx 0.20$$

$$\text{RMS beam radius} = R \approx 0.78 \text{ cm}$$

$$\gamma \approx 2.57 \text{ (800 keV)}$$

$$\text{normalized emittance} = \frac{\epsilon_n}{\pi} = \gamma R \delta\beta_{\perp} \approx 400 \text{ mrad-cm}$$

$$@ I = 374 \text{ A.}$$

Stage 1

Z-POSITION

0.000 4.000 8.000 12.000 16.000 20.000 24.000

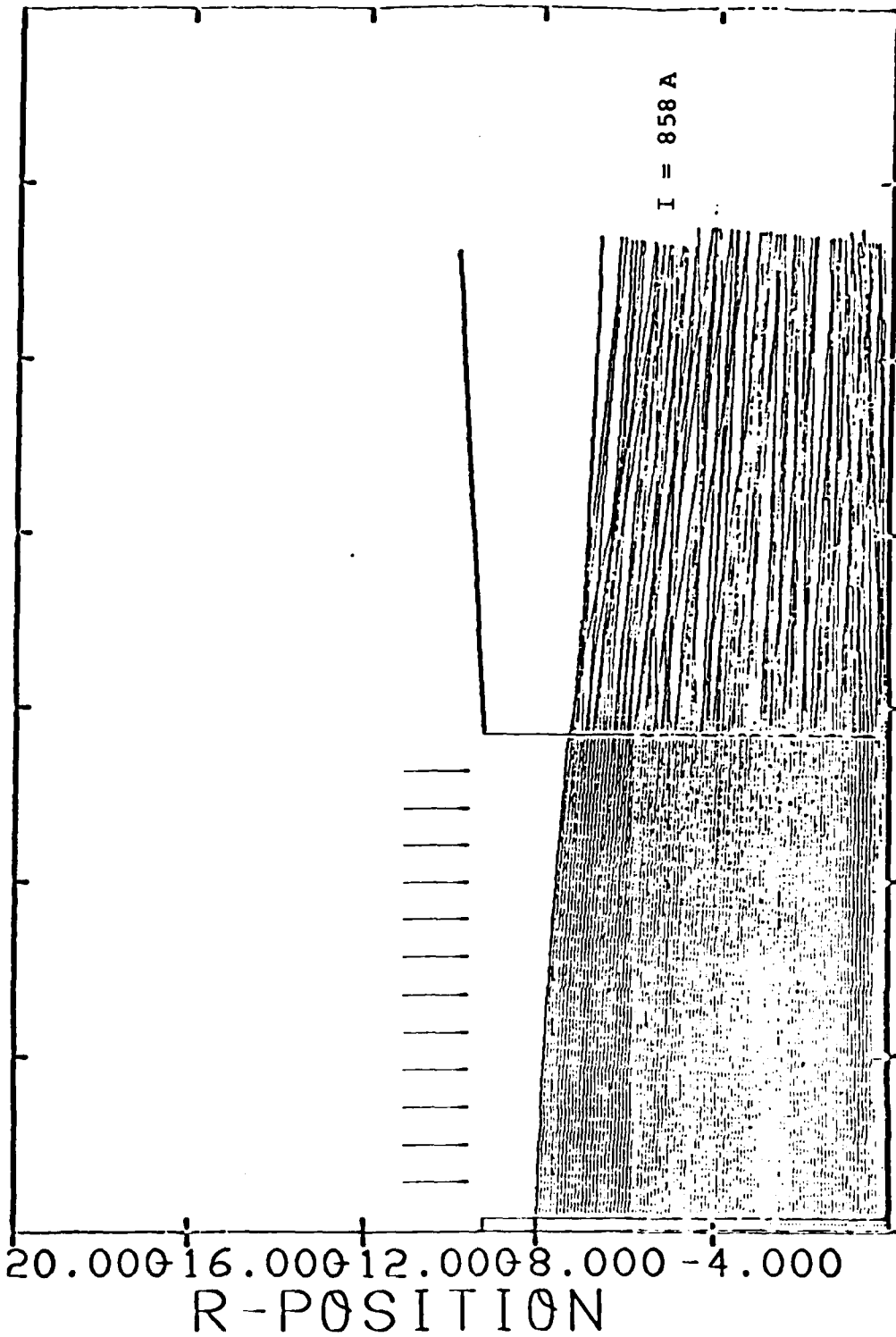


Figure 9. Laminar Diode Flow with Anode Mesh Scattering of $\theta_{\text{RMS}} \approx 2.83^\circ$

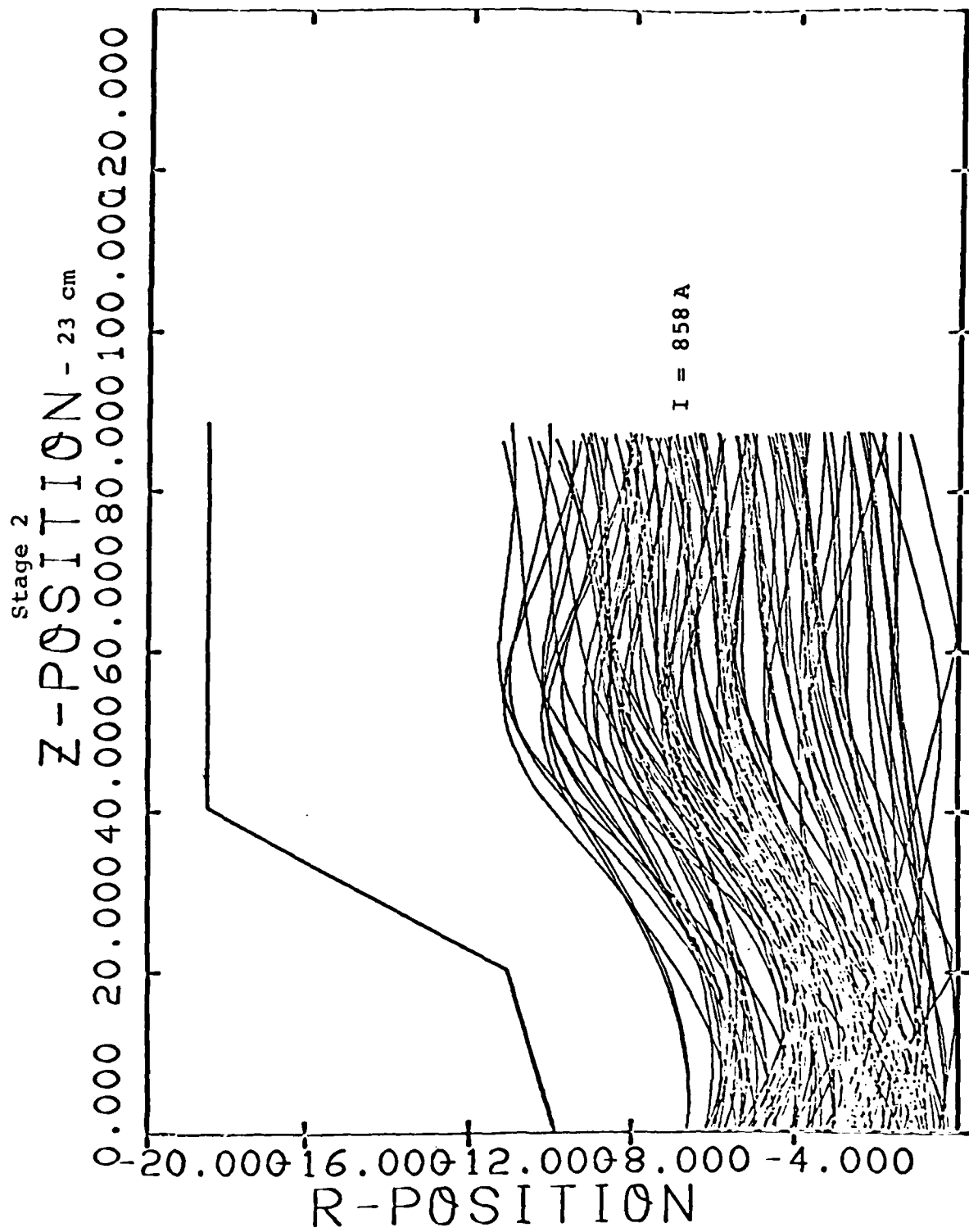
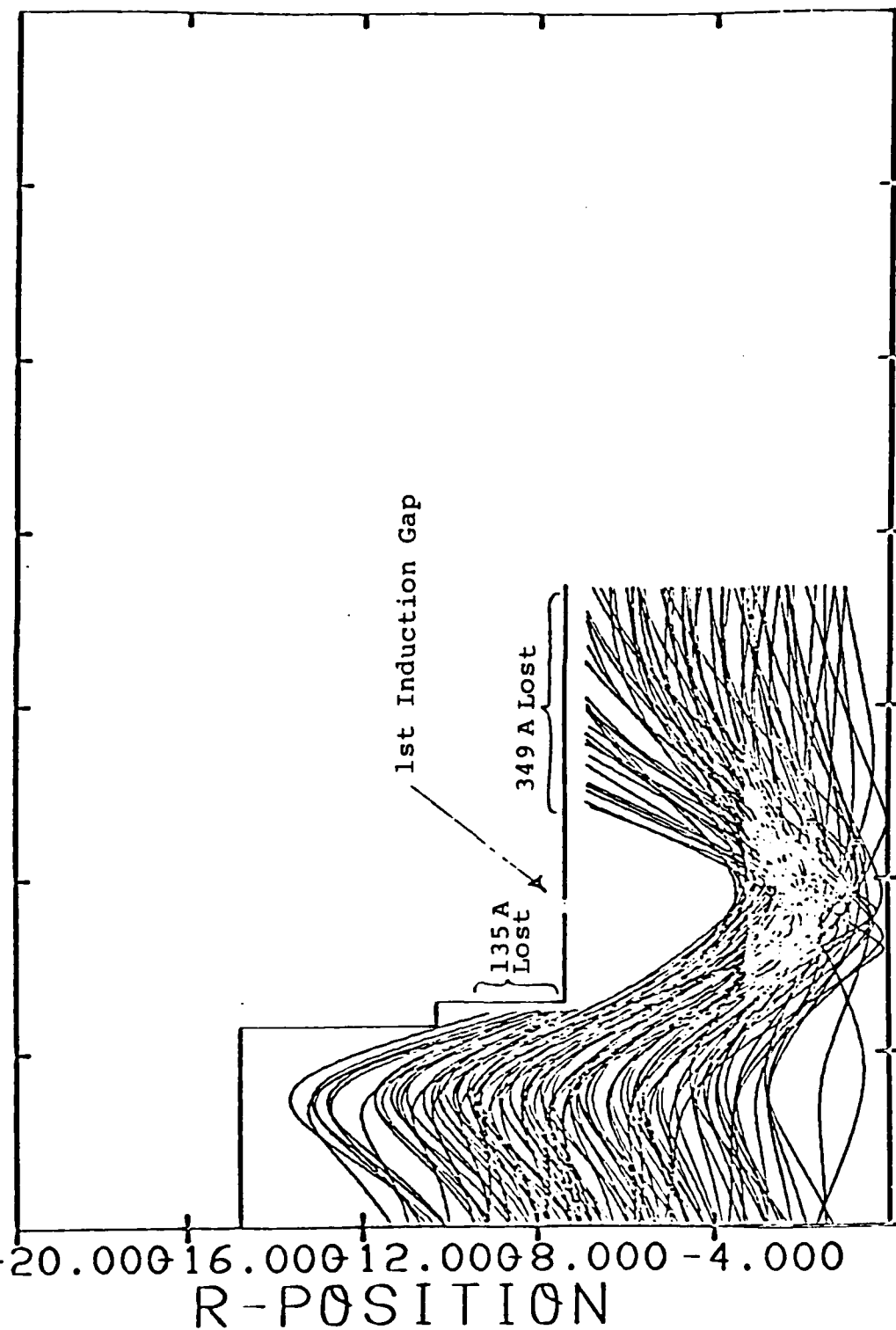


Figure 10. Scattered Flow @ Stage 2

Stage 3

Z-POSITION -111 cm

0.000 40.000 80.000 120.000 160.000 200.000 240.000

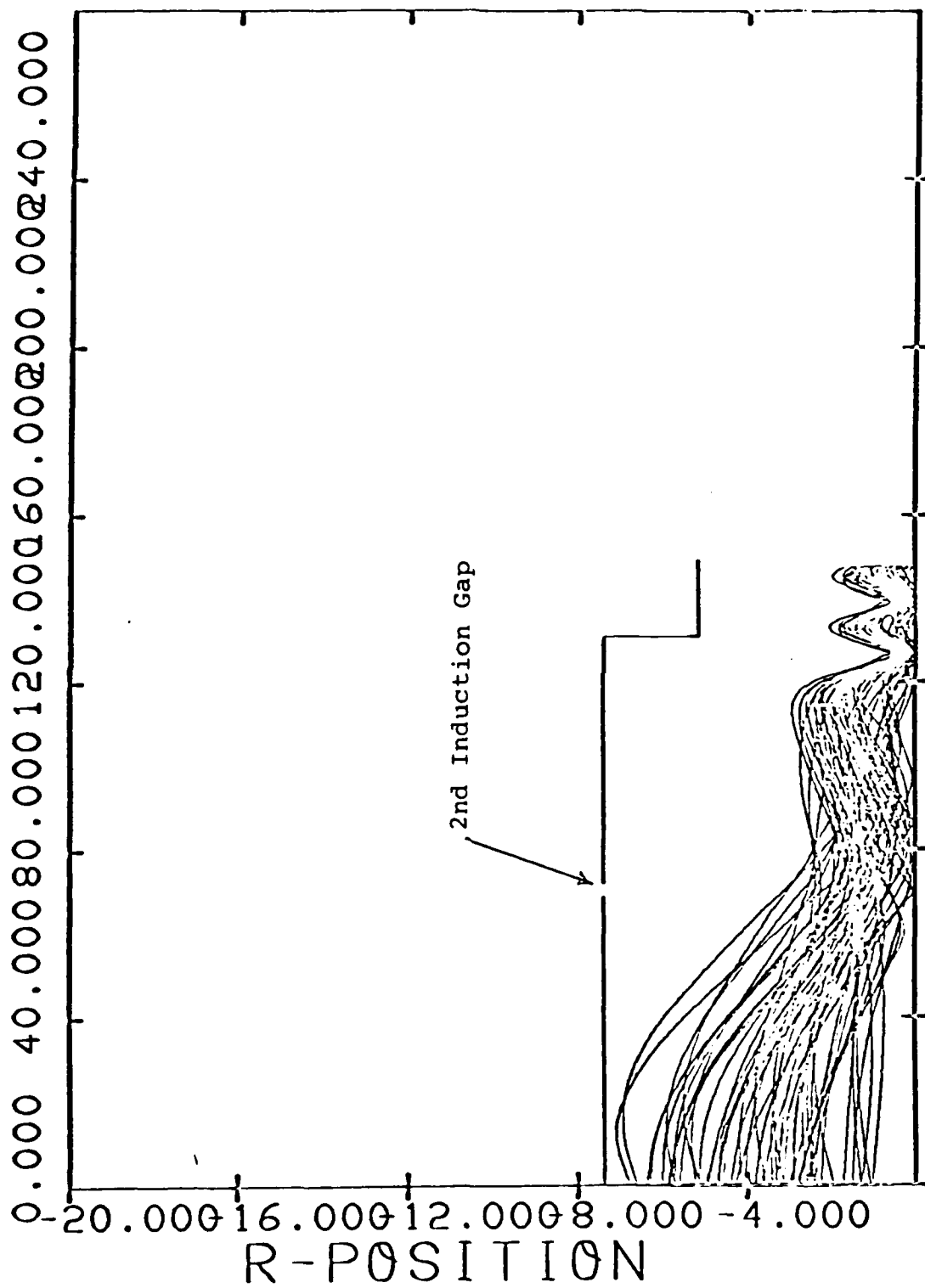


858 A 723 A 374 A

Figure 11. Scattered Flow Thru Stage 3, with Current Loss

Stage 4

Z-POSITION - 258 cm



↑
I = 374 A

Figure 12. Transmission of Residual Scattered Current Thru Stage 4 Compression

Stage 4

Z-POSITION -258 cm

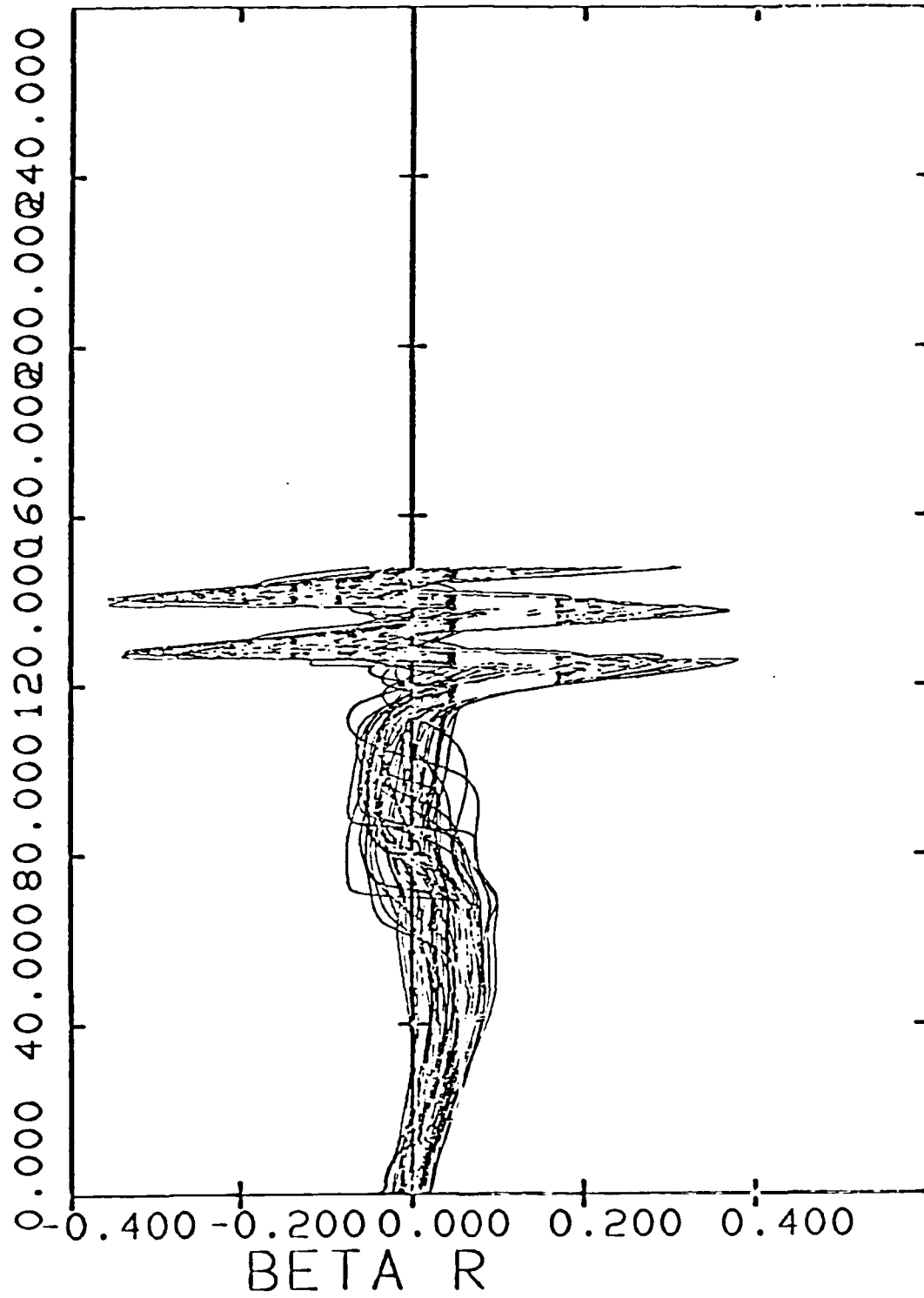


Figure 13. Compression of Scattered Beam Flow @ Stage 4

Stage 4

Z-POSITION - 258 cm

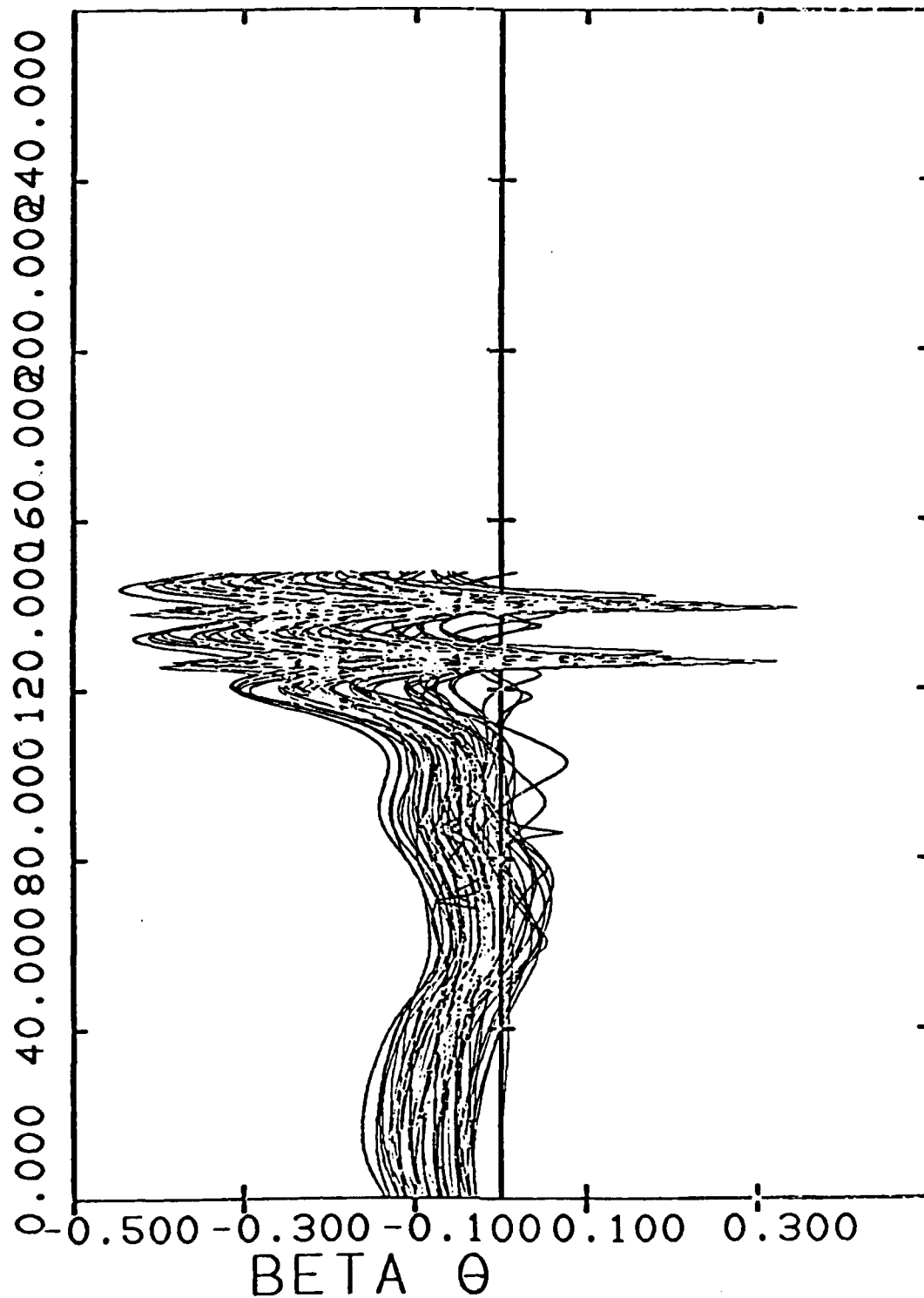


Figure 14. Compression of Scattered Beam Flow @ Stage 4

This illustrated transport calculation is neither the most careful attempt to duplicate experimental conditions nor an optimized transport design. However, it does illustrate the capabilities of the STAGEN code. Experimental measurements have been reported which indicate beam current loss at the same two locations indicated in Figure 11, but we have not yet duplicated the experimental situation well enough to be able to claim good quantitative agreement. Such transport calculations are currently underway, using the sub-Child-Langmuir potential grading which is experimentally in place and which yields more convergent flow in the injector diode.

APPENDIX E REFERENCES

1. Letter reports from J. R. Thompson to C. W. Roberson, dated April 2, 1982; April 27, 1982; and May 13, 1982.
2. J. E. Boers, "Digital Computer Simulation of High-Current, Relativistic, and Field Emission Electron Tubes," Record of 11th Symposium on Electron, Ion, and Laser Beam Technology, San Francisco Press, Inc.

A P P E N D I X F

Review of Previous Results on Beam Transport Studies

Appendix A of Renewal Proposal No. I-ARA-84-U-7 (ARA-511),
"Studies of the Formation and Transport of High Quality, High
Current Electron Beams, and of the Phase Area Displacement
Operation of a Free Electron Laser Driven by a Circulating High
Current Electron Beam," May 1984.

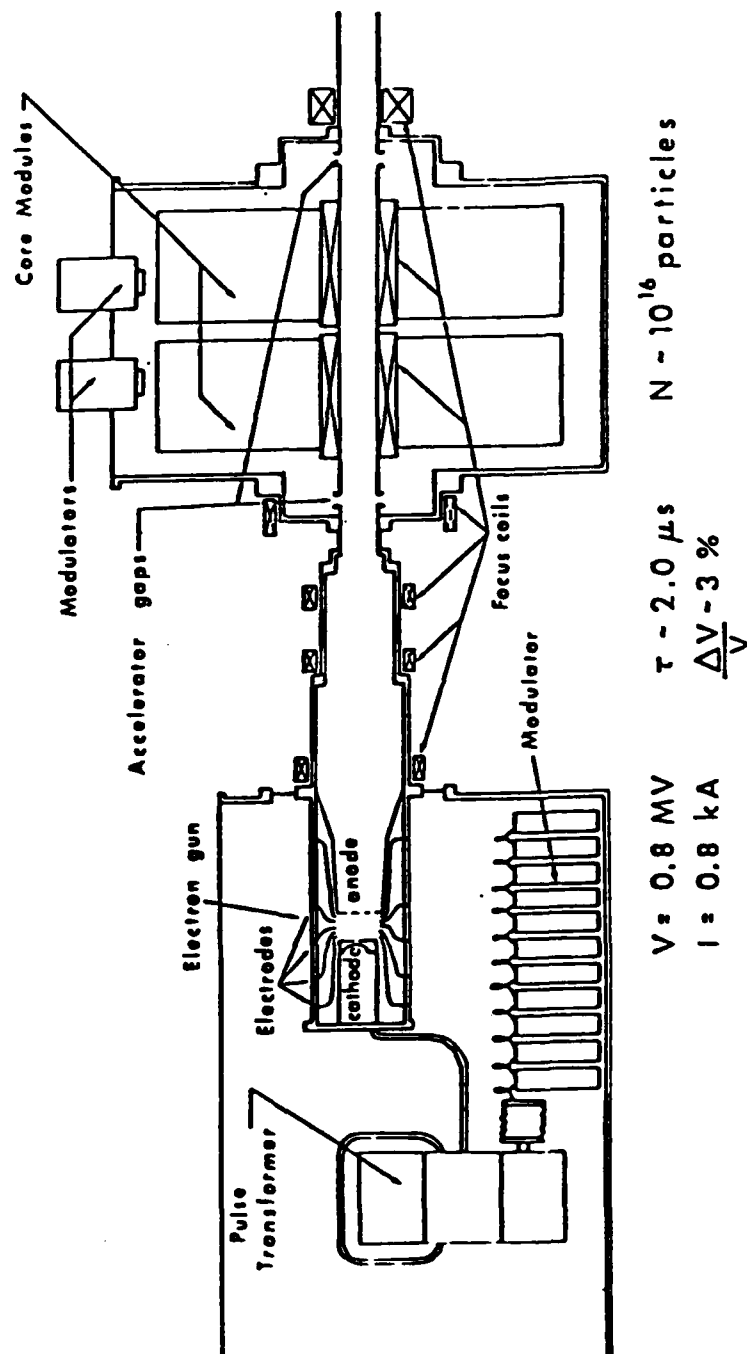
REVIEW OF PREVIOUS RESULTS

ON BEAM TRANSPORT STUDIES

Results of our calculations of beam formation and transport through the system illustrated in Figure 1 have previously been discussed during several site trips to NRL, in several letter progress reports,^{1,2} and were presented at the 1982 annual meeting of the Division of Plasma Physics.³ They are briefly reviewed herein.

Beam formation in the injector has been studied using the REEFER code⁴ and the STAGEN code (developed at Austin Research Associates) to compute steady state diode flow patterns in r, z geometry. Early examination of a cantilevered button field emission cathode of 14 cm radius, 2.5 cm thickness, and -400 kV potential inside a grounded cylindrical housing of 19 cm radius with a grounded anode mesh located 10 cm downstream, revealed that pre-breakdown electric field stresses on the cathode tip would exceed 170 kV/cm. This was found to lead to complete breakdown of the cathode surface, a current density profile highly peaked on edge, some 5 kA of emitted current, and an expanding flow pattern in the anode-cathode gap in the absence of a strong magnetic guide field. This beam was judged unacceptable due to its excessive size (> 14 cm vs. < 0.6 cm desired downstream in the wiggler), its excessive current (5 kA vs. ~ 1 kA desired), and its expansive flow in the diode--making laminar compression

Figure 1. INDUCTION LINAC



difficult downstream. Consequently, the remainder of our diode studies contemplated the use of either warm or cold cathodes with annular electrode rings in the anode-cathode gap to provide a graded potential axially through the diode and to reduce the pre-breakdown stresses on the cathode surface, with emission out to ~ 8 cm radius controlled by the presence of fibers on the cathode.

Such controlled emission cathodes were found to produce reasonable, high quality beams with laminar flow patterns. Diode parameters selected were

anode-cathode gap spacing = $d = 11.0$ cm

cathode emission radius = $a = 8.0$ cm

cathode potential = $-\Delta\phi = -400$ kV.

The gap spacing of 11 cm is sufficient to minimize the problem of diode closure at velocities of ~ 2.5 cm/sec during the 1-2 μ sec pulse time of the beam. The emission radius of 8 cm is large enough to ensure that the current density at the cathode surface is less than 4 A/cm^2 , as required for reliable operation and to avoid the Child-Langmuir space charge limit. However, the requirement that the beam should eventually be compressed to a radius of about 0.6 cm in the wiggler solenoid places a very high premium on techniques for beam convergence.

It is easy to see that complete reliance on magnetic compression to achieve this hundredfold increase in the beam

current density is hardly feasible. hundreds of gauss would be required to tie the beam well to field lines in the diode region and then compression to some tens of kilogauss would be needed to reduce the magnetic flux surface radius to 0.6 cm in the wiggler solenoid. Consequently, it is desirable to achieve some beam convergence electrostatically while the magnetic field is weak, leaving a lesser amount of compression to be achieved magnetically. Electrostatic beam convergence is possible in a graded potential parallel plate geometry. The resistively graded electrodes lead to a radial boundary condition in the anode-cathode gap which may be modeled as

$$\frac{\phi(r=b,z) - \phi_{\text{cathode}}}{\Delta\phi} = \left(\frac{z}{d}\right)^p$$

By varying p , one may vary the cathode stresses, the radial current density profile, and the diode flow pattern. The most desirable results were obtained for a sub-Child-Langmuir grading of $p = 1.52$, which produced relatively weak cathode stresses, current of $I_b \approx 720$ A, and a convergent flow pattern with axially peaked current density as illustrated in Figures 2 and 3. The convergent beam flow occurs because the graded electrode structure tends to short out the radial electric fields normally associated with the beam space charge, such that the $v_z \times B_\theta$ pinch force is left to compress the beam radially.

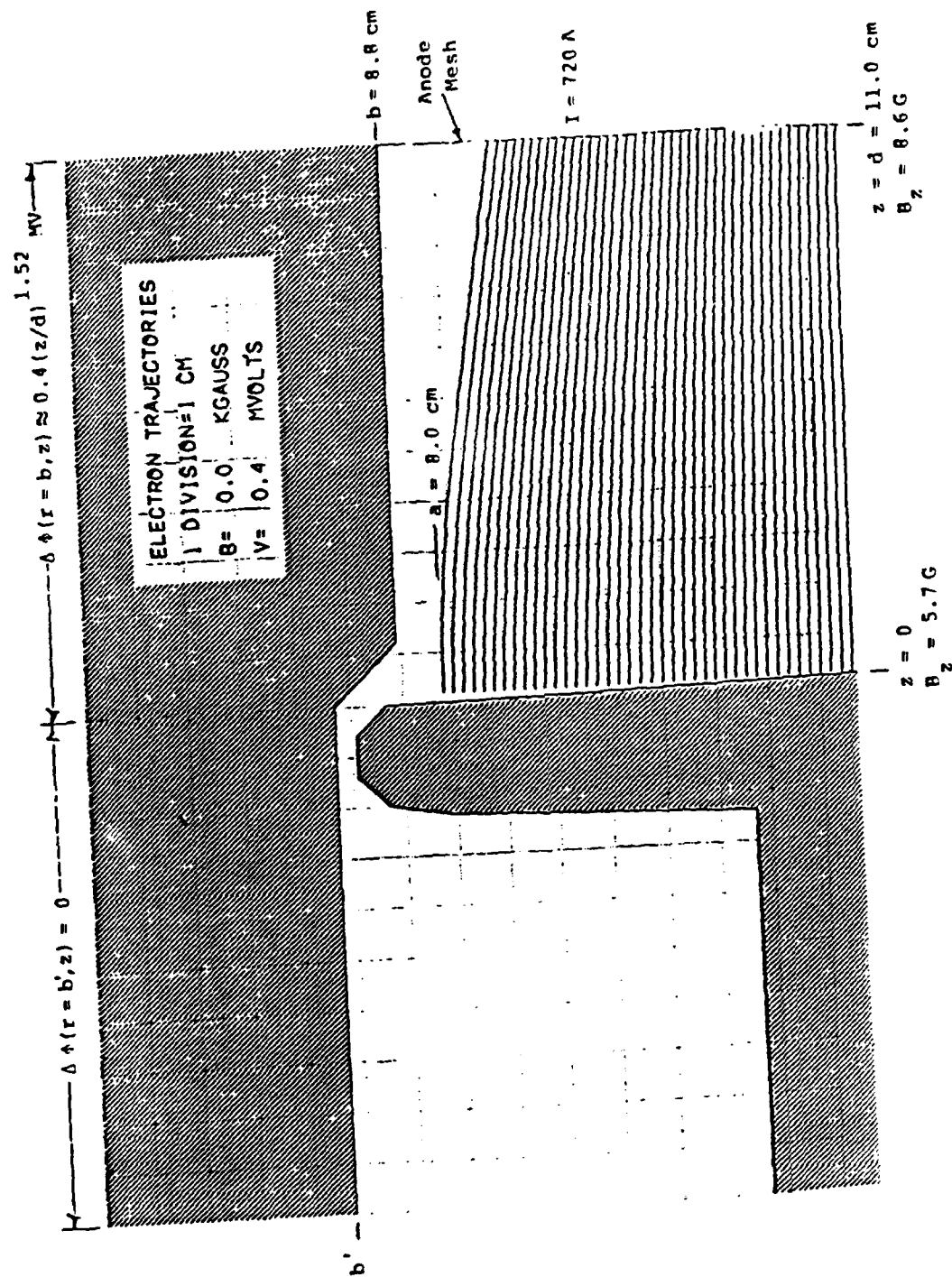
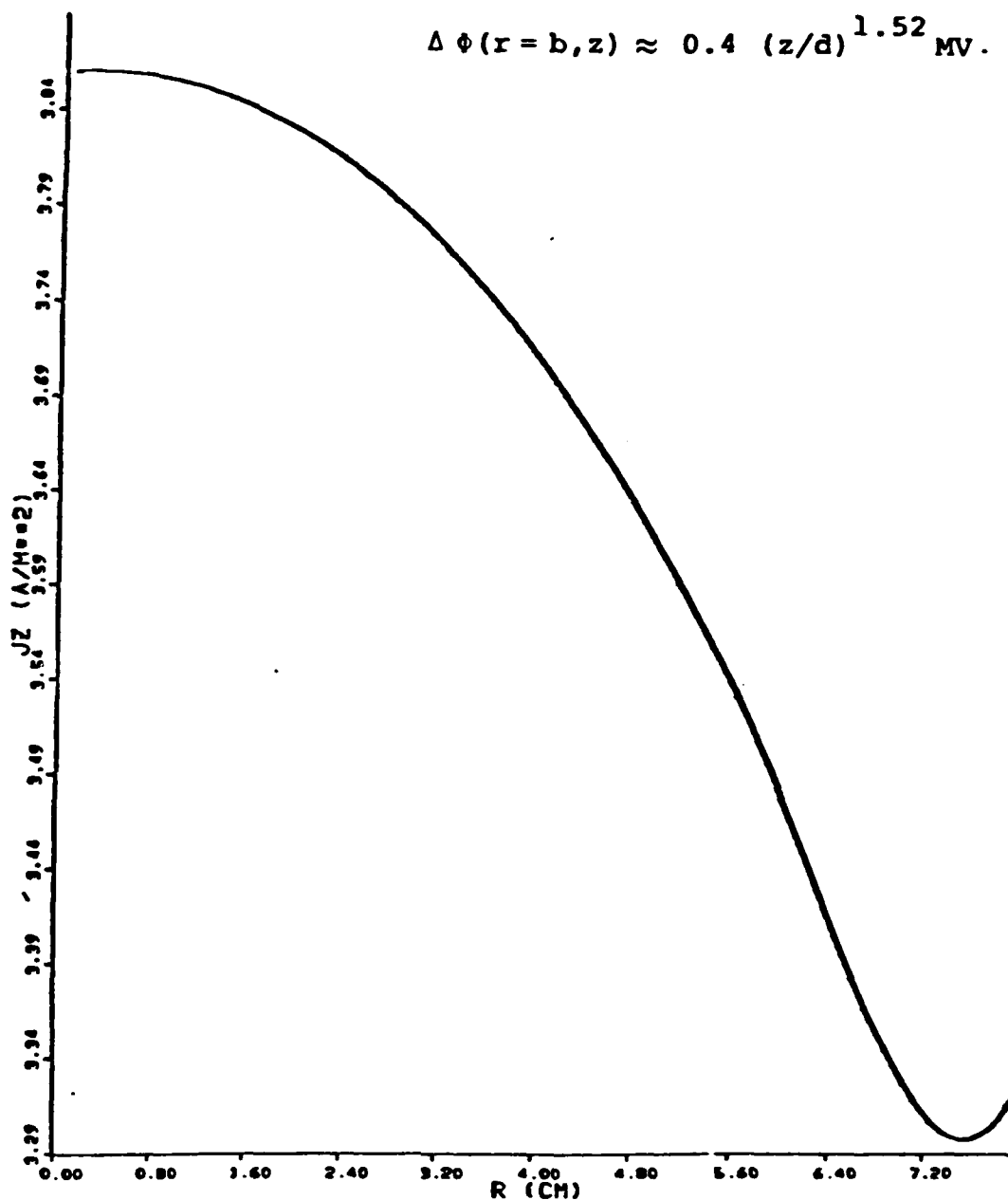


Figure 2. Cold Cathode with Sub-Child-Langmuir Potential Grading



JZ VS R

Figure 3. Current Density Profile @ Cathode for Sub-Child-Langmuir Potential Grading (Modified Design)

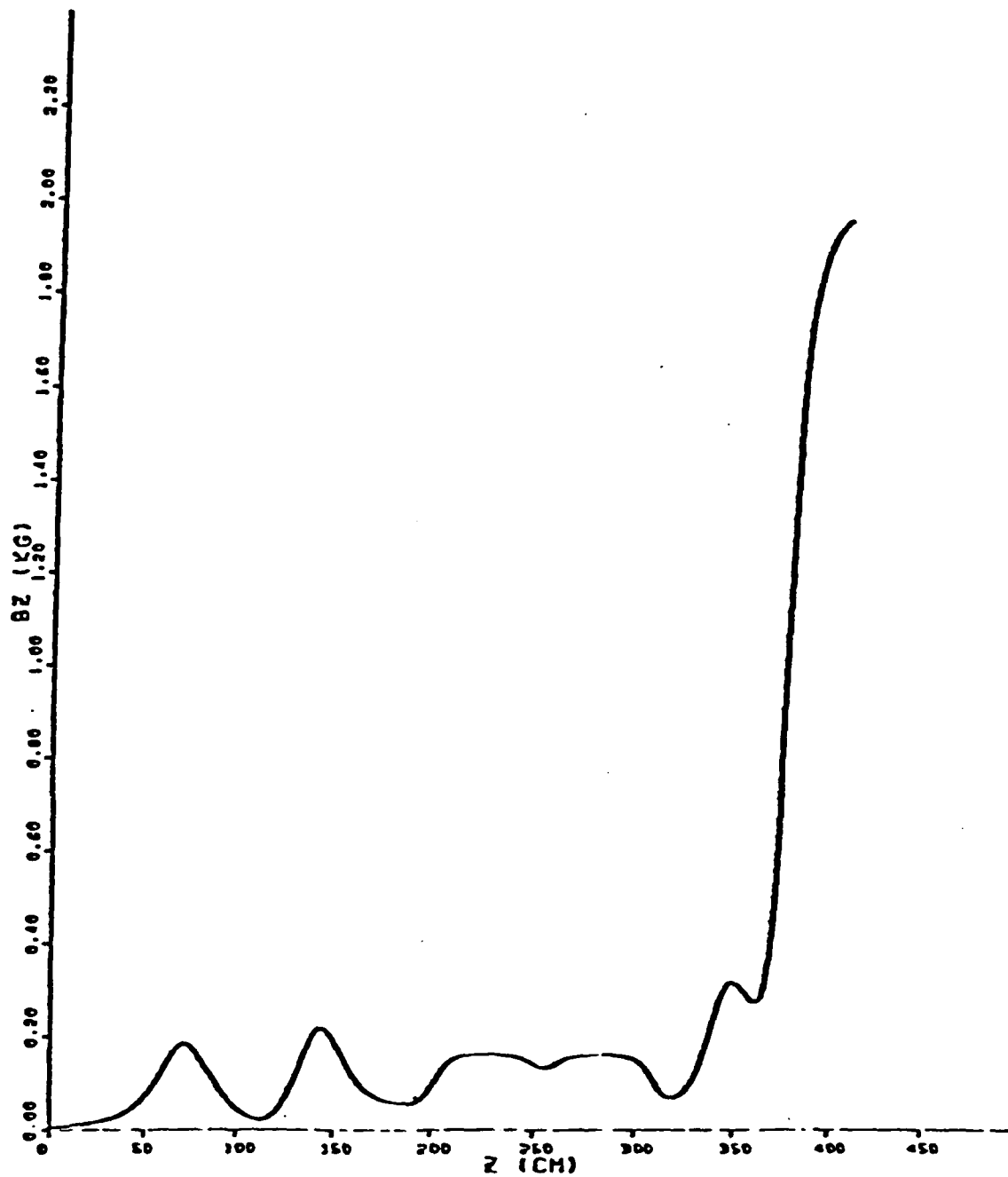
13-MAY-82
06:42:45

As shown in Figure 1, the electron beam, once formed, must be transported through a complex array of magnetic field coils and radially varying conducting boundaries, and through two accelerating gaps in the induction module before being finally compressed and injected into the wiggler solenoid, which begins 380 cm downstream of the cathode surface. In order to study this challenging transport problem, we have employed in addition to theoretical analysis, a one-dimensional $R(z)$ beam envelope code and the two-dimensional (r,z) , steady state, relativistic particle simulation code STAGEN.

The STAGEN code retains all three components of velocity and of the electric and magnetic fields, but is restricted to the two independent variables r,z , appropriate to situations which are symmetric in the azimuthal coordinate θ . In order to reduce the computing requirements to a manageable level, the axial transport is divided into four "stages." The first stage extends to $z = 23$ cm, encompassing the 11 cm length of the anode-cathode region plus 12 cm beyond the anode mesh. The flow is initiated from an equipotential near but not on the cathode surface--typically $\phi - \phi_{\text{cathode}} \leq 20$ kV. Stage 2 extends from $z = 23$ cm to $z = 111$ cm, encompassing the initial focusing coil and the conductor wall flaring out to a radius of 17.5 cm. Stage 3 extends from $z = 111$ cm to $z = 258$ cm, and encompasses three more focusing coils, the first induction accelerating

gap (of 200 kV), and the first induction solenoid. Stage 4 extends from $z = 258$ cm to $z = 406$ cm, and encompasses the second induction solenoid, the second induction accelerating gap (also of 200 kV), another focusing coil, and the first 26 cm of the wiggler solenoid.

Under this contract, STAGEN has been exercised repeatedly to examine the beam transport through the first four meters of the long pulse induction linac for a variety of diode potential gradings and for several magnetic field configurations. Because the constraints of operating with the existing coil configuration and achieving an order of magnitude beam radius compression into the wiggler solenoid make the transport so difficult, emphasis on the STAGEN runs was first placed on simulating typical experimental parameters. In this way, support for the experiment could be provided, feedback could be received, and an appreciation for the crucial elements of the transport physics could be obtained. An example of these transport simulations is provided in Figures 4-10. Figure 4 displays the magnetic field profile in the LPIL for a typical set of coil currents, including the magnetic ramp into the 2 kG wiggler solenoid. Figure 5 shows the Stage 1 transport through the diode. Theoretical calculations indicated that momentum scatter at the anode mesh should create emittance of only $\sim 25\pi$ mrad-cm. However, experimental indications suggested an emittance of $\sim 200\pi$ mrad-cm created at the surface of the hairbrush



BZ VS Z

Figure 4. Magnetic Field Profile from
December 1981 Data

2-APR-82
12:20:30

(000)

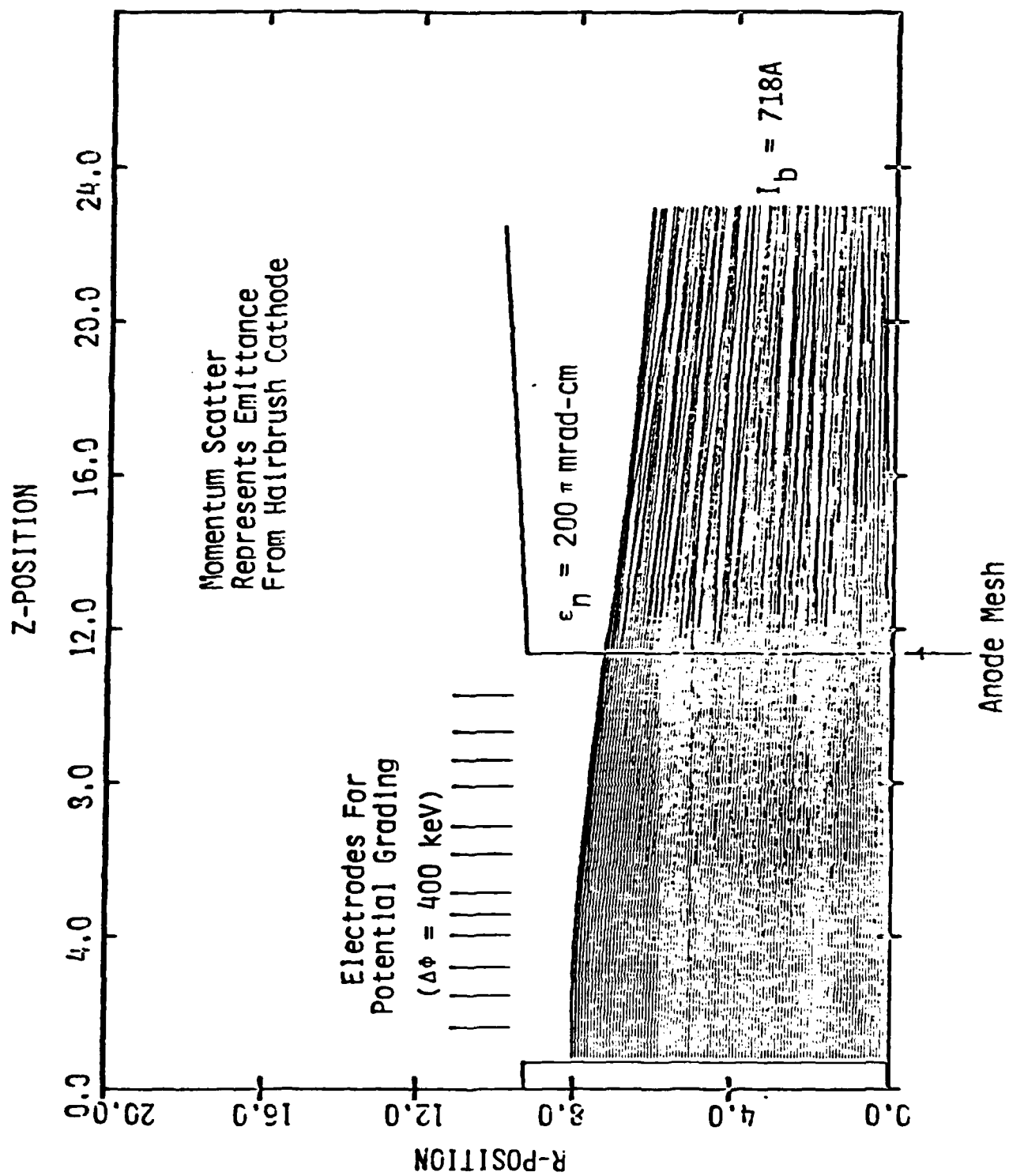


Figure 5. Beam Transport through Stage 1

AD-A174 586

CALCULATIONS OF THE FORMATION AND TRANSPORT OF HIGH
QUALITY HIGH CURRENT (U) AUSTIN RESEARCH ASSOCIATES TX
J R THOMPSON ET AL OCT 86 I-ARA-86-U-44

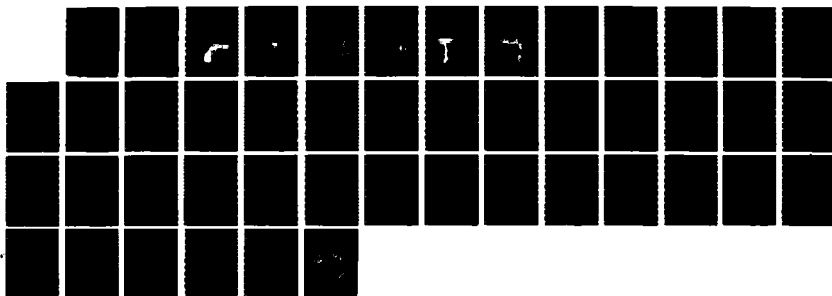
3/3

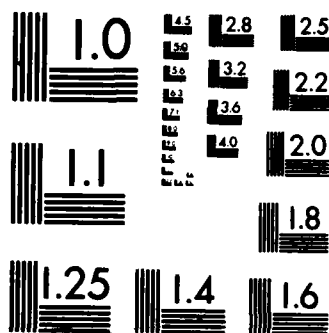
UNCLASSIFIED

N00014-81-C-0704

F/G 20/7

NL





MICROCOPY RESOLUTION TEST CHART
NATIONAL BUREAU OF STANDARDS-1963-A

cathodes. To mock up this effect, a scatter corresponding to 200π mrad-cm emittance was therefore introduced at the anode mesh for these runs. Figure 6 shows the equipotential contours in the diode region. Figures 7, 8 and 9 display the beam transport through Stages 2, 3 and 4. In Figure 8, it may be seen that 135 A of current is lost to the wall just beyond the first induction gap. For this particular case, the second induction gap was inactive. The strong beam compression of the remaining 583 A of current is seen in Figure 9. However, this strong compression excites large amplitude zero frequency cyclotron oscillations which are displayed in the β_r - z phase space plot of Figure 10. This strong sausaging will soon phase mix to create an emittance of $\sim 940\pi$ mrad-cm for this example. In Figure 11, the variation of γ_z with z is displayed for the electrons in Stage 4. At the throat of the wiggler, the median value of γ_z is found to be ≈ 1.6 ; there is a considerable spread since the outer electrons have been excited to much higher transverse velocities than have the inner electrons. These details on the phase space distribution of the electrons turned out to be quite useful⁵ in interpreting that certain of the radiation measurements indeed signify an FEL mode, as expected.

The chief difficulty in this beam transport is the large emittance growth experienced during the magnetic compression at the mouth of the wiggler solenoid. Guidance for improving the transport in this respect was obtained from

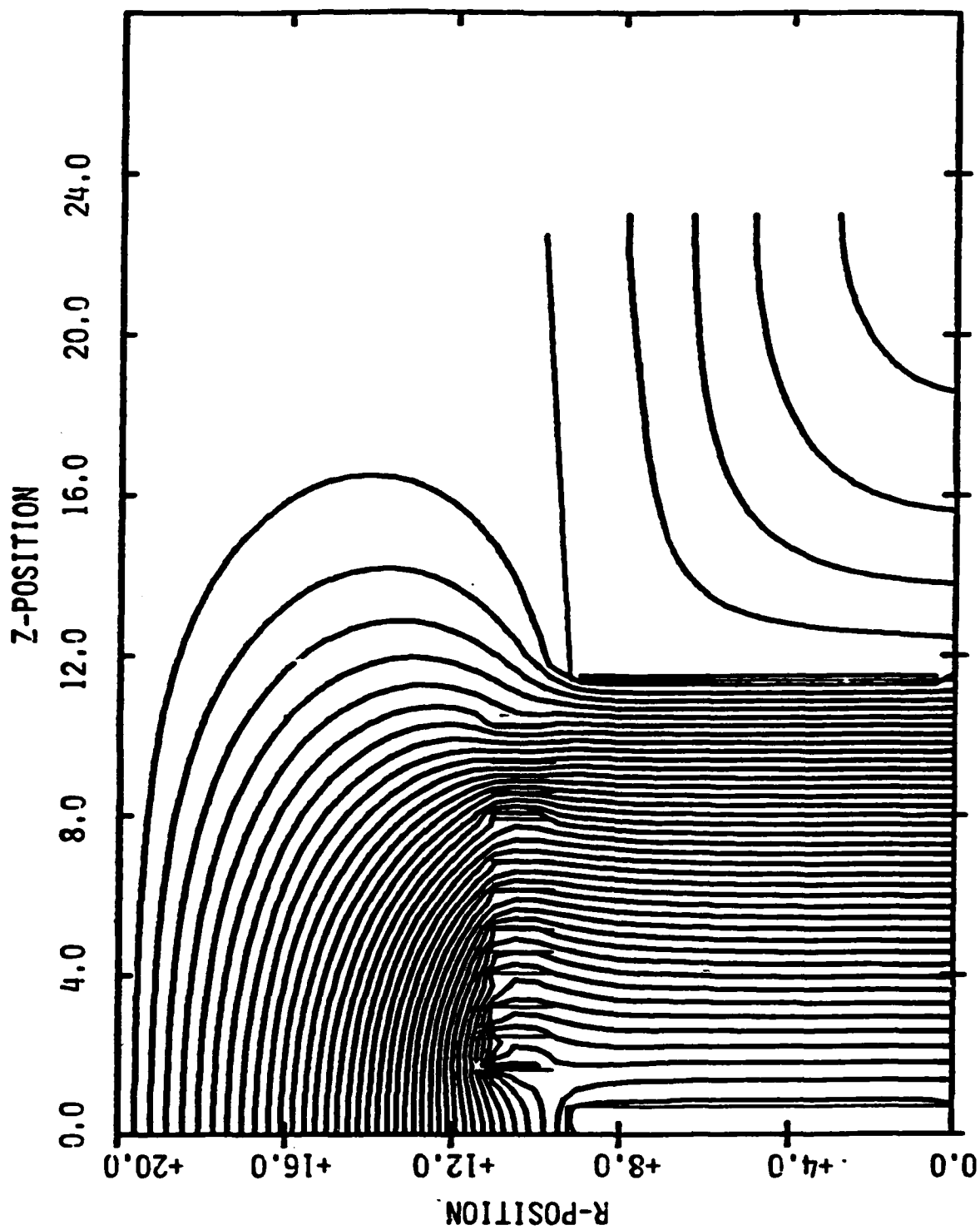


Figure 6. EQUIPOTENTIAL CONTOURS a DIODE REGION

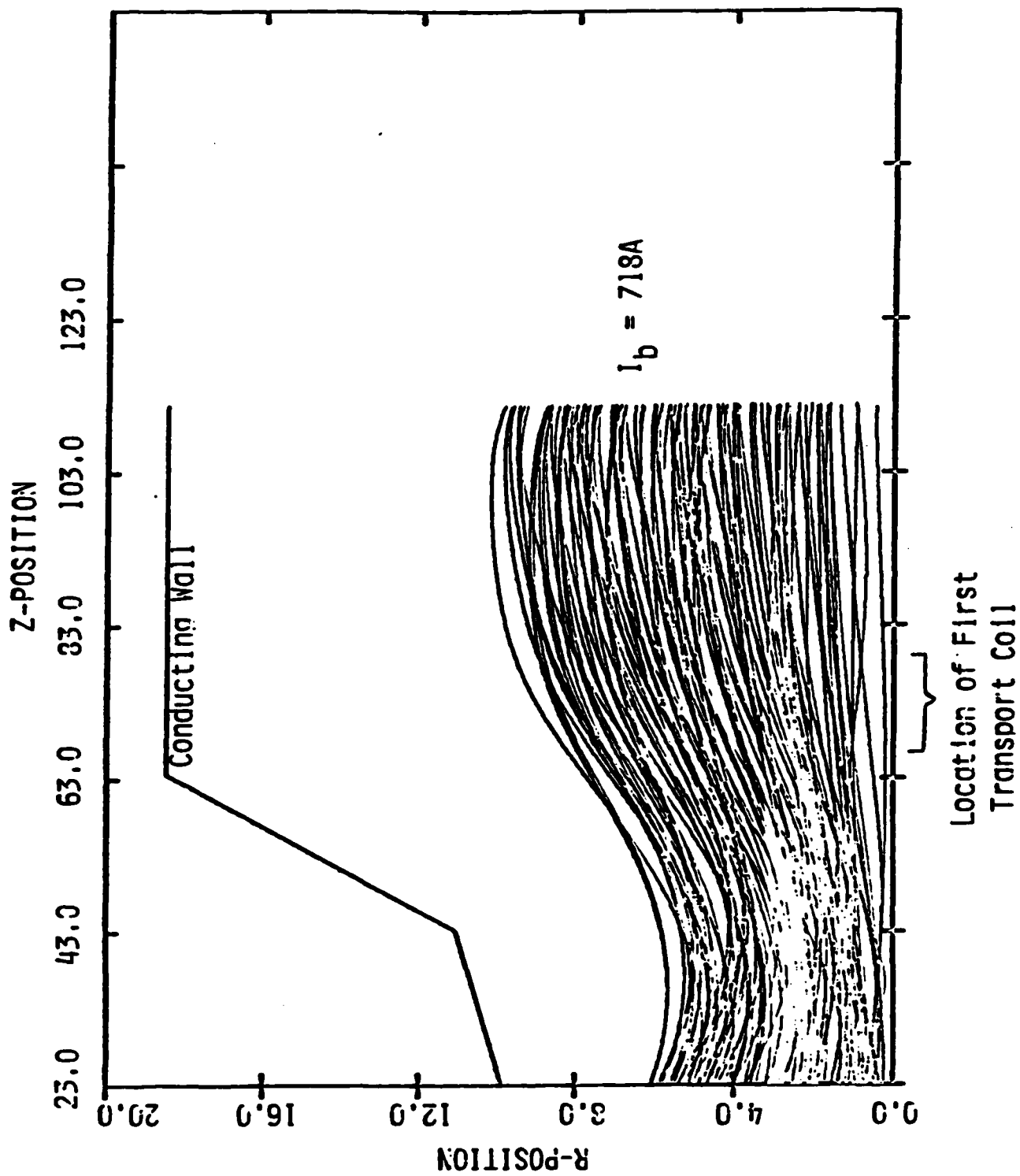


Figure 7. Beam Transport through Stage 2

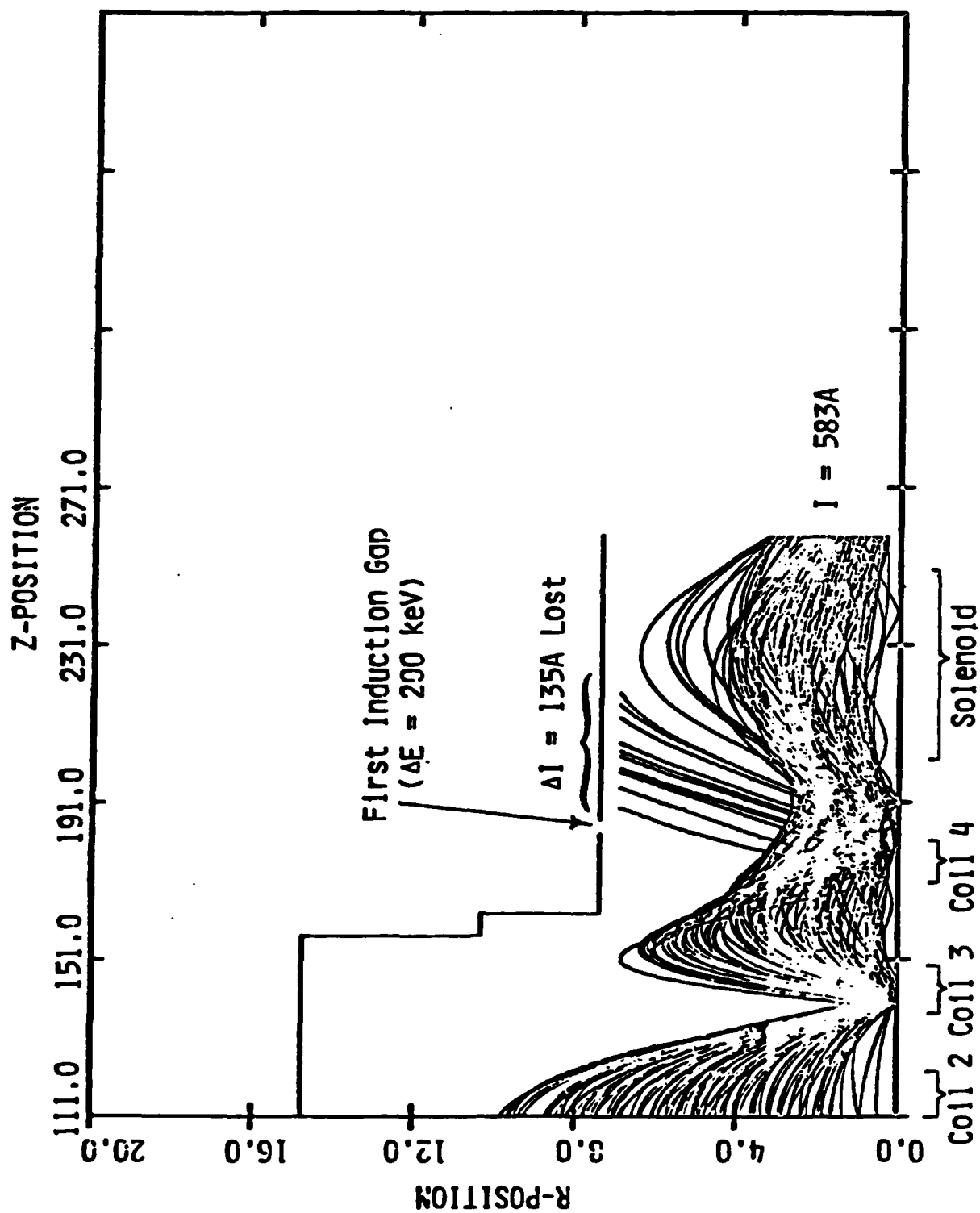


Figure 8. Beam Transport through Stage 3

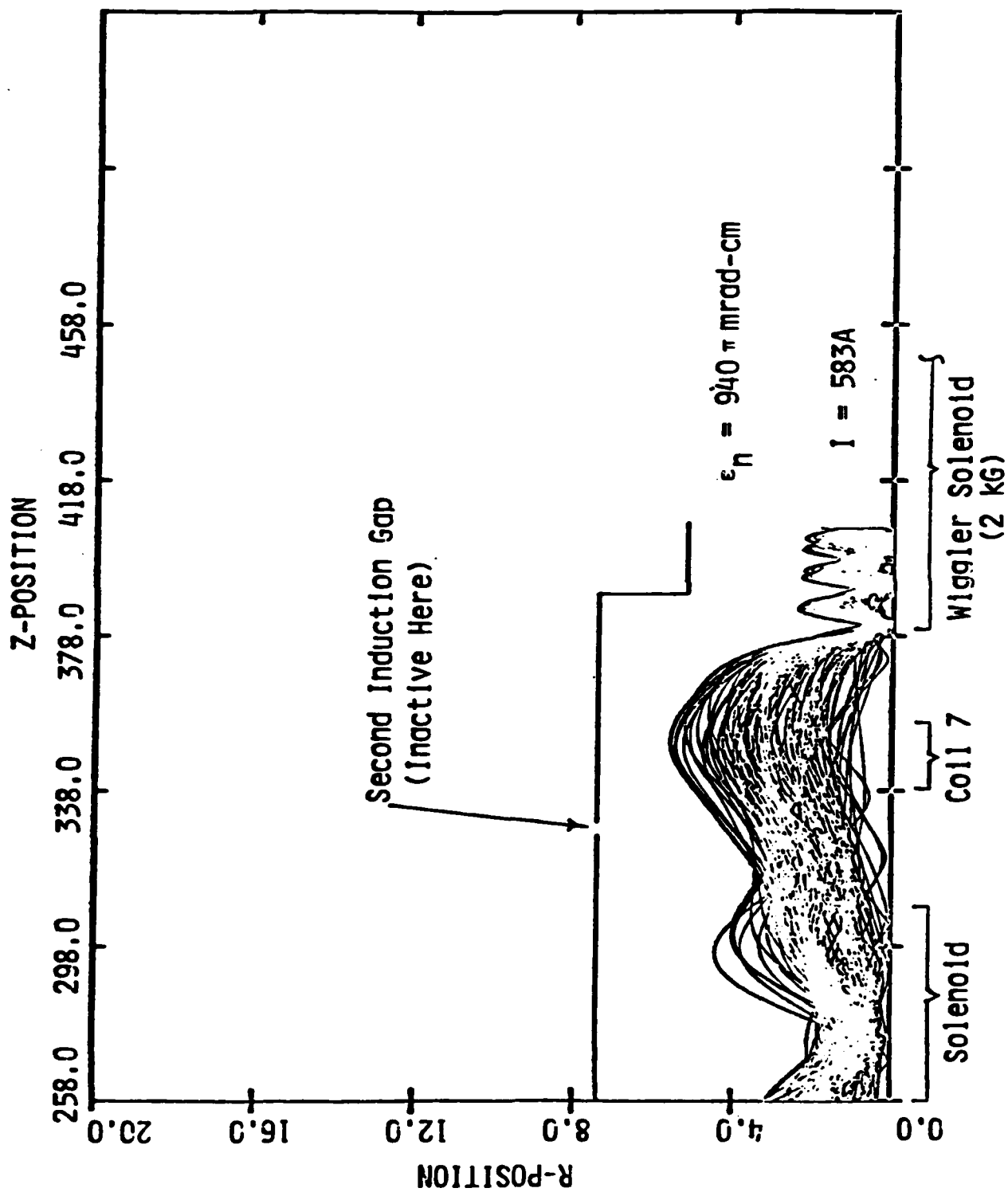


Figure 9. Beam Transport through Stage 4

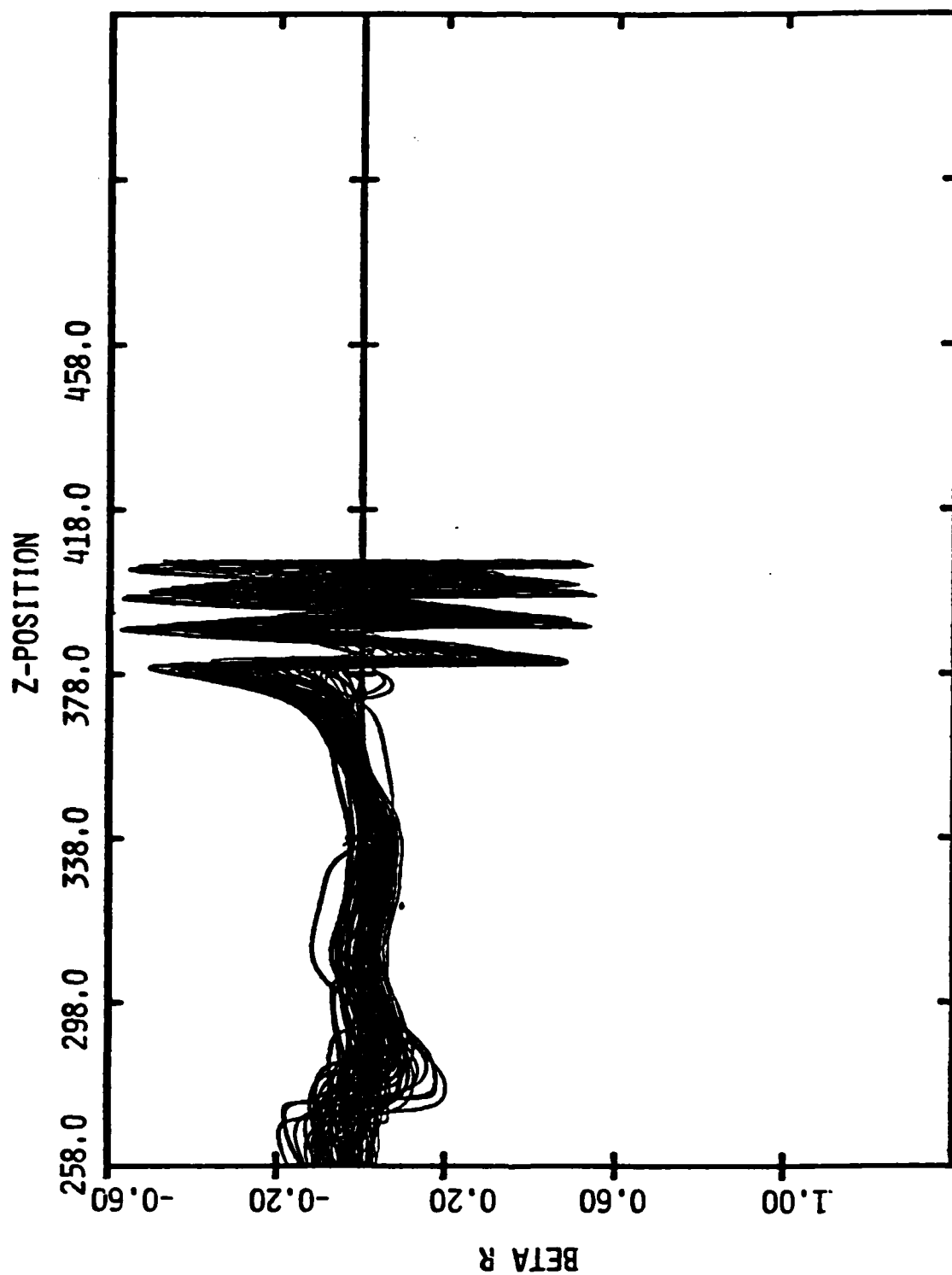


Figure 10. β_r -Z Phase Space a Stage 4 (2nd Induction Gap Off)

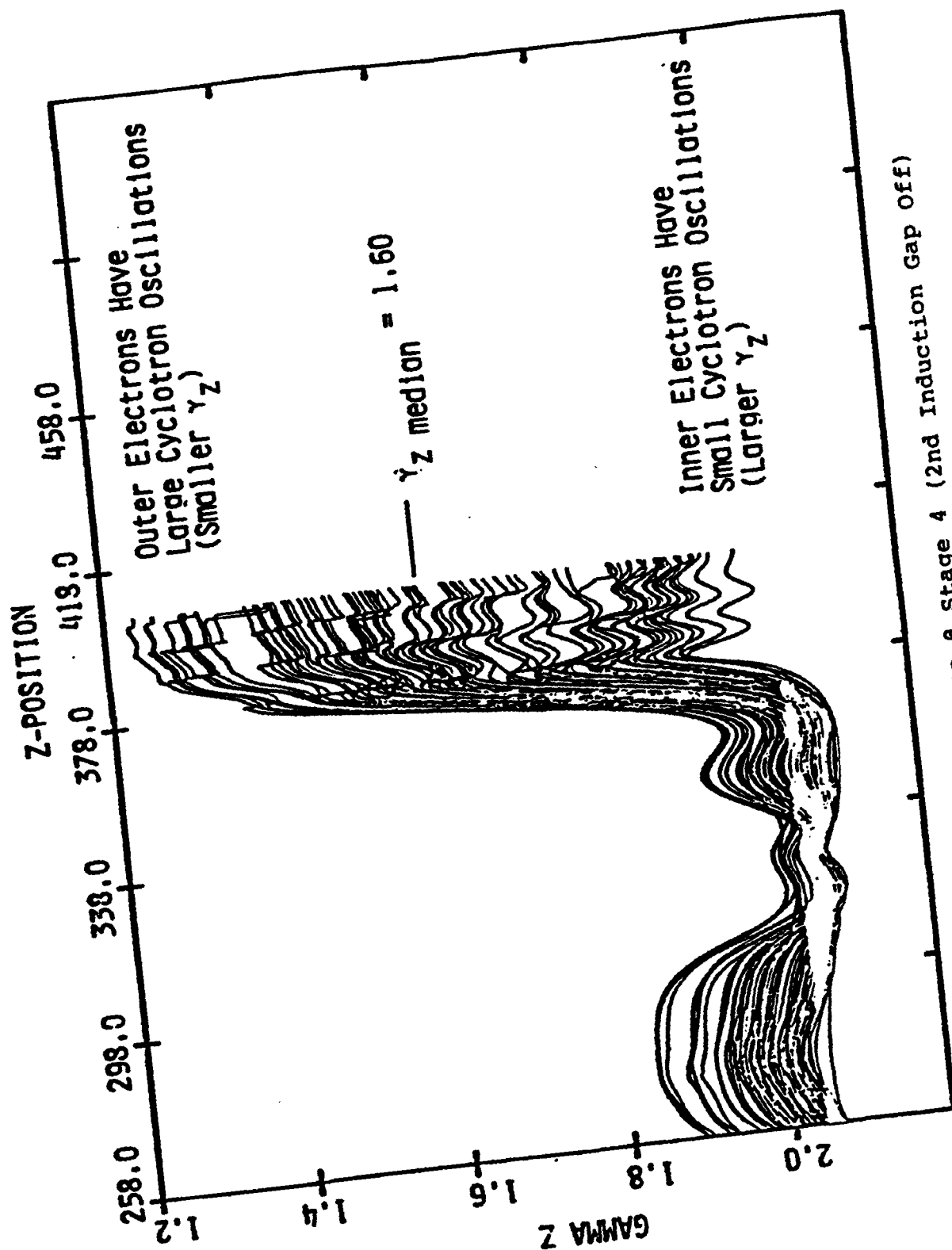


Figure 11. $\gamma_z - z$ Phase Space @ Stage 4 (2nd Induction Gap Off)

analysis with a one-dimensional envelope equation for $R(z)$, similar to the equation developed by Lee and Cooper.⁶ The assumptions, equations, and symbols used in this analysis are summarized in Tables 1 and 2. Table 3 summarizes the relative significance of the various radial "force" terms in the envelope equation. The γ'^2 term is seen to represent the focusing kicks that the beam receives in the diode and in the induction gaps. During the early portion of the transport, while $B_z \lesssim 200$ G, the beam radius is determined by competition between the magnetic $v_\phi B_z$ focusing force and the defocusing space charge force [terms (1) and (3) of Table 3]. However, as the magnetic field is increased toward 2 kG, the defocusing space charge force is outweighed by the centrifugal and pressure forces [term (4) of Table 3].

In Table 4, a Hamiltonian analysis of the cyclotron oscillations excited by these dominant forces is summarized. The beam envelope oscillations may thus be viewed as anharmonic oscillations in the pseudopotential $P(R)$, illustrated in Figure 12. This theoretical analysis suggests that large cyclotron oscillations of the magnitude observed should indeed be created if the magnetic field is suddenly increased greatly at a point where the beam radius is relatively large. On the other hand, it should theoretically be possible to minimize the oscillations by:

Table 1

ONE-DIMENSIONAL ENVELOPE EQUATIONS FOR TRANSPORT OF A
RELATIVISTIC ELECTRON BEAM THROUGH VACUUM

Reference: E. P. Lee and R. K. Cooper, Particle Accelerator 7, 83(1976)

Assumptions

- | | |
|--|---|
| (1) $B_z \neq B_z(r)$ | -- neglect diamagnetism and other radial gradients in B_z |
| (2) $\frac{\partial}{\partial \phi} = 0$ | -- assume azimuthal symmetry |
| (3) $\gamma \neq \gamma(r)$ | -- neglect transverse mass spread |
| (4) $ \beta_{\perp} \ll \beta_z $ | -- paraxial ray approximation |
| (5) $\frac{\partial}{\partial t} = 0$ | -- assume steady state behavior |
| (6) $J_z \neq J_z(r); E_r, B_{\phi} = 0$ | -- assumed for convenience |

Equations

$$\gamma(z) = \gamma_0 + \frac{e \epsilon_{\text{wall}}(z)}{mc^2} - \frac{I_b}{mc^3/e} \frac{2}{\beta} \ln \frac{b(z)}{R(z)}$$

$$R'' + \frac{\gamma'}{\beta^2 \gamma} R' + \left[\frac{\Omega_0^2(z)}{4\gamma^2 \beta^2 c^2} + \frac{\gamma''}{2\gamma \beta^2} \right] R - \frac{I_b}{\gamma^3 \beta^3 mc^3/e} \frac{1}{R} - \frac{(\epsilon^2 + P^2)}{\gamma^2 \beta^2 R^3} = 0$$

or

$$R'' + \left[\frac{\Omega_0^2(z)}{4\gamma^2 \beta^2 c^2} + \frac{(\gamma^2 + 2)\gamma'^2}{4\gamma^4 \beta^4} \right] R - \frac{I_b}{mc^3/e} \frac{1}{\gamma^2 \beta^2} \frac{1}{R} - \frac{(\epsilon^2 + P^2)}{R^3} = 0$$

Table 2. Definitions

$$\eta = \frac{d}{dz}$$

$$(\gamma_0 - 1)mc^2 = \text{electron beam energy at the anode potential}$$

$$\beta = (1 - \gamma^{-2})^{\frac{1}{2}} = \beta_z = \text{normalized axial velocity}$$

$$R(z) = \text{rms beam radius}$$

$$a(z) = \sqrt{2} R(z) = \text{outer beam radius}$$

$$R(z) = (\gamma\beta)^{\frac{1}{2}} R(z)$$

$$b(z) = \text{conducting wall radius}$$

$$e\phi_{\text{wall}}(z) = \text{wall potential (varies in acceleration regions)}$$

$$mc^2 = 511 \text{ keV}$$

$$I_b = \text{beam current}$$

$$mc^3/e = 17 \text{ kA}$$

$$\Omega_0(z) = \frac{eB_z(z)}{mc} = \text{nonrelativistic cyclotron frequency}$$

$$\epsilon = \gamma R \delta \beta_{1 \text{ rms}} = \text{normalized beam emittance (rad-cm), a constant}$$

$$P_\phi = \gamma R \beta_\phi - \frac{\Omega_0(z)}{2c} R^2 = \text{canonical momentum of beam, a constant}$$

$$\beta_r = \beta R' = \text{normalized radial fluid velocity of beam}$$

$$\beta_\phi = \frac{\Omega_0(z)}{2\gamma c} R + \frac{P_\phi}{\gamma R} = \text{normalized azimuthal fluid velocity of beam}$$

$$\beta_\perp = \left[\beta^2 R'^2 + \beta_\phi^2 + \frac{\epsilon^2}{\gamma^2 R^2} \right]^{\frac{1}{2}} = \text{normalized transverse velocity}$$

$$\frac{\epsilon}{\gamma R} = \text{normalized thermal velocity}$$

$$\epsilon_f = \left[\gamma^2 \epsilon^2 R^2 R'^2 + \gamma^2 R^2 \beta_\phi^2 \right]^{\frac{1}{2}} = \text{"fluid emittance"}$$

Table 3

RELATIVE SIGNIFICANCE OF TERMS IN ENVELOPE EQUATION

- (1) $\frac{\Omega_o^2(z)}{\gamma^2 \beta^2 c^2} R$ -- Magnetic $v_\phi B_z$ focusing forces which are important everywhere except in the diode region where B_z is very weak.
- (2) $\frac{(\gamma^2+2)\gamma'^2}{4\gamma^4 \beta^4} R$ -- Radial focusing forces which are significant (for beam current \ll Alfven current) only in the diode and in the induction gaps. These forces represent the replacement of E_r by E_z fields, and tend to locally unbalance the radial force equilibrium.
- (3) $\frac{I_b}{\gamma^2 \beta^2 mc^3/e} \frac{1}{R}$ -- Defocusing space charge forces which are in competition with magnetic focusing forces during the first three meters of large radius beam transport.
- (4) $\frac{\epsilon^2 + P_\phi^2}{R^3}$ -- Centrifugal and pressure forces which are in competition with magnetic focusing forces during the strong magnetic compression of the beam to a very small radius. Both ϵ and P_ϕ are constant downstream of the anode, and $\epsilon_{\text{diode}} \approx 200\text{-}300 \text{ mrad-cm}$ dominates the $P_\phi \approx 50 \text{ mrad-cm}$ due to the weak leakage magnetic field at the cathode.

Table 4

ANALYSIS OF INCREASE IN ZERO FREQUENCY CYCLOTRON
OSCILLATIONS DURING MAGNETIC COMPRESSION

ASSUME $\gamma' = \gamma'' = P_\phi = 0$

$$R'' + \frac{\Omega_0^2(z)}{4\gamma^2\beta^2c^2} R - \frac{I_b}{\gamma^3\beta^3mc^3/e} \frac{1}{R} - \frac{\epsilon^2}{\gamma^2\beta^2R^3} = 0$$

LET $H = \frac{1}{2} p^2 + P(R) = \text{Hamiltonian}$

$$P(R) = \frac{\Omega_0^2(z)}{8\gamma^2\beta^2c^2} R^2 - \frac{I_b}{\gamma^3\beta^3mc^3/e} \ln R + \frac{\epsilon^2}{2\gamma^2\beta^2R^2}$$

$$p \leftrightarrow R', \quad q \leftrightarrow R, \quad t \leftrightarrow z$$

(1) If $\Omega_0'(z) = 0$, $H = \text{constant of motion} = P(R_+) = P(R_-) \equiv P_0$

R_+, R_- = turning points of $R(z)$

(2) If $\Omega_0(z)$ increases adiabatically, then $H = P_0(z)$ increases adiabatically such that $J = \oint p dq$ is an adiabatic invariant.

$$\text{When } I_b \text{ term is negligible, } \frac{J}{\pi} = \frac{2\gamma\beta c P_0(z)}{\Omega_0(z)} - \frac{\epsilon}{\gamma\beta}$$

and one finds $R_{\text{max}}'^2 = \Omega_0(z)$, $R_+^2 = \Omega_0^{-1}(z)$

so that $\epsilon_f^2 = \gamma^2\beta^2R^2R'^2 + \frac{\Omega_0^2R^4}{4c^2} = \text{adiabatically invariant}$

and emittance should not be enhanced.

(3) If $\Omega_0(z)$ increases suddenly, the constant H is incremented

by $\Delta H = \frac{R^2}{8\gamma^2\beta^2c^2} \Delta\Omega_0^2$ before R and R' can change.

Thereafter, $H = \text{constant}$. When $\Delta\Omega_0^2$ is large, oscillations

are enhanced if $\Delta\Omega_0^2(z)$ occurs where R^2 is large. If

$R = R_+$ where $\Delta\Omega_0^2$ occurs, R_+ is unchanged, but

$R_{\text{max}}'^2 = \Omega_0^2(z)$, so that $\epsilon_f^2 \sim \Omega_0^2(z_+)^2 R_+^4/c^2$, and emittance is greatly enhanced.

- a) timing a sudden increase in magnetic field to occur when the beam envelope is near a radial minimum; or
- b) increasing the magnetic field strength only adiabatically in z .

Some attempts were subsequently made experimentally to comply with these theoretical recommendations--subject to constraints of the existing coil geometry. An additional transport coil was added to make the compression more adiabatic and some improvement in transport was seen. However, the continuing necessity for such substantial magnetic compression and the constraints of working with the existing accelerator configuration imply a limitation to the improvements which may be practically realized in this way.

APPENDIX F REFERENCES

1. Letter reports from J. R. Thompson to C. W. Roberson, dated April 2, 1982; April 27, 1982; and May 13, 1982.
2. Letter report from B. N. Moore to C. W. Roberson, dated June 29, 1982.
3. J. R. Thompson, B. N. Moore, M. L. Sloan and J. R. Uglum, Bull. Am. Phys. Soc. 27, 1011 (1982).
4. J. E. Boers, "Digital Computer Simulation of High-Current, Relativistic, and Field Emission Electron Tubes," Record of 11th Symposium on Electron, Ion, and Laser Beam Technology, San Francisco Press, Inc. (1971).
5. C. W. Roberson, J. A. Pasour, F. Mako, R. Lucey, and P. Sprangle, "A Free Electron Laser Driven by a Long Pulse Induction Linac," NRL Memo Report 5013 (1983).
6. E. P. Lee and R. K. Cooper, Particle Accelerators 7, 83 (1976).

A P P E N D I X G

Beam Emittance Due to Excitation and Phase
Mixing of Cyclotron Oscillations

BEAM EMITTANCE DUE TO EXCITATION AND PHASE MIXING OF CYCLOTRON OSCILLATIONS

Consider a cold, fluid, relativistic electron beam which is magnetized and is smoothly propagating in a "slowly rotating" beam equilibrium. Suppose that the electron beam propagates axially through a spatial magnetic discontinuity. This will set up cyclotron oscillations upon the beam which will ring downstream of the discontinuity until they phase mix into an effective beam temperature, or transverse emittance. We wish to compute an expression for this cyclotron emittance as a function of the magnetic discontinuity and the other equilibrium parameters.

For the purposes stated above, we may employ the beam envelope equations to compute the amplitude of the cyclotron oscillations prior to phase mixing. Then an average of the cyclotron oscillations over the axial coordinate may be performed analytically to recover the effect of phase mixing.

The beam envelope equation may be expressed in the "edge notation" form

$$r'' + \frac{(e B_z / mc)^2}{4 \gamma^2 \beta^2 c^2} r - \underbrace{\frac{2 I_b}{\gamma^2 \beta^3 mc^3 / e}}_{\frac{2v}{\gamma^3 \beta^2}} \frac{1}{r} - \frac{(\epsilon_{th}^2 + p_{\theta}^2)}{\gamma^2 \beta^2} \frac{1}{r^3} = 0 \quad (1)$$

where $r(z)$ = radius of the outer edge of the beam

$$r' = \frac{dr}{dz}$$

$$v = \frac{I_b}{\beta mc^3/e} = \frac{\omega_p^2 \bar{r}^2}{4c^2} = \frac{|I_b (kA)|}{17\beta} \quad (2)$$

$$P_\theta = \gamma r \beta_\theta + \frac{(eB_z/mc)}{2c} r^2 = \text{normalized canonical momentum}$$

$$\epsilon_{th} = \gamma r \delta \beta_{th} = \text{normalized edge emittance}$$

It may be shown that

$$P_\theta' = 0 \quad \text{for } \theta\text{-symmetric beams} \quad (3)$$

$$\epsilon_{th}' = 0 \quad \text{for vacuum propagation} \quad (4)$$

and it has been assumed that $\gamma' = \gamma'' = 0$.

The coefficient v is positive for electron beams traveling in either direction. We have assumed that the beam is traveling in the \hat{z} direction, so that $\beta_z \approx \beta > 0$. For electrons, $e = -|e|$ so that the vector potential piece of P_θ is < 0 when $B_z > 0$.

β_θ represents the normalized θ -velocity of the beam as a whole, and is characteristic of an outer, edge electron.

$\delta\beta_{th}$ represents the normalized thermal velocity of the beam as a whole, and is also characteristic of an outer, edge electron.

It should be noted that the above quantities differ by factors of 2 or $\sqrt{2}$ from the corresponding quantities in the envelope equations of Lee and Cooper (Ref. 1). This is because Lee and Cooper used $R(z)$ = rms radius of the beam, and correspondingly:

$$\begin{aligned} r(z) &\longleftrightarrow R(z) = r(z)/\sqrt{2} \\ \delta\beta_{th} &\longleftrightarrow \delta\beta_{rms} = \delta\beta_{th}/\sqrt{2} \\ \beta_{\theta}(\text{edge}) &\longleftrightarrow \beta_{\theta}(R) = \beta_{\theta}(\text{edge})/\sqrt{2} \\ P_{\theta}(\text{edge}) &\longleftrightarrow P_{\theta}(R) = P_{\theta}(\text{edge})/2 \\ \epsilon_{th}(\text{edge}) &\longleftrightarrow \epsilon_{th}(R) = \epsilon_{th}(\text{edge})/2 \end{aligned}$$

The emittance which appears in the envelope equations is defined in terms of an average over the beam particles of the square of the transverse particle velocities. For example, in the "rms notation" of Lee and Cooper, one has

$$\epsilon_{th}(R)^2 \equiv \gamma^2 R^2 \left[\langle \beta_{\perp}^2 \rangle - \beta^2 R'^2 - \beta_{\theta}(R)^2 \right] \equiv \gamma^2 R^2 \delta\beta_{rms}^2 \quad (5)$$

where

$$\langle \beta_{\perp}^2 \rangle \equiv \frac{1}{I_b} \int_0^{\infty} dr \, 2\pi r J_b(r) (\beta_r^2 + \beta_{\theta}^2) = \beta_{\perp rms}^2$$

This equation may be reexpressed in "edge notation" as follows:

$$\epsilon_{\text{tot}}^2 \equiv \gamma^2 r^2 \beta_{\text{edge}}^2 = \underbrace{\gamma^2 \beta^2 r^2 r'^2 + \gamma^2 r^2 \beta_{\theta}(r)^2}_{\epsilon_f(\text{edge})^2} + \epsilon_{\text{th}}(\text{edge})^2 \quad (6)$$

where $\beta_{\text{edge}}^2 = 2 \beta_{\text{rms}}^2$
 $r = \text{edge radius} = \sqrt{2} R$

$\epsilon(\text{edge}) = 2 \epsilon(\text{rms})$

$\beta r' = \beta \frac{dr}{dz} = \beta_r(r) = \beta_r(\text{edge}) = \text{normalized "fluid" radial velocity of the beam as a whole, characteristic of an outer, edge electron}$

$\beta_{\theta}(r) = \text{normalized "fluid" azimuthal velocity of the beam as a whole, characteristic of an outer, edge electron}$

$\delta\beta_{\text{th}}(r) \equiv \frac{\epsilon_{\text{th}}(\text{edge})}{\gamma r} = \text{normalized thermal velocity of the beam as a whole, characteristic of an outer edge electron.}$

Note that:

$$\beta_{\text{edge}}^2 = \beta_r(\text{edge})^2 + \beta_{\theta}(r)^2 + \delta\beta_{\text{th}}(r)^2 .$$

The emittance which appears in the envelope equation is ϵ_{th} . It characterizes the beam temperature and is a constant of the motion (i.e., $\epsilon_{\text{th}}' = 0$) for the case of vacuum beam propagation--under the assumptions used in deriving the envelope equations. However, these assumptions included such things as neglecting the radial dependence of γ and β_z . Therefore, it is possible for cyclotron oscillations to be excited upon the

electron beam, which are initially fluidlike (i.e., nonthermal)--but which, because of the radial variations in γ and β_z , eventually lead to phase variations in the cyclotron motion as the beam propagates axially downstream. If the radial averages required in the emittance definition are repeated at an axial position downstream of the cyclotron excitation, the corresponding "phase mixing" will lead to an increase in the beam temperature or emittance, which is not predicted strictly from the envelope equations alone for the reason that these equations neglect the radial dependences which produce the cyclotron phase variations. However, it is possible to compute the amplitude of the initial fluid cyclotron oscillations from the envelope equations, and this is sufficient to imply the post-phase-mixing emittance since the effect of the phase-mixing averages is easily obtained by analytically performing averages over the axial variation in the cyclotron oscillations.

For the specific problem which we have posed, we suppose that the electron beam is initially cold in the region upstream of the magnetic discontinuity, so that $\epsilon_{th} \approx 0$. However, the magnetic discontinuity will excite fluid cyclotron oscillations, for which the corresponding fluid emittance (in edge notation) is

$$\epsilon_f^2(z) = \gamma^2 \beta^2 r^2(z) r'^2(z) + \gamma^2 r^2(z) \beta_\theta^2(z) = \gamma^2 r^2(z) \beta_{\perp f}^2(z) \quad (7)$$

The eventual downstream thermal emittance which results from the phase mixing of these fluid oscillations may be computed by performing a z-average to correspond to the effect of the phase mixing, and then subtracting off the residual, nonthermal portion of $\epsilon_f^2 = \gamma^2 r^2 \beta_{lf}^2$ which is due to the mean fluid precession of the beam in the downstream equilibrium. This leads to

$$\Delta \epsilon_{th}^2 = \gamma^2 \beta^2 \left\langle r^2(z) r'^2(z) \right\rangle_z + \gamma^2 \left\langle r^2(z) \beta_\theta^2(z) \right\rangle_z - \gamma^2 \left\langle r(z) \beta_\theta(z) \right\rangle_z^2 \quad (8)$$

where $\gamma^2 \left\langle r(z) \beta_\theta(z) \right\rangle_z^2$ is the component of $\epsilon_f^2 = \gamma^2 r^2 \beta_{lf}^2$ due to the mean fluid precession of the beam in the downstream equilibrium. Here $\left\langle \right\rangle_z$ represents a z-average over one cycle of the cyclotron oscillations.

By employing the canonical momentum (constant) Equation (2), one may eliminate $\beta_\theta(z)$ in favor of $r(z)$, so that the increase in thermal emittance may finally be expressed in terms of the beam radius function $r(z)$ alone.

$$\gamma r(z) \beta_\theta(z) = P_\theta + \frac{\Omega_0}{2c} r^2(z) \quad (9)$$

where $\Omega_0 \equiv \frac{|e| B_z}{mc} > 0$.

It follows that

$$\Delta \epsilon_{th}^2 = \gamma^2 \beta^2 \left\langle r^2(z) r'^2(z) \right\rangle_z + \frac{\Omega_0^2}{4c^2} \left[\left\langle r^4(z) \right\rangle_z - \left\langle r^2(z) \right\rangle_z^2 \right] \quad (10)$$

It remains only to compute the envelope oscillations which are excited by a magnetic discontinuity, and then to evaluate $\Delta\epsilon_{th}^2$ which results from the phase mixing of these oscillations.

Roberson (Ref. 2) linearized the envelope Equation (1) and solved for the linearized envelope response to the magnetic perturbation shown in Figure 1, which is

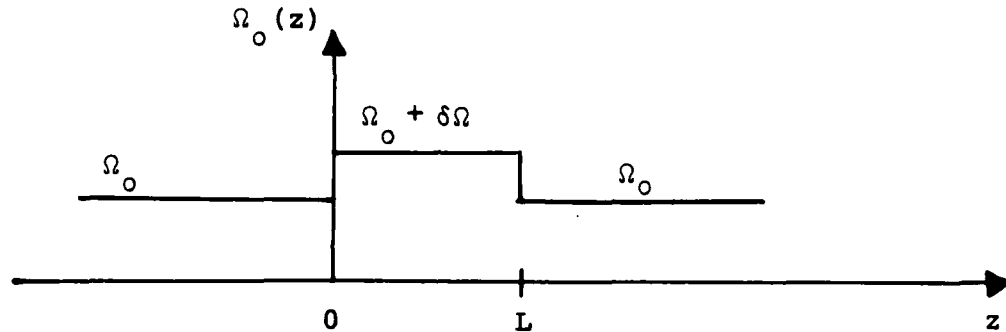


Figure 1. Magnetic discontinuity which excites cyclotron oscillations upon an electron beam.

$$\Omega_0(z) = \frac{|e| B_z(z)}{mc} = \begin{cases} \Omega_0 & , \quad z < 0 \\ \Omega_0 + \delta\Omega & , \quad 0 < z < L \\ \Omega_0 & , \quad L < z \end{cases} \quad (11)$$

where $\delta\Omega = \frac{|e| \delta B_z}{mc}$

and $\delta\Omega$ can be of either sign. The solution to Equation (1) is found to be

$$r(z) = \begin{cases} r_0 & ; z \leq 0 \\ r_0 \left[1 - \frac{\Omega_0 \delta\Omega}{k^2 \gamma^2 \beta^2 c^2} \sin^2\left(\frac{kz}{2}\right) \right] & ; 0 \leq z \leq L \\ r_0 \left[1 - \frac{\Omega_0 \delta\Omega}{k^2 \gamma^2 \beta^2 c^2} \sin \frac{kL}{2} \sin\left(kz - \frac{kL}{2}\right) \right] & ; L \leq z \end{cases} \quad (12)$$

where

$$k^2 \equiv \frac{\Omega_0^2}{\gamma^2 \beta^2 c^2} - \frac{4v}{\gamma^3 \beta^2 r_0^2} \quad (13)$$

In the downstream region $L \leq z$, the linearized cyclotron oscillations have the form

$$r(z) = r_0 + \delta r \sin\left(kz - \frac{kL}{2}\right) \quad (14)$$

where

$$\delta r \equiv - \frac{r_0 \Omega_0 \delta\Omega}{k^2 \gamma^2 \beta^2 c^2} \sin \frac{kL}{2} \quad (15)$$

If this form is inserted into the expression (10) for $\Delta\epsilon_{th}^2$ and the result is evaluated to lowest order in $\delta r^2/r_0^2$, one obtains the result

$$\Delta \epsilon_{th}^2 \approx \frac{1}{2} k^2 \gamma^2 \beta^2 r_0^2 \delta r^2 + \frac{\Omega_0^2}{2c^2} r_0^2 \delta r^2$$

$$\Delta \epsilon_{th}^2 \approx \delta r^2 \left[\frac{\Omega_0^2 r_0^2}{c^2} - \frac{2v}{\gamma} \right] = 2 \left[\frac{\Omega_0^2 r_0^2}{c^2} - \frac{2v}{\gamma} \right] \langle \delta r^2(z) \rangle_z \quad (16)$$

As an aside, consider for a moment the beam equilibrium. If the linearized form $r = r_0 + \delta r \sin(kz - kL/2)$ is inserted into the envelope equation and the equation is then averaged in z , there results

$$\frac{p_\theta^2}{r_0^2} \left(1 + 3 \frac{\delta r^2}{r_0^2} \right) = \frac{\Omega_0^2 r_0^2}{4c^2} - \frac{2v}{\gamma} \left(1 + \frac{\delta r^2}{2r_0^2} \right) - \frac{\epsilon_{th}^2}{r_0^2} \left(1 + 3 \frac{\delta r^2}{r_0^2} \right) \geq 0 \quad (17)$$

where the equation is carried to $\mathcal{O}(\delta r^2/r_0^2)$ to suggest the influence of δr^2 upon the equilibrium. The assertion that the RHS above must be positive gives one of the equilibrium criteria. In the limit that $\delta r = 0$ and $\epsilon_{th} = 0$, this reduces to one of the usual criteria for cold, fluid equilibria:

$$1 \geq \frac{2v}{\gamma} \frac{4c^2}{\Omega_0^2 r_0^2} \approx \frac{I_b \text{ (kA)}}{0.7 B_z^2 \text{ (kG)} r_0^2 \text{ (cm)} \gamma \beta} \quad (18)$$

It may be noted that when $\delta r^2 \neq 0$, the equilibrium criteria is more difficult to satisfy. Likewise, increasing ϵ_{th}^2 makes

equilibrium more difficult. Suppose that the above equilibrium inequality is well satisfied, so that $\Omega_o^2 r_o^2 / 4c^2$ dominates the RHS. Then, by expansion, one has

$$\frac{P_\theta}{r_o} \approx \frac{-\frac{\Omega_o r_o}{2c}}{\left(1 + \frac{3\delta r^2}{r_o^2}\right)^{\frac{1}{2}}} \left\{ 1 - \left[\frac{\frac{2v}{\gamma} \left(1 + \frac{\delta r^2}{2r_o^2}\right) + \frac{\epsilon_{th}^2}{r_o^2} \left(1 + \frac{3\delta r^2}{r_o^2}\right)}{(\Omega_o^2 r_o^2 / 2c^2)} \right] \right\} \quad (19)$$

(Recall that at slow equilibrium precession, $P_\theta < 0$ for electrons with $B_z > 0$.)

From the P_θ Equation (2), one may define a z-averaged value of the mean precessional velocity as

$$\bar{\beta}_\theta \equiv \frac{\langle \gamma r(z) \beta_\theta(z) \rangle_z}{\langle \gamma r(z) \rangle_z} = \frac{P_\theta}{\gamma r_o} + \frac{\Omega_o r_o}{2\gamma c} + \frac{\Omega_o \delta r^2}{4\gamma c r_o} \quad (20)$$

Using the previous equilibrium expression for P_θ gives

$$\bar{\beta}_\theta \approx \frac{\Omega_o r_o}{2\gamma c} \left\{ \frac{2\delta r^2}{r_o^2} + \frac{\frac{2v}{\gamma} \left(1 - \frac{\delta r^2}{r_o^2}\right) + \frac{\epsilon_{th}^2}{r_o^2} \left(1 + \frac{3}{2} \frac{\delta r^2}{r_o^2}\right)}{(\Omega_o^2 r_o^2 / 2c^2)} \right\} \quad (21)$$

$$< \sqrt{1 - \beta_z^2} \approx \frac{1}{\gamma}$$

The second equilibrium criteria comes from requiring that the mean precessional velocity should obey $\bar{\beta}_\theta < \sqrt{1 - \beta_z^2} \approx 1/\gamma$ as shown above. It may be seen that the presence of waves (i.e., $\delta r^2 \neq 0$) causes the mean precessional velocity to increase, and hence makes this second equilibrium criteria more difficult to satisfy as well. In the limit of $\delta r = 0 = \epsilon_{th}$, this criterion reduces to the second criterion for cold, fluid equilibria:

$$1 \geq \frac{2v}{\gamma} \frac{c}{\Omega_0 r_0} = \frac{I_b \text{ (kA)}}{5 B_z \text{ (kG)} r_0 \text{ (cm)} \gamma \beta} \quad (22)$$

and for large values of $\Omega_0 r_0 / c$, this criterion is the more demanding.

If the above expression for $\bar{\beta}_\theta$ is employed, one may show that

$$\frac{\langle \gamma r(z) \beta_\theta(z) \rangle_z^2}{\langle \gamma^2 r^2(z) \beta_\theta^2(z) \rangle_z} = \frac{\left[\delta r^2 + \frac{2vc^2}{\gamma \Omega_0^2} + \frac{\epsilon_{th}^2 c^2}{\Omega_0^2 r_0^2} \right]^2}{\frac{1}{2} r_0^2 \delta r^2 + \left[\frac{2vc^2}{\gamma \Omega_0^2} + \frac{\epsilon_{th}^2 c^2}{\Omega_0^2 r_0^2} \right]^2} \quad (23)$$

where the $\delta r^2 / r_0^2$ corrections to v and ϵ_{th}^2 have been omitted.

When $\delta r^2 \rightarrow 0$, $\langle \gamma r \beta_\theta \rangle_z^2 \rightarrow \langle \gamma^2 r^2 \beta_\theta^2 \rangle_z$ so that $\gamma^2 r^2 \beta_\theta^2$ is dominated by the fluid piece $\langle \gamma r \beta_\theta \rangle_z^2$, and $\Delta \epsilon_{th}^2 \rightarrow 0$. However, if the beam is excited to the degree that

$$\delta r^2 > \left[\frac{2v c^2}{\gamma \Omega_0^2} + \frac{\epsilon_{th}^2 c^2}{\Omega_0^2 r_0^2} \right]^2 / r_0^2 \quad (24)$$

then

$$\frac{\langle \gamma r \beta_\theta \rangle^2}{\langle \gamma^2 r^2 \beta_\theta^2 \rangle} \ll 1 \quad (25)$$

so that the fluid precessional piece of $\gamma^2 r^2 \beta_\theta^2$ is negligible in comparison with the cyclotron wave piece.

When the magnetic guide field is strong enough that the equilibrium criteria are very well obeyed, the increased thermal emittance due to the phase mixing of cyclotron oscillations is given by

$$\Delta \epsilon_{th}^2 \approx \frac{2 \Omega_0^2 r_0^2}{c^2} \langle \delta r^2(z) \rangle_z = \frac{\Omega_0^2 r_0^2 \delta r^2}{c^2} \quad (26)$$

If this "cyclotron wave emittance" is the dominant source of parallel velocity spread, then

$$\frac{\Delta \gamma_{||}}{\gamma} = \gamma^2 \beta_z \Delta \beta_z \approx \frac{\Delta \epsilon_{th}^2}{2 r_0^2} \approx \frac{\Omega_0^2 \langle \delta r^2(z) \rangle_z}{c^2} = \frac{\Omega_0^2 \delta r^2}{2 c^2} \quad (27)$$

APPENDIX G REFERENCES

1. E. P. Lee and R. K. Cooper, Particle Accelerators 7, 83 (1976).
2. Charles W. Roberson, IEEE J. Quan. Electronics QE-21, 860 (1985).

A P P E N D I X H

A Brief Note on Beam Quality in High Current, Field-Immersed Diodes

Appendix B of Renewal Proposal No. I-ARA-84-U-7 (ARA-511),
"Studies of the Formation and Transport of High Quality,
High Current Electron Beams, and of the Phase Area
Displacement Operation of a Free Electron Laser Driven by
a Circulating High Current Electron Beam," May 1984.

A BRIEF NOTE ON BEAM QUALITY IN HIGH
CURRENT, FIELD IMMERSED DIODES*

M. L. Sloan and J. R. Thompson

I. INTRODUCTION

Analytical calculations and numerical particle simulations have indicated that very significant improvements in the quality of high current relativistic electron beams are possible through the use of appropriately shaped diode structures which are immersed in very strong, longitudinal magnetic guide fields. Improvements in the beam emittance of one to two orders of magnitude over the Lawson-Penner emittance

$$\epsilon_n = \gamma \beta R \theta = 320 \sqrt{I_b \text{ (kA)}} \text{ mrad-cm} \quad (1)$$

have been observed in some cases.

Increasing the strength of the axial magnetic field can in itself reduce the transverse velocity acquired by beam

*This work was supported by the Office of Naval Research under Contract No. N00014-81-C-0704.

electrons in traversing a given diode structure. As shown in Section II, theoretical estimates are that magnetic fields sufficient for

$$1 \ll \frac{\Omega \Delta z}{\beta_z c} = \frac{e B_z \Delta z}{\gamma \beta_z m c^2} \quad (2)$$

are required for significant beam quality improvement, where Δz is the gradient length of transverse diode forces. Depending upon the type of diode structure, the transverse electron velocity perturbations acquired may scale as $(\Omega \Delta z / \beta_z c)^{-1}$ or as $\exp(-\Omega \Delta z / \beta_z c)$.

For a given magnetic guide field strength, sufficient that the electrons are well tied to field lines, beam quality may be strongly enhanced or degraded by changes in the shape of the anode and cathode structure. The effects of such changes may be explored via numerical particle simulations. Austin Research Associates has developed a code DIODESIGN¹ which is very useful for such high magnetic field diode studies, since it allows a direct calculation of the shape of the cathode structure required to produce a desired current density profile. It is generally found that the best beam quality results from gently-shaped anode and cathode

¹M. L. Sloan and H. A. Davis, Phys. Fluids 25, 2337 (1982).

structures which create electric fields whose radial components have axial gradient lengths long compared to the inverse cyclotron wave number $\beta_z c/\Omega$.

To illustrate these ideas, we have performed several calculations for a diode structure similar to the VEBA apertured diode which has been employed in free electron laser experiments at NRL.² Figure 3, taken from Reference 2, illustrates the VEBA geometry. It is reported that with this geometry, with the guide field strength set at 15 kG, $\beta_1 \sim 0.034$ for the transmitted beam electrons. Figure 1 displays the geometry adopted for our computer simulation studies. In Table 1, parameters are listed for three simulations which have been selected to illustrate the effects of magnetic field strength and of diode geometry upon the transverse velocity acquired by the beam electrons.

It may be observed that for a fixed smooth anode taper (i.e., e-folding length $\simeq 0.51$ cm), increasing the magnetic field from 7.44 kG to 15.0 kG results in the average β_1 decreasing from 0.0221 to 0.0024--a factor of nine! In this diode geometry, it is believed that the primary source of transverse velocity perturbations is the axially varying radial electric field near the entrance to the drift tube. As shown in Section II, such downstream perturbations should

²Robert H. Jackson, et. al., IEEE J. Quantum Electron. QE-19, 346 (1983).

JACKSON *et al.*: COLLECTIVE MILLIMETER-WAVE FEL

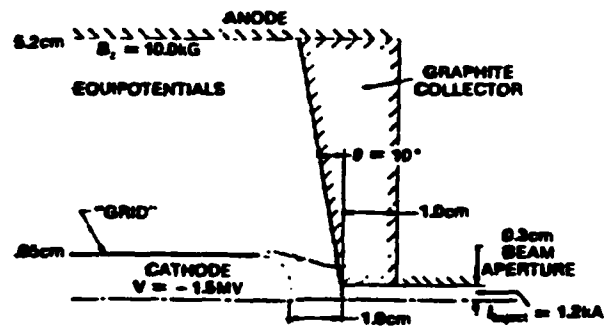


Fig. 3. The VESA apertured diode with the calculated electron trajectories (only half of the trajectories are shown). Note the paraxial flow close to the axis between the cathode and anode, and the defocusing effect of the aperture.

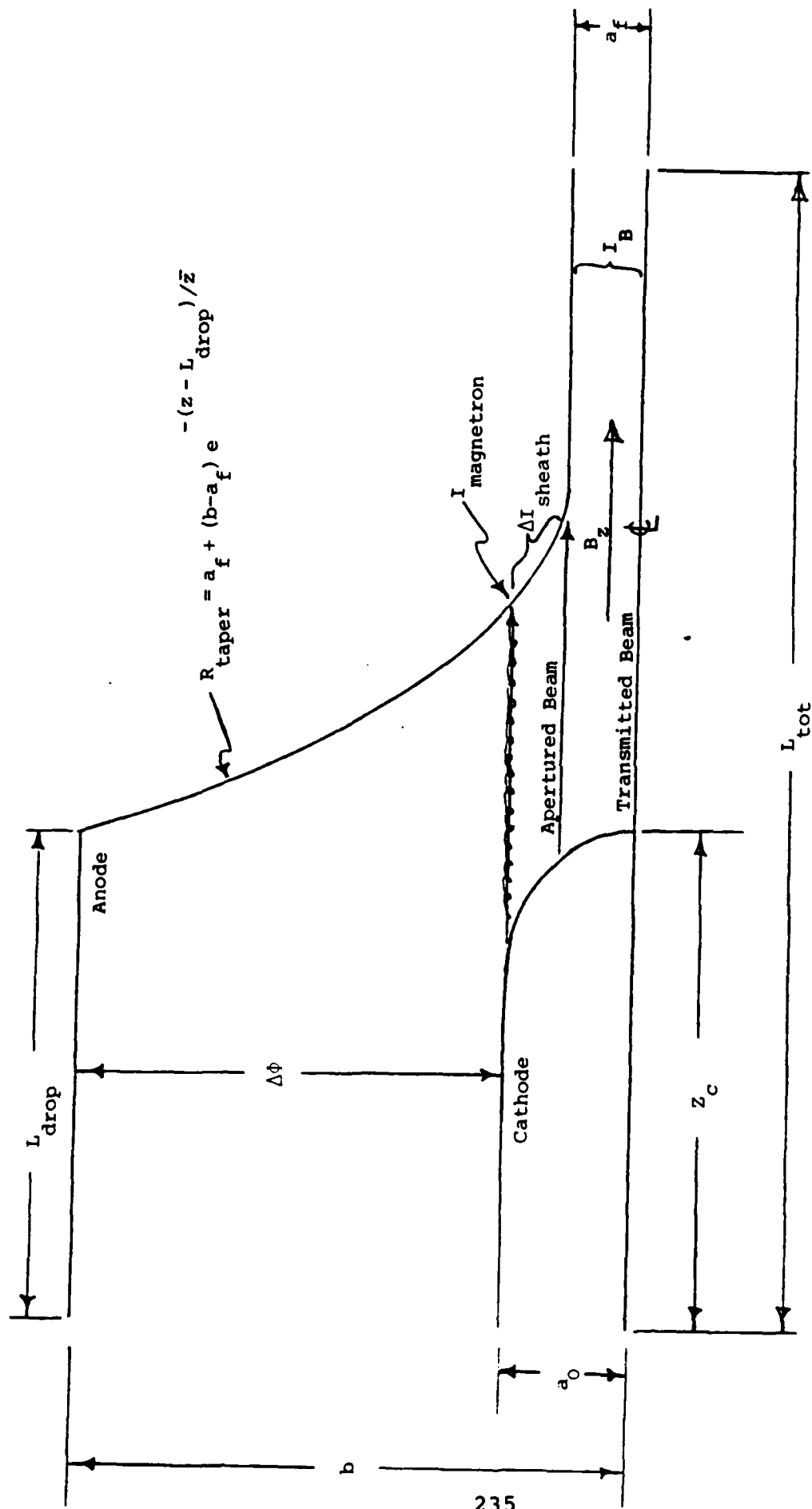


Figure 1. VEBA-like Foilless Diode Geometry

TABLE 1

PARAMETERS FOR BEAM QUALITY STUDIES
IN A MAGNETIZED, FOILLESS DIODE

	<u>Low B_z, Smooth Anode Taper</u>	<u>High B_z, Smooth Anode Taper</u>	<u>High B_z, Sharp Anode Taper</u>
$\Delta\phi$	1.5 MV	1.5 MV	1.5 MV
$I_{\text{magnetron}}$	1.81 kA	0.47 kA	0.47 kA
ΔI_{sheath}	6.3 kA	8.0 kA	8.0 kA
I_B	1.2 kA	1.2 kA	1.2 kA
b	5.20 cm	5.20 cm	5.20 cm
a_o	0.85 cm	0.85 cm	0.85 cm
a_f	0.306 cm	0.306 cm	0.306 cm
L_{tot}	15.20 cm	15.20 cm	15.20 cm
L_{drop}	6.80 cm	6.80 cm	6.80 cm
z_c	6.60 cm	6.60 cm	5.64 cm
\bar{z}	0.51 cm	0.51 cm	0.034 cm
B_z	7.44 kG	15.0 kG	15.0 kG
$\langle \beta_{\perp} \rangle$	0.0221	0.0024	0.0605
$\gamma \langle \beta_{\perp} \rangle a_f$	27 mrad-cm	3 mrad-cm	73 mrad-cm
$\beta_z c / \Omega$	0.87 cm	0.43 cm	0.43 cm

fall off roughly exponentially as the magnetic field strength is raised.

It may also be observed that for a fixed, strong magnetic field of 15 kG, a dramatic sharpening in the anode taper length (from 0.51 cm to 0.034 cm) results in the average β_1 increasing from 0.0024 to 0.0605--a factor of twenty-five! What has happened, of course, is that a sharp corner has been created near the mouth of the drift tube, which creates radial forces with a short axial gradient length. The sharpness of the corner in this third simulation is actually a bit worse than the actual corner shown in Figure 3 for the VEBA diode, which accounts for the simulation β_1 of 0.0605 being almost twice the value reported in the actual VEBA experiment. Nevertheless, it seems clear that the experimental beam quality could undoubtedly be improved significantly if the anode taper were made more gentle.

Our studies suggest that by employing magnetic fields strong enough that beam electrons are tied to the field lines and that $\beta_2 c / \Omega$ is short compared to the axial gradient length of radial forces, and by designing smooth anode-cathode structures, extremely high quality electron beams may be created. Although it has not been considered in this note, it should also be recognized that before such high quality beams can be exploited, it is necessary to design a

beam transport system capable of transporting the beam to the point of use without degrading the previously-acquired quality.

II. DEPENDENCE OF BEAM TEMPERATURE ON MAGNETIC GUIDE FIELD STRENGTH

We assume an axisymmetric diode operated in a strong longitudinal magnetic field $\underline{B} = B_0 \hat{z}$ where the beam is sufficiently cold (or conversely B_0 sufficiently large) that the Larmor radius ($\propto p_\perp/B_0$) is small compared to the dimensions or gradient lengths of the system. We also assume that to lowest order the slow beam rotation is negligible so that

$$\underline{p} \approx p_z \hat{z}$$

$$\frac{dz}{d\tau} = p_z = \gamma \beta_z c \tag{3}$$

$$\frac{d}{d\tau} \equiv \gamma \frac{d}{dt}$$

where τ is the proper time measured along the beam orbit. For such a strong, straight magnetic field, the beam electron radial displacement can be neglected to lowest order, and the beam velocity perturbations may be computed by integrating the force equations along straight line orbits. The perpendicular force equations are

$$\begin{aligned}\frac{dp_r}{d\tau} &= -p_\phi \Omega_0 + F_r \\ \frac{dp_\phi}{d\tau} &= p_r \Omega_0 + F_\phi\end{aligned}\tag{4}$$

where $\Omega_0 \equiv eB_0/mc$, $e = |e|$, and F_r, F_ϕ are the normalized forces on the electrons due to the applied and self fields.

Under the assumption that the gyroradius is small and the electron moves in z according to Equation (3), we introduce

$$p^\pm \equiv p_r \pm ip_\phi$$

to obtain a compact form for Equation (4)

$$\frac{d}{d\tau} p^\pm \mp i\Omega_0 p^\pm = F_r \pm iF_\phi\tag{5}$$

which has an immediate integral

$$p^\pm e^{\mp i\Omega_0 \tau} = \int_0^\tau d\tau' (F_r \pm iF_\phi) e^{\mp i\Omega_0 \tau'}\tag{6}$$

where the integration is taken along the zero order path

$$r = \text{constant}$$

$$\frac{dz}{d\tau} = p_z \quad (7)$$

and the origin $\tau = 0$ is taken at the cathode surface.

The initial condition $p^\pm|_{\tau=0} = 0$ is assumed.

We assume that far downstream of the diode region the beam is again in force equilibrium, for which $F_r \pm iF_\phi \rightarrow \text{constant}$, beyond some τ_{max} , and hence for $\tau > \tau_{\text{max}}$ the upper limit of the integral in Equation (6) may be extended to infinity. Thus the solution for the perturbed beam velocities far downstream of the diode may be written as

$$p^\pm = e^{\pm i\Omega_0 \tau} \int_0^\infty d\tau' (F_r \pm iF_\phi) e^{\mp i\Omega_0 \tau'} \quad (8)$$

Defining $p_1^2 \equiv p_r^2 + p_\phi^2$, we obtain

$$p_1^2 = p^+ p^- = \left| \int_0^\infty d\tau' (F_r + iF_\phi) e^{-i\Omega_0 \tau'} \right|^2 \quad (9)$$

Thus the transverse beam temperature is related to the Fourier transform of the forces acting upon the electrons in the diode region, evaluated at the gyrofrequency.

The transverse forces are given by

$$F_r = \frac{\gamma e}{m} (-E_r + \beta_z B_\phi) + \frac{p_\phi^2}{r} \approx \frac{\gamma e}{m} (-E_r + \beta_z B_\phi)$$

$$F_\phi = -\frac{p_r p_\phi}{r} \approx 0$$
(10)

where the centrifugal and centripetal forces may be neglected in the strong magnetic field. Hence

$$\gamma \beta_\perp = \frac{1}{c} \left| \int_0^\infty d\tau F_r(\tau) e^{-i\Omega_0 \tau} \right|$$

$$= \frac{e}{mc} \left| \int_0^\infty \frac{dz}{c\beta_z} (-E_r + \beta_z B_\phi) e^{-\left(\frac{i\Omega_0}{c} \int_0^z \frac{dz'}{\gamma\beta_z}\right)} \right|$$
(11)

It is apparent from Equation (11) that large transverse velocity perturbations may result when the fields $E_r - \beta_z B_\phi$ have significant components on the same scale length as $\gamma\beta_z c/\Omega_0$. Likewise, increasing B_0 should significantly reduce β_\perp by reducing the latter gyrolength below the transverse force gradient lengths.

Qualitatively, the forces F_r tend to scale as the beam current, although they also reflect the applied diode fields. These forces will tend to be relatively larger for the outer beam electrons than for axial electrons. If unused, to-be-apertured beam electrons are present, these will tend to shield the interior electrons somewhat from the effects of applied transverse diode fields.

To proceed further with this calculation requires detailed knowledge of the diode field structure. However, we may examine two model calculations which serve to illustrate the scalings. The integrand in Equation (11) may be seen to have variations near the cathode due to variations in β_z as the electrons are first accelerated, with the integrand declining as β_z increases. These cathode effects may be roughly modeled as

$$F_r(\tau) = F_0 e^{-\tau/\Delta\tau_0} \quad (12)$$

which leads immediately to the result

$$\beta_{\perp 0} = \frac{F_0 \Delta\tau_0}{\gamma c (1 + \Omega_0^2 \Delta\tau_0^2)^{1/2}} \quad (13)$$

where

$$F_0 = \frac{\gamma e}{m} (-E_r + \beta_z B_\phi) \bigg|_{z=0} \approx - \frac{e E_r}{m} \bigg|_{z=0}$$

$$\Delta\tau_0 \approx \frac{\Delta z_0}{\gamma \beta_z c}$$

and Δz_0 is the acceleration scale length. Since E_r is normally small near the cathode, these β_{10} perturbations should be small and should fall off as B_0^{-1} as B_0 is made very large.

The integrand in Equation (11) may also acquire significant variations downstream of the cathode near any apertures or electrical constrictions near the beam path. The amplitude of these variations may be much larger. Such downstream effects may be modeled as

$$F_r(\tau) = \frac{F_1}{1 + (\tau - \tau_1)^2 / \Delta\tau_1^2} \quad (14)$$

When the width $\Delta\tau_1$ is much less than the location τ_1 , the lower limit on the integral in Equation (11) may be extended from 0 to $-\infty$, and the immediate result is

$$\beta_{11} = \frac{\pi F_1 \Delta\tau_1 e^{-\Omega_0 \Delta\tau_1}}{\gamma c} \quad (15)$$

where

$$F_1 = \frac{\gamma e}{m} (-E_r + \beta_z B_\phi) \Big|_{\tau=\tau_1}$$

$$\Delta\tau_1 \approx \frac{\Delta z_1}{\gamma \beta_z c}$$

and Δz_1 is the effective axial scale length of the radial forces near the downstream constriction at $\tau = \tau_1$. Although F_1 may be rather large, in this case the β_{11} perturbations may be made exponentially small when $\gamma \beta_z c / \Omega_0$ is reduced below Δz_1 .

END

12-86

DTIC